Water calorimetry-based radiation dosimetry in iridium-192 brachytherapy and proton therapy

Arman Sarfehnia

Department of Physics
McGill University, Montreal
March 2010

A thesis submitted to the Faculty of Graduate Studies and Research in partial fulfillment of the requirements of the degree of Doctor of Philosophy.

Dedicated to all those fighting cancer.
May you stay strong and win.
And in loving memory of my grandmother, Mahin.

> “Tell your heart that the fear of suffering is worse than the suffering itself. And that no heart has ever suffered when it goes in search of its dreams, because every second of the search is a second's encounter with God and with eternity.”
>
> L’Alchimiste
> Paulo Coelho

ABSTRACT

The aim of this work is to develop and evaluate a primary standard for HDR ^{192}Ir brachytherapy sources as well as for active spot scanning proton radiotherapy beams based on stagnant 4 °C water calorimetry.

The measurements were performed using an in-house built water calorimeter and a parallel-plate calorimeter vessel. The dose measurement results of the McGill calorimeter were validated in high energy photon beams against Canada's national established primary standard at the NRC. The measurements in brachytherapy were performed with a spring-loaded catheter holder which allowed for the ^{192}Ir source to come directly inside the water calorimeter. The COMSOL MULTIPHYSICS^{TM} software was used to solve the heat transport equation numerically for a detailed geometrical model of our experimental setup. In brachytherapy, reference dosimetry protocols were also developed and used to measure the dose to water directly using thimble type ionization chambers and Gafchromic films with traceable ^{60}Co (or higher energy photons) calibration factor.

Based on water calorimetry standard, we measured an absolute dose rate to water of 361±7 μGy/(h•U) at 55 mm source-to-detector separation. The 1.9 % uncertainty on water calorimetry results is in contrast with the current recommended AAPM TG-43 protocol that achieves at best an uncertainty (k=1) of 2.5 % based on an indirect dose to water measurement technique. All measurement results from water calorimetry, ion chamber, film, and TG-43 agreed to within 0.83 %.

We achieved an overall dose uncertainty of 0.4 % and 0.6 % for scattered and scanned proton radiation water calorimetry, respectively. The water calorimetry absorbed dose to water results agreed with those obtained through the currently recommended IAEA TRS-398 protocol (measurements made using an ionization

chamber with a ^{60}Co calibration factor) to better than 0.14 % and 0.32 % in scattered and scanned proton beams, respectively.

In conclusion, this work forms the foundation for a primary standard in ^{192}Ir brachytherapy and scanning proton radiotherapy using water calorimetry. Not only have we been able to directly and absolute measure the absorbed dose to water, but the uncertainties of dose results over the current accepted protocols have been improved dramatically.

ABRÉGÉ

L'objectif premier de ce travail est de déveloper un standard de référence pour des sources à haut taux d'irradiation ^{192}Ir utilisées en curiethérapie ainsi qu'un autre standard pour un protocole calorimétrique d'irradiation par balayage focalisé avec proton de l'eau inerte à 4 °C.

Les mesures ont été effectuées à partir d'un calorimètre concu et réalisé ici à McGill et d'un autre contenant calorimétrique à plaques parallèles. En curiethérapie calorimetrique ^{192}Ir, un support additionel à ressort pour un catheter a été utilisé permettant l'introduction des sources dans l'eau du calorimètre. Les résultats dosimétriques obtenus par faisceaux d'irradiation à haute énergie de protons dans le calorimètre de McGill, ont été validé par rapport aux standard primaires du NRC du Canada. Le logiciel « COMSOL MULTIPHYSICS » a permi de résoudre les équations numériques de tranfert de chaleur afin de modéliser géométriquement notre montage experimental.

En se référant aux standards calorimétriques de l'eau, nous avons mesuré un taux de dose absolu à l'eau de 361±7 μGy/(h•U) à 55 mm de l'interface de la source et au détecteur. L'incertitude de 1.9% des résultats calorimétriques mesurés D_w sont en contradiction avec l'actuel protocole recommendé par l'AAPM TG-43 qui propose au mieux une mesure d'incertitude de 2.5% avec k=1 basé sur une mesure de transfert d'énergie rayonnante par unité de volume de matière désigné par « air-kerma strength . »

En thérapie d'irradiation par protons et en relation avec les propiétés calorimétriques de l'eau, nous avons obtenu une mesure d'incertitude de dose de 0.4% et 0.6% respectivement pour un faisceau de protons dispersé d'une part et d'un faisceau balayé d'autre part. Ceci représente une amélioration significative par rapport à la valeur d'incertitude exprimée de 2.5% du protocole presentement recommendé IAEA TRS-398 pour k=1 de l'indice D_w. Les résultats

absolus de mesures calorimétriques de l’indice D_w sont indirectement en accord avec l’incertitude proposé par protocole TRS-398 et meilleurs de 0.34% et 0.42% respectivement pour un faisceau de protons dispersé d’une part et faisceau balayé d’autre part.

ACKNOWLEDGMENTS

First and foremost, I would like to thank my wonderful PhD supervisor Dr. Jan Seuntjens to whom I am indebted forever. This project could not have gone so smoothly without his expertise and his immense knowledge in the field, as well as his patience to teach me and guide me every step of the way. I thank him for his kindness, his understanding, and his patience with me.

Many thanks also to Dr. Ervin Podgorsak. He was kind to me from the very first day I arrived in Montreal. He has taught me physics, but he has also taught me about life. He is a great teacher, and a great mentor. For that I am grateful.

Many thanks to Dr. Kristin Stewart for being my friend and an awesome office-mate, but also for teaching me about water calorimetry and standard dosimetry. Many thanks to Dr. Emily Poon for her help with running some of the GEANT4 simulations required in this work. Also, my sincere thanks to my good friend Eunah Chung for her help during the long experiment nights at the proton center. This project would not have been possible without the help of the three engineers of the oncology department of the Montreal General Hospital: Joe Larkin, Bhavan Siva, and Pierre Leger. A special thank you to Pierre for translating my abstract from English to French. Moreover, I would like to express my sincere gratitude to Robin Van Gils, the electro-mechanical technician of the Medical Physics department for his help with building many of the instruments I used throughout this work.

Many thanks to everyone at the NRC for teaching me and helping me throughout various stages of this work: Dr. Iwan Kawrakow helped me immensely by running the EGS++ simulation code for the chamber simulations; David Marchington constructed the thermistors, and never hesitated to give us high purity water; Dr. Carl Ross spent many hours with us doing the measurements under the NRC beam, and helped us pinpoint some of the initial problems with our water calorimeter; Dr. Malcom McEwan taught me much about physics, primary standards, and often life in general after a beer or two.

I would like to acknowledge the help of all our collaborators at the Harvard Medical School and the Massachusetts General Hospital. Sincere thanks to Dr. Benjamin Clasie for his help with proton measurements and making the delivery plans. Dr. Harald Paganetti, Dr. Jay Flanz, Dr. Martijn Engelsman, Dr. Hsiao-Ming Lu, and Mr. Ethan Cascio also helped us immensely throughout the proton measurements.

I thank the CIHR for their doctoral fellowship award, as well as the MUHC award committee for their doctoral scholarship support. This work has also been supported in parts by NSERC grants.

I would like to express my gratitude to Margery Knewstubb and Tatjana Nisic, the department secretaries, without whom we would be lost. I like to thank all the staff, professors, and clinical physicists at McGill medical physics unit for their help, support, and smiles. Special thanks to Dr. Slobodan Devic, Mr. Michael Evans as well as Mr. William Parker.

My sincere thanks to all my friends, colleagues and fellow students (Marie-Joelle, Russell, Emily, Tanner, Ismail, Mark, Danielle, Derek, Erika, Andrew, Magdalena, Keyvan, Genevieve, Gabriella, Michelle, Victor, Nader, Mahvash, Nima, Myriam, Mahdi, Jongmin, Pierre, Sammy, Patrick,… the list is endless).

Many thanks to both my parents, Mehran and Homa, my grandmother Paridokht, my aunts, Hida and Parisa, my uncles, Hormoz and Farhad, and my little cousin Vista for their help, love, and moral support throughout the years. They all believed in me no matter what. It was only through their encouragement and support that I have been able to go on and discover the field I truly love.

TABLE OF CONTENTS

LIST OF TABLES

LIST OF FIGURES

Statement of Originality

To the best of our knowledge, the methods, results and conclusion of the work presented in this thesis have not been previously published. The concept of water calorimetry is not new, and it has been used for radiation dosimetry in high energy photon beams for many years. Indeed, a few chapters of this work have been devoted to explaining the techniques and methodologies used in it.

However, to the best of the authors' knowledge, prior to our work on the subject, no one has published any work on a water calorimeter-based absorbed dose standard in ^{192}Ir brachytherapy. Indeed, our published work has been cited on several occasions as being the first to both numerically and experimentally show the feasibility of this technique. The modifications made to the water calorimeter to make it capable of measuring the absorbed dose in ^{192}Ir brachytherapy, the detailed study of the effects of various parameters on the final dose measurement results, and the post-measurement analysis techniques suggested and used in this work to make HDR ^{192}Ir brachytherapy calorimetry possible are also original and have not been discussed in literature previously.

Moreover, the protocols proposed and followed in this work to measure the absorbed dose to water using ionization chambers and Gafchromic films are also original. As far as we know, the inter-comparison of various reference dosimetry techniques with the water calorimetry primary standard in ^{192}Ir brachytherapy is the most comprehensive work published on the subject.

The use of water calorimetry in passive double scattering proton beams is not new and has been published previously[1]. Although the water calorimeter used in this work had a completely different design from the one used in the previous publication, and while the setup and approach taken in this work was different from the previous work, we do not claim this portion of the study to be original. Indeed, we only use these results as a validation of proper system operation, as well as a verification of the results of the previous study on this subject. However, the work done towards experimentally measuring the absolute absorbed dose in actively scanned proton beams is new. Sassowsky *et al*[2] have numerically shown the feasibility of water calorimetry in scanning delivery; however, again to the best of our knowledge, our experimental measurement of the absorbed dose to water in these beam types is original. Moreover, our detailed study of the effects of the glass vessel (and the effects of the vessel window thickness on the final dose results) in actively scanned proton beams has certainly not been performed previously. This work for the first time experimentally shows the feasibility of developing a water calorimetry-based standard with potentially much higher dose determination accuracy in scanning proton beams.

---

[1] H. Palmans, J. Seuntjens, F. Verhaegen, J. Denis, S. Vynckier, and H. Thierens, "Water calorimetry and ionization chamber dosimetry in an 85-MeV clinical proton beam," Med Phys 23, 643-650 (1996).

[2] M. Sassowsky and E. Pedroni, "On the feasibility of water calorimetry with scanned proton radiation," Phys Med Biol 50, 5381-5400 (2005).

Contribution of Authors

The thesis contains four manuscripts. All manuscripts have been written by me, although help from co-authors in reviewing the papers have been greatly appreciated.

The initial proposal to use water calorimetry to directly measure the absolute absorbed dose to water in ^{192}Ir brachytherapy and active scanning proton beams was initiated by my supervisor, Dr. Jan Seuntjens. His continuous support and help throughout this entire thesis is much appreciated, and of course he is a co-author on all the joint manuscripts we have published. The detailed list of my contribution to each of the four manuscript is listed below.

First manuscript entitled "An absorbed dose to water standard for HDR ^{192}Ir brachytherapy sources based on water calorimetry: numerical and experimental proof-of-principle. "
I performed all the measurements, simulations, and analysis in this work.
Dr. Kristin Stewart helped with her initial design of the ^{192}Ir brachytherapy source holder. Many fruitful discussions with Dr. Stewart are also greatly appreciated.

Second manuscript entitled "Development of a water calorimetry-based standard for absorbed dose to water in HDR ^{192}Ir brachytherapy. "
I have performed all the measurements, simulations, and analysis for this work.

Third manuscript entitled "Direct measurement of absorbed dose to water in HDR ^{192}Ir brachytherapy-water calorimetry, ionization chamber, Gafchromic Film, and TG-43. "
I have performed all the measurements, majority of the simulations and all the analysis for this work.

Dr. Iwan Kawrakow helped with simulating the ^{192}Ir source in egs++ Monte Carlo code, and providing us with the simulation results for the ionization chamber portion of this work.

Fourth manuscript entitled " Development of a water calorimetry based standard in active scanning proton therapy. "

As I could not operate the proton therapy cyclotron by myself, operators from the Massachusetts General Hospital helped me with the operation of the machine. I was fortunate enough to have help at various stages of the measurements from Dr. Ben Clasie, Dr. Hsiao-Ming Lu, Mr. Ethan Cascio, Ms. Eunah Chung, and Dr. Jan Seuntjens. Fruitful discussions with Dr. Matijn Engelsman, Dr. Jay Flanz, and Dr. Harald Paganetti are most appreciated.

Chapter 1

Introduction

1.1 CANCER AND ITS TREATMENT

Cancer is currently the leading cause of premature death in Canada. In 2009, the new number of cancer cases is estimated to reach 171 000 representing approximately 470 Canadians being diagnosed with cancer per day[1]. Excluding non-melanoma skin cancers, lung, colorectal, breast (in women) and prostate (in men) remain the most common cancer types diagnosed, accounting for roughly one half the total number of new cases[1]. Roughly one in every four Canadians will die from cancer, with the risk slightly higher for men than women[1].

Although on the first sight the data looks grim, improvements in the field of cancer detection and cancer therapy have resulted in significant advancements in diagnosis and treatment of cancer resulting in superior patient care and quality of life after treatment. According to the World Health Organization (WHO), roughly one third of all cancer cases around the globe could be cured if they were to be detected early and properly treated[2]. In Canada, improved and early diagnosis of the disease as well as better treatment techniques have resulted in a steady decline in the annual rate of cancer mortality since 1995[1]. Moreover, patients enjoy a higher quality of life during and post treatment with lower side effects and improved survival rates.

Currently, there are four prevailing techniques of treating cancer. These include surgery, chemotherapy, hormonal therapy, and radiation therapy. Surgery strives to remove the tumour (or in some cases the entire organ affected). However, in many instances surgery is not possible due to the type, stage, or location of the tumour. Chemotherapy is the controlled use of drugs to attempt to control the disease, although almost all chemotherapy drugs do not have high enough specificity to leave the patient unharmed, and indeed result in some degree of toxicity to the patient. Hormonal therapy is the attempt to control gene expression in certain cancer cells through administration of hormones. Radiation therapy uses ionizing radiation to kill cancerous cells and shrink the tumours. About half of all cancer patients receive radiation therapy as part of their treatment (either as the sole mode of treatment or in combination with the other three modalities)[3].

Radiation therapy can use either directly ionizing radiation (charged particles including electrons, protons, heavy ions) or indirectly ionizing radiation (neutral particles such as photons and neutrons) to achieve its means. It can also be delivered either externally (often with high energy medical accelerators) or internally (by placing a radioactive source inside the patient close to the tumour). High energy external beam radiation therapy remains the most commonly used form of radiation treatment in cancer therapy[3].

1.2 RADIATION THERAPY

The goal of radiation therapy is to deliver the maximum possible energy to the malignant cancerous cells and to minimize the energy deposited to the healthy normal cells. To that end, radiation therapy has evolved to automatically select one or more beam types, with appropriate energies directed at the tumour from one or more directions, while potentially being modulated in intensity and/or gated in time, all in order to achieve a maximization of tumour control probability and a minimization of normal tissue complication probability. Below some of the various treatment beam modalities will be described.

High Energy Photon and Electron Therapy

The vast majority of all cancer patients around the world are treated with photon and electron beams (75% with photons, and 15% with electrons). The invention of cobalt-60 teletherapy machines in the early 1950s gave a significant boost to the use of external beam radiotherapy in treatment of cancer. Since then, many of the ^{60}Co teletherapy machines have been replaced especially in developed countries in the past two decades with medical linear accelerators (linacs). Clinical linacs can produce electron energies ranging between 4 MeV to 30 MeV. To treat the patients with electrons, the pencil sharp electron beam is directed at a scattering foil and is scattered into a larger field that is later collimated to the shape of the target volume. Photons can be produced by directing the electron beam on a target material[4]. Primarily as a result of Coulomb interactions between incident electrons with the nuclei of the target material, a bremsstrahlung photon spectrum is produced and used for treatment. The linac is normally mounted on a gantry (see Fig. 1.1(A)) that can rotate around the patient and treat the target volume by irradiating it from different directions.

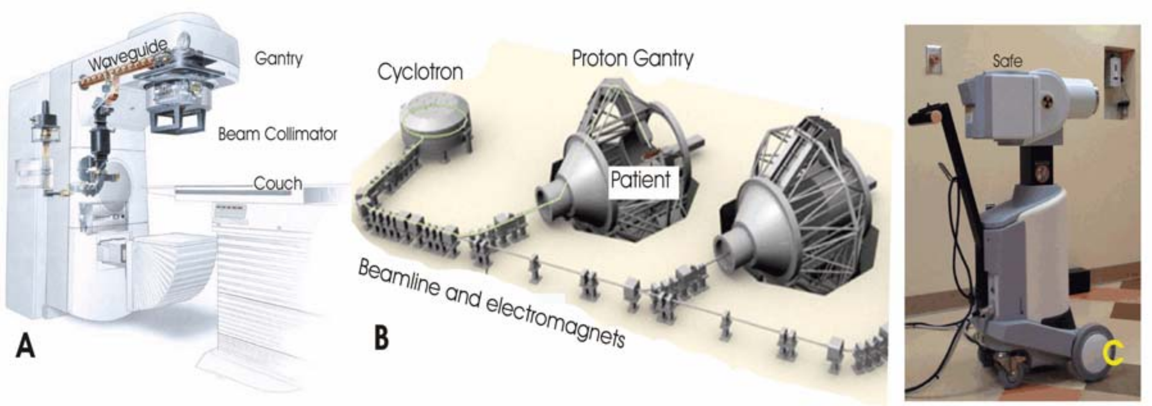

Figure 1.1: A schematic diagram of a clinical linear accelerator (A), as well as that of a proton gantry setup with a cyclotron accelerator (B). A picture of the Nucletron microSelectron ^{192}Ir brachytherapy afterloader is also shown (C).

Particle Therapy

In the recent years, there has been a significant push towards particle therapy in general, and proton therapy in particular[5]. The primary rationale for proton therapy is the potential ability of this modality to deliver a conformal dose to the target while sparing critical organs nearby, while also delivering a reduced total body dose to patients. A characteristic behaviour of protons is that they deposit only a relatively small portion of their energy upon entering tissue, and following a very slow rise in energy deposition with depth, the protons dump all the rest of their energy in a well defined and narrow depth[6] (called Bragg peak). Figure 1.2 compares the relative depth dose distribution of various beam types used in radiotherapy. When normalized to 100% at the maximum dose, the relative depth dose distribution is referred to as percentage depth dose (PDD). PDD will be discussed in greater detail in Chapter 2. The Bragg peak of a mono-energetic proton beam can clearly be seen from the figure.

Since proton therapy is the most common used particle therapy modality[7], and this work focuses on this treatment type alone, we will only focus our discussion on proton therapy. Figure 1.1(B) shows a schematic diagram of a proton therapy facility. Protons are normally accelerated by a cyclotron or a synchrotron to energies of up to 250 MeV[4,6]. The maximum proton energy is normally selected based on the depth of tumours in the body[8]. This is because the most distal parts of the target volume need to be covered by the Bragg peak of the highest energy proton used in treatment. Low energy (60-80 MeV) protons are used in some centers for treatment of malignant disease in the eye (ocular melanoma)[6].

A mono-energetic proton beam’s Bragg peak is normally spread out such that a uniform dose distribution covering the tumour (in depth) is achieved. This is often referred to as a spread-out Bragg peak (SOBP). Currently there are two principle techniques of ‘shaping’ the proton beams, and tailoring their energy deposition distribution to the shape of the target volume. The first and most commonly used technique is referred to as passive double scattering technique, see Fig. 1.3(A).

In this technique, similar to electrons being scattered with a scattering foil, the proton beam is scattered laterally (through multiple Coulomb scattering) using two separate scattering foils[9]. In between the two scatterers, a so-called range modulator wheel is placed[9].

As shown in Fig. 1.3(A), a range modulator, sometimes referred to as a variable degrader, can be either a rotating wheel of varying thickness or a wobbling plate with wedge shaped engravings (also referred to as ridge filter). The purpose of the range modulator (shown in Fig. 1.4) is to introduce a varying thickness of attenuator into the proton beam, thus changing its energy.

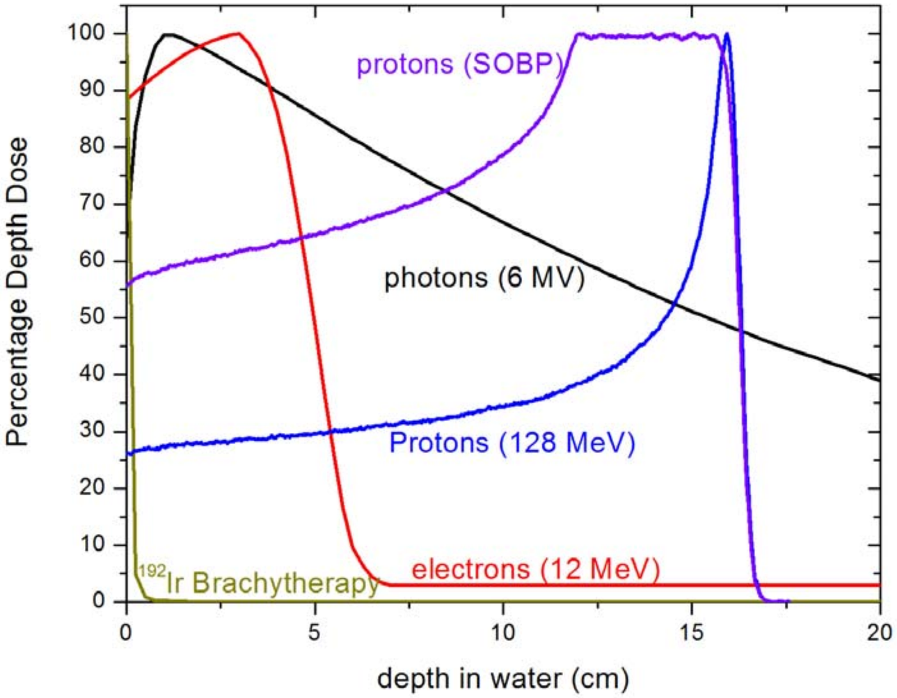

Figure 1.2: A comparison of the percentage depth dose distribution (PDD) curves of electrons, photons, ^{192}Ir brachytherapy and protons. The data reflects a source to surface distance (SSD) of 100 cm for photons and electrons, and 227 cm for protons. In ^{192}Ir brachytherapy, the depth in water is measured from the center of the radioactive source. The PDDs shown are typical PDDs used for patient treatment. A proton SOBP obtained through active spot scanning beam shaping is also displayed.

The rapid energy change translates to a shift of the Bragg peak back and forth in depth, thus producing a spread-out Bragg peak, SOBP. The SOBP has the characteristic of having a sharp distal edge, and is simply the superposition of many modulated Bragg peaks which together yield a relatively uniform energy distribution around the position of the tumour. The large scattered beam is shaped laterally with large patient specific collimators.

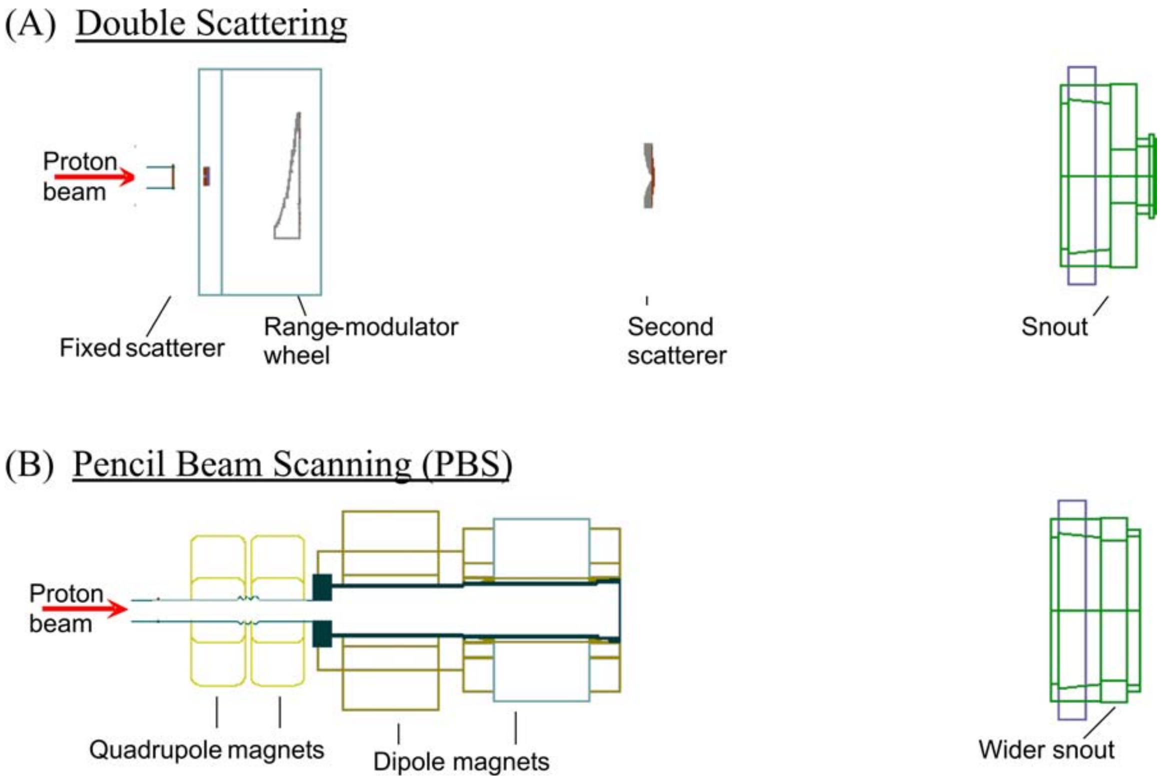

Figure 1.3: A schematic diagram of the important elements in a proton gantry able to shape the beam using passive double scattering (A) and active spot scanning (B) technique.

Figure 1.4: A picture of a range-modulator wheel used to attenuate the proton beam and modulate it in depth[10].

The second proton delivery technique is called the active scanning (or dynamic beam spreading)[9]. It simply consists of magnetically scanning the positively charged proton beam laterally across a layer, see Fig 1.3(B). The energy of the beam is then changed, and a second layer is 'painted.' The final distribution is simply the sum of all individually painted layers. Although much simpler conceptually, technical difficulties in ensuring a safe and accurate delivery have hindered the use of this delivery technique until recently.

The advantages of passive delivery technique include its technical simplicity which directly translates to easier and better beam monitoring and dosimetry[6]. The coupling of field size and maximum beam range is one of the disadvantages of this technique[6]. In order to increase the field size in passive double scattering delivery, a thicker scattering foil has to be used which results in loss of residual treatment range and potential inability of treating deep-seated targets. Furthermore, patient specific physical apertures and blocks must be made to shape the beam laterally. Aside from the incredible amount of resource and time that goes into production of these individual apertures, they are often bulky, heavy, difficult to manually lift, and often get activated by the proton beams. The active scanning beam avoids the need for the extra beam-shaping collimation while minimizing the amount of scatterers and attenuators in the direct path of the beam, hence resulting in minimal neutron contamination in the beam[6]. The complexity of the delivery, potential patient motion during the often lengthy irradiation times, and the increased difficulty in dosimetry mark some of the disadvantages of this technique.

Brachytherapy

Brachytherapy (also referred to as Curietherapy or endocurietherapy) is a form of cancer treatment where a small sealed radionuclide is placed close to the tumour inside the patient. Traditionally radioactive nuclides have been used as brachytherapy sources. Moreover, with the more recent advancements in miniature x-ray tube technology, electronic brachytherapy sources (XOFT Inc.) have become available.

Traditionally, several different radionuclides have been used in several different forms (needles, tubes, seeds, wires, …) to act as the brachytherapy source. These sources are generally categorized into two broad groups of low dose rate (LDR) and high dose rate (HDR) sources. The LDR sources are implanted temporarily or permanently inside the tumour volume (interstitial)[11]. The HDR sources, on the other hand, are always used on a temporary basis and in fact for short durations using either manual or remote afterloading procedures. Figure 1.1(C) shows a Nucletron HDR ^{192}Ir brachytherapy remote afterloader, where the source is kept inside a large tungsten safe. Appropriate catheters can be placed inside body cavities and close to the tumour (intracavitary), implanted surgically within the tumour volume (interstitial), among other techniques. A transfer tube is used to connect the afterloader source ejection channel to the catheter. During radiation beam delivery, the source (firmly attached to the end of a stainless steel cable) is remotely pushed out of the afterloader safe, through the transfer tube and catheter, to the appropriate irradiation position (called dwell position).

1.3 ACCURATE DOSIMETRY

Delivering radiation without a means to quantify and measure it is meaningless. Absorbed dose is defined as the energy deposited per unit mass. The ICRU report 24[12] recommends an overall accuracy of ±5 % on the dose delivery based on a comprehensive analysis of dose response data and clinical outcomes due to errors in dose delivery. Indeed a 5 % change in dose could potentially result in a 10 % to 20 % change in tissue response[13].

There are four major stages in the radiotherapy process, each one with its own uncertainty that contributes to the total uncertainty on the final dose delivered to the patient[13]. These stages are:

1. Absorbed dose to water measurement at a reference point under reference conditions;
2. Relative dose measurements at other depths and non-reference conditions;
3. Dose calculation for treatment planning;
4. Patient setup and irradiation.

Currently research is underway to improve the accuracy of each stage in the radiation therapy process. Through developing more conformal beam delivery techniques and combining them with more sophisticated online or offline imaging techniques, the overall accuracy of patient irradiation is hoped to improve. Through using such sophisticated techniques as Intensity modulated radiation therapy (IMRT), Image Guided Radiation therapy (IGRT), volumetric modulated arc therapy (VMAT), or through combining various beam types such as photons with electron boosts, or protons (and such techniques as intensity modulated proton therapy, IMPT), the uncertainty on the fourth stage of radiation therapy process is being reduced. Research towards more sophisticated treatment planning systems based on convolution/superposition, collapsed cone algorithm, or Monte Carlo show significant promise in reducing the uncertainty in the third stage of the radiotherapy process.

The advancements of new detectors with better spatial resolution, ease of use, and lower energy dependence comprise an attempt to improve the accuracy of the second stage of radiation therapy process. Moreover, in an attempt to better understand better and evaluate many of the novel 4D 'time-dependent' radiation therapy modalities, much research has also been directed in recent years to design and build appropriate phantoms that mimic the human body and its motion (e.g., due to respiration) during treatment. Improvements of the first stage depends clearly on advances in standards at the national and international levels as well as improvements in reference dosimetry protocols at the level of individual clinics. This work tries to improve the radiation therapy process by primarily focusing on the first stage: The measurement of absorbed dose to water under reference conditions.

1.4 THESIS HYPOTHESIS

Currently there are no primary dosimetry standards in either HDR ^{192}Ir brachytherapy or in proton therapy. Standard laboratories rely on indirect dose to water measurements which are often dependent upon calculated and/or interpolated correction factors. We hypothesize that, by using a water calorimeter based radiation standard, the absolute absorbed dose to water can directly be measured in ^{192}Ir brachytherapy and proton radiotherapy which will allow for an evaluation of the current indirect dosimetry protocols and will help establish a more accurate uncertainty budget based on direct dose to water measurements.

1. **HDR ^{192}Ir brachytherapy**: The current dosimetry protocols make use of indirect measurement of absorbed dose using detectors that have been calibrated for photon beam energies that are significantly different from the

effective ^{192}Ir beam energy. Moreover, the calibration is directly dependent upon using an interpolative technique which increases the uncertainty on the entire calibration coefficient. Furthermore, the measurements are performed in air, and calculated conversion coefficients are subsequently used to convert the measurements to in-water dose results. In this work, we attempt to use a water calorimeter to measure directly the absorbed dose to water at a point in absolute terms, hence eliminating the need for any of the currently required calibration or conversion coefficients (and thus removing their uncertainty from the overall uncertainty budget of the final dose measurement results). The uncertainty of the current indirect method of dose measurement is 2.5-3.0 % (k=1).

We also attempt to design robust protocols to measure the absorbed dose to water directly using ionization chamber and radiochromic film measurements. The in-water measurement results are to be compared with the currently accepted dosimetry protocols used in ^{192}Ir brachytherapy, as well as water calorimetry primary standard.

2. **Proton therapy**: The current dosimetry protocols are based on an indirect measurement of the dose using detectors that have been calibrated under ^{60}Co beam. By using a chamber specific, beam quality dependent conversion factor, the ^{60}Co-based detector calibration coefficient is converted from its reference conditions to the new measurement conditions (in protons). In this work, we attempt to eliminate the need for such conversion factors in proton dosimetry and to improve the accuracy of dose measurements through the direct and absolute measurements of absorbed dose to water. The uncertainty with the current dosimetry technique is 1.8-1.9 % (k=1).

1.5 THESIS OBJECTIVES

To test the hypotheses of this work, the McGill water calorimeter (MWC) was modified to measure the dose in HDR ^{192}Ir brachytherapy and external proton radiotherapy beams. The objectives of this thesis are:

1. To validate the MWC response in high energy photon beams, since water calorimetry standard has been well established for these beams.

2. To study numerically the effects of heat transfer (conduction and convection) in water using COMSOL MULTIPHYSICS^{TM} partial differential equation solver, and to compare its calculated results to the currently available published data and experiments.

3. To calculate the correction coefficients for water calorimetry using COMSOL MULTIPHYSICS^{TM} and Monte Carlo calculation software programs for both ^{192}Ir brachytherapy and proton radiotherapy beams.

4. To measure accurately the absolute absorbed dose to water in HDR ^{192}Ir brachytherapy and proton radiotherapy, and to establish a new primary standard protocol based on water calorimetry in these two treatment modality techniques.

5. To design robust protocols for measurement of absorbed dose to water directly using ionization chamber and radiochromic film reference dosimetry. This includes accurate calculation of correction and conversion factors that are required to convert the measured quantity (dose to detector material) into the desired quantity (absorbed dose to water) according to our designed reference dosimetry protocol.

6. To measure accurately the dose to water using reference dosimetry in ^{192}Ir brachytherapy and compare the results to current accepted protocols and water calorimetry primary standard.

1.6 THESIS ORGANIZATION

Chapter 2 reviews some of the relevant topics in medical radiation physics and dosimetry, and describes the current techniques and protocols used in primary standard. Chapter 3 discusses the water calorimeter built and used in this project, along with detailed discussions of its most important components. Chapter 4 describes in detail the theory behind water calorimetry. Chapters 5 through 8 are four manuscripts that have been published through this work. The measurement of dose to water in HDR ^{192}Ir brachytherapy using water calorimetry primary standard (Chapters 5 and 6), and using ionization chambers and radiochromic films reference dosimetry (Chapter 7) are discussed. Chapter 8 summarizes our work in proton therapy water calorimetry.

1.7 REFERENCES

[1] Canadian Cancer Society/National Cancer Institute of Canada, Canadian Cancer Statistics 2009. Toronto, Canada, 2009.

[2] World Health Organization, The World Health Organization's Fight Against Cancer: Strategies That Prevent, Cure and Care. Geneva, Switzerland, 2007.

[3] National Cancer Institute, Radiation Therapy for Cancer: Questions and Answers. 2009.

[4] E. B. Podgorsak, "Review of Radiation Oncology Physics: A Handbook for Teachers and Students," in *Treatment Machines for External Beam Radiotherapy*, edited by E. B. Podgorsak (International Atomic Energy Agency, Vienna, 2005).

[5] O. Jakel, G. H. Hartmann, C. P. Karger, P. Heeg, and J. Rassow, "Quality assurance for a treatment planning system in scanned ion beam therapy," Med Phys 27, 1588-1600 (2000).

[6] D. W. Miller, "A review of proton beam radiation therapy," Med Phys 22, 1943-1954 (1995).

[7] D. E. Bonnett, "Current developments in proton therapy: a review," Phys Med Biol 38, 1371-1392 (1993).

[8] A. R. Smith, "Proton therapy," Phys Med Biol 51, R491-504 (2006).

[9] W. T. Chu, B. A. Ludewigt, and T. R. Renner, "Instrumentation for treatment of cancer using proton and light-ion beams," Rev. Sci. Instrum. 64, 2055-2122 (1993).

[10] H. Paganetti and T. Bortfeld, "Proton Beam Radiotherapy - The State of the Art," in *New Technologies in Radiation Oncology (Medical Radiology Series)*, edited by T. Schlegel, T. Bortfeld, and A. L. Grosu (Springer Verlag, Heidelberg, 2005).

[11] N. Suntharalingam, E. B. Podgorsak, and H. Tolli, "Brachytherapy: Physical and Clinical Aspects," in *Review of Radiation Oncology Physics: A Handbook for Teachers and Students*, edited by E. B. Podgorsak (2005).

[12] ICRU (1976) report 24 "Determination of absorbed dose in a patient irradiated by beams of X or gamma rays in radiotherapy procedures."

[13] *The Modern Technology of Radiation Oncology: A Compendium for Medical Physicists and Radiation Oncologists,* edited by J. Van Dyk (Medical Physics Publishing, Madison, WI, 1999)

Chapter 2

Radiation dosimetry

2.1 CONCEPTS AND NOMENCLATURES

This section begins by describing various relevant radiation dosimetry definitions and concepts. The discussions will be brief as they are provided for reference purposes only. Since this work revolves around the establishment of a primary absorbed dose standard for two different radiotherapy modalities, we devote a short section to describing the characteristics of the two radiation types used, while also discussing the various radiation standard techniques.

2.1.1 Nomenclature

KERMA or Kinetic Energy Released per unit MAss is the average energy transferred by photons to electrons in a volume element without taking into account subsequent interactions of the electrons[1]. Its unit is joule per kilogram (J Kg^{-1}) or gray (Gy). Kerma is further subdivided into a collision (K_{col}) and a radiation part (K_{rad}). The former is the portion of kerma arising from inelastic collisions with orbital electrons (includes soft and hard collisions resulting in atomic excitations and ionizations), while K_{rad} is the part of kerma arising from inelastic radiation interactions of the ionizing particle with the nucleus.

MASS ENERGY TRANSFER COEFFICIENT $\left(\mu_{\text{tr}}/\rho\right)$ is an attenuation coefficient proportional to the average energy transferred by photons traversing the medium to the charged particles (electrons and positrons) of the medium. For a mono-energetic beam, the multiplication of this coefficient by the photon energy fluence Ψ yields kerma. Energy fluence is the product of a beam's fluence Φ and photon energy E, $\Psi(E) = \Phi(E) \cdot E$.

MASS ENERGY ABSORPTION COEFFICIENT $\left(\mu_{\text{en}}/\rho\right)$ is proportional to the fraction of energy transferred to the medium that is actually absorbed in the medium. The fraction of the energy transferred to charged particles of the medium that is lost through radiative processes is represented by a factor referred to as radiation yield $\bar{g}$; hence, the mass energy absorption coefficient and the mass energy transfer coefficient are related through,

$$\frac{\mu_{\text{en}}}{\rho} = \frac{\mu_{\text{tr}}}{\rho}\left(1-\bar{g}\right). \tag{2.1}$$

Hence, for a mono-energetic beam, all components of kerma can be explained through the following three relations

$$K = K_{\text{col}} + K_{\text{rad}} = \Phi E \frac{\mu_{\text{tr}}}{\rho} = \Psi \frac{\mu_{\text{tr}}}{\rho}, \tag{2.2}$$

$$K_{\text{col}} = K(1-\bar{g}) = \Phi E \frac{\mu_{\text{en}}}{\rho} = \Psi \frac{\mu_{\text{en}}}{\rho}, \tag{2.3}$$

$$K_{\text{rad}} = K\bar{g} = \Phi E \frac{\mu_{tr}}{\rho}\bar{g} = \Psi \frac{\mu_{tr}}{\rho}\bar{g}. \tag{2.4}$$

ABSORBED DOSE is defined as the energy deposited by ionizing radiation per unit mass of a given material. Although energy is transferred to charged particles (KERMA), not all of it is absorbed in the medium since some of it is lost in radiative processes and leaves the medium. Hence, absorbed dose is kerma less the energy transferred away through radiation losses (bremsstrahlung and annihilation in flight). Absorbed dose is also measured in Gy and is often the quantity of interest in radiation therapy.

CHARGED PARTICLE EQUILIBRIUM (CPE): As photons travel through the medium, more and more electrons are set into motion, increasing the number of ionizations, while on the other hand, photon attenuation results in a reduction in the total number of photons available for energy transfer. These two opposing effects give rise to a point of equilibrium, where the number of electrons entering a given volume equals the number of electrons leaving it, thus producing a condition termed “charged particle equilibrium”. Past this point, photon attenuation becomes the dominant factor resulting in a gradual decrease in kerma and absorbed dose. Since the absorbed dose at any point beyond the peak is due to the kerma further upstream, the absorbed dose curve is always above the collision kerma curve[2]. The region past the depth of maximum dose is referred to as the region of the TRANSIENT CHARGED PARTICLE EQUILIBRIUM (TCPE). Figure 2.1 shows the relation between collision kerma and dose as a function of depth in the medium. Past the depth of maximum dose (in TCP region), the relation between dose and collision kerma is described by a constant factor β, where

$$D = K_{\mathrm{col}}\beta \, . \tag{2.5}$$

PERCENTAGE DEPTH DOSE or PDD is defined as the ratio, expressed as a percentage, of absorbed dose at any depth z to the absorbed dose at a reference depth z_{ref} along the central axis of the beam. The reference depth z_{ref} is normally taken as the depth of the maximum dose z_{max}. It is a function of beam energy, field size on the surface of the phantom, distance between radiation source and the surface of the phantom (SSD), and depth in material z. Figure 2.1 shows a generic PDD curve for a megavoltage beam if the maximum dose was to be normalized to 100 %.

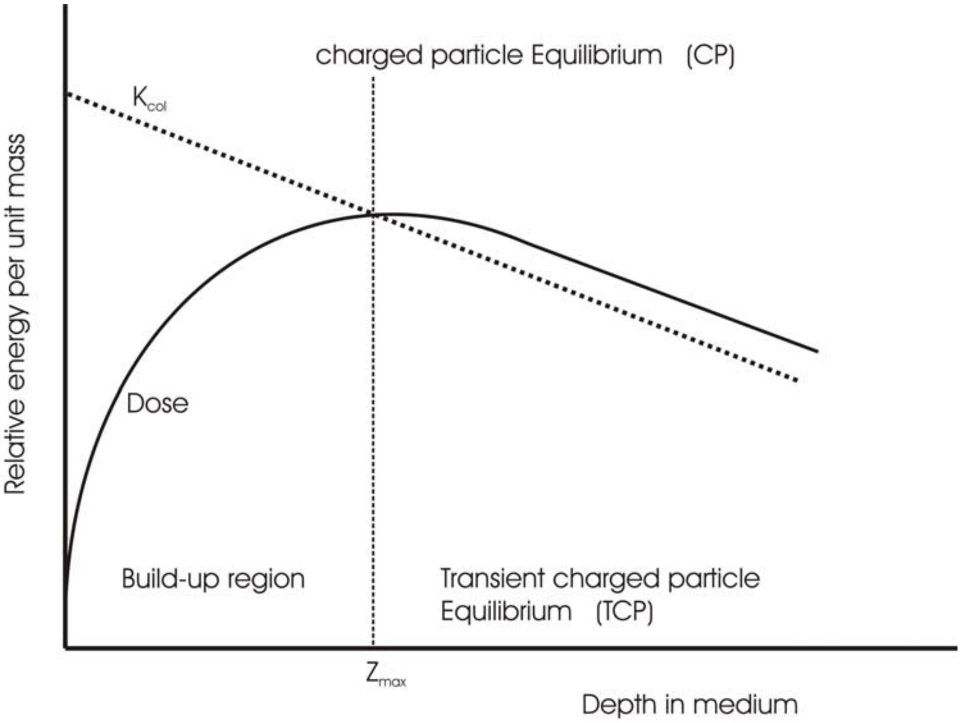

Figure 2.1: A generic graph showing the behaviour of absorbed dose and collision kerma (K_{col}) as a function of depth in medium for a megavoltage beam. If the max dose at $z_{\max}$ was to be normalized to 100 %, the curve entitled 'Dose' would represent a PDD curve.

TOTAL MASS STOPPING POWER (S/ρ) describes the amount of energy loss by a particle per unit length along its track. Its unit is commonly taken to be (MeV cm^2 g^{-1}). Similar to kerma, the total mass stopping power consists of two components: the mass collision stopping power which results from interactions of the ionizing particles with orbital electrons, and the mass radiative stopping power which results from inelastic interactions of the ionizing particle with atomic nuclei. In radiation dosimetry, a closely related concept, the restricted stopping power (L_{Δ}/ρ) is also often used. It is that fraction of collision stopping power that excludes hard collisions resulting in delta rays with energies greater than a cut-off value Δ.

LINEAR ENERGY TRANSFER (LET) describes the rate at which a directly ionizing particle deposits energy along its track. LET is indeed equivalent to the restricted stopping power when attention is focused on the absorbing medium and the way energy is actually deposited along the particle's track. Expressed in (keV μm^{-1}), LET is often used to describe the quality of radiation.

2.1.3 Cavity Theory

In order to measure the absorbed dose in a medium, a radiation detector needs to be introduced into the volume. Generally, the detector and its sensitive volume are not of the same material as the surrounding medium. The cavity theory is concerned with the conversion of measured dose in the detector (dosimeter) material into absorbed dose to surrounding medium.

In *Section 2.1.1*, dose and kerma were defined and were shown to be in fact closely related past the charged particle equilibrium. Given a mono-energetic charged particle beam traversing a given medium, the dose delivered to the medium D_{med} can be described by[3,4]

$$D_{\mathrm{med}} = \Phi_{\mathrm{med}} \left(\frac{S_{\mathrm{col}}}{\rho} \right)_{\mathrm{med}}, \qquad (2.6)$$

where Φ_{med} is the particle fluence inside the medium and $\left(S_{\mathrm{col}}/\rho \right)_{\mathrm{med}}$ is the (unrestricted) mass collision stopping power of the particles in the medium, as previously defined. Generalizing Eq. 2.6 to a beam with a spectrum of energies $\Phi_{\mathrm{med}}\left(E\right)$, we get,

$$D_{\mathrm{med}} = \int_0^{E_{\mathrm{max}}} \Phi_{\mathrm{med}}(E) \left(\frac{S_{\mathrm{col}}\left(E\right)}{\rho} \right)_{\mathrm{med}} \mathrm{d}E, \qquad (2.7)$$

where the absorbed dose to the medium is simply the sum of the deposited dose for every energy interval dE in the full range of electron energies up to the maximum electron energy E_{max}.

Bragg-Gray Cavity Theory

Many of the applications in radiotherapy involve the use of a detector whose sensitive volume is small relative to the range of the electrons that have been set in motion and are traversing the medium. In such cases, if it can be assumed that the detector only 'senses' the electrons without perturbing the charged particle fluence (both number and energy fluence), then the Bragg-Gray cavity theory can be applied[3,5-7]. Generally, a second assumption is noted which states that the dose in the detector material should come solely from the charged particles crossing the cavity. In such cases, given the primary charged particle's fluence map $\Phi_{\mathrm{med}}^{\mathrm{prim}}(E)$ (which by the assumption made in Bragg-Gray cavity theory is equivalent to the fluence through the detector's cavity), the dose to detector material D_{det} can be converted to dose to the medium D_{med} by using Eq. 2.7 (where $X_{\mathrm{det}}^{\mathrm{med}}$ is a shorthand notation for $X_{\mathrm{med}}/X_{\mathrm{det}}$)

$$\frac{D_{\mathrm{med}}}{D_{\mathrm{det}}}=\frac{\int_{0}^{E_{\max}}\Phi_{\mathrm{med}}^{\mathrm{prim}}(E)\cdot\left(\frac{S_{\mathrm{col}}(E)}{\rho}\right)_{\mathrm{med}}\mathrm{d}E}{\int_{0}^{E_{\max}}\Phi_{\mathrm{med}}^{\mathrm{prim}}(E)\cdot\left(\frac{S_{\mathrm{col}}(E)}{\rho}\right)_{\mathrm{det}}\mathrm{d}E}=\left(\frac{\bar{S}_{col}}{\rho}\right)_{\mathrm{det}}^{\mathrm{med}}. \tag{2.8}$$

Spencer-Attix Cavity Theory

The application of Eq. 2.8 and its accuracy in radiotherapy are limited. In reality, the primary radiation beam will interact everywhere (both inside and outside the finite volume of the detector cavity), and the electrons produced inside the cavity may indeed lose a fraction of their energy as they leave the cavity. The requirement for the cavity not to disturb the fluence implies that for every secondary (or higher generation) electron that enters the cavity, one of the same energy should leave. This can only be true if either the secondary electrons produced by hard collisions (δ rays) are absorbed on the spot (Bragg-Gray's assumption) or that both the detector and its surrounding are of exactly the same material.

Spencer and Attix[8] approached the problem without restricting themselves to zero-range δ rays. They assumed that the primary charged particles lose energy in a continuous slowing down approximation (CSDA) fashion, and they allowed for the higher generation electrons (secondary, tertiary, etc.) to travel a given distance. Spencer and Attix did not differentiate the various generations of electrons, however, but rather looked at the full spectrum of all electrons set in motion.

They divided the full spectrum of electrons into two categories based on their energies using an energy threshold Δ which is calculated based on the size of the cavity. This threshold is taken to be the minimum energy of the electrons required to cross the length of the cavity. The approach assumes that all electrons with energy higher than Δ cross the cavity and, as such, a state of charged particle equilibrium for these particles is assumed to exist. In this sense, the dose deposited in a medium D_{med} given a total electron fluence spectrum (containing all generations of electrons) $\Phi_{\mathrm{med}}^{\mathrm{tot}}(E)$ can be calculated by,

$$D_{\mathrm{med}} = \int_{\Delta}^{E_{\max}} \Phi_{\mathrm{med}}^{\mathrm{tot}}(E) \cdot \left(\frac{L_{\Delta}(E)}{\rho} \right)_{\mathrm{med}} \mathrm{d}E\,, \tag{2.9}$$

where $\left(L_{\Delta}(E)/\rho\right)_{\mathrm{med}}$ is the restricted stopping power defined in *Section 2.1.1*. Hence, to the first order, Spencer and Attix only looked at electrons with energies larger than the threshold Δ, while only the fraction of collision stopping power resulting to energy losses less than Δ are accounted for.

If Eq. 2.9 was to be used alone, we would have simply ignored all delta rays with energies below the threshold. Although they deposit their energies locally, these low energy electrons may be produced inside the cavity as well which means that Eq. 2.9 would underestimate the dose. Nahum[9,10] describes an additional term accounting precisely for this 'end track' effect which is described by

$$\Phi_{\mathrm{med}}^{\mathrm{tot}}(\Delta)\left[S_{\mathrm{col}}(\Delta)/\rho\right]_{\mathrm{med}}\Delta\,. \tag{2.10}$$

Nahum argues that the product of total electron fluence at energy Δ and collision stopping power calculated at Δ approximates the number of electrons slowing down past Δ, which when multiplied by energy Δ, gives the total energy due to track length. The full Spencer-Attix cavity theory with Nahum track end correction yields a dose to detector material D_{det} to dose to medium D_{m} conversion of (combining Eq. 2.9 and 2.10)[3]

$$\frac{D_{\text{med}}}{D_{\text{det}}} = \left(\frac{\overline{L}_{\Delta}}{\rho}\right)_{\text{det}}^{\text{med}} = \frac{\int_{\Delta}^{E_{\max}} \Phi_{\text{med}}^{\text{tot}}(E)\cdot\left(\frac{L_{\Delta}(E)}{\rho}\right)_{\text{med}} \mathrm{d}E + \Phi_{\text{med}}^{\text{tot}}(\Delta)\cdot\left(\frac{S_{\text{col}}(\Delta)}{\rho}\right)_{\text{med}}\cdot\Delta}{\int_{\Delta}^{E_{\max}} \Phi_{\text{med}}^{\text{tot}}(E)\cdot\left(\frac{L_{\Delta}(E)}{\rho}\right)_{\text{det}} \mathrm{d}E + \Phi_{\text{med}}^{\text{tot}}(\Delta)\cdot\left(\frac{S_{\text{col}}(\Delta)}{\rho}\right)_{\text{det}}\cdot\Delta} . \tag{2.11}$$

The cavity theory as described for electrons is valid for any type of primary charged particles traversing the medium. Hence, similar formulation as above can be used for primary proton beams as long as the assumptions of the cavity theory hold for the specific situation[11].

2.1.4 Ionization Chamber Dosimetry

We shall apply the cavity theory obtained above to two special cases of ionization chamber cavities, and explain the procedures used to obtain the dose to medium.

Thick wall chamber

As the name implies, a thick wall chamber has a wall thickness which is thick enough to act as medium for the air cavity of the ionization chamber (i.e., all charged particles that pass through the cavity and contribute to the total signal are initiated inside the chamber wall).

For depths past that are required for CPE conditions, Eq. 2.5 relates dose to kerma. Furthermore, Eq. 2.3 describes the relation between collision kerma and photon energy fluence. Combining the two equations and generalizing Eq. 2.3 to take into account a photon spectrum (in its original form, Eq. 2.3 is only valid for simple mono-energetic beams), the dose to medium can be obtained by

$$D_{\mathrm{med}} = \beta \left(K_{\mathrm{col}}\right)_{\mathrm{med}} = \beta \int_{0}^{E_{\max}} \Psi(E) \left(\frac{\mu_{\mathrm{en}}(E)}{\rho} \right)_{\mathrm{med}} \mathrm{d}E = \beta \Psi \left(\frac{\bar{\mu}_{\mathrm{en}}}{\rho} \right)_{\mathrm{med}}, \quad (2.12)$$

where $\left(\bar{\mu}_{\mathrm{en}}/\rho\right)_{\mathrm{med}}$ is defined as,

$$\left(\frac{\bar{\mu}_{\mathrm{en}}}{\rho} \right)_{\mathrm{med}} = \frac{\int_{0}^{E_{\max}} \Psi(E) \left(\frac{\mu_{\mathrm{en}}(E)}{\rho} \right)_{\mathrm{med}} \mathrm{d}E}{\int_{0}^{E_{\max}} \Psi(E) \mathrm{d}E} = \frac{\left(K_{\mathrm{col}}\right)_{\mathrm{med}}}{\Psi}. \quad (2.13)$$

Ignoring the cavity altogether and assuming the wall of the chamber to be a large photon detector, the dose contribution in the center of the detector is dominated by the electrons produced by photons interacting within the detector. Hence, the ratio of the dose at the center of the detector can be related to the dose at the same point in an otherwise uniform medium by taking the ratio of two collision kermas. Using Eq. 2.12, we get

$$D_{\mathrm{med}}^{\mathrm{det}} = \left(K_{\mathrm{col}}\right)_{\mathrm{med}}^{\mathrm{det}} = \left(\frac{\bar{\mu}_{en}}{\rho} \right)_{\mathrm{med}}^{\mathrm{det}}. \quad (2.14)$$

To obtain the simple relation in Eq. 2.14, the assumption has been made that the detector provides buildup without disturbing the photon energy fluence. As such, the ratio of the total energy fluence is taken to be unity (i.e. $\Psi_{\mathrm{m}_1}^{\mathrm{m}_2} = 1$). Moreover, we have assumed that the range of electrons is similar in both materials resulting in the factor β relating dose to collision kerma to be a constant, the ratio of which is unity. For not too dissimilar materials, both assumptions are valid.

Equipped with Eq. 2.14, we shall now approach the original problem, that of a thick wall large cavity chamber. Under the same assumptions as before, the doses in the wall and in the medium are related through

$$D_{\text{med}} = D_{\text{wall}} \left(\frac{\bar{\mu}_{\text{en}}}{\rho} \right)_{\text{wall}}^{\text{med}} . \tag{2.15}$$

Now, let us consider the air cavity. Since the wall is assumed to be thick enough to act as the medium for the air cavity of the ionization chamber, we can argue that the dose measured inside the chamber's gas cavity (we shall refer to in our equations as 'gas') is related to dose in the wall surrounding it through Eq. 2.11. Hence,

$$D_{\text{wall}} = D_{\text{gas}} \left(\frac{\bar{L}_{\Delta}}{\rho} \right)_{\text{gas}}^{\text{wall}} . \tag{2.16}$$

Last thing that remains is to note that in fact an ionization chamber does not measure dose directly, but as the name implies, it measures ionization (or ion pairs). The dose to detector is in fact calculated through a quantity $\left(\bar{W}_{\text{air}}/e\right)$ which describes energy required for an electron to produce an ion pair in air. Hence, we have finally obtained a very good approximation to the total dose deposited in the medium as measured by a thick wall chamber cavity (by combining Eq.'s 2.15 and 2.16)

$$D_{\text{med}} = \left(\frac{Q_{\text{air}}}{m_{\text{air,gas}}} \right) \left(\frac{\bar{W}_{\text{air}}}{e} \right) \left(\frac{\bar{L}_{\Delta}}{\rho} \right)_{\text{gas}}^{\text{wall}} \left(\frac{\bar{\mu}_{\text{en}}}{\rho} \right)_{wall}^{\text{med}} , \tag{2.17}$$

where the first term in bracket (*Q/m*) is simply the charge per unit mass measured inside the air chamber cavity of the ionization chamber. Although, we have been referring to the material inside the cavity chamber as 'gas', normally, for almost all commonly used chambers, the gas is nothing but air.

Thin wall chamber

We shall now discuss the second of the two scenarios. A chamber with a thin wall placed inside a medium. This is much closer to the measurement conditions faced in clinics where a thin wall ionization chamber is used in water (or solid water, for convenience) to measure the dose to medium. In these cases, the thin wall does not act as the medium for the cavity, but rather is simply accounted for through a correction[4]. In the example above, the medium providing the electrons that pass through the chamber cavity is water (or solid water). As such a simple Spencer-Attix cavity theory (Eq. 2.11) will be used to calculate the dose to the medium by

$$D_{\text{med}} = \left(\frac{Q_{\text{air}}}{m_{\text{air,gas}}} \right) \left(\frac{\overline{W}_{\text{air}}}{e} \right) \left(\frac{\overline{L}_{\Delta}}{\rho} \right)_{\text{gas}}^{\text{med}} \prod_i p_i \, , \tag{2.18}$$

where p_i are correction factors that account for various effects including wall perturbation, electron fluence perturbation, and the perturbations due to the presence of the central electrode, among other things.

2.2 CALIBRATION CHAIN

Perhaps one of the most important reasons for the rapid development of science, technology and medicine remains to be the implementation of a minimum level of standardization and quality control. A traceable standard allows for comparison of results, exchange of ideas, and subsequent improvement of outcome.

A standard in radiation therapy dosimetry calls for traceability of dose measurements performed at, e.g., a cancer institute to a national standard and subsequently to an international regulatory body. To achieve this, there are several stages of metrological bodies. The primary standard dosimetry laboratory (PSDL) is a national body assigned by the government to maintain and improve the radiation dosimetry standard[12]. They are in charge of calibrating secondary detectors, based on their established standard, for their users which include hospitals, cancer centers, and other laboratories across the nation.

Bureau International des Poids et Mesures (BIPM) is an international laboratory that facilitates comparisons of data and standards between various PSDLs around the world[13]. For countries without a PSDL, BIPM establishes a minimum level of standard by directly calibrating the secondary standards that are kept at the countries' national measurement institute[12].

Secondary standard dosimetry laboratories (SSDL) are normally empowered by the national government to provide calibration services to users across the country (sometimes in the absence of a national PSDL)[12]. In the United States, due to overwhelming demand for calibration services from the country's PSDL, three additional agencies (similar in concept to SSDL) were formed to maintain traceable standards and disseminate the standard to users across the nation. These agencies have been granted the status of accredited dosimetry calibration laboratories (ADCL). In Canada, the nation's PSDL, the Ionization Radiation Standards group of the National Research Council of Canada (NRC), is the sole body in charge of maintaining absorbed dose and air kerma based standards and cross-calibrating users' secondary standards.

The concept of traceability of a user's ionization chamber (detector of choice in radiation therapy for dose traceability due to its robustness and high sensitivity) to a national primary standards dosimetry laboratory implies that the chamber's calibration factor was obtained from either: 1. PSDL (directly in terms of a primary standard); 2. ADCL or SSDL (with secondary standards traceable to PSDL); or 3. Another chamber which satisfied either 1 or 2 (cross calibration is done in-house). It should be noted that the shorter the traceability link (i.e., the fewer the number of cross-calibrations) the smaller the overall uncertainty on the results, as every cross-calibration adds an uncertainty to the overall dose uncertainty.

Absolute dosimetry refers to the measurement of ‘absolute absorbed dose’ based on one of the three currently accepted standards (see *Section 2.3*) usually at a PSDL level. Unfortunately, the term ‘absolute dosimetry’ is sometimes loosely used to refer to the absorbed dose measurement in hospitals and cancer clinics using calibrated detectors that are traceable to a PSDL. Since these measurements are not absolute in the strictest sense of the word but only relative to a dosimetry standard through a calibration coefficient, it is more accurate to refer to them as ‘clinical reference dosimetry’.

2.3 ABSORBED DOSE STANDARDS

Absorbed dose is currently taken as the best physical indicator for quantification of radiation effects on biological organisms. Moreover, since human tissue is mostly composed of water, the absorbed dose to water has become the quantity of interest in radiotherapy. As a result, normally, regardless of the detector used for measurement, conversion coefficients are used to convert the quantity measured in the detector medium into dose to water.

Currently, one of three radiation sensitive detectors is used by standard laboratories to establish an absorbed dose standard: 1. Ionization chamber; 2. Fricke dosimeter; 3. Calorimeter. The general form describing the conversion of a detector measurement M_d into absorbed dose to water D_w can be summarized by[14]

$$D_\mathrm{w} = M_\mathrm{d}\ C\ R_\mathrm{m}^\mathrm{w} \prod_i k_i\ , \qquad (2.19)$$

where C converts the measured quantity into absorbed dose (all in the detector medium), while R_m^w is the ratio of dose to water to dose to detector medium. Several correction factors k_i are usually applied to account for non-ideal measurement conditions.

2.3.1 Calorimetry

Calorimetry measures the absorbed dose or energy deposited per unit mass from its fundamental definition in terms of temperature rise. Currently, both graphite calorimeters as well as water calorimeters are in use as primary standards. The basic dose measurement principle is simple and can be represented by

$$D_{\mathrm{w}} = \underbrace{\Delta T}_{M}\ \underbrace{c_{\mathrm{m}}}_{C}\ \underbrace{f_{\mathrm{m}}^{\mathrm{w}}}_{R_m^w}\ \underbrace{\prod_i k_i}_{\prod_i k_i}\ , \tag{2.20}$$

where a temperature change ΔT can be converted to dose to water D_{w} by its multiplication with the specific heat capacity of the medium c_{m} and the dose conversion coefficient medium-to-water $f_{\mathrm{m}}^{\mathrm{w}}$. The various elements of Eq. 2.20 categorized according to Eq. 2.19 have been shown. As the principles of water calorimetry are described in detail in Chapter 4, we will focus our attention on graphite calorimetry in this section and postpone the discussion of water calorimetry to future chapters. It suffices to say that in water calorimetry, the temperature rise at a point in an extended body of water is measured and converted to dose to water using Eq. 2.20 where $f_{\mathrm{m}}^{\mathrm{w}} = 1$. Water calorimetry is the most widely-used primary standard available in radiation dosimetry today.

Theory of graphite calorimetry

Figure 2.2 shows a picture (a) and a schematic diagram (b) of a graphite calorimeter. In short, a graphite calorimeter consists of a graphite core embedded inside several layers (referred to as ‘jackets’), with ‘vacuum’ gaps thermally insulating each layer from the next. Materials such as silk thread or Styrofoam balls are used in the evacuated ‘vacuum’ gap to hold the core in place[15]. There are several sensing and heating thermistors embedded inside the core/jacket structure, while the surface of the jacket is covered with aluminized Mylar foil to reduce radiation transfer[15]. The entire structure is placed inside a graphite phantom.

Although the small specific heat capacity of graphite relative to that of water results in much larger temperature rises during irradiation than is the case in water calorimetry (hence, large signal to noise ratio), the small thermal diffusivity of graphite causes rapid heat dissipation within the solid. By designing the calorimeter in layers and insulating each layer from surrounding layers, the heat transfer between the calorimeter core and its surrounding jackets is minimized.

Since the mean dose deposited over the core volume $\bar{D}_{\text{core}}$ is simply the ratio of the energy imparted by radiation E_{rad} to the core mass m_{core}, the absorbed dose to graphite D_{graphite} can directly be calculated from this quantity. This relation can be written as (where k_i are correction factors that will be discussed)

$$D_{\text{graphite}} = \bar{D}_{\text{core}} \prod_i k_i = \frac{E_{\text{rad}}}{m_{\text{core}}} \prod_i k_i \,. \tag{2.21}$$

Furthermore, Eq. 2.22 describes the relation between the total energy deposited inside the core $\Delta E_{\text{tot, thermal}}$ and the resulting temperature rise ΔT_{core}. $\Delta E_{\text{tot, thermal}}$ has three components: Energy imparted from radiation E_{rad}, electrical heating ΔE_{elec}, and heat transfer from surrounding $\Delta E_{\text{transfer}}$

$$\Delta T_{\text{core}} = \frac{\Delta E_{\text{tot, thermal}}}{m_{\text{core}} c_{\text{g}}} = \frac{\left(E_{\text{rad}} + \Delta E_{\text{elec}} + \Delta E_{\text{transfer}}\right)}{m_{\text{core}} c_{\text{g}}}. \tag{2.22}$$

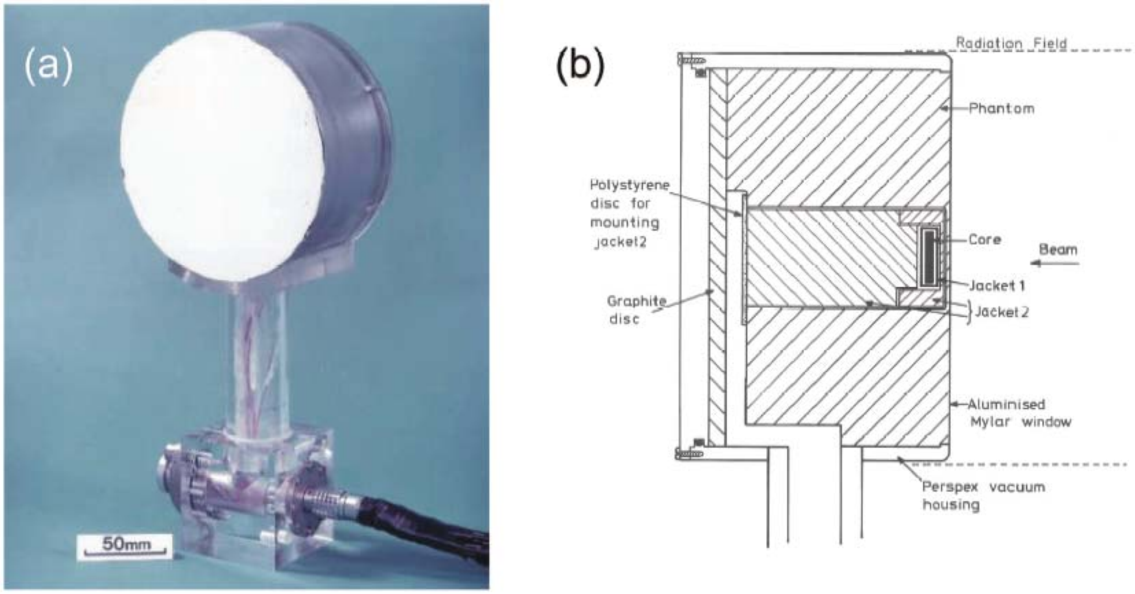

Figure 2.2: A picture (a) and a schematic diagram (b) of the UK's national physical laboratory (NPL) graphite calorimeter (Figure from Seuntjens and DuSautoy (2003) and Stewart (2007)).

A graphite calorimeter can be operated in three modes:

1. Quasi-adiabatic radiation mode: The measurements are performed in the absence of electrical heating (i.e., with heating thermistors turned off, $\Delta E_{\text{elec}} = 0$), and in a radiation field which is large enough to fully cover both the core and the 1st jacket surrounding it. Since the mass and heat capacity of the core and 1st jacket are kept similar in Domen type graphite calorimeters[16], the temperature rise in both parts (core and jacket) is approximately the same. Hence, from the perspective of the core, a quasi-adiabatic condition is in effect[17]. In this mode, by measuring the absolute temperature rise, and using Eq. 2.20, the dose to medium can be determined.

2. Quasi-adiabatic electrical (or heat loss-compensated) mode: In this mode, the electrical heat is delivered to the core alone, while the temperature in both the core and 1st jacket are monitored. In this mode of operation, no radiation is

delivered ($E_{\mathrm{rad}} = 0$). Domen and Lamperti[16] have shown that the core temperature rise under quasi-adiabatic radiation (QAR) mode equals the sum of the temperatures in the core and 1st jacket under heat quasi-adiabatic electrical mode (QAE), such that

$$\Delta T_{\mathrm{core,QAR}} = \Delta T_{\mathrm{core,QAE}} + \Delta T_{\mathrm{jacket,QAE}} \,. \tag{2.23}$$

In this mode, instead of measuring the temperature rise directly, the electrical energy required to realize a given temperature rise is measured.

3. Isothermal mode: In this mode of operation, any increase in the core temperature is compensated for by electrical heat dissipation. As such, the core temperature is kept constant and temperature drift is zero[18]. The measurement of the radiation energy deposited is done through substitution by measuring the amount of electrical heat energy required to nullify the effects of radiation energy.

Once the temperature rise of the core is determined through one of the three techniques above, dose to graphite is calculated by using Eq. 2.20 in its full detailed form

$$D_{\mathrm{g}} = c_{\mathrm{g}} \Delta T_{\mathrm{core}} k_{\mathrm{ht}} k_{\mathrm{gap}} k_{\mathrm{other}} \,. \tag{2.24}$$

Normally, instead of using a reference value, the specific heat capacity of graphite c_{g} is determined for the specific calorimeter by dissipating a known amount of electrical energy into the core in the absence of radiation (quasi-adiabatic electrical mode), and measuring the resulting temperature rise of the core.

Heat transfer correction factor k_{ht} needs to be calculated as $\Delta E_{\mathrm{transfer}}$ is always non-zero due to conduction between the core and its surrounding environment in spite of construction efforts to minimize this effect. Gap effect correction factor k_{gap} has been studied using Monte Carlo numerical studies[19] as well as with chamber measurements[20]. k_{gap} corrects for the difference in dose at the center of the core in the presence and absence of the 'vacuum' gaps that separate the successive layers[17]. Boutillon has shown that the presence of the gap in the calorimeter results in a decrease in dose to the core, the magnitude of which can be significant dependent on gap size and beam energy[19]. Other correction factors accounting for such effects as heat defect (absorbed energy not fully converting to heat), non-uniformity of dose distribution, and presence of non-graphite materials in the core are all grouped under the same category k_{other}.

Dose to water conversion

The conversion of dose to graphite to dose to water can be accomplished in two ways. The first technique is the photon fluence scaling method[21,22] where the dose to graphite is simply converted to dose to water by taking the ratio of calculated $\left(D_{\mathrm{w}}/D_{\mathrm{g}}\right)^{\mathrm{calc}}$ factor. Since past the depth of maximum dose and in the region of TCPE, Eq. 2.5 describes the relation between dose and collision kerma, the dose to water can be calculated through

$$D_{\mathrm{w}} = D_{\mathrm{g}}\left(\frac{D_{\mathrm{w}}}{D_{\mathrm{g}}}\right)^{\mathrm{calc}} = D_{\mathrm{g}}\left[\frac{K_{\mathrm{coll,w}}\beta_{\mathrm{w}}}{K_{\mathrm{coll,g}}\beta_{\mathrm{g}}}\right]^{\mathrm{calc}} = D_{\mathrm{g}}\left[\left(\frac{\bar{\mu}_{\mathrm{en}}}{\rho}\right)_{\mathrm{g}}^{\mathrm{w}}\left(\Psi_{\mathrm{g}}^{\mathrm{w}}\cdot\beta_{\mathrm{g}}^{\mathrm{w}}\right)\right]^{\mathrm{calc}}, \quad (2.25)$$

where all components are defined earlier in *Section 2.1* and in context of Eq. 2.14. Additional corrections to Eq. 2.25 are necessary for air attenuation and finite source size among other small effects.

The second technique involves finding a conversion factor simply with an ionization chamber used as the transfer instrument. The chamber is essentially calibrated in a graphite phantom representation of the calorimeter and subsequently used to measure dose in water[17]. Depending on the chamber wall thickness, either Eq. 2.17 or Eq. 2.18 is used. For a thick wall chamber (Eq. 2.17), the dose to water formulation becomes

$$D_{\mathrm{w}} = D_{\mathrm{g}}\left(\frac{D_{\mathrm{w}}}{D_{\mathrm{g}}}\right)^{\mathrm{meas}} = D_{\mathrm{g}}\frac{M_w\left(\frac{\overline{L}_{\Delta}}{\rho}\right)_{\mathrm{gas}}^{\mathrm{wall}}\left(\frac{\overline{\mu}_{\mathrm{en}}}{\rho}\right)_{\mathrm{wall}}^{\mathrm{w}}\beta_{\mathrm{w}}\prod p_{\mathrm{i,w}}}{M_g\left(\frac{\overline{L}_{\Delta}}{\rho}\right)_{\mathrm{gas}}^{\mathrm{wall}}\left(\frac{\overline{\mu}_{\mathrm{en}}}{\rho}\right)_{\mathrm{wall}}^{\mathrm{g}}\beta_{\mathrm{g}}\prod p_{\mathrm{i,g}}} = D_{\mathrm{g}}M_{\mathrm{g}}^{\mathrm{w}}\left(\frac{\overline{\mu}_{\mathrm{en}}}{\rho}\right)_{g}^{w}\beta_{\mathrm{g}}^{\mathrm{w}}p_{\mathrm{g}}^{\mathrm{w}}, \tag{2.26}$$

where $\beta_{\mathrm{g}}^{\mathrm{w}}$ has been included for accuracy, while $p_{\mathrm{g}}^{\mathrm{w}}$ is shorthand for the ratio of products of chamber correction coefficients water to graphite, $\prod p_{\mathrm{i,w}} \big/ \prod p_{\mathrm{i,g}}$.

For a thin wall chamber using Eq. 2.18, the conversion becomes

$$D_{\mathrm{w}} = D_{\mathrm{g}}\left(\frac{D_{\mathrm{w}}}{D_{\mathrm{g}}}\right)^{\mathrm{meas}} = D_{\mathrm{g}}\frac{M_{\mathrm{w}}\left(\frac{\overline{L}_{\Delta}}{\rho}\right)_{\mathrm{air}}^{\mathrm{w}}p_{\mathrm{w}}}{M_{\mathrm{g}}\left(\frac{\overline{L}_{\Delta}}{\rho}\right)_{\mathrm{air}}^{\mathrm{g}}p_{\mathrm{g}}}. \tag{2.27}$$

2.3.2 Ionometry

Boutillon and Perroche[23] at the BIPM described the use of an ionization chamber with relatively large sensitive volume and thick graphite walls to perform ionometric absorbed dose to water measurements. Their design consists of a parallel-plate chamber (effective volume ~ 6.9 cm^3) with a circular disk collecting plate in the center of the chamber. The measurements are performed inside a water phantom. Boutillon and Perroche[23] take a similar approach as the thick wall cavity dose to water formulation expressed in Eq. 2.17. The exact equation describing the D_{w} measurement is

$$D_w = \underbrace{Q_{air}}_{M}\underbrace{\left(\frac{1}{\rho_{\mathrm{air}}V_{\mathrm{det}}}\right)\left(\frac{\overline{W}_{air}}{e}\right)}_{C}\underbrace{\left(\frac{\overline{L}_{\Delta}}{\rho}\right)_{\mathrm{air}}^{\mathrm{wall}}\left(\frac{\overline{\mu}_{\mathrm{en}}}{\rho}\right)_{\mathrm{wall}}^{\mathrm{w}}\left(\Psi_{\mathrm{wall}}^{\mathrm{w}}\cdot\beta_{\mathrm{wall}}^{\mathrm{w}}\right)k_{\mathrm{cav}}}_{R_{\mathrm{air}}^{\mathrm{w}}}\underbrace{k_{\mathrm{h}}k_{\mathrm{pf}}k_{\mathrm{ion}}k_{\mathrm{m}}k_{\mathrm{other}}}_{\prod_i \mathrm{k}_i}. \tag{2.28}$$

Once again, the various fundamental elements of Eq. 2.28 as described by Eq. 2.19 are shown. Q_{air} is the charge collected inside the chamber's air cavity with a known (measured through mechanical means) volume V_{det}. The product of air density ρ_{air} and V_{det} gives the mass of the air inside the chamber cavity. To maintain accuracy, Boutillon and Perroche[23] include $\left(\Psi_{\mathrm{wall}}^{\mathrm{w}} \cdot \beta_{\mathrm{wall}}^{\mathrm{w}}\right)$ in the equation. The correction factors are:

k_{cav}	corrects for inconsistencies between the chamber cavity used and a perfect Bragg-Gray cavity (since the chamber does perturb the beam to some extent); it is calculated using a semi-analytical method developed by Boutillon[17,21,24],
k_{h}	corrects Q_{air} for the lack of ion collection due to humidity effects inside the cavity chamber,
k_{pf}	corrects for the front plate of the phantom which is not water-equivalent,
k_{m}	corrects for the lateral non-uniformity of the field,
k_{ion}	corrects for ion recombination,
k_{other}	corrects for other small effects such as chamber support and holder corrections among other things.

The largest source of uncertainty in ionization chamber-based standard dosimetry is the determination of $\left(\bar{W}_{\mathrm{air}}/e\right)$ and the stopping power ratios. $\left(\bar{W}_{\mathrm{air}}/e\right)$ is the link between the measured quantity (ionization) to energy deposition, and yet there is no direct way of determining its value. The current recommended value of 33.97 J C^{-1} has been determined through the measurement of the product $\left(\bar{W}_{\mathrm{air}}/e\right)\left(\bar{L}_{\Delta}/\rho\right)_{\mathrm{air}}^{\mathrm{wall}}$ and its division by $\left(\bar{L}_{\Delta}/\rho\right)_{\mathrm{air}}^{\mathrm{wall}}$[17,25]. The product can be determined by comparing measurements from ionometry standard for absorbed dose to graphite (instead of water) to dose results from graphite calorimetry. By considering graphite ionometry, several factors$\left(\text{i.e., } \left(\bar{\mu}_{\mathrm{en}}/\rho\right)_{\mathrm{wall}}^{\mathrm{w}}, \Psi_{\mathrm{wall}}^{\mathrm{w}}, \beta_{\mathrm{wall}}^{\mathrm{w}}\right)$ in Eq. 2.28 become unity as the wall material and the medium become identical. More recent measurements of the product suggest discrepancies of up to 1 % in the previously determined values[26].

2.3.3 Fricke Dosimetry

Absorbed dose measurement based on chemical dosimetry using ferrous sulphate solution was proposed by Fricke and Morse[27]. Fricke dosimetry relies on a radiation-induced oxidation reaction of ferrous ions (Fe^{+2}) into ferric ions (Fe^{+3}).[4] This reaction results in a change in optical density which can be measured using absorption spectrometry with ultraviolet light at 304 nm that is strongly absorbed by the ferric ion[4].

The measurements are performed by placing a vial of Fricke solution (typical vial size: 3 cm thick and 6 cm in diameter) in the direct path of the radiation beam. Although vials of different sizes and materials have been used, vials made of Pyrex or Quartz are often used to maintain purity, although such vials require large corrections for perturbing the dose distribution[17]. The dose to water using Fricke dosimetry is obtained by

$$D_{\mathrm{w}} = \underbrace{\frac{\Delta\mathrm{OD}}{\rho\ell}}_{\mathrm{M}}\,\underbrace{\frac{1}{(\varepsilon G)_{\mathrm{Fe}^{+3}}}}_{\mathrm{C}}\,\underbrace{f_{\mathrm{w,F}}}_{R_{\mathrm{F}}^{\mathrm{w}}}\,\underbrace{k_{\mathrm{vial}}k_{\mathrm{dd}}k_{\mathrm{E}}k_{other}}_{\prod_{i} k_{i}}, \tag{2.29}$$

where,

ΔOD is the change in the optical density of the solution,

ρ is the density of ferrous sulphate solution,

ℓ is the optical path length,

$\varepsilon_{\mathrm{Fe}^{+3}}$ is the molar extinction coefficient of Fe^{+3} which is simply a measure of how strongly the ferric ions absorb the ultraviolet light,

$G_{\mathrm{Fe}^{+3}}$ is the chemical yield in (mol g^{-1}) and describes the number of ferric molecules produced per 100 eV of absorbed energy,

$f_{\mathrm{w,F}}$ is the ‘dose to Fricke’ to ‘dose to water’ conversion factor,

k_{vial} corrects for the non-Fricke walls of the vials,

k_{dd} corrects for lateral field non-uniformity,

k_{E} corrects for energy dependence of $(\varepsilon G)_{\mathrm{Fe}^{+3}}$.

Similar to $\left(\bar{W}_{\mathrm{air}}/e\right)$, the product $(\varepsilon G)_{\mathrm{Fe}^{+3}}$ can only be found by using a calibrated radiation source, through either comparison against calorimetry[28] or by total absorption of electron radiation in Fricke solution[29]. In the former technique, D_{w} is determined through a calorimetric technique and is used to obtain the $(\varepsilon G)_{\mathrm{Fe}^{+3}}$. In the second technique, first the energy and fluence of an electron beam are measured using the setup shown schematically in Fig. 2.3. The energy of an electron beam is measured using a 180° magnet whose magnetic field is adjusted until the electron current reading by the Faraday cup is maximum. The total deposited dose to the Fricke solution volume D_{F} is then determined by[25]

$$D_{\mathrm{F}} = \frac{E_{\mathrm{e}} N}{m} f_{\mathrm{T}} , \qquad (2.30)$$

where E_{e} is the energy of mono-energetic electrons, N is the total number of electrons absorbed and m is the mass of the Fricke solution. f_{T} corrects for the effects of bremsstrahlung losses, backscattering of primary electrons, and energy losses in the accelerator exit window and entrance wall of the Fricke vessel[25].

In Eq. 2.29, k_{E} corrects for energy variations of the $(\varepsilon G)_{\mathrm{Fe}^{+3}}$ factor which is different by as much as 0.7 % ± 0.3 % between ^{60}Co and 20 MV photons[28]. The best G-value measurement available for ^{60}Co beam is 15.6 Fe^{+3} molecules produced per 100 eV of dose deposited[4].

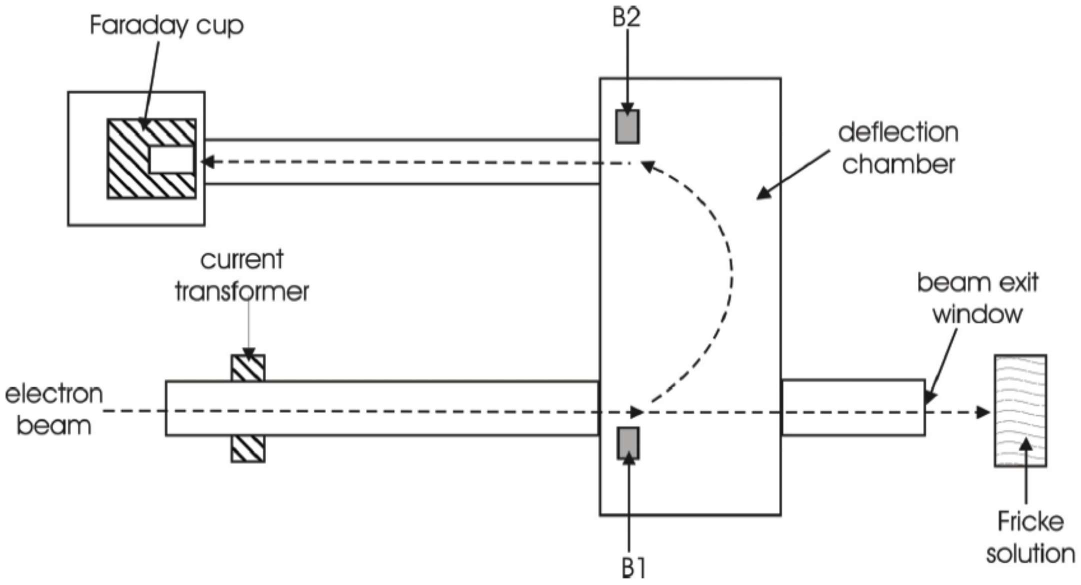

Figure 2.3: A schematic diagram showing the setup for total absorption measurements to determine the conversion factor in Fricke dosimetry (based on Feist (1982), from Stewart (2007)).

k_{vial} corrects for the effects of dose perturbation because of the presence of walls of the vials and has been calculated both using analytical methods as well using Monte Carlo techniques. Glass vials increase the dose in the Fricke solution because of increased electrons scattering from the glass (up to 2 % in 24 MV beams). In plastic vials, the dose perturbation effects are small (< 0.5 %)[30,31]. Moreover, a similar correction to f_T in Eq. 2.30 accounting for energy losses in the vessel and accelerator needs to be calculated and used in Eq. 2.29. Vörös and Stucki[32] have calculated this correction to be between 3 % (5 MeV) and 8 % (22 MeV) with bremsstrahlung correction dominating at all energies.

2.3.4 Comparison

A primary standard is defined by McEwen[25] to be "a standard widely acknowledged to be of the highest metrological calibre available, without any reference to other standards of the same quantity." In this sense, a requirement for a dosimetry standard to also be a primary standard is that the conversion factor C in Eq. 2.19 must be independently determined without any references back to other existing radiation standards.

However, as evident from previous discussions on various dosimetry standards, except for calorimetry, this is not the case. Neither $\left(\bar{W}_{\text{air}}/e\right)$, in case of ionization chamber, nor $\left(\varepsilon G\right)_{\text{Fe}^{+3}}$, in case of Fricke dosimeters, can be measured in the absence of a calibrated radiation field. Both of these dosimetry techniques are used as standards because a relatively robust consensus on the value of the conversion factors exists. As discussed, however, in both Fricke dosimetry and ionometry, inter-comparisons with calorimetry and other techniques are necessary to quantify the value of the conversion factor. To maintain clarity, we should note that a primary standard dosimetry laboratory (PSDL) does not always offer a primary standard in the strictest sense.

Calorimetry is the only true absolute primary standard because its conversion factor, the specific heat capacity, is determined in the absence of a radiation field. Water calorimetry has an additional advantage because it does not require the R_{m}^{w} factor (see Eq. 2.19). Since the medium surrounding the detector is water, water calorimetry avoids the uncertainties involved with calculation or measurement of factors required for dose to medium—dose to water conversion. Moreover, water calorimetry is the only technique in which the dose is measured at a 'point' by using a thermistor detector bead in an extended body of water. This is not the case in other instruments: In ionometry, the ionization signal obtained is averaged over the volume of the chamber; in Fricke dosimetry, the net optical density change is averaged over the volume of the Fricke solution in the vial; and in graphite calorimetry, the temperature rise is an averaged value over the core volume.

Water calorimeter-based D_w measurements in ^{60}Co and high energy photons achieve a dose uncertainty of 0.2 % to 0.4 % (1σ)[18,33,34], while in graphite calorimetry an uncertainty of 0.41 % to 0.46 % is achievable[17,18,35,36]. The largest source of uncertainty in water calorimetry remains to be the heat defect (0.14 % to 0.3 %)[18,33,34], while in graphite calorimetry, a large portion of the overall uncertainty can be attributed to dose to water to dose to graphite conversion factor (0.19 % to 0.35 %)[35,36].

The ionization chamber absorbed dose uncertainty as quoted by Boutillon and Perroche[23] is 0.43 % (1σ) with a 0.3 % uncertainty associated with stopping power ratio calculation, 0.14 % uncertainty on mass energy absorption coefficient ratio, and a 0.15 % uncertainty on the consensus value of $\left(\bar{W}_\mathrm{air}/e\right)$.

The uncertainty of Fricke dosimetry was calculated by Feist[29] to be 0.51 % (1σ), 0.3 % of which is due to the assumption of $\left(\varepsilon G\right)_{\mathrm{Fe}^{+3}}$ being beam quality and energy independent, and 0.19 % of which is the uncertainty on energy loss correction calculation. From the uncertainty discussion presented above, it can be observed that one of the largest sources of uncertainty in all dosimetry standards except water calorimetry is that of dose to medium—dose to water conversion factor.

2.4 CLINICAL REFERENCE DOSIMETRY

Dosimeters used at standard laboratories that act as national standards are difficult to use, are often bulky, and do not necessarily result in large signal to noise ratios which means that large number of measurements are necessary to obtain good statistics on the results. As such, more robust and simpler to use dosimeters with traceable calibration factors to a dosimetry standard are often used by individual users (see *Section 2.2*).

In this work an ionization chamber and radiochromic films were used for reference dosimetry. Three different types of ionization chambers were used. The current protocol for absorbed dose to water determination in HDR ^{192}Ir brachytherapy is the American Association of Physicists in Medicine's Task Group 43 (AAPM TG-43)[37]. This protocol requires a well-type ionization chamber to be used for measurements. We used a Standard Imaging HDR 1000 Plus well-type chamber with an air kerma strength S_K calibration factor provided by the University of Wisconsin ADCL (UW-ADCL). Moreover, for reference dosimetry measurements in ^{192}Ir brachytherapy, a Standard Imaging A1SL miniature Shonka thimble type chamber was used. This chamber was also calibrated in a standard ^{60}Co setup at UW-ADCL, and was cross-calibrated in-house against several orthovoltage energies using an NRC-calibrated A12 chamber. Also for the purposes of reference dosimetry, EBT-1 radiochromic films were used in ^{192}Ir brachytherapy.

In proton therapy, the International Atomic Energy Agency's TRS 398 report[38] is the currently accepted protocol. In addition to water calorimetry, reference dosimetry was also performed based on the TRS-398 using an Exradin T1 thimble type chamber with NIST-traceable calibration factor. The readings from all chamber measurements were measured with a Keithley 6517A electrometer. EBT-1 radiochromic films were read with an EPSON Expression 1680 flatbed scanner. Further details will be provided in Chapters 5-8.

2.5 REFERENCES

[1] ICRU (1980), Radiation Quantities and Units, Report 33 of the International Commission on Radiation Units and Measurements (Bethesda, MD).

[2] H. E. Johns and J. R. Cunningham, "The physics of radiology," 4th ed (Charles C. Thomas, Springfield, IL, 1983).

[3] A. E. Nahum, "Cavity Theory, Stopping-Power Ratios, Correction Factors," in *Clinical dosimetry measurements in radiotherapy*, edited by D. W. Rogers and J. E. Cygler (Medical Physics Publishing, Madison, WI, 2009).

[4] E. B. Podgorsak, "Review of Radiation Oncology Physics: A Handbook for Teachers and Students," in *Treatment Machines for External Beam Radiotherapy*, edited by E. B. Podgorsak (International Atomic Energy Agency, Vienna, 2005).

[5] W. H. Bragg, "Studies in Radioactivity," (Macmillan, New York, 1912).

[6] L. H. Gray, "The absorption of penetrating radiation," Proc R Soc A 122, 647-668 (1929).

[7] L. H. Gray, "An ionisation method for the absolute measurement of gamma-ray energy," Proc R Soc A 156, 578-596 (1936).

[8] L. V. Spencer and F. H. Attix, "A theory of cavity ionisation," Radiat Res 3, 239-254 (1955).

[9] A. E. Nahum, PhD Dissertation (University of Edinburgh, Edinburgh, 1976).

[10] A. E. Nahum, "Water/air mass stopping-power ratios for megavoltage photon and electron beams," Phys Med Biol 23, 24-38 (1978).

[11] W Wieszczycka and W. H. Scharf, "Proton radiotherapy accelerators," (World Scientific Publishing Co. Pte. Ltd., Singapore, 2001).

[12] J. Seuntjens and M. McEwen, "The calibration chain: Role of BIPM, PSDLs and ADCLs," in *Clinical Dosimetry Measurements in Radiotherapy*, edited by D. W. Rogers and J. E. Cygler (Medical Physics Publishing, Madison, 2009).

[13] P. J. Allisy, D. T. Burns, and P. Andreo, "International framework of traceability for radiation dosimetry quantities," Metrologia 46, S1-S8 (2009).

[14] K. R. Shortt, C. K. Ross, and J. P. Seuntjens, "The role of comparisons in confirming the accuracy of dosimetric standards" *Proc. International Workshop on Accurate Radiation Dosimetry (Montreal) (AAPM Proceedings Series 13)* ed J. P. Seuntjens and P. N. Mobit (Madison, WI: Med Phys Publishing) pp 196-213

[15] K. Stewart, Ph.D. dissertation (McGill University, Montreal, 2007).

[16] S. R. Domen and P. J. Lamperti, "A heat-loss compensated calorimeter: Theory, design and performance," J Res Natl Bur Stand 78, 595-610 (1974).

[17] J. Seuntjens and S. Duane, "Photon absorbed dose standards," Metrologia 46, S39-S58 (2009).

[18] J. P. Seuntjens and A. R. DuSautoy, "Review of calorimeter based absorbed dose to water standards," Standards and Codes of Practice in Medical Radiation Dosimetry (Proc. Int. Symp. Vienna, 2002), IAEA Vienna (2003) IAEA-CN-96/3.

[19] M. Boutillon, "Gap correction for the calorimetric measurement of absorbed dose in graphite with a ^{60}Co beam," Phys Med Biol 34 (1989).

[20] B. Owen and A. R. DuSautoy, "Correction for the effect of the gaps around the core of an absorbed dose graphite calorimeter in high energy photon radiation," Phys Med Biol 36, 1699-1704 (1991).

[21] J. E. Burns, "Absorbed-dose calibrations in high-energy photon beams at the National Physical Laboratory: conversion procedure," Phys Med Biol 39, 1555-1575 (1994).

[22] R. Nutbrown, S. Duane, D. R. Shipley, and R. A. Thomas, "Evaluation of factors to convert absorbed dose calibrations from graphite to water for the NPL high-energy photon calibration service," Phys Med Biol 47, 441-454 (2002).

[23] M. Boutillon and A. M. Perroche, "Ionometric determination of absorbed dose to water for ^{60}Co gamma rays," Phys Med Biol 38, 439-454 (1993).

[24] M. Boutillon, "Perturbation correction for the ionometric determination of absorbed dose in a graphite phantom for ^{60}Co gamma rays," Phys Med Biol 28, 375-388 (1983).

[25] M. McEwen, "Primary standards of air kerma for ^{60}Co and x-rays and absorbed dose in photon and electron beams," in *Clinical dosimetry measurements in radiotherapy*, edited by D. W. Rogers and J. E. Cygler (Medical Physics Publishing, Madison, WI, 2009).

[26] L. L. W. Wang and D. W. Rogers, "The replacement correction factor for the BIPM flat cavity ion chamber and the value of W/e," Med Phys 35, 4410-4416 (2008).

[27] H. Fricke and S. Morse, "The actions of x-rays on ferrous sulfate solutions," Phil Mag 7, 129 (1929).

[28] N. V. Klassen, K. R. Shortt, J. Seuntjens, and C. K. Ross, "Fricke dosimetry: the difference between G(Fe3+) for 60Co gamma-rays and high-energy x-rays," Phys Med Biol 44, 1609-1624 (1999).

[29] H. Feist, "Determination of the absorbed dose to water for hisgh-energy photons and electrons by total absorption of electrons in ferrous sulphate solution," Phys Med Biol 27 (1982).

[30] C. M. Ma and A. E. Nahum, "Dose conversion and wall correction factors for Fricke dosimetry in high-energy photon beams: analytical model and Monte Carlo calculations," Phys Med Biol 38, 93-114 (1993).

[31] C. M. Ma, D. W. Rogers, K. R. Shortt, C. K. Ross, A. E. Nahum, and A. F. Bielajew, "Wall-correction and absorbed-dose conversion factors for Fricke dosimetry: Monte Carlo calculations and measurements," Med Phys 20, 283-292 (1993).

[32] S. Vörös and G. Stucki, " Simulation Monte Carlo pour la réalisation d'un étalon primaire de la dose absorbée dans l'eau pour des faisceaux d'electrons " Radioprotection 42, 565-575 (2007).

[33] A. Krauss, "The PTB water calorimeter for absolute determination of absorbed dose to water in ^{60}Co radiation," Metrologia 43, 259-272 (2006).

[34] M. G. Mitch, L. DeWerd, R. Minniti, and J. F. Williamson, "Treatment of Uncertainties in Radiation Dosimetry," in *Clinical Dosimetry Measurements in Radiotherapy*, edited by D. W. Rogers and J. E. Cygler (AAPM, Colorado, 2009).

[35] J. Daures, A. Ostrowky, P. Gross, J. P. Jeannot, J. Gouriou, "Calorimetry for absorbed dose measurements at BNM-HNHB" Proc. Workshop on Recent Advances in Calorimetric Absorbed Dose Standards (Teddington, UK, 1999) ed A. J. Williams and K. E. Rosser Rep. CIRMS 42 National Physical Laboratory, Teddington, UK, 15-21 (2000)

[36] R. B. Huntley, K. N. Wise, and J. F. Boas, "The Australian standard of absorbed dose" Proc. Workshop on Recent Advances in Calorimetric Absorbed Dose Standards (Teddington, UK, 1999) edited A. J. Williams and K. E. Rosser Rep. CIRMS 42 National Physical Laboratory, Teddington, UK, 37-46 (2000)

[37] R. Nath, L. L. Anderson, G. Luxton, K. A. Weaver, J. F. Williamson, and A. S. Meigooni, "Dosimetry of interstitial brachytherapy sources: recommendations of the AAPM Radiation Therapy Committee Task Group No. 43. American Association of Physicists in Medicine," Med. Phys. 22, 209-234 (1995).

[38] IAEA INTERNATIONAL ATOMIC ENERGY AGENCY, "Absorbed dose determination in external beam radiotherapy: An international code of practice for dosimetry based on standards of absorbed dose to water," Technical Report Series no. 398, IAEA, Vienna (2000).

Chapter 3

McGill water calorimeter:

Design, construction, and operation

3.1 MCGILL WATER CALORIMETER: EQUIPMENTS AND CIRCUITRY

This section provides an overview of the McGill water calorimeter from a hardware point of view (equipment and circuitry). This section is meant to serve as a ‘big picture’ prior to us diving into the details. The remainder of this Chapter focuses on the details of the various components of the calorimeter, as well as an explanation on the methodologies employed throughout the experimental portion of this work. Chapter 4, on the other hand, describes the theory behind water calorimetry and provides the details of signal analysis. Readers are encouraged to refer back to this section and specifically to Fig. 3.1 (showing our setup) for reference as they go through the remainder of this thesis.

Figure 3.1 shows a schematic diagram of the entire experimental setup, including the most important components and electrical connections. A water calorimeter is simply a water phantom with an elaborate system of temperature cooling and temperature control. The temperature of water is cooled to 4 °C (water's highest density) to reduce convection, while the temperature of the entire phantom has to be controlled so that sub-millikelvin temperature rises from radiation are not overcome by larger thermal drifts.

A Keithley K2000 digital multimeter was used to measure the resistance of the three PT-100 RTD temperature probes (Thermo Kinetics, R21-D100E4) that were used to monitor the temperature of the water phantom. This temperature reading was used as feedback to adjust the temperature of a fridge (cooling fluid circulator) in order to prevent temperature drifts and provide temperature equilibrium stability (5 mK stability over several hours).

A thermistor is a temperature sensitive resistor that is used as the 'thermometer' of choice in water calorimetry. Using two such thermistor beads, temperature rises of few hundred microkelvin (μK) are measured in water. For a typical temperature rise of roughly 240 μK/Gy, the thermistor's resistance changes by roughly 96 mΩ. The small resistance changes are measured using a Wheatstone-type bridge. Using this technique, the signal is obtained in terms of voltage change which for the above example corresponds to 4.8 μV.

In this work, we used a bridge circuit system referred to as an 'active bridge.' Unlike a Wheatstone bridge (also referred to here as a 'passive bridge') which only uses resistors and capacitors, an active bridge also uses operational amplifiers and produces more robust voltage reading with lower uncertainties. An SR510 lock-in amplifier (Stanford Research Systems) was used to measure the output voltage from the bridge. The lock-in allows accurate measurements of an AC signal down to a few nanovolts. It accomplishes this task through a phase-sensitive detection technique whereby the component of the signal at a specified frequency and phase is singled out; hence, the lock-in feeds the system with an internally generated reference sinusoidal frequency (V_{peak}=1.5 V, 1 Hz), and simply looks at the component of the signal that is at the same frequency as the reference internal oscillator. As such, the lock-in allows us to measure very low signal-to-noise ratios, as it acts like an extremely low pass filter.

A Burster 1408 high-precision resistance decade box is used to balance the thermistor resistance in the bridge circuit. It consists of high precision Zeranin® resistors with a nominal 0.01-0.02 % accuracy (0.02 % stability over years). The case of the resistance decade box is grounded, and the bridge is directly connected to the decade box via a well-shielded coax cable.

All major devices are connected through a General Purpose Interface Bus (GPIB, IEEE-488) with each other and with the computer. Since the operator must be outside the treatment room in the control area during experiments (due to radiation hazards), a GPIB extender device is used to transfer the data over a 15 m coax cable to the computer outside. To avoid ground loops, all devices and cables are grounded through a single power supply ground point. The power supplies, however, are not shown in Fig. 3.1.

An x-t paper chart recorder (Soltec, 1242) is directly connected to analogue output of the lock-in amplifier and is used to plot the output signal. This is a duplicate of the signal that is also transmitted and displayed on the computer. The plots and data from chart recorder have never been used for analysis, rather served only as a visual tool helping to follow the calorimeter response and to track behaviour of the system as a whole over long time periods. All equipment was controlled remotely via the computer from the operator area.

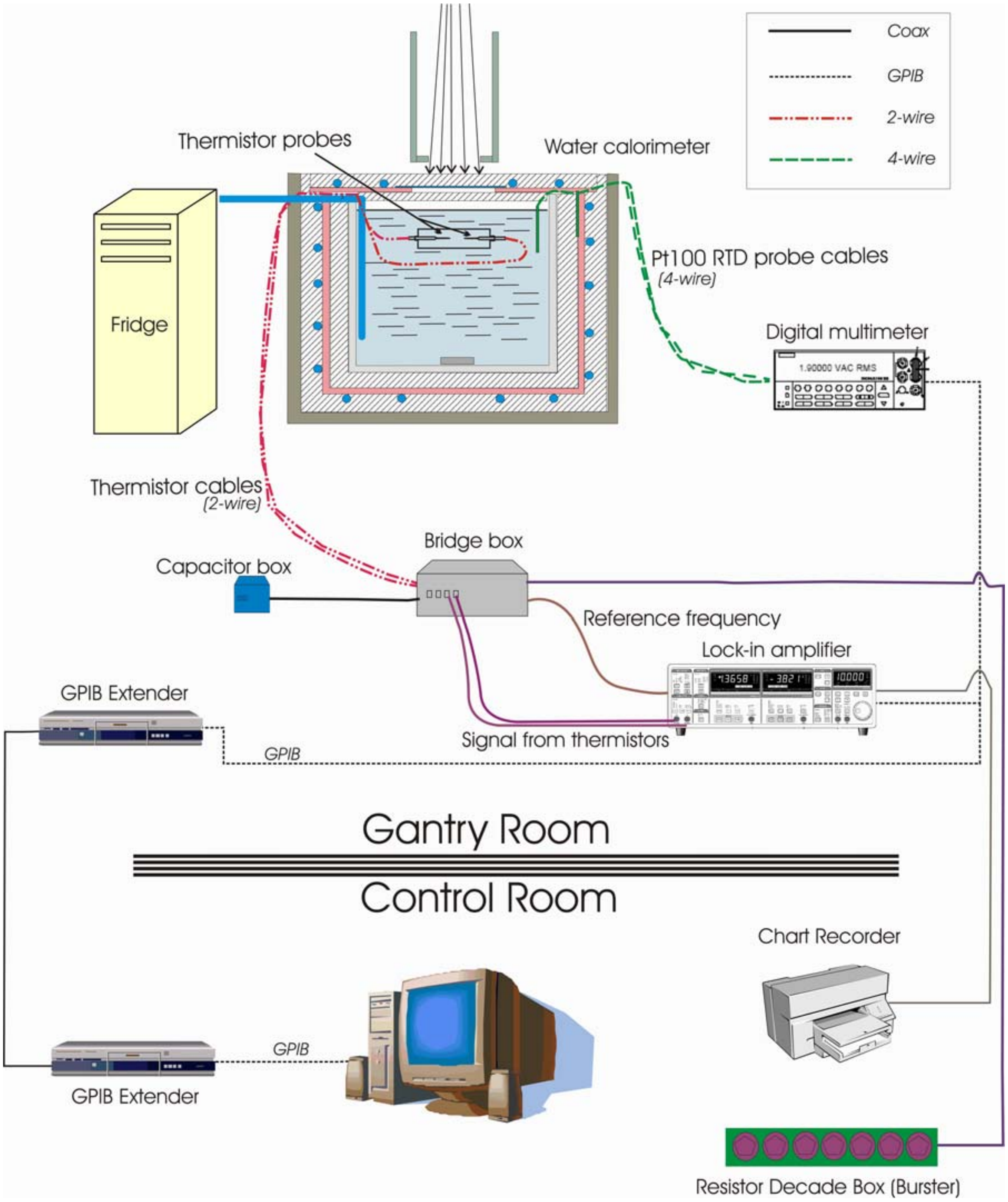

Figure 3.1: A schematic diagram of the full experimental setup. All components, their location (inside treatment room or control room), as well as the electrical circuitry (legend provided) are shown. The power supplies are not included to maintain clarity.

3.2 WATER CALORIMETER

The McGill in-house built stagnant 4 °C water calorimeter (MWC) was used in this work. A short introduction of this device is included in Chapters 6 and 8 (manuscripts). However, a detailed description of this device with minimal overlap with materials presented in the later two chapters is provided here.

Figures 3.2 and 3.3 show a schematic diagram of the MWC as well as a picture of the device. The calorimeter consists of a 30x30x20 cm^3 Lucite water tank with an integrated cooling and temperature control system. The Lucite tank is surrounded by two 5 cm thick Styrofoam slabs that are separated by a 5 mm temperature controlled copper plate. The copper enclosure surrounds the tank on all sides except for the top surface (the lid) that contains a 12x12 cm^2 opening. The opening window is covered by a 0.15 mm thick brass foil that is attached to the larger copper thermal shield with silver-based conductive glue. The top window opening allows for the external radiation beam to enter the calorimeter with minimal attenuation and scatter. The entire system is housed inside a plywood box of 55x55x40 cm^3.

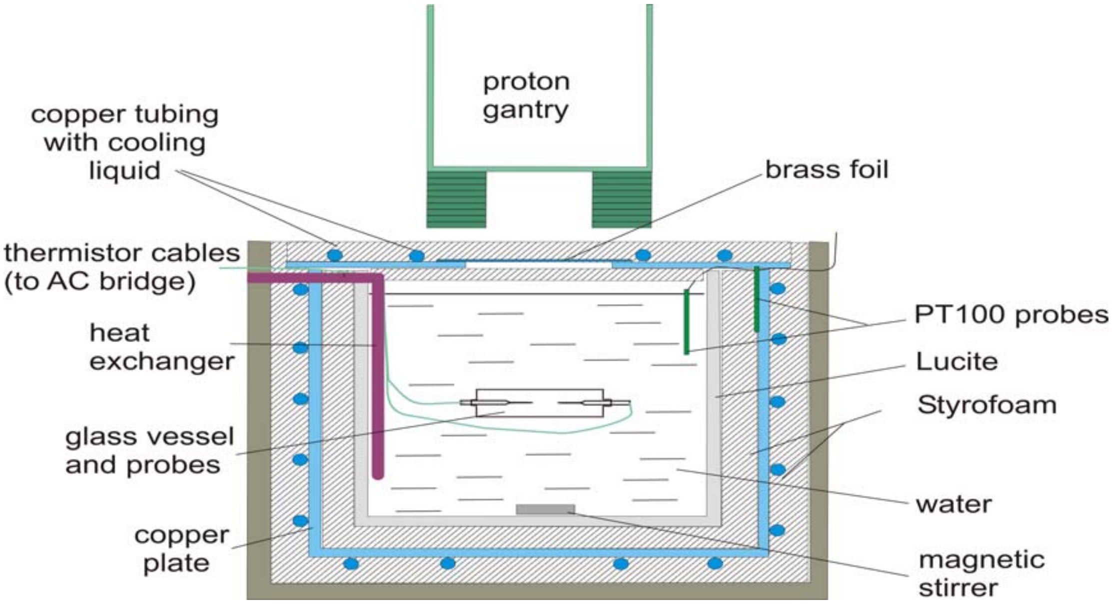

Figure 3.2: A schematic diagram of the McGill water calorimeter positioned under a vertically incident radiation beam.

Copper tubing has been soldered to the copper plate (in a zigzag fashion) on all sides of the calorimeter (represented in the cross-section view in Fig. 3.2 as blue circles attached to the copper plate). A Neslab RTE-7 refrigerated bath/circulator (Thermo Scientific) is used to actively control the temperature of the copper plate by circulating a cooled fluid through the tubing. The temperature of the cooling fluid can be controlled down to 0.1 °C.

The calorimeter is also equipped with a heat exchanger, a 4 mm diameter temperature controlled anodized aluminum tube that is in direct contact with the calorimeter water and is used for rapid temperature manipulations of the water phantom (exp. Initial cooling of the water from room temperature to 4 °C). The heat exchanger is also connected to the refrigerator bath and the cooling fluid network through a valve which can be opened/closed as desired. Measurements are always performed with the heat exchanger valve closed because a true temperature equilibrium state cannot be reached inside the water phantom with cooling fluid running through the heat exchanger.

A magnetically coupled stirrer (Corning 84302) at the bottom of the water tank is used to mix the water in between sets of calorimetric runs and remove any temperature gradients built up during subsequent runs. The phantom water temperature is monitored by taking the average reading of two platinum resistance temperature detectors (PT-100 RTD); a third RTD probe is used to measure the copper temperature. The probes' temperature reading is being monitored continuously and is used as feedback to adjust the bath (fridge) temperature in order to avoid drifts.

The heart of a calorimeter contains the thermistor probes and the vessel enclosing them. To accurately position the vessel, a precise vertical depth positioning device was fixed to one side of the inner Lucite wall of the phantom (see Fig. 3.3). The vessel is then mounted onto a holder device which itself is mounted onto the positioning bracket with three plastic screws. A stainless steel ball bearing is used as a pivot point (positioned in between the three screws) such that the screws can be used to make fine adjustments to the tilt of the vessel.

In order to cross calibrate a chamber with the water calorimeter, the chamber is placed inside the water tank (this avoids any uncertainties due to experimental setup differences). In such cases, a modified holder is used to support the chamber as opposed to the vessel. Moreover, during such measurements, the water temperature is normally brought back up to room temperature level.

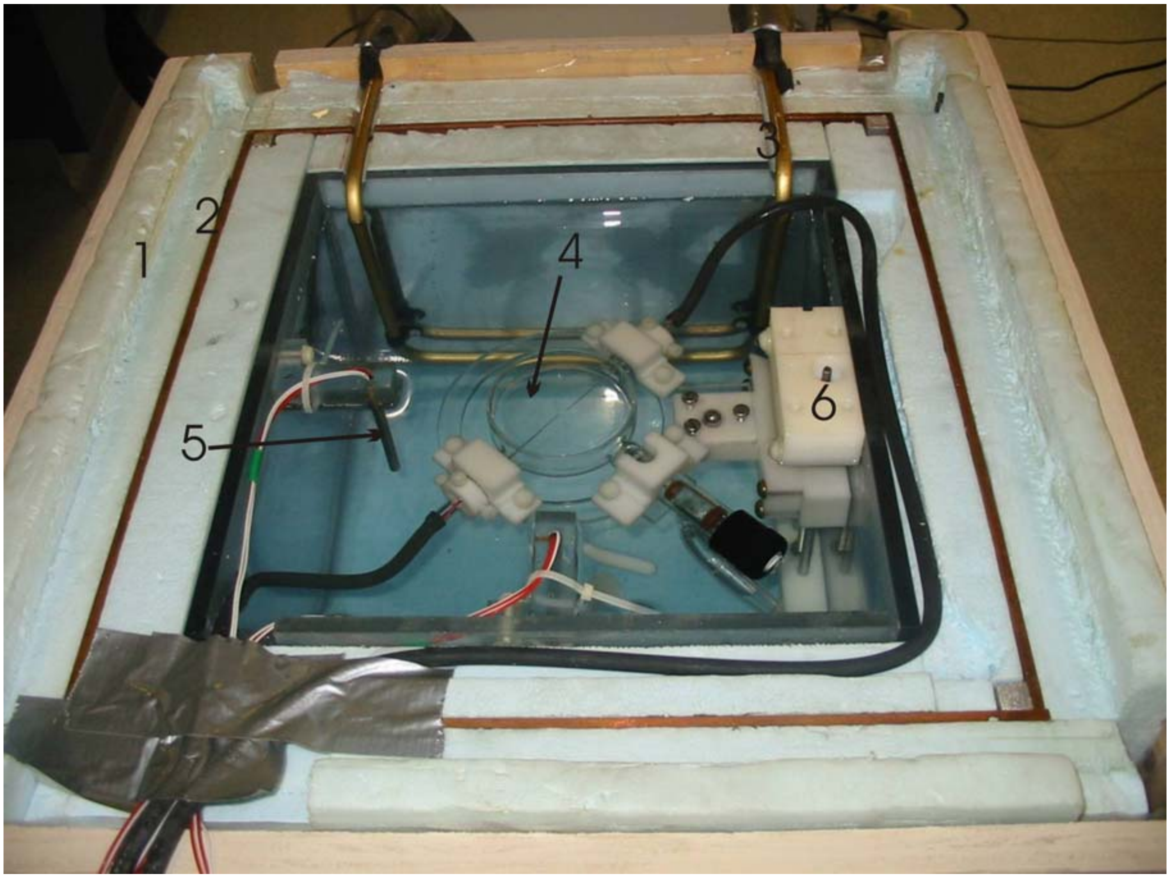

Figure 3.3: A picture of the MWC. The number references are as follow: 1. Styrofoam; 2. copper thermal shield; 3. Aluminum heat exchanger; 4. Calorimeter vessel (The two needle-like thermistors are clearly visible inside the vessel); 5. PT100 RTD probes; 6. Vertical positioning device, and holder.

3.3 CALORIMETER VESSEL

Figure 3.4 shows a schematic diagram of the calorimeter vessel. A parallel plate ('pancake' cylindrical design) Pyrex glass vessel was used. The vessel has a side glass thickness of 1.96 mm with an outer diameter of 79 mm, as well as a front and back window thickness of 1.12 mm with an inner separation of 22.66 mm. There are two side ports to the glass vessel through which the thermistor detectors can be inserted. Since the purpose of the vessel is to seal the high purity water around the thermistors (as will be described in *Section 4.6*), CAPFE® Teflon encapsulated O-rings were used. A third port in the vessel facilitates the filling and bubbling of pure water. This port is sealed using a glass stopcock also equipped with CAPFE® O-rings. The vessel design includes a small glass bulb on the vessel arm in which a small gas bubble can be trapped after the full bubbling procedure (*Section 3.9*). This accommodates possible volume changes of water with temperature.

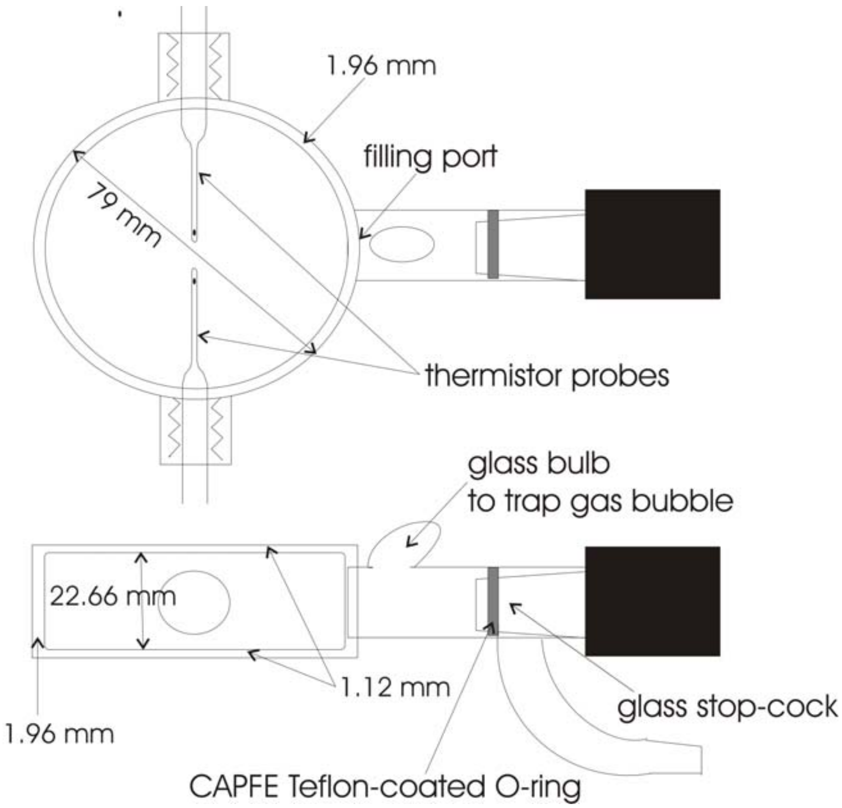

Figure 3.4: A schematic diagram of the MWC vessel with 2 thermistors positioned inside (reproduced from Stewart[1] (2007) with Permission).

3.4 THERMISTOR PROBE

Used in calorimetry as temperature detectors, a thermistor is a temperature-sensitive resistor. A thermistor bead is not, of course, directly placed in water, but rather is inserted to the very end (tip) of a closed Pyrex glass pipette, see Fig. 3.5. The pipette has a diameter of 8 mm and wall thickness of 1 mm at one end while at the very tip it is pulled to an outside diameter of 0.6 mm, and an inside diameter of 0.3 mm.

NTC BR11 Thermobead (Thermometrics) glass-coated thermistor beads were used in this work. With a diameter of 0.25 mm, these beads have a nominal resistance of 10 kΩ at 4 °C. Exhibiting a nominal resistance change of 400 Ω/K, the thermistors make accurate measurement of few hundred μK temperature rises with noise levels of better than 10 μK (normally between 2-5 μK possible).

The thermistor platinum alloy leads are 7.9 mm long and are soldered to two leads from a foil-shielded twin-lead cable. Epoxy is used to fix the lead to the side of the pipette and to provide strength and strain relief. As shown in the figure, latex tubing is stretched partially over the glass pipette and the wires in order to make the thermistor detector structure waterproof.

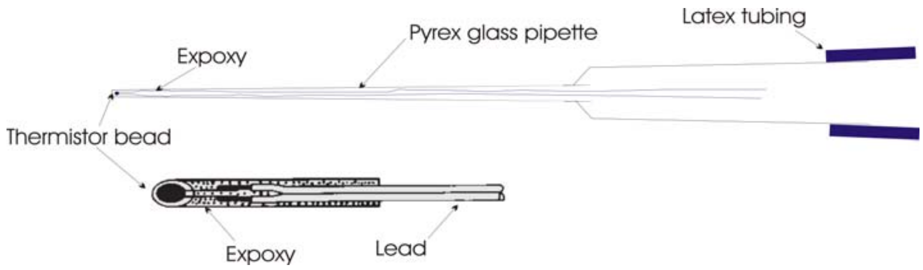

Figure 3.5: A schematic diagram of the thermistor probe as well as a close up view of the NTC BR11 series thermistor beads (Thermometrics[2])

3.4.1 Thermistor Power Dissipation

Since a voltage bias has to be applied across the thermistors to measure a resistance, the thermistors, like any other resistors, warm up and dissipate heat energy. This power dissipation, when kept sufficiently low (< 40 μW), has a very small effect on the overall signal and is often ignored for all intents and purposes in external radiation beam water calorimetry. However, in HDR ^{192}Ir brachytherapy water calorimetry, as shall be discussed, water convection cannot be ignored. As such, the thermistor power dissipation must be accounted for and included in the simulations because of its role in the onset of a small convective current inside the calorimeter vessel.

In the active bridge setup, a sinusoidal excitation of 1.5 V (peak voltage V_p) at 10 Hz was applied by the lock-in amplifier across the 'thermistors' arm of the bridge circuit (see Fig. 3.7). The power generated by the thermistor P_therm can easily be calculated from

$$P_\mathrm{therm} = I_\mathrm{rms} V_\mathrm{rms}^\mathrm{therm} = \left(\frac{V_\mathrm{rms}}{R_\mathrm{tot}} \right) V_\mathrm{rms}^\mathrm{therm}, \qquad (3.1)$$

where I_rms is the effective current across the thermistor, and $V_\mathrm{rms}^\mathrm{therm}$ is the effective voltage drop across each thermistor. $V_\mathrm{rms}^\mathrm{therm}$ equals one quarter of the total voltage drop V_rms across the 'thermistors + decade resistor box' arm of the bridge. This is because each thermistor has a nominal resistance of 9.35 kΩ at 4 °C operation temperature, and the decade box connected serially to the two thermistors is normally balanced during measurements (i.e., the resistance of the resistor box is set to match the combined resistance of the two thermistors, 18.7 kΩ). Since, $V_\mathrm{rms} = V_p / \sqrt{2}$, a thermistor power dissipation of 30 μW is calculated.

3.5 BRIDGE CIRCUIT

As shown in Fig. 3.1, in order to measure the small resistive change of the thermistors, the lock-in amplifier's internal oscillator provides a reference frequency into the bridge, and detects the portion of the output signal that is in phase with the initial input frequency. In order to understand the active bridge circuit better, we start by describing the passive Wheatstone bridge.

3.5.1 Passive Bridge

Figure 3.6 shows a schematic diagram of the passive bridge circuitry. One arm of the bridge contains the two thermistors as well as the decade resistor box connected in series. While on the other arm, two fixed 20 kΩ (±0.01 %) Zeranin® resistors (Burster) are serially connected. A reference AC excitation signal (from lock-in amplifier's internal oscillator) is put into one end of the bridge, while the other end is grounded. The lock-in amplifier is used to measure the voltage difference between points A and B. Although not shown, capacitors are included into the circuitry to balance the 90 ° out of phase (capacitive) component of the output signal. A balanced bridge is achieved when the resistance of the decade resistor box is adjusted such that it perfectly matches the combined resistance of the two thermistors, resulting in zero voltage difference between points A and B.

3.5.2 Active Bridge

Figure 3.7 shows a simplified circuit diagram of the active bridge design used in this work (see Seuntjens (1991) for original design)[3]. In this design, two operational amplifiers (OP177 op-amps, Analog Devices) are used: one acting as a unity gain amplifier, while the other acts as a voltage inverter. These are powered by +/- 15 V using a Systron-Donner TL8-3 power supply. Four 10 kΩ (±0.01 %) Zeranin® resistors (Burster) along with several other resistors are used in the circuitry. As shown in Fig. 3.1, a decade capacitor box (IET Labs, CSH4-10pf-WC) is also added to the circuit to balance the capacitive component of the signal.

The perfectly out-of sync voltage applied across the voltage divider (thermistors arm of the circuit) gives this design a unique and important advantage over a passive bridge design. In this setup, the lock-in amplifier compares the voltage difference of the thermistors arm to ground. Unlike the passive bridge in which a signal is the difference between two non-zero voltages (with their own respective uncertainties), the active bridge only compare the voltage change at a single point relative to a fixed ground, without the need for further resistors in the other arm of the bridge, thus significantly reducing the uncertainty on the signal.

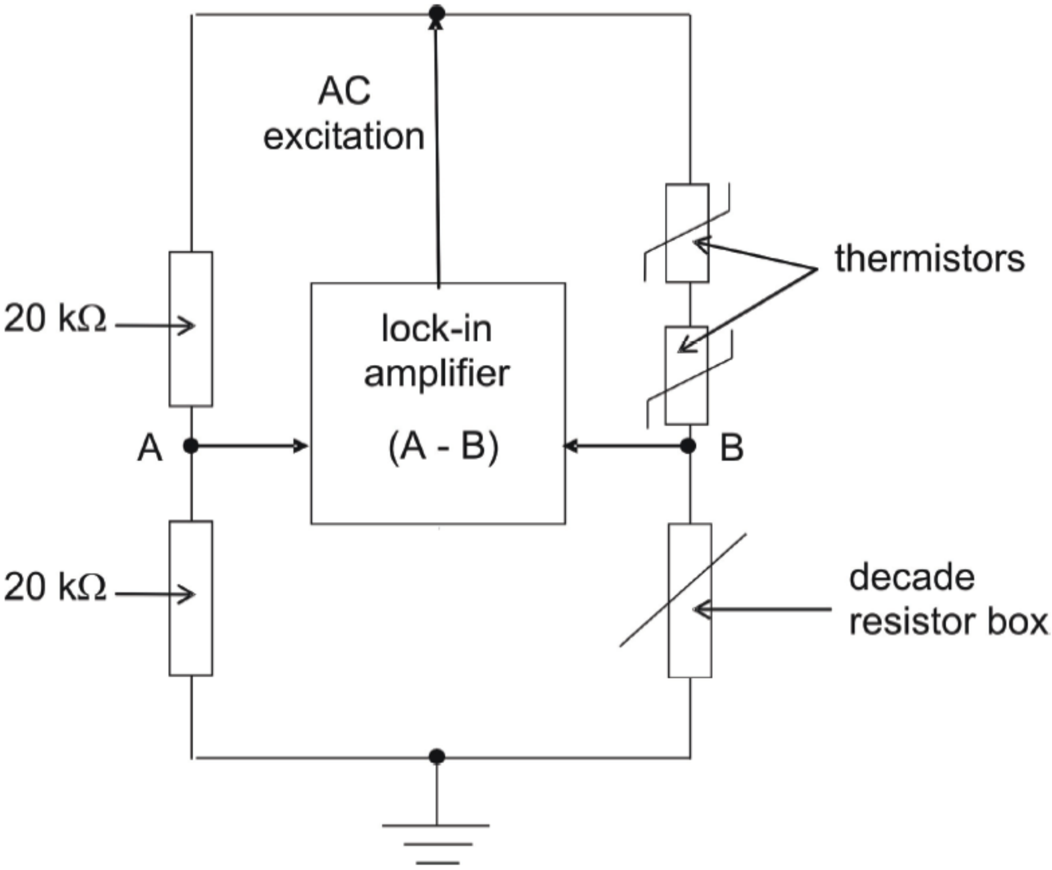

Figure 3.6: A schematic circuit diagram of the passive “Wheatstone” AC bridge”[1].

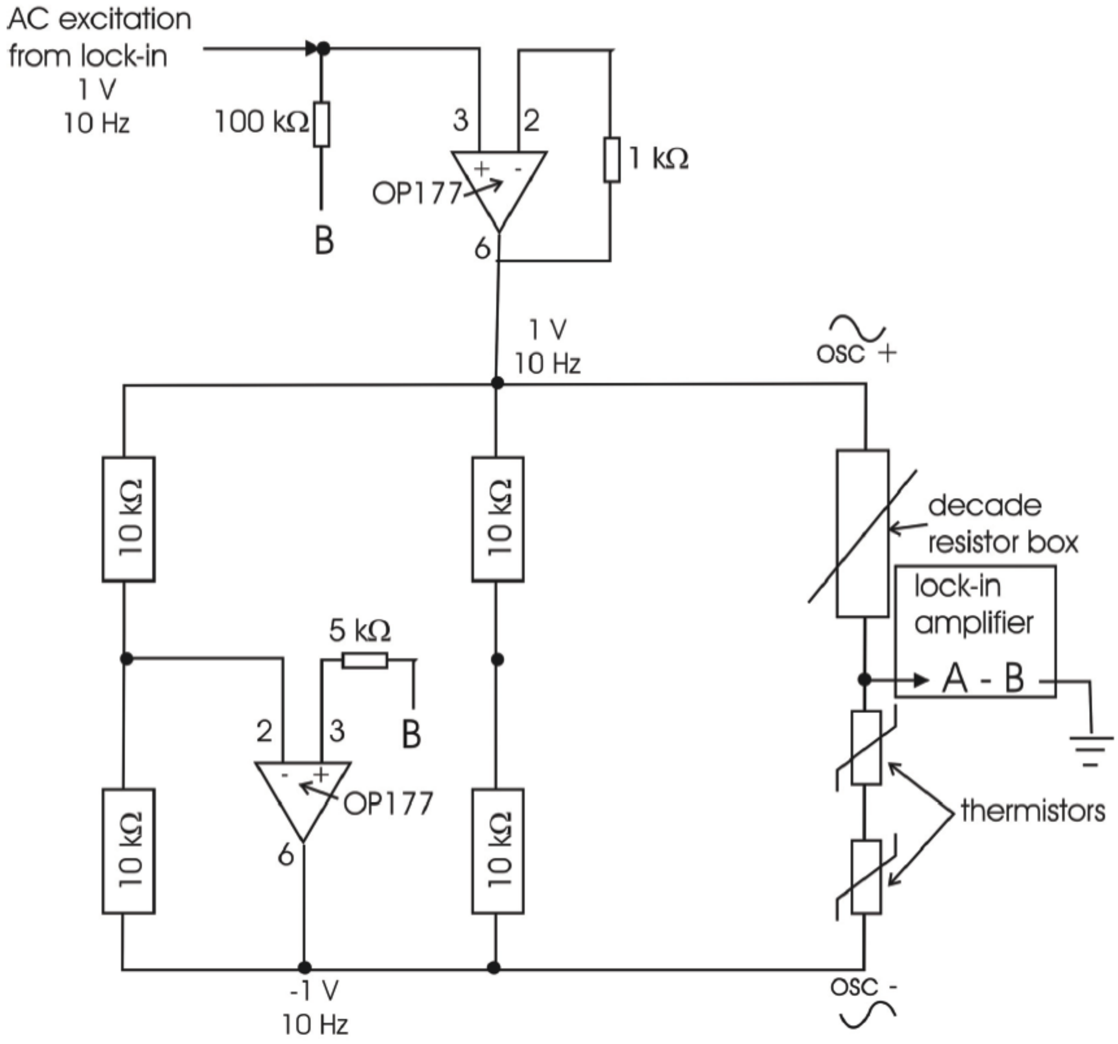

Figure 3.7: A schematic circuit diagram of the active AC bridge[1].

3.6 RTD PROBES

Three platinum resistance temperature detectors (PT-100 RTD) were used in this work to continuously monitor the average temperature of water and copper thermal shield. The probes have a nominal resistance of 100 Ω at reference temperature 0 °C, and display a nominal 0.39 Ω resistive change per degree

Kelvin. The RTDs are connected to the multimeter via 4-wire resistance measurement mode.

When the resistances to be measured are small relative to the total resistance across the length of the wire r_{wire}, the ohmmeter resistance reading error introduced by the wire's resistance can be substantial. In such instances, a 4-wire resistance measurement mode proves useful. As shown in Fig. 3.8, in 4-wire mode, the resistance of a device is measured indirectly by measuring the current going through the resistor (with an ammeter) and the voltage drop across the resistor (with a voltmeter) measured at points close to the resistor. This technique yields the resistance of the RTD detectors R_{RTD} without the effect of the lead wires.

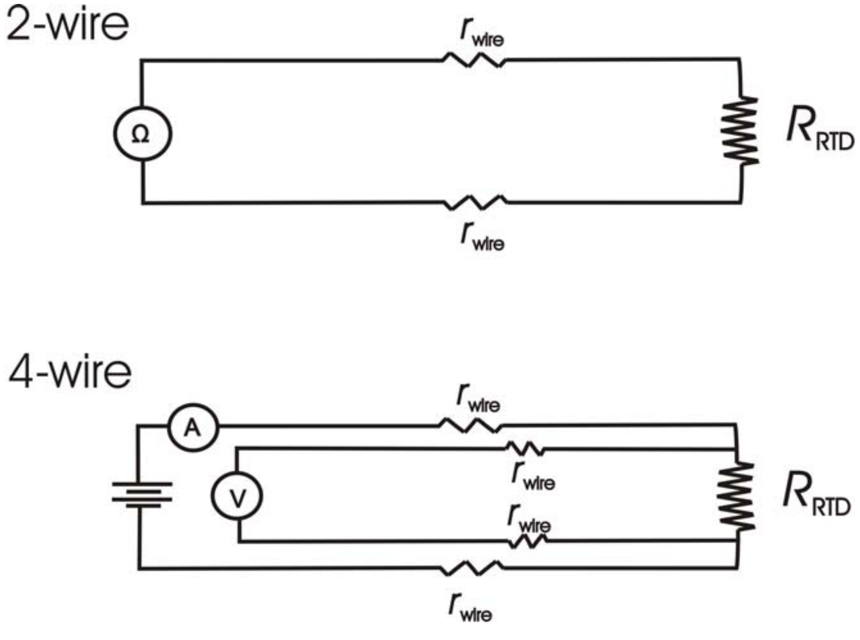

Figure 3.8: A schematic diagram showing 2-wire and 4-wire resistance measurements.

3.7 SOFTWARE PROGRAMS

Four in-house programmed computer software programs were used throughout this work to operate the calorimeter and analyze the measured experimental data. Three have been initially designed and programmed in C-language by Togane and Seuntjens (1997) for the NRC water calorimeter system. Modifications to the software programs were made to make them compatible with the McGill water calorimeter equipment. The fourth is programmed throughout this project in Matlab and is specifically optimized for brachytherapy water calorimetry. The programs share a parameter file which contains all necessary information regarding various devices (their GPIB ID), as well as various physical parameters and operation default settings. A brief description of all programs is provided below:

- H2ORUN: The main program used during the actual measurements, H2ORUN program is used to remotely control the entire calorimeter and all equipment that are connected to the main control computer through GPIB connection. The software has three operation modes: 1. Idle mode is used in between caloric runs, and facilitates the measurement of water temperature and copper thermal shield temperature. The data are used to control drift and ensure temperature equilibrium stability. 2. Ohm calibration mode is used to calibrate the bridge response in order to obtain a voltage-resistance calibration curve (*Section 3.8.3*). 3. Run mode is used to collect temperature data during irradiation measurements directly from the lock-in amplifier output.

- H2OVIEW: This software is used to analyse the ohm calibration runs as well as the caloric run data obtained (and stored) with H2ORUN.

- BRKYVIEW: A software similar in purpose to H2OVIEW, but optimized to be used in brachytherapy water calorimetry. The Matlab-based program is able to upload the caloric run measurement and ohm calibration data from H2ORUN files. What makes the program unique is its ability to communicate directly with COMSOL MULTIPHYSICS™ software. COMSOL is the heat transport simulation program that is used to calculate one of the largest correction factors in water calorimetry, the heat transfer correction factor (*Section 4.5*). Hence, instead of the user having to model the geometrical setup, running the simulations, and analyzing the simulation data to obtain the corrections to raw measurement data, BRKYVIEW offers the user the option to input information regarding the specific details of a generic experimental setup, and the program can automatically model, run, and analyze the COMSOL data and include the corrections into the final absorbed dose results. Moreover, BRKYVIEW presents the user with the option to analyse the measurement data using either the conventional technique, or the technique devised and used in this work for brachytherapy caloric runs (*Section 6.2.3*).

- PROBECAL: A program used only during PT100-RTD and thermistor temperature calibrations. Not only does the software communicate with the Keithley 2000 Multimeter to read off the probe temperature, but it also directly communicates with the fridge in order to control the cooling fluid’s temperature.

3.8 CALIBRATION

As discussed earlier, a water calorimeter is commonly referred to as a primary standard because it can measure absorbed dose from radiation without ever being cross-calibrated against a radiation device. Indeed, as long as temperature can be defined, a calorimeter can measure dose. However, the temperature is not measured directly, but rather from a measurement of the voltage response of the bridge as a result of a change in thermistors’ temperature-dependent resistance. There are three sets of calibration curves that are required for successful water calorimetry. They are described in the following subsections.

3.8.1 RTD Probe Calibration

All three RTD probes are calibrated against a mercury thermometer (Kessler) with a NIST traceable calibration certificate. With the fridge disconnected from the calorimeter, the calibration is performed directly inside the cooling fluid bath of the fridge in a temperature range of -4 °C to 12 °C. The RTD probes were read in the 4-wire resistance mode via the Keithley 2000 Multimeter.

Both the fridge and the multimeter were connected to the control computer and were monitored by the PROBCAL software through RS-232 and GPIB communication, respectively. The software slowly increases the bath temperature at 1 °C intervals, allows for the temperature equilibrium to stabilize such that a temperature variation of less than 10 mK/min is achieved, and prompts the user for the bath temperature. Using the calibrated mercury thermometer, the temperature of the bath could be read off to better than 0.02 °C. An average of 15 resistance readings per RTD probe was used at each temperature. As such, a ‘resistance vs. temperature’ calibration curve for each RTD probe was established.

3.8.2 Thermistor Probe Calibration

Using the now calibrated RTD probes, the thermistor calibration is done automatically while monitored by the PROBECAL software. The three RTD probes as well as the two thermistor probes are placed inside the cooling fluid bath. The RTD resistance is measured in 4-wire mode, while the thermistor resistance is measured in 2-wire mode. The calibration is performed once again over a -4 °C to 12 °C temperature range at 1 °C intervals. The bath temperature is evaluated by taking the average temperature reading of the three cross-calibrated RTD probes. Similar to RTD calibration, 15 measurements of thermistor resistance were obtained and averaged when the temperature equilibrium reached a stability of better than 0.4 mK/min corresponding to a thermistor resistance change of less than 0.005 %. There are two effects that need to be corrected for:

1. Since thermistor resistance measurements are done in 2-wire resistive mode, the 1 Ω lead wire resistance is subtracted to obtain the true resistance of the thermistor bead.

2. Since during thermistor calibration, a current, albeit small, passes through the thermistors, the measurements must be corrected for the effects of thermistor power dissipation as a result of the calibration procedure itself. Equation 3.1 can be used to calculate the heat dissipation by each thermistor with a bias voltage across it. With a 10 µA current flowing through the nominal 9.3 kΩ thermistors, a nominal power dissipation of 0.93 µW can be calculated. Since the heat generated by the thermistors is typically 2 mK/µW, an added temperature rise of just under 2 mK is generated which is also corrected for.

The resistance of each thermistor *R* as a function of temperature *T* over the 16 °C calibration temperature range can be accurately described by[4]

$$\ln(R) = a + \frac{b}{T} + \frac{c}{T^2}, \qquad a, b, c \in \mathbb{R}. \tag{3.2}$$

A solution to the relation presented in Eq. 3.2 is

$$R = R_o e^{\beta\left(\frac{1}{T} - \frac{1}{T_o}\right)}, \tag{3.3}$$

where T_o is 25 °C (298 K), and R_o and β are functions of temperature and are described by

$$\begin{aligned} \beta(T) &= b + \frac{2c}{T}, \\ R_o(T) &= \exp\left[a + \frac{\beta(T)}{T_o} - \frac{c}{T^2}\right]. \end{aligned} \tag{3.4}$$

Together, $\beta(T)$ and $R_o(T)$ describe the thermistor calibration curve, and are calculated for each of the two thermistors. Although calibration is performed over a 16 °C temperature range, the measurements are often performed over a 0.2 °C temperature range around the 4 °C calorimeter operation temperature. As such, the slow varying functions $R_o(T)$ and $\beta(T)$ are often approximated as constants for a particular thermistor and are calculated at 4 °C. Sensitivity S for a thermistor is defined as

$$S = \frac{1}{R}\frac{\mathrm{d}R}{\mathrm{d}T} = -\frac{\beta}{T^2}. \tag{3.5}$$

Both the RTD calibration and thermistor calibration are performed once to twice a year to monitor potential drifts. Figure 3.9(A) shows a typical calibration curve for a thermistor probe. The measured values of β and R_o are listed. A sensitivity of 4 % is measured at 277 K.

3.8.3 Bridge Calibration

In the active bridge setup shown in Fig. 3.7, the lock-in amplifier would detect a non-zero voltage when the combined thermistors resistance and the resistance of the decade box are not perfectly equal. This can happen either because of a variation in thermistors resistance as their temperature changes, or it can be accomplished by physically changing the resistance of the decade box. The former provides the signal during measurements, while the latter technique is used (in the absence of strong temperature drifts) to calibrate the bridge.

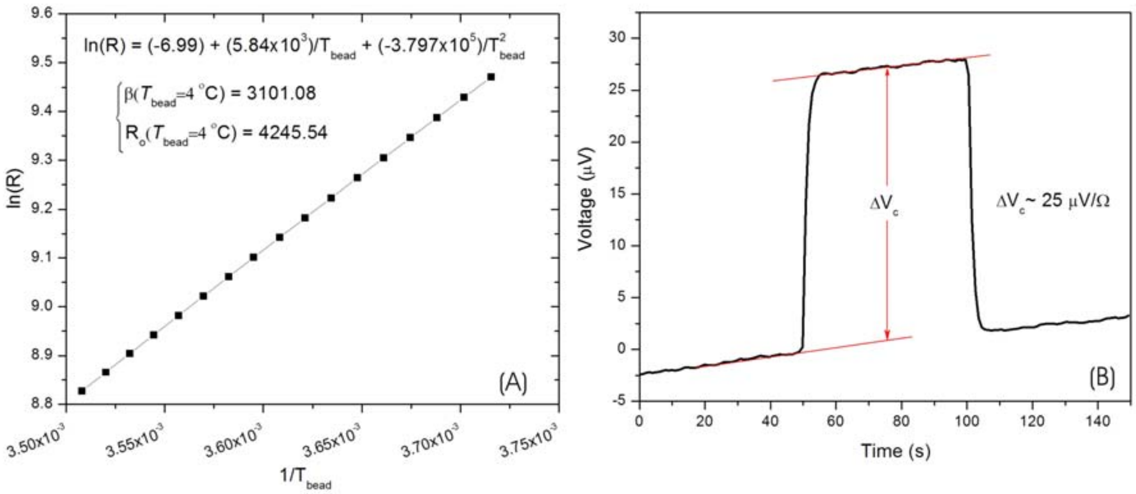

Figure 3.9: A typical thermistor calibration curve plotted in terms of logarithm of thermistor resistance to inverse of thermistor temperature (A). By fitting a quadratic equation to data, the values of constants and therefore the values of $\beta(T)$ and $R_o(T)$ can be determined. A typical ohm run calibration curve is also shown (B).

Thus, the bridge calibration procedure involves changing the resistance of a balanced decade box by 1 Ω, and measuring the voltage change recorded by the lock-in amplifier, see Fig. 3.9(B). The bridge calibration is performed in the absence of large drifts throughout the experiment at various different equilibrium temperatures (corresponding to different balanced decade resistor box settings). By combining all the results, a bridge calibration relating voltage change per ohm to Burster resistance (i.e. $\Delta V_{1\Omega} \Leftrightarrow R_{\text{burster},1\Omega}$) is obtained.

3.9 PREPARING FOR MEASUREMENTS

Prior to the placement of the vessel inside calorimeter and cooling the entire water phantom down to 4 °C, the vessel needs to be prepared for successful caloric measurements. There are four steps as discussed below:

1. After being thoroughly washed and cleaned with deionised water, the two calibrated thermistors are placed inside the vessel such that the tips are separated by only 2-3 mm centered on the central axis of the vessel. The thermistors are sealed by CAPFE® Teflon-encapsulated O-rings and threaded Teflon bushings. As can be seen in Fig. 3.3, there are four orthogonal plastic screws on each bushing that allow for making fine adjustments to the position of the probe tip.

2. The vessel is rinsed several times with deionised water, followed by being rinsed with pure water (organic content < 2 ppb). MilliQ-UV Plus (Millipore) water purification system was used to produce the ultra pure water. The vessel is subsequently filled with this pure water, and is bubbled with either pure hydrogen or nitrogen (99.999 % purity, Alphagaz) for a minimum of three hours. The bubbling is performed by inserting a 4-French Teflon tube down the bubbling port inside the vessel. At the end of the bubbling procedure, a gas bubble is trapped inside the vessel's small glass bulb, prior to the removal of the tube and complete seal of the vessel by closing the glass stopcock.

3. Subsequently, the vessel is irradiated by 200-400 Gy of dose from 6 MV radiation. Radiation facilitates the onset of radiation-induced chemical reactions that occur in presence of impurities in water (discussed in detail in *Section 4.6*). By irradiating the system to high doses prior to start of the irradiation, one could ensure that the system reaches a chemical equilibrium state in which no further heat gain or loss occurs as a result of exothermic/endothermic chemical reactions.

4. The position of the thermistor with respect to the front glass window of the vessel is subsequently measured with a travelling (measuring) microscope. Performing positioning measurements in brachytherapy are more complicated, as a catheter holder is mounted onto the calorimeter vessel to allow for the accurate positioning of the ^{192}Ir source with respect to the thermistor detectors. Using a 'dummy' source which mimics the shape of the actual source, both the

vertical (in depth) and lateral position of the source with respect to the middle of the two thermistors is measured.

All position measurement are made with a travelling microscope (OptiTech), see Fig. 7.2. Measuring the separation of two object vertically is simple: The microscope is focused (with 25x magnification) on each of the two surfaces of interest. The difference between the position of the optical tube at the two locations adjusted for the index of refraction of non-air materials equals the separation between the two surfaces. Since the calorimeter glass vessel is transparent, the travelling microscope is certainly ideal for the measurement of the depth of the thermistor beads inside the vessel. A measuring microscope allows us to make individual position measurements to the nearest 0.01 mm. However, since the thermistor depth is determined by taking an average of at least 20 measurements (while repeating the entire measurement setup several times to account for setup uncertainties) both before and after the caloric measurements, we achieved a positioning uncertainty of 0.13-0.40 mm.

Although depth measurements are trivial, the measurement of the lateral position of a source with respect to the middle of the two thermistor beads is difficult. In such cases, as shown in Fig. 6.3, the optical tube is turned horizontally and the device is used in its telescope mode. By focusing from distance on the setup, the position of a ‘dummy’ source with respect to the thermistor bead can be determined to within 0.4 mm.

3.9.1 Autoradiography

Due to radiation hazards, all brachytherapy source positioning measurements were performed with a ‘dummy’ simulator source instead of the hot active source. The dummy mimics the active source (shape, size) in all respects. During the positioning measurements, the dwell position (i.e., resting position) of the dummy source along the length of the catheter is determined. The dwell position is entered into the afterloader computer during the actual irradiation measurements, and it is assured that the hot ^{192}Ir source travels to the same position as the dummy source. It is clear that a successful experiment relies heavily on the afterloader being able to consistently and accurately replicate the dwell positions that are measured with the dummy source.

In order to quantify the discrepancy between the exact position of the dummy and the active source, an x-ray image of the dummy source was superimposed on an autoradiograph taken with the active source. As such, the source catheter is taped to a piece of film. The dummy source is brought into the catheter at a certain dwell position and an x-ray of the dummy is taken. Subsequently, the catheter taped on the film is connected to the afterloader and the machine is programmed to bring out the source to the same dwell position as measured with the dummy. As such, an image of the ^{192}Ir source (due to the radiation from the source itself) is also captured on the same film.

Figure 3.10(A) shows a Matlab-processed image of the hot ^{192}Ir source (in very close proximity to the film). Figure 3.10(B) shows an x-ray image of our dummy simulator source, while Fig. 3.10(C) shows an autoradiograph. Figure 3.10(D) shows a profile through the autoradiograph. A short Matlab program was written to simply do a fit to the profiles of both the dummy source x-ray and the autoradiograph. By measuring the separation between the tip of the dummy to center of the hot active source (see Fig. 3.10(D)) on the autoradiograph and half the full length of the dummy (see Fig. 3.10(B)), the relative agreement between the measured and delivered dwell positions was quantified, and was found to be better than 0.15 mm.

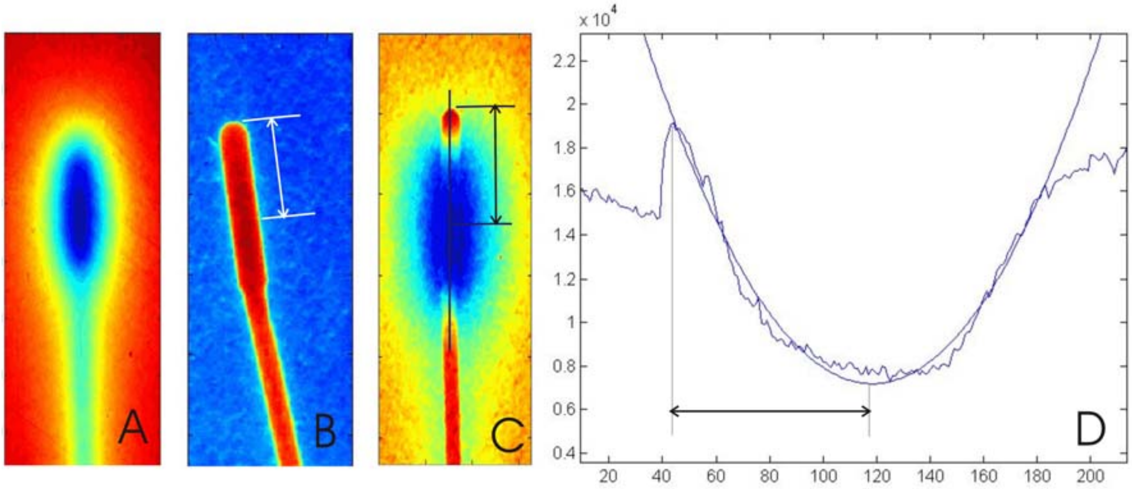

Figure 3.10: (A) A radiochromic film irradiated directly by a hot ^{192}Ir source; (B) An x-ray image of the ‘dummy’ simulator source; (C) An autoradiograph of the hot and dummy source combination; (D) A profile through the center of the autoradiograph, as shown in C, along with a quadratic fit.

3.10 REFERENCES

[1] K. Stewart, Ph.D. dissertation (McGill University, Montreal, 2007).

[2] *General Electric Technologies, NTC Glass Thermistors, NTC Thermistors: Type BR11/14/16/23 manual, WWW document, (http://www.gesensing.com/products/resources/datasheets/br111416.pdf)*, WWW Document,

[3] J. Seuntjens, Ph.D. Thesis (Ghent University Ghent, 1991).

[4] R. B. Barnett, Ph.D. dissertation (University of Calgary, Alberta, 1986).

Chapter 4

Principles of water calorimetry

4.1 THEORY

Water calorimetry measures the dose to water based on its fundamental definition in terms of temperature rise based on the following equation[1]

$$D_{\mathrm{w}}(\vec{r}) = c_{\mathrm{w,p}} \cdot \triangle T(\vec{r}) \cdot \prod_{i} k_i = c_{\mathrm{w,p}} \cdot \triangle T(\vec{r}) \cdot k_{\mathrm{ht}} k_{\mathrm{hd}} k_{\mathrm{dd}} k_{\mathrm{p}} k_{\rho} \ , \qquad (4.1)$$

where ΔT is the temperature rise at the point of measurement $\vec{r}$ due to radiation, $c_{\mathrm{w,p}}$ is the specific heat capacity of water at constant pressure, and k_{i} refers to correction factors that take the non-ideal measurement conditions into account. This chapter will focus on describing the details of the various components of Eq. 4.1, and explaining the principle behind water calorimetry and signal analysis.

4.2 SPECIFIC HEAT CAPACITY

The specific heat capacity of water is a function of water temperature. Normally, in external beam water calorimetry, the temperature gradients formed in water from radiation are of the order of microkelvin; hence, a constant $c_{\mathrm{w,p}}$ value at nominal calorimeter operation temperature is used. However, in our measurements with HDR ^{192}Ir brachytherapy (Chapter 6), the water temperature (especially close to the source) may be large enough that taking the temperature dependence of heat capacity into account may become necessary.

In 1921, Jaeger and Steinwehr[2] described $c_{\mathrm{w,p}}$ for distilled water as a function of temperature T using the empirical formula

$$c_{\mathrm{w,p}} = 1.00492 - 4.22542 \times 10^{-4} \cdot T + 6.32379 \times 10^{-6} \cdot T^2 , \qquad (4.2)$$

for $0 < T < 50\ ^{\circ}\mathrm{C}$. The most comprehensive work on $c_{\mathrm{w,p}}$, however, is that of Osborne *et al*[3] who determined $c_{\mathrm{w,p}}$ to five significant figures. For our work in proton therapy, since temperature gradients are small, we used a constant $c_{\mathrm{w,p}}$ at 4 °C calorimeter operation temperature $c_{\mathrm{w,p}}(T = 4\ ^{\circ}\mathrm{C}) = 4.205 \times 10^{3}\ \mathrm{J\ kg^{-1}\ K^{-1}}$. In the case of ^{192}Ir brachytherapy water calorimetry, three piecewise 5th order polynomial fit to CRC data[4] were used to describe the behaviour of $c_{\mathrm{w,p}}(T)$ over a temperature range from 2 °C to 30 °C.

4.3 TEMPERATURE MEASUREMENT

Figure 4.1 shows a typical water calorimeter measurement run, referred to also as a temperature drift curve. An ohm calibration run (see *Section 3.8.3*), representing the response of the bridge to a 1 ohm change in the decade box, has been included for comparison purposes. Although the ordinate is in units of voltage, it is proportional to temperature. A caloric run is composed of three parts (shown in Fig. 4.1):

- Predrift: This is the temperature drift measured by the detectors prior to the start of radiation. An ideal measurement is one with zero predrift, although, this is not a necessity for successful calorimetric measurements. As long as the drift throughout a caloric run is small enough that it can be approximated to be linear over the time span of the experiment, it can be corrected for in the analysis.

- Irradiation period: This is the temperature rise (due to radiation) at a point. Unlike other radiation detectors such as ionization chambers that average the energy deposited over a volume, the thermistor beads in stagnant water calorimetry allow for the measurement of temperature rise at virtually a point.

- Postdrift: This is the temperature drift measurement following the end of irradiation. In an ideal world where heat transfer (conduction and convection) is absent, postdrift should have exactly the same slope as the predrift. However, in reality, this is not the case because the temperature gradients formed inside the calorimeter as a result of non-uniform dose distribution result in transfer of heat from regions of warmer temperature to regions of colder temperature (i.e., drifts occur).

Temperature rise can be measured from a caloric run by measuring the difference between linear extrapolations of the predrift and postdrift to midrun. Normally, in the absence of strong non-linear drifts, ΔT results should be relatively insensitive to the predrift and postdrift intervals used for fitting and extrapolation purposes. However, in this work, we normally take equal time intervals for all three regions (i.e., the length of the predrift and postdrift used for fitting and extrapolation are equal to the length of the irradiation period).

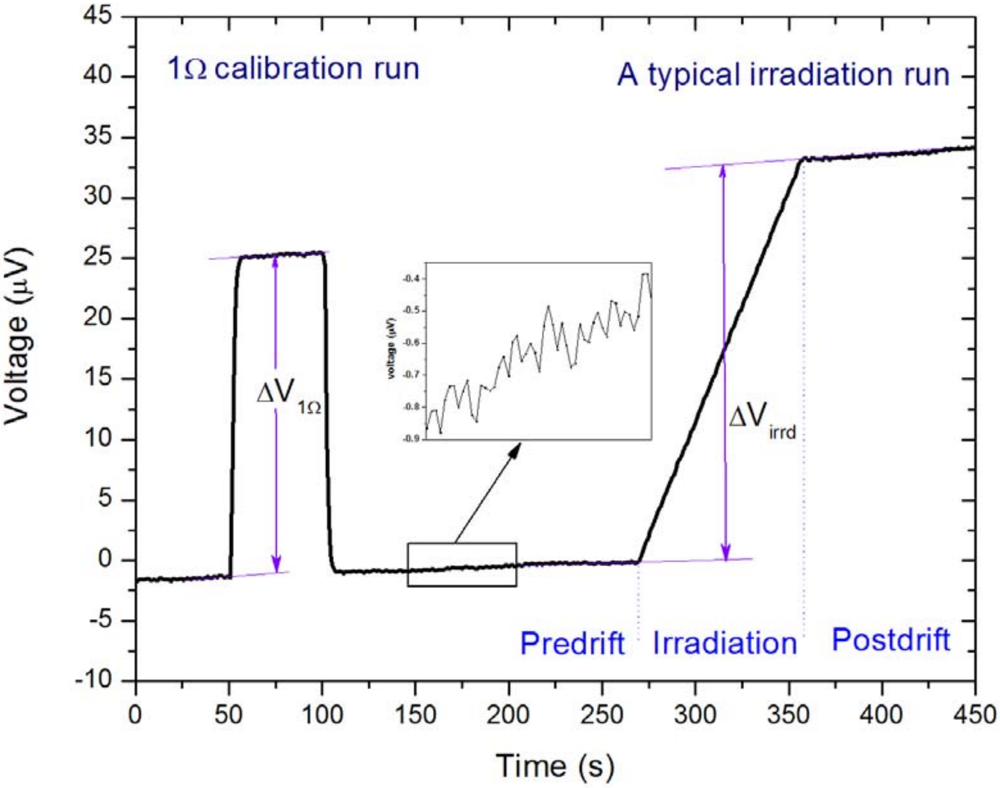

Figure 4.1: A typical caloric run showing the three stages of an experiment: predrift, irradiation, and postdrift. Note that the signal is in voltage and not temperature, although the two are quasi proportional, as discussed in *Section 4.3.1*.

4.3.1 Principles of Signal Analysis

As described in *Section 3.1*, we measure small voltage changes with a lock-in amplifier (as opposed to direct temperature changes) in water calorimetry. The measured quantity and the quantity of interest are related through AC bridge and thermistor calibrations: The bridge ohm-calibration relates voltage to resistance, while the thermistor calibration relates resistance to temperature.

Single Thermistor Detector

Given Eq. 3.3 describing the resistance of a thermistor as a function of temperature and Eq. 3.5 defining the sensitivity of a thermistor, if only a single thermistor was to be used as the temperature detector, the equation describing the relation between a sub-milli-Kelvin temperature rise ΔT and the resulting thermistor relative resistance change (signal) $\Delta R/R$ would be

$$\Delta T = \frac{\Delta R}{R}\frac{T^2}{\beta}\left(1+\frac{\Delta R}{2R}\right) + \text{higher order terms in } \frac{\Delta R}{R}. \qquad (4.3)$$

In external radiotherapy beams, temperature rises at the point of measurement are often very small and as a result $\Delta R/R$ is normally of the order of 10^{-6}; hence, all second order terms and higher in $\Delta R/R$ in Eq. 4.3 can be neglected. Although this assumption has been validated for several different radiation types in external beam water calorimetry, we shall show that it still holds (that $\Delta R/R$ is still small) for the largest temperature rises occurring in HDR ^{192}Ir brachytherapy water calorimetry.

Given the highest source activity used in clinics, a 10 Ci (41 000 U) source, and the closest source-to-detector separation deemed feasible for measurements (see Chapter 5), 25 mm, the rate of temperature increase is 4.75×10^{-6} K s^{-1}. For a 40 second irradiation period, we obtain a total temperature rise of 190 µK. Given a typical (400 Ω / 1 K) thermistor calibration and a typical decade resistor box setting of 18500 Ω (at 4 °C), we calculate $\Delta R/R \approx 5 \times 10^{-6}$ for HDR ^{192}Ir brachytherapy which can be completely ignored relative to unity as usually done in external beam calorimetry.

Going back to the definition of sensitivity (Eq. 3.5), and ignoring 2nd order and higher $\Delta R/R$ terms in Eq. 4.3, Eq. 4.3 can be rewritten as

$$\Delta T = \frac{\Delta R}{R} S^{-1}. \qquad (4.4)$$

Two Serially Connected Thermistor Detectors

In order to improve the signal in calorimetry, two thermistors connected serially are used to measure the temperature increase. Strictly, for a linearly varying dose gradient between the two thermistor tips, the temperature rise at a point in the middle of a line connecting the two tips, noted in Eq. 4.1, is an average of the temperature rise measured by two thermistors: $\Delta\bar{T} = \left(\sum_{i=1,2}\Delta T_i\right)\Big/2$, where ΔT_i is the change in temperature for each individual thermistor.

We described in *Section 3.9* that the thermistors are positioned with the tips across from each other, separated by few millimetres on either side of the central axis of dose distribution. We shall assume a small difference between the readings of the two thermistors such that the ratio of the measured temperatures is different from unity by a small amount 2δ

$$\frac{\Delta T_1}{\Delta T_2} = 1 + 2\delta\,. \tag{4.5}$$

In external beam radiotherapy water calorimetry, the uniformity of lateral dose profiles and flatness of the fields used during the measurement results in extremely small values of δ. This is not the case in ^{192}Ir brachytherapy water calorimetry where sharp dose gradients are formed in water (both laterally and in-depth). We calculated δ to range between 0.01-0.03 in HDR brachytherapy in the worst case. As a result, we can in general approximate $\Delta\bar{T}$ to be

$$\Delta\bar{T} = \Delta T_1(1+\delta) = \Delta T_2(1-\delta)\,. \tag{4.6}$$

Using the serially connected thermistor and bridge setup (see *Section 3.5*), we cannot separate the signal between the two thermistors, but rather we get the relative change in the sum of the two thermistors' resistance as a result of a temperature change. In other words, the total change in thermistors resistance $\Delta(R_1 + R_2)$ is the only quantity that can be measured, while the resistance of a balanced bridge at the start of the caloric run simply equals the sum of the two thermistors' resistance $\left(R_1+R_2\right)$. Thus, we can write the relationship between the measured signal $\Delta\left(R_1+R_2\right)/\left(R_1+R_2\right)$ and the average temperature rise resulting in the signal $\Delta\bar{T}$ (by using Eq. 4.5 and a rearranged Eq. 4.4)

$$\begin{aligned}\frac{\Delta\left(R_1+R_2\right)}{R_1+R_2}=\frac{\Delta R_1+\Delta R_2}{R_1+R_2}&=\frac{R_1S_1\Delta T_1+R_2S_2\Delta T_2}{R_1+R_2}\\&=\left(\frac{R_2S_2+R_1S_1}{R_1+R_2}+\delta\frac{R_2S_2-R_1S_1}{R_1+R_2}\right)\Delta\bar{T}\end{aligned}\tag{4.7}$$

The second term in brackets in Eq. 4.7 is on the order of 10^{-4}-10^{-5} and can be ignored. Hence, by defining $\bar{S}$ which represents the first term in brackets in Eq. 4.7

$$\bar{S}=\frac{R_2S_2+R_1S_1}{R_1+R_2},\tag{4.8}$$

Equation 4.7 can be rewritten in a much simpler form

$$\Delta\bar{T}=\frac{\Delta\left(R_1+R_2\right)}{R_1+R_2}\bar{S}^{-1}.\tag{4.9}$$

We now have an explicit description of temperature rise in terms of the total relative resistance change of the two thermistors. However, as described previously, using a Wheatstone bridge, we do not measure resistance change, but rather we measure a voltage change.

To describe the voltage reading in terms of relative resistance change, the ohm calibrations are used. As explained in *Section 3.8.3,* the AC bridge ohm calibration provided a relationship between a resistance change of precisely 1 Ω ($\Delta R_{1\Omega}$) at a given decade resistance box setting ($R_{\text{burster},1\Omega}$), and the resulting voltage change ($\Delta V_{1\Omega}$). Several tens of ohm run calibrations at various equilibrium temperatures (corresponding to different decade box settings) are performed. By putting all ohm run calibrations together, a function describing $\Delta V_{1\Omega}$ in terms of the decade box setting is found.

Hence, given a measured voltage change during an irradiation (ΔV_{irrd}) at a given initial balanced decade box setting $R_{\text{burster,irrd}} = R_1 + R_2$, the sum of thermistors resistance change $\Delta\left(R_1 + R_2\right)$ can be determined by using the ohm calibration curve (i.e., $\Delta V_{1\Omega} \Leftrightarrow \Delta R_{1\Omega} / R_{\text{burster},1\Omega}$ relationship). Indeed, the total resistance change as a function of the measured voltage signal ΔV_{irrd} is $\Delta\left(R_1 + R_2\right) = \frac{\Delta V_{\text{irrd}}}{\Delta V_{1\Omega}} \Delta R_{1\Omega}$, where the appropriate $\Delta V_{1\Omega}$ is interpolated from the ohm calibration curve at the specific value of $R_{\text{burster,irrd}}$. We can finally write the exact process through which the dose is obtained in water calorimetry using two thermistor detectors (from Eq. 4.1)

$$D_{\text{w}} = c_{\text{w,p}} \cdot \Delta\bar{T} \cdot \prod_i k_i = c_{\text{w,p}} \cdot \bar{S}^{-1} \frac{\Delta V_{\text{irrd}}}{\Delta V_{1\Omega}} \frac{\Delta R_{1\Omega}}{R_{\text{burster,irrd}}} \cdot \prod_i k_i \ . \tag{4.10}$$

Corrections k_i will be discussed in the following sections. All that remains here is to calculate $\bar{S}$ from its definition in Eq. 4.8. To do so, individual thermistor sensitivities (S_1 and S_2) and resistances (R_1 and R_2) need to be calculated. Sensitivity of each individual thermistor was defined earlier as $S = -\beta / T^2$ and can thus easily be calculated from thermistor calibration data (Eq. 3.4) and the thermistor bead temperature, which in turn can be derived from the water temperature and the thermistor excess temperature at the power level at which the thermistor is run. The individual thermistor resistances (R_1 and R_2) can be calculated using thermistor calibration data (Eq. 3.3).

Since the sum of the thermistor resistances (R_1+R_2) can be measured experimentally (with the decade resistor box balancing the thermistors), the accuracy of our calculation can be checked by comparing the calculated sum with the actual measured resistance sum of the serially connected thermistor pair. A discrepancy of the order of 0.01 % to 0.1 %, depending on the drift rate, has been observed.

4.4 CORRECTION FACTORS k_{dd}, k_p, AND k_ρ

Dose profile correction factor k_{dd} accounts for the difference between dose measured at the thermistor probes and at the central axis of the beam. Since, each thermistor is few millimetres offset from the central axis, the average dose measured by the thermistors needs to be scaled by the average lateral dose profile at the two thermistor positions. Both the correction and its uncertainty are often small in external radiotherapy beams because a uniform dose distribution with extremely flat dose profiles (especially in a few millimetres radius around the central axis) can be achieved. As we will see in Chapter 6, this is not the case in ^{192}Ir brachytherapy water calorimetry.

The perturbation correction factor k_p accounts for the effects of non-water materials present in the water calorimeter. Normally, the largest contributing factor to this correction is the glass vessel which encompasses the thermistor probes. For the brachytherapy work, a Monte Carlo (MC) simulation of the setup geometry in DOSRZnrc, EGSnrcMP[5] was used to determine the value of k_p correction. k_p is the ratio of the dose scored at the thermistor position for two similar MC simulations, one with non-water materials modelled (glass vessel included) and one in pure water (i.e., all non-water material properties are changed to water). The magnitude of the perturbation is determined by two competing effects: attenuation which decreases the dose and requires a correction factor greater than unity, and scatter which increases the dose, thus requiring a correction factor that is less than unity.

The water density correction factor k_ρ corrects for the difference in water density at calorimeter operation temperature (4 °C) and the water temperature at which other detectors are cross-calibrated against the calorimeter (room temperature). The dependence of water density on water temperature is well studied[4]. The density difference between the two temperatures manifests itself as a small difference in the effective measurement depth: a 0.2 mm difference at 8 cm water depth. As a result, k_ρ correction uses the depth dose curve to find the relative dose difference between the measurement depth and density-corrected depth. The magnitude of k_ρ depends on the depth of measurement and the gradient of dose distribution, and was never found to be higher than 0.4 %.

4.5 HEAT TRANSPORT CALCULATION

The heat transfer correction factor k_{ht} corrects for the effects of heat transfer due to conduction and convection on the temperature distribution inside the calorimeter (radiative effects are negligible for temperature differences generated in radiation therapy). k_{ht} is defined as the ratio of the ideal temperature rise (a temperature rise solely due to locally deposited absorbed dose in the absence of heat transfer) to the actual temperature rise (with the effects of heat transfer taken into account) at a given point. Whereas the ideal temperature rise is easy to calculate analytically with a knowledge of depth dose curve, the actual temperature rise in the presence of heat transfer can only be solved for by using numerical techniques.

The COMSOL MULTIPHYSICS$^{\mathrm{TM}}$ software was used in this work to calculate the heat transfer correction factor using the Finite Element Method (FEM). FEM is a numerical technique of solving partial differential equations (PDE). At its core, it relies on ‘discretizing’ the original PDE problem into a problem that has a finite number of unknown parameters (degrees of freedom). The new problem is then solved over a ‘discretized’ geometry where the original potentially complex geometrical model is subdivided into many smaller ‘mesh’ elements or volumes. The biggest challenge in FEM is the selection of a numerically stable approximate system of equations to the initial PDE problem.

COMSOL MULTIPHYSICS was found to be able to handle all the problems of interest that are faced in k_{ht} calculation in various radiotherapy beams. To solve a problem, the system of PDE equations to be solved needs to be determined. The software allows for a coupling of different physics modules. Furthermore, the software requires a geometrical model of the setup, the details of all boundary conditions, and all heat sources and heat sinks. Although the software is a general purpose FEM solver, we shall focus only on the areas specifically important to k_{ht} calculation.

4.5.1 Conduction and Convection

The general heat transport problem (based on both conduction and convection) can be fully described by three PDE[6]

$$\rho c_p \frac{\partial T}{\partial t} + \nabla \cdot (-k\nabla T + \rho c_p \vec{u} T) = Q\,, \tag{4.10}$$

$$\nabla \cdot \vec{u} = 0\,, \tag{4.11}$$

$$\rho \frac{\partial \vec{u}}{\partial t} - \eta \nabla^2 \vec{u} + \rho\left(\vec{u} \cdot \nabla\right)\vec{u} + \nabla p = \vec{F}\,, \tag{4.12}$$

where,

ρ, c_p, k	refer to physical properties (density, specific heat capacity at constant pressure, and conductivity) of the simulated media,
T	is the temperature field,
t	is the time,
Q	is the heat source,
$\vec{u}$	is the velocity field vector ($\vec{u} \equiv u\hat{i} + v\hat{j} + w\hat{k}$) in this case of water,
p	is the pressure field,
η	is the dynamic viscosity of the medium, in this case water,
$\vec{F}$	is the volume (body) force such as gravity.

Equation 4.10 describes the conservative formulation of the heat flow (due to conduction and convection effects). Equations 4.11 and 4.12 describe the incompressible flow and general motion flow equations, respectively. These two constitute the Navier-Stokes incompressible fluid model.

In 4 °C water calorimetry, the operation of the water calorimeter in a tight temperature range around 4 °C (more specifically 3.98 °C) minimizes the effects of convective flow. Since the water density is highest and the volumetric expansion coefficient of water is zero at 3.98 °C, it is common practice, as is a good approximation, to ignore the effects of convection during simulation. As shall be described in the next section, although this approximation can be exercised in external radiotherapy where the temperature non-uniformities are small (due to relatively uniform dose distribution), it is not necessarily valid in HDR ^{192}Ir brachytherapy due to large temperature gradient formation.

Ignoring the effects of convective flow ($\vec{u}=0$) simplifies the heat transfer problem (Eq.'s 4.10-4.12) to a single PDE describing conduction, given by

$$\rho c_{\mathrm{p}} \frac{\partial T}{\partial t} + \nabla \cdot (-k \nabla T) = Q\,. \tag{4.13}$$

When $\vec{u}=0$ assumption cannot be made, a coupling of the 'conduction and convection heat transfer' module with the 'incompressible Navier-Stokes fluid' module becomes necessary. All three PDEs need to be used and the two modules are coupled through the temperature field T and velocity field $\vec{u}$. Since the approximation of incompressible flow motion (defined by Eq. 4.11) can be made in water calorimetry, the general heat flow equation (Eq. 4.10) can be simplified to

$$\rho c_p \frac{\partial T}{\partial t} + \nabla \cdot (-k \nabla T) = Q - \rho c_p \vec{u} \cdot \nabla T\ . \tag{4.14}$$

The temperature dependence of water density can be described by

$$\rho(T) = \rho_o + \frac{\partial \rho}{\partial t}\left(T - \widehat{T}\right) = \rho_o\left[1 - \alpha\left(T - \widehat{T}\right)\right], \tag{4.15}$$

where the product of the thermal expansion coefficient α and the local rise in temperature $(T - \widehat{T})$ produces the local density decrease over the nominal density ρ_o . Although it is most appropriate to define $\widehat{T}$ as the temperature of the volume element at the immediate previous time step, in the COMSOL software, the user does not have access to such information. Hence, an approximation was used where $\widehat{T}$ was defined as the sum of the initial temperature (at the beginning of the simulation) and the temperature rise due to known accumulated local dose deposition *Q*. This approximation assumes that the local heat transfer into or out of the volume element is negligible. Although the best approximation available, this evaluation clearly does not yield accurate results in regions inside large temperature non-uniformities where conductive and convective effects are significant.

The body force and pressure gradient are manifestations of the temperature-dependent density variations (Eq. 4.15). Hence, the only force of interest in water calorimetry (in Eq. 4.12) is gravity, is directed towards the earth, and can be described by (where *g* is the gravitation constant)

$$\vec{F} = g\rho_o\left[1-\alpha\left(T-\widehat{T}\right)\right]. \qquad (4.16)$$

4.5.2 Modeling Considerations

The memory requirements and solution time of the software depend strongly on the number of degrees of freedom (DOF) of the model. The number of DOF is proportional to the number of mesh elements in the geometry and the number of dependent variables in the physics model.

The software allows for 2D axially symmetric as well as 3D modeling of the geometry. Simplification of the geometrical model by recognizing symmetries or making approximations can dramatically reduce the size and complexity of the actual geometry, hence drastically reducing the number of mesh elements required to describe the geometry.

Moreover, approximating the effects of convention to be negligible (in all beams except ^{192}Ir brachytherapy) drastically reduces the number of dependent variables: From five when convection is modeled (velocity: u, v, w, pressure: p, and temperature: T) to a single variable T when it is ignored.

The simulations were performed on a 32 bit Mac OS (2x2.66 GHz Dual Core Intel Xeon) with 4 GB of RAM. Although this computer had sufficient memory to solve all water-calorimetry 3D models in the absence of convection, the more sophisticated convective flow-based problems could only be solved with a 2D axially symmetric approximation model. The use of parallel processing with 64 bit computers can drastically reduce time restrictions.

4.5.3 Modeling

Throughout this work, two generic models of the calorimeter were used: one model simulated the geometrical setup in a 2D axial symmetric coordinate system, while the other one modeled a quarter of the full geometrical setup in 3D, (referred to hereon as 2D and 3D models). As described in *Section 4.5.2*, the 3D model could only handle conductive problems, while the 2D model could solve the combined conduction and convection heat transfer problem. For the sake of simplicity, we shall refer to the simulations based only on conduction as “conduction models,” while we address the simulations that couple ‘conduction/convection’ and ‘Navier-Stokes incompressible fluid’ models as “convection model.” This is done in full understanding that ‘convection models’ do fully include all heat transport effects arising from conductive effects.

For a convection model, a ‘conduction/convection’ module was coupled with two ‘Navier-stoke Incompressible fluid’ modules (for inside and outside the glass vessel separately since the solid glass vessel acts as a convective barrier). A ‘no slip’ boundary condition was used at all glass-water interfaces.

The sidewalls of the calorimeter, the air above the water surface, and the calorimeter lid were not modeled. Their effect on the final temperature distribution results is negligible. Moreover, the geometrical shape of the thermistor needle could not be modeled fully in the 2D model (since it was not axially symmetric); hence, only the thermistor bead was modeled in such cases. In convection models, the thermistor power dissipation was also taken into account as a heat source. The results of 2D conduction models were often in close agreement with those of 3D models for similar geometrical models and physical parameters. Images of COMSOL geometrical models (both 2D models in HDR ^{192}Ir brachytherapy, and 3D models in proton therapy) are provided in Chapters 5-8 (e.g., Fig. 6.5).

Although k_p corrects the dose results for all perturbation effects, to accurately calculate k_ht, the dose distribution that is put into the COMSOL model as a source term in the heat transport equations also needs to be corrected for such effects. In case of external proton beam water calorimetry, the brass foil in the calorimeter lid as well as the glass vessel itself result in dose perturbations. In HDR ^{192}Ir brachytherapy, since the source is brought inside the calorimeter, only the glass perturbation effect is dominant. The corrections can be made analytically (as described in *Section 8.2.3* in case of proton beams), or using Monte Carlo techniques for more accurate results (in case of brachytherapy). For the latter case, a Monte Carlo simulation similar to that used to obtain k_p is employed, except that instead of scoring the dose just at a point, the dose is scored in the entire volume; Hence, a full 3D perturbation correction is obtained which can be applied to the otherwise raw dose distribution in COMSOL. Figure 4.2 shows a picture of such a correction calculated in HDR brachytherapy. Upstream from the vessel ($r < 2$ cm) the correction is unity as the scatter from the glass is minimal. However, the perturbation effect becomes significantly larger for points around and inside the glass vessel.

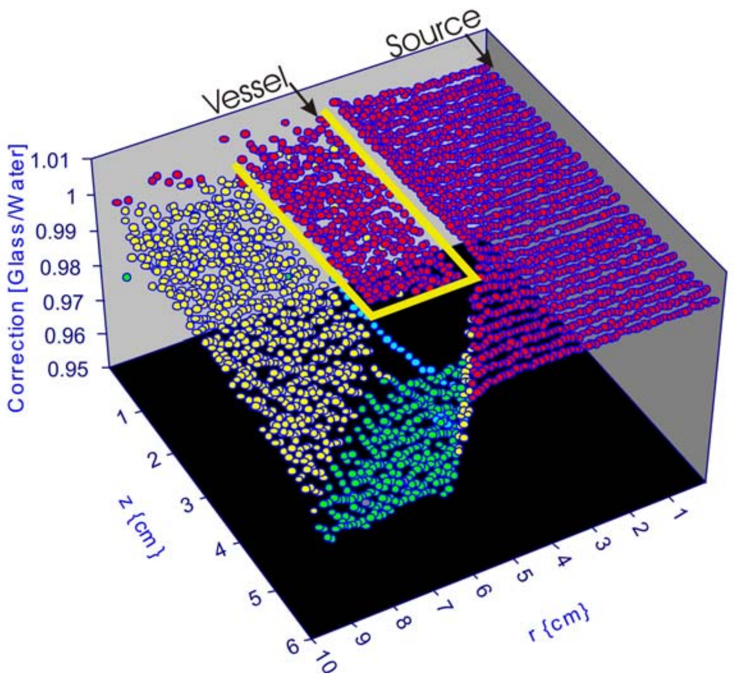

Figure 4.2: Dose perturbation correction factor calculated as a ratio of dose scored in the presence and absence of the calorimeter glass vessel in a DOSRZnrc Monte Carlo model of the setup geometry similar to one shown in Fig 6.5.

4.5.4 COMSOL Modeling Validation

It is important to validate the heat transport results of the software both in the presence and absence of convection. The simplest approach taken was to ensure that the numerical results of a ‘convection model’ simplify to those of a ‘conduction model’ for a uniform temperature rise across the water phantom. Moreover, heat transport due to conduction alone was studied in simple standard geometries. The numerical results were found to agree with analytical ones with sub-percent accuracy.

To validate more sophisticated geometrical and physics models, we compared the results of COMSOL software both to experiments and to other independent FEM-based heat transport solvers. In the case of conduction alone, the results of our calculations were contrasted against those performed by Carl Ross of the National Research Council of Canada using the FlexPDE software. The extrapolated sub-percent k_{ht} results were found to agree between the two software programs to better than 0.03 % for various different simulation setups and high energy photon energies.

In the case of full convection and conduction model, the COMSOL results were compared with the results obtained from an in-house FEM-based software programmed by Seuntjens *et al*[7] at the NRC. This program shall be referred to as NRCFEM. Combining Eq.'s 4.10-4.12, the software solves the full heat transport problem in a 3D regular hexahedral meshed geometry. The numerically calculated drift curves of NRCFEM have been contrasted against experiment at several photon and electron energies. Except for the first run, excellent agreement was found between calculation and experiment[7] for all successive runs.

The numerical results of COMSOL were validated against those of NRCFEM for a uniformly distributed dose deposition as well as a 20 MV photon beam incident vertically on an NRC calorimeter at both 4 °C and 22 °C. An NRC calorimeter consists of a 300 mm cubic water tank (1 mm thick side walls) with a $65 \times 54 \times 100$ mm^3 vessel (1 mm thick vessel walls). Inside the vessel, the two thermistors separated by 8 mm (tip-to-tip) were modeled as $0.40 \times 0.40 \times 46$ mm elongated rectangular box glass probes dissipating 6.4 µW of power at the tips[7]. Differences in geometrical models as well as meshing do exist due to the 3D Cartesian coordinate system of the NRCFEM and the 2D axially symmetric (cylindrical) coordinate system of the COMSOL (as described earlier, COMSOL convection models could not be solved in 3D with the available computer power).

Both the full temperature drift curve as well as the maximum velocity inside and outside the vessel at various time intervals were compared.

Figure 4.3 shows a comparison of the first 3 calorimetric runs following a 1000 s predrift. The results shown in the figure were calculated for a uniform irradiation of an NRC calorimeter vessel operated at 22 °C, with a thermistor power dissipation of 6.4 μW. The large initial temperature rise (in the absence of radiation) is due to the thermistor power dissipation. Figure 4.3(A) shows the percent difference between the calculated temperature evolution using COMSOL and NRCFEM. Moreover, Fig. 4.3(B) compares the calculated velocities both inside and outside the vessel using either simulation programs.

Sub-percent agreement of the temperature drift curves for all the various scenarios modeled in NRCFEM and COMSOL was obtained. At 4 °C and in the absence of extremely large dose gradients, the convective flow is minimal, and the solution converges to that of a model with only conductive heat transfer. For a 6.4 μW power dissipation and a uniform dose distribution, the velocities outside the vessel are 3 to 4 orders of magnitude smaller at 4 °C relative to 22 °C. A difference of 2 to 3 orders of magnitude between the two cases for velocities inside the vessel was observed.

At 22 °C, the maximum velocity both inside and outside the vessel generally agreed to about 30 %, but discrepancies as high as 65 % were observed (see for example Fig. 4.3(B)). Given the full range of differences between the two models (due to differences in geometry, meshing, and software-related), the differences in velocities were deemed acceptable.

In addition to validating COMSOL as a viable FEM-based solver for water calorimetry heat transport simulations, it should be noted that convective flow only becomes critical for calorimeter operations at room temperature. At 4 °C operation temperature, convection can be ignored virtually in all external radiation beams. In ^{192}Ir brachytherapy, the insertion of the hot active source inside the calorimeter results in extremely large temperature gradients which in turn produce convective flow. The convection will be greatest in the vicinity of the source. The results in ^{192}Ir brachytherapy will be discussed in detail in Chapter 6.

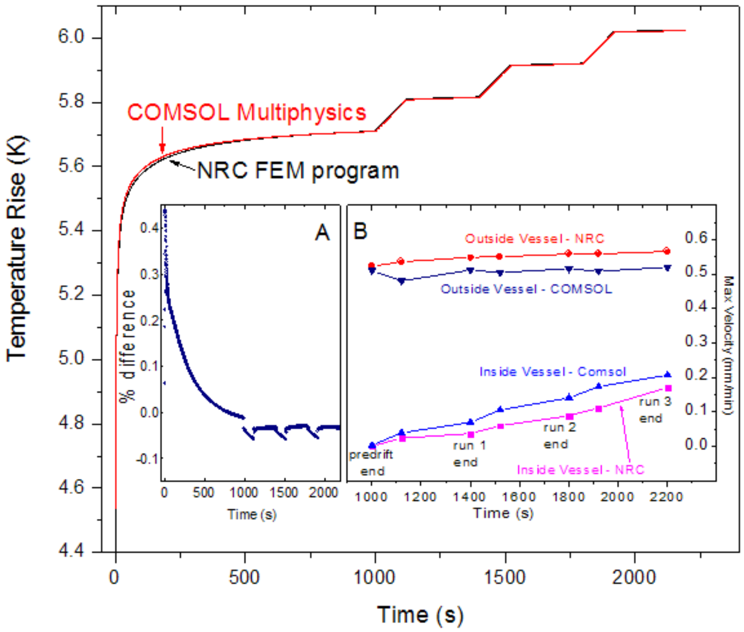

Figure 4.3: The figure shows a comparison of the first 3 calorimetric runs following a 1000 s predrift. The simulation was performed for a uniform irradiation of an NRC calorimeter vessel operated at 22 °C with a thermistor power dissipation of 6.4 μW. The difference between the calculated temperature increase using the two simulation programs is shown (A). The calculated velocities at inside and outside the vessel using the two programs are also shown (B).

4.6 HEAT DEFECT

Early water calorimeters exhibited anomalous behaviour resulting in dose measurement values that were different from results obtained by graphite calorimetry or ion chamber dosimetry by 2–5 %[8-11]. These results were indeed too large to be accounted for by the uncertainty on the measurement. A closer look at Domen's first operational water calorimeter[8,9] revealed that although the water inside the calorimeter was thermally isolated from surrounding environment, it was not protected against the exchange of gases or other impurities.

As such, a heat defect correction factor k_{hd} is introduced into Eq. 4.1

$$k_{\mathrm{hd}} = \frac{1}{1-h}, \text{ where } h = \frac{E_{\mathrm{a}} - E_{\mathrm{h}}}{E_{\mathrm{a}}}. \qquad (4.16)$$

The heat defect h is defined as the difference between energy absorbed E_{a} from radiation, and the energy which appears in the form of heat E_{h}. Ross *et al*[12,13] describe four techniques which can result in heat defect including two kinds of radiation-induced optical emission, acoustic energy generated by energetic charged particles, as well as radiation-induced chemical reactions. They show that chemical reactions are most likely the only significant source of heat defect with the first three effects contributing a total of less than 0.1 %[14]. Heat defect h in Eq. 4.16 is positive for exothermic reactions which release heat, while it is negative for endothermic processes which absorb energy from the surrounding.

The effects of heat defect are minimized in current water calorimeters by encompassing the thermistor detectors inside a vessel. Although the purity of water and concentration of dissolved gases cannot be controlled in the entire volume of water inside the calorimeter, it can certainly be controlled to a much greater extent in the small volume of water sealed in the glass vessel. By filling the vessel with extra pure water and saturating it through bubbling with pure known gases (procedure described in *Section 3.9*), the concentration of impurities and dissolved gases inside the vessel can be estimated; in this way, not only can heat defect be minimized, but it can also be numerically calculated. Moreover, it should be noted that Pyrex glass is the material of choice for vessel fabrication as opposed to other materials with closer physical or thermal properties to that of water. This is because unlike glass, most other materials, including plastics, tend to leak impurities into pure water over time.

4.6.1 Radiation Chemistry

As ionizing radiation traverses medium, it deposits energy not in a continuous fashion, but rather through individual interactions in a discontinuous manner, depositing discrete amounts of energy in discrete volumes. Since the amount of energy deposited in every cluster (event) can vary widely, it is categorized into three groups[15]:

- 'Spurs' referring to an energy deposition of 6-100 eV/event
- 'Blobs' referring to an energy deposition of 100-500 eV/event
- 'Short tracks' referring to an energy deposition of 500-5000 eV/event

The concept of dose deposition along the path of the particle is of course closely related to that of linear energy transfer LET, defined in *Section 2.1.1*. Since high energy photons and electrons are the most widely studied radiation type in water calorimetry, data on low LET radiation is abundant[16-22]. However, protons can have a range of LET values as they slow down, with the maximum LET occurring near the distal edge (LET values can reach 20 eV nm^{-1} or higher). There is a smaller body of work on radiation chemistry in the medium LET regime[23-25]. We shall present a summary of the radiation chemistry of water to shed light on heat defect.

For low LET radiation, about 70 % of the energy is deposited in spurs. Radiation chemistry in water occurs over a relatively large time range of 10^{-17} s to several seconds. At the onset of irradiation, and upon absorption of energy, the earliest changes to water begin (10^{-17} s)

$$\begin{aligned} &\text{(a)} \quad H_2O \rightarrow H_2O^+ + e^-, \\ &\text{(b)} \quad H_2O \rightarrow H_2O^*, \end{aligned} \qquad (4.17)$$

where H_2O^* is a water molecule in an excited state. After about a picosecond (10^{-12} s), the earliest chemical reactions begin to occur

$$\begin{aligned} &(a)\quad e^{-} \rightarrow e^{-}_{aq}, \\ &(b)\quad H_2O^{+} + H_2O \rightarrow H_3O^{+} + OH^{\bullet}, \\ &(c)\quad H_3O^{+} \rightarrow H^{+} + H_2O, \\ &(d)\quad H_2O^{*} \rightarrow H^{\bullet} + OH^{\bullet}, \end{aligned} \qquad (4.18)$$

where e^{-}_{aq} is a free electron solvated in water (referred to as a solvated or hydrated electron). e^{-}_{aq} often has the chance to move away from the point of radiation interaction by about 2 nm prior to thermalization (being trapped by the surrounding molecules). The chemical reaction noted in 4.18(c) follows quickly after that presented in 4.18(b). At the picosecond time scale, $H^{\bullet}$ and $OH^{\bullet}$ are radicals that are still within 2 molecular diameter of the center of the spur.

Because of the large concentration of free radicals and extremely reactive species in the vicinity of each other, a number of spur reactions follow quickly (between 10^{-12} s and 10^{-7} s). Concentration of reactive species is so high at this stage that spur reactions are not affected by low concentrations of reactive solutes (impurities) in water. However, the fraction of radicals that do recombine is a function of ionization density and LET. The most important spur reactions are

$$\begin{aligned} &(a)\quad H^{\bullet} + H^{\bullet} \rightarrow H_2, \\ &(b)\quad H^{\bullet} + OH^{\bullet} \rightarrow H_2O, \\ &(c)\quad OH^{\bullet} + OH^{\bullet} \rightarrow H_2O_2, \\ &(d)\quad e^{-}_{aq} + OH^{\bullet} \rightarrow OH^{-}, \\ &(e)\quad e^{-}_{aq} + H^{+} \rightarrow H + H_2O. \end{aligned} \qquad (4.19)$$

Concurrent with the above reactions taking place, radiolytic species diffuse out and away from the spur. In the third phase of the reactions, after about 10^{-7} to 10^{-6} s, the spurs start loosing their identity, and the reactive species from different spurs start interacting with each other as well as with impurities in water (present in millimolar concentrations) that may act as scavengers.

In radiation chemistry, for a given LET, yield of a given species X, denoted as *G*(X), is the number of molecules of that particular specie (free radical, ion, etc) produced per 100 eV of energy absorbed that escape the spur (do not react within the first 0.1 μs). For water, the G-values of various species that escape from the spurs have been studied for a wide range of LET[18,26]. A graph summarizing this information is reproduced from Ross and Klassen[12] in Fig. 4.2. A study of G-values are important as they are used in numerical simulations of the heat defect.

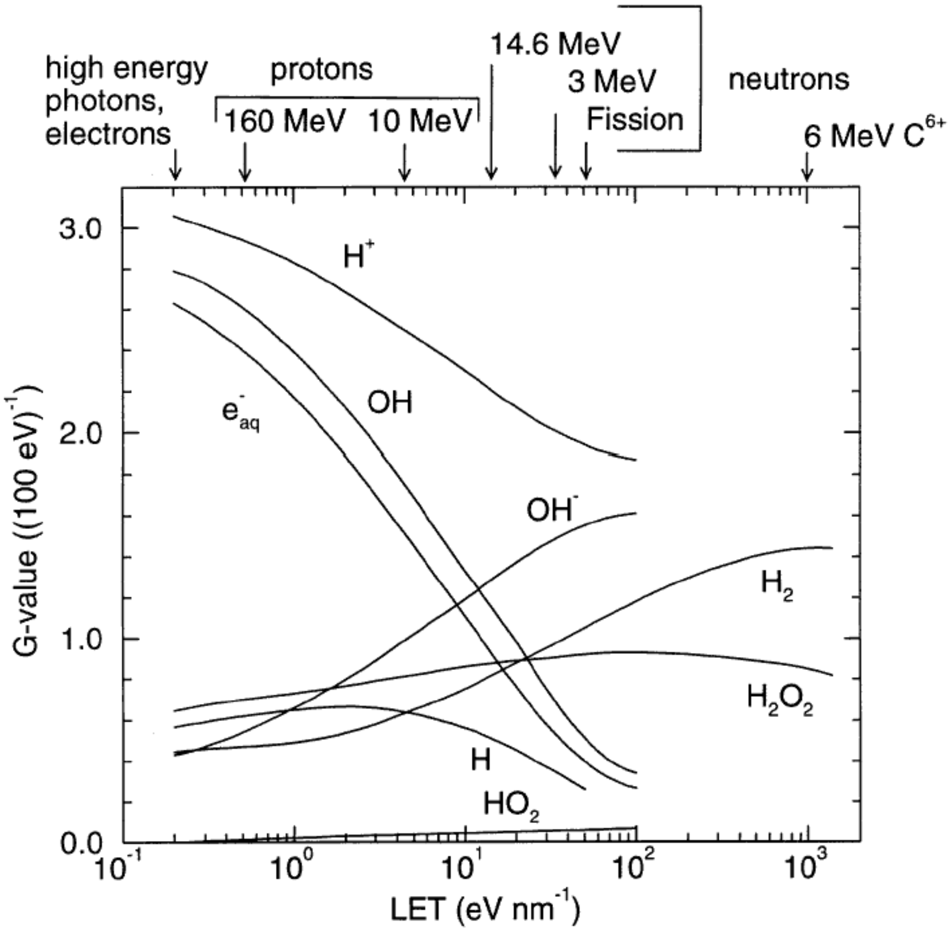

Figure 4.4: G-values of several spur products as a function LET (image from Ross and Klassen (1996), with permission).

4.6.2 Heat Defect Measurements

Using small, sealed vessels filled with highly purified water, the overall response of the system saturated with various gases has been studied. Subsequently, measurements are compared to simulations that use the G-value (directly related to production rate) of the most important species, as well as the forward and backward rate constants of the dominant chemical reactions as input. In such simulations, a homogeneous kinetics is followed, i.e., since the time scale of interest is longer than 10^{-7} s, one could assume that the species have moved away from the spur to an extent that they can be considered uniformly distributed in the solution[12]. As such, the heat defect for various aqueous systems (saturated with different gases) can be obtained. Ross and Klassen[12] report a maximum discrepancy between measured and calculated heat defect values of 0.8 %. Figure 4.5 shows a comparison of the measured and calculated heat defect for six such systems. The results have been calculated for low LET radiation.

Klassen and Ross[21] describe that in pure water, the largest source of uncertainty in dose measurement and heat defect is impurities acting as scavengers and reacting with hydroxyl radicals ($OH^{\bullet}$). Hence, they divide the heat saturated aqueous systems into two categories on whether or not a scavenger for hydroxyl radical exists[12,20]. Systems with excess concentrations of an organic impurity such as Na COOH (formate) or saturated with CO or H_2 are quite insensitive to impurity concentrations, as these molecules themselves act as scavengers for $OH^{\bullet}$, and since in high concentrations, they completely overcome the effects of trace amounts of impurities. Systems in which $OH^{\bullet}$ radical is not scavenged (such as an N_2 saturated system) seem to be more susceptible to impurities.

Normally, regardless of the aqueous system used, the prepared vessel is pre-irradiated to a large dose. Depending on the system, a state of energy balance can be obtained where dissociation of water in reactive products is in balance with creation of water from its products. In this case the heat defect is zero by definition. Alternatively, when impurities are present in excess, a situation of apparent steady-state can be achieved where the heat defect is not zero, but no longer dependent on accumulated dose, until the impurities are used up at which point the heat defect approaches zero. In the latter case, if the concentration of impurities is known, the heat defect can be calculated, but it then depends on the exact chemical and irradiation conditions. In this work, an N_2 and an H_2 saturated systems were used which are systems that approach zero heat defect. The N_2 system was used in ^{192}Ir brachytherapy. N_2 gas is meant to replace any dissolved oxygen. Klassen and Ross[20] discuss that O_2 also acts as an impurity and that oxygen concentrations as low as 10^{-7} mol L^{-1} require a minimum dose of 30 Gy before being used up and allowing the system to reach a steady state.

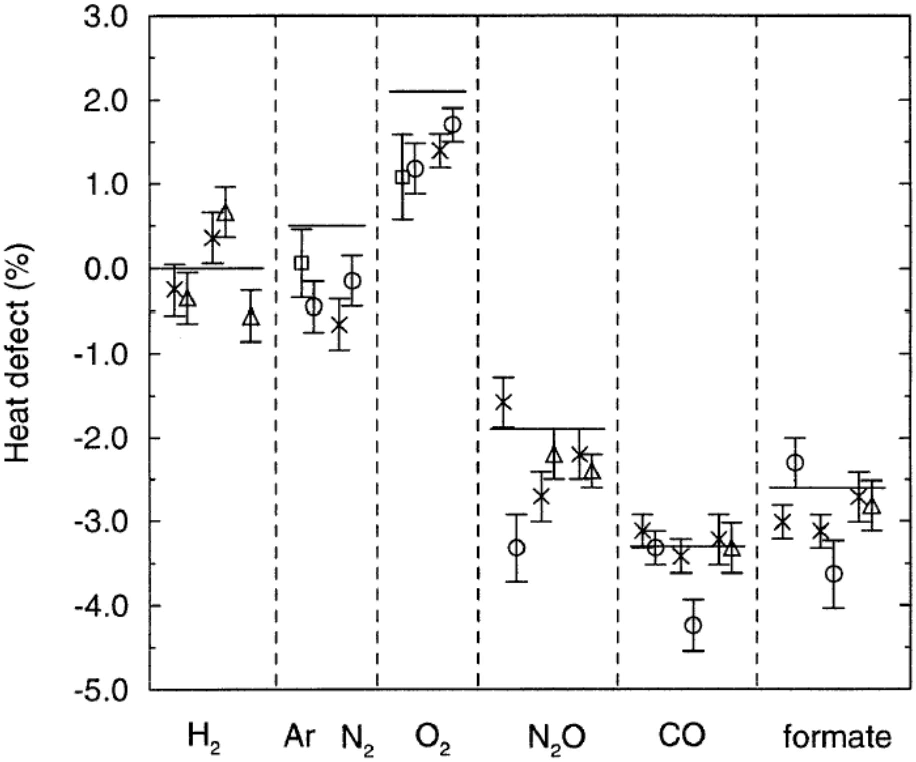

Figure 4.5: Comparison of heat defect for systems saturated with different gases. The horizontal line represents calculated heat defect, whereas the symbols indicate independent measurements (image from Ross and Klassen (1996), with permission).

An H_2-saturated system was used in proton therapy. Sassowsky and Pedroni[23] have shown that for high LET radiation, production of H_2O_2 is greater than its subsequent decomposition. As shown in Figure 4.6, reproduced from their work, an N_2-saturated system does not reach an equilibrium state at high LET. However, the authors find that an H_2 system leads to an increased decomposition of the H_2O_2 through two consecutive reactions in which the hydroxyl group acts as a catalyst

$$\begin{aligned} &\text{(a)}\quad OH^{\bullet} + H_2 \rightarrow H^{\bullet} + H_2O, \\ &\text{(b)}\quad H^{\bullet} + H_2O_2 \rightarrow OH^{\bullet} + H_2O. \end{aligned} \qquad (4.20)$$

As shown in Fig. 4.6, a H_2-saturated system is indeed found to reach an equilibrium state (and the system to attain zero heat defect) for concentrations of H_2 that are as low 1 μmol L^{-1}. An additional benefit of a H_2 system is that once the system reaches a steady state, it no longer deviates from a zero heat defect. However, H_2 systems are very sensitive to trace amounts of O_2. As the system is irradiated and oxygen is being used up, often a characteristic sharp exothermic peak is observed that corresponds to the O_2 depletion and is followed by a zero heat defect equilibrium state.

As described in *Section 3.9*, since we irradiated the vessel to doses well beyond the minimum required dose to achieve zero heat defect, in both ^{192}Ir brachytherapy (using an N_2 system), and proton therapy (using an H_2 system), we assumed a zero heat defect with a non-zero uncertainty (1.000 ± 0.003).

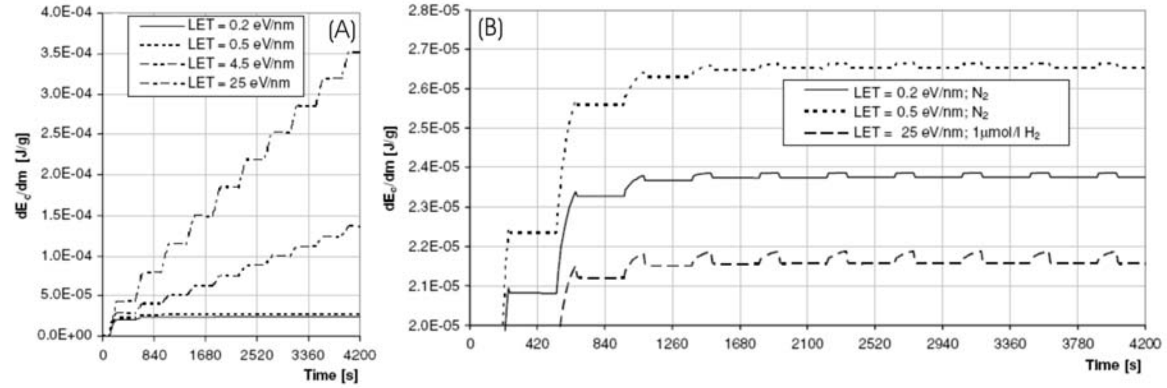

Figure 4.6: Calculated increase of the chemical energy per mass element with time for different LET values for an N_2-saturated (A) and an H_2-saturated (B) systems. No equilibrium is reached in an N_2-saturated system at high LET values. However, for an H_2-system, even at high LET values, the system attains an equilibrium (image from Sassowsky and Pedroni (2005), with permission).

4.7 REFERENCES

[1] J. Seuntjens and S. Duane, "Photon absorbed dose standards," Metrologia 46, S39-S58 (2009).

[2] W. Jaeger and H. Steinwehr, "Die Wärmekapazität des Wassers zwischen 5° und 50° in internationalen Wattsekunden," Annalen der Physik 4, 305-366 (1921).

[3] N. S. Osborne, H. F. Stimson, and D. C. Grinnings, "Measurements of heat capacity and heat of vaporization of water in the range 0 to 100 C," J Res Natl But Stand 23, 197-259 (1939).

[4] CRC handbook of Chemistry and Physics, 57th edition, edited by R. C. Weast (CRC Press, Cleveland, OH, 1976).

[5] I. Kawrakow and D. W. Rogers, "The EGSnrc Code System: Monte Carlo Simulation of Electron and Photon Transport," NRC Reports, PIRS-701 (2006).

[6] S. V. Patankar, "Numerical heat transfer and fluid flow," (Hemisphere Publishing Corporation, Washington, 1980).

[7] J. Seuntjens, I. Kawrakow, and C. K. Ross, "Revisiting Convective Motion in Stagnant Water Calorimeters Operated at Room Temperature," presented at the NPL Workshop on Recent Advances in Calorimetric Absorbed Dose Standards, National Physical Laboratory, Teddington, UK, 2000 (unpublished).

[8] S. R. Domen, "Absorbed dose water calorimeter," Med Phys 7, 157-159 (1980).

[9] S. R. Domen, "An absorbed dose water calorimeter: Theory, design, and performance," J Res Natl Bur Stand 87, 211-235 (1982).

[10] H. Kubo, "Absorbed dose determination with a water calorimeter in comparison with an ionisation chamber," Phys Med Biol 28, 1391-1399 (1983).

[11] A. Marles, Ph.D. thesis (University of Texas, Houston, 1981).

[12] C. K. Ross and N. V. Klassen, "Water calorimetry for radiation dosimetry," Phys. Med. Biol. 41, 1-29 (1996).

[13] C. K. Ross, N. V. Klassen, K. R. Shortt, and G. D. Smith, "Water calorimetry, with emphasis on the heat defect," presented at the Proceedings of the NRC Workshop on water calorimetry, June 6-7, 1988, 69-75.

[14] C. K. Ross, N. V. Klassen, K. R. Shortt, and Smith G. D., "A direct comparison of water calorimetry and Fricke dosimetry," Phys Med Biol 34, 23-42 (1989).

[15] A. Mozumder and J. L. Magee, "Model of tracks of ionizing radiations for radical reaction mechanisms," Radiat Res 20, 203-214 (1966).

[16] A. W. Boyd, M. B. Carver, and R. S. Dixon, "Computed and experimental product concentrations in the radiolysis of water " Radiat Phys Chem 15, 177-185 (1980).

17 M. B. Carver, D. V. Hanley, and K. R. Chaplin, "MAKSIMA-CHEMIST: A program for mass action kinetics simulation by automatic chemical equation manipulation and integration using stiff techniques," AECL, Chalk River Nuclear Laboratories AECL-6413 (1979).

18 A. J. Elliot, "Rate constants and G-values for the simulation of the radiolysis of light water over 0-300 C range," AECL, Chalk River Nuclear Laboratories AECL-11073 (1994).

19 J. W. Fletcher, "Radiation chemistry of water at low dose rates-emphasis on the energy balance: a computer study " AECL, Chalk River Nuclear Laboratories AECL-7834 (1982).

20 N. V. Klassen and C. K. Ross, "Water Calorimetry: The Heat Defect," J Res Natl Inst Stand Technol 102, 63-74 (1997).

21 N. V. Klassen and C. K. Ross, "Water calorimetry: A correction to the heat defect calculations," J Res Natl Inst Stan 107, 171-178 (2002).

22 N. V. Klassen and C. K. Ross, "Water calorimetry: A correction to the heat defect calculations," J Res Natl Inst Stan Technol 107, 171-178 (2002).

23 M. Sassowsky and E. Pedroni, "On the feasibility of water calorimetry with scanned proton radiation," Phys Med Biol 50, 5381-5400 (2005).

24 J. Seuntjens, Ph.D. Thesis (Ghent University Ghent, 1991).

25 R. J. Schulz, L. J. Verhey, M. S. Huq, and N. Venkataramanan, "Water calorimeter dosimetry for 160 MeV protons," Phys Med Biol 141992).

26 R. F. Anderson, B. Vojnovic, and B. D. Michael, "The radiation-chemical yields of H_3O^+ and OH^- as determined by nanosecond conductimetric measurements " Radiat Phys Chem 26, 310-313 (1985).

Chapter 5

An absorbed dose to water standard for HDR ^{192}Ir brachytherapy sources based on water calorimetry: Numerical and experimental proof-of-principle

Published in Medical Physics, this manuscript provides the results of our feasibility study and shows both numerically and experimentally that water calorimetry can be used as a primary standard in HDR ^{192}Ir brachytherapy dosimetry. We present the results of our numerical calculations which show the range of possible source to detector separations that allow for successful water calorimetry in HDR ^{192}Ir brachytherapy. The initial setup modifications and experimental results are shown and explained. Potential future improvements to the design and experimental procedures are also discussed.

Authors: Arman Sarfehnia, Kristin Stewart, Jan Seuntjens
Medical Physics Unit, McGill University, Montréal, Québec, Canada
*Medical Physics **34,** 4957-4961 (2007)*

ABSTRACT

Water calorimetry is an established technique for absorbed dose to water measurements in external beams. In this paper, the feasibility of direct absorbed dose measurements for high dose rate (HDR) iridium-192 (^{192}Ir) sources using water calorimetry is established. Feasibility is determined primarily by a balance between the need to obtain sufficient signal to perform a reproducible measurement, the effect of heat loss on the measured signal and the positioning uncertainty affecting the source-detector distance. The heat conduction pattern generated in water by the Nucletron microSelectron-HDR ^{192}Ir brachytherapy source was simulated using COMSOL MULTIPHYSICS™ software. Source heating due to radiation self-absorption was calculated using EGSnrcMP. A heat-loss correction k_c was calculated as the ratio of the temperature rise under ideal conditions to temperature rise under realistic conditions. Our calorimeter setup used a parallel-plate calorimeter vessel of 79 mm diameter and 1.12 mm thick front and rear glass windows located 24 mm apart. Absorbed dose was measured with two sources with nominal air kerma strengths of 38000 and 21000 U, at source-detector separations ranging from 24.7 to 27.6 mm and irradiation times of 36.0 to 80.0 s. The preliminary measured dose rate per unit air kerma strength of (0.502±0.007) μGy/(s.U), compares well with the TG-43 derived 0.505 μGy/(s.U). This work shows that combined dose uncertainties of significantly less than 5 % can be achieved with only modest modifications of current water calorimetry techniques and instruments. This work forms the basis of a potential future absolute dose to water standard for HDR ^{192}Ir brachytherapy.

5.1 INTRODUCTION

In 1980, Domen[1] established that, because of the low thermal diffusivity of water, water calorimetry was a viable technique for use in external radiation beams to measure absorbed dose at a point in water. Over the last two decades, with the tendency to move reference dosimetry towards absorbed dose to water standards, efforts at standards labs have concentrated on providing absorbed dose calibrations for ^{60}Co, high energy photon beams and, more recently, high energy electron beams. In these efforts, water calorimetry has played a pivotal role.

For brachytherapy, the air-kerma based reference dose calculation formalism, described in AAPM Task Group 43[2] and its update[3], is currently recommended for low and high dose rate interstitial brachytherapy sources. Uncertainty in the dose rate calculation arises partially because the factors used in TG-43 are largely calculation-based. At secondary standards laboratories, ^{192}Ir air kerma calibrations are obtained through interpolation of calibration factors for thimble chambers obtained at beam energies spanning the effective energy of the ^{192}Ir source[4]. However, this protocol has been shown to have several shortcomings[5]. Only recently, primary labs have established the feasibility of a more fundamental measurement of air kerma in ^{192}Ir photon fields using cavity chambers and Monte Carlo derived correction factors to account for the breakdown of Spencer-Attix cavity theory[6].

A direct calibration of ^{192}Ir sources in terms of absorbed dose to water could reduce some of the basic reference dosimetry uncertainties. Despite recent work on standards for energy output measurements of low dose rate radioactive sources[7], absorbed dose water calorimetry for high dose rate (HDR) sources has not yet been explored and could potentially open doors for a novel generation of standards for these sources including electronic brachytherapy sources. One of the main anticipated problems has been the source self-heating that is expected to create a steep temperature gradient in addition to the inherent steep radial dose profile close to the source, impairing reliable experimental determination of absorbed dose. Since both positioning uncertainties and source self-heating effects increase with decreasing distance from the source, whereas signal decreases with increased distance from the source, feasibility and operating conditions of the technique will be determined by how these competing effects balance.

5.2 METHODS

5.2.1 Water Calorimeter

Figure 5.1(a) shows a schematic diagram of the McGill in-house built Domen-type water calorimeter[8] used in this work. The calorimeter is built and operated similar to many standard stagnant 4.00 ºC water calorimeters using an active AC-bridge setup[9].

Figure 5.1(b) shows the plane-parallel vessel used in this experiment. The vessel has a diameter of 79 mm, and 1.12 mm thick front and rear glass windows located 24 mm apart. Also shown in Fig. 5.1(b) is the acrylic holder designed to mount onto the vessel with several four French (inner diameter of 1.2 mm) nylon-12 catheters affixed inside the holder at roughly 5 mm separations, with the closest catheter being at a distance of 10 mm from the front surface of the vessel. This allowed for flexibility in absorbed dose determination at several measurement positions from the source. The vessel was filled with high purity water (organic content < 2 ppb). In order to remove any dissolved gases, the water inside the vessel was bubbled with high purity (99.999%) nitrogen for 3 h.

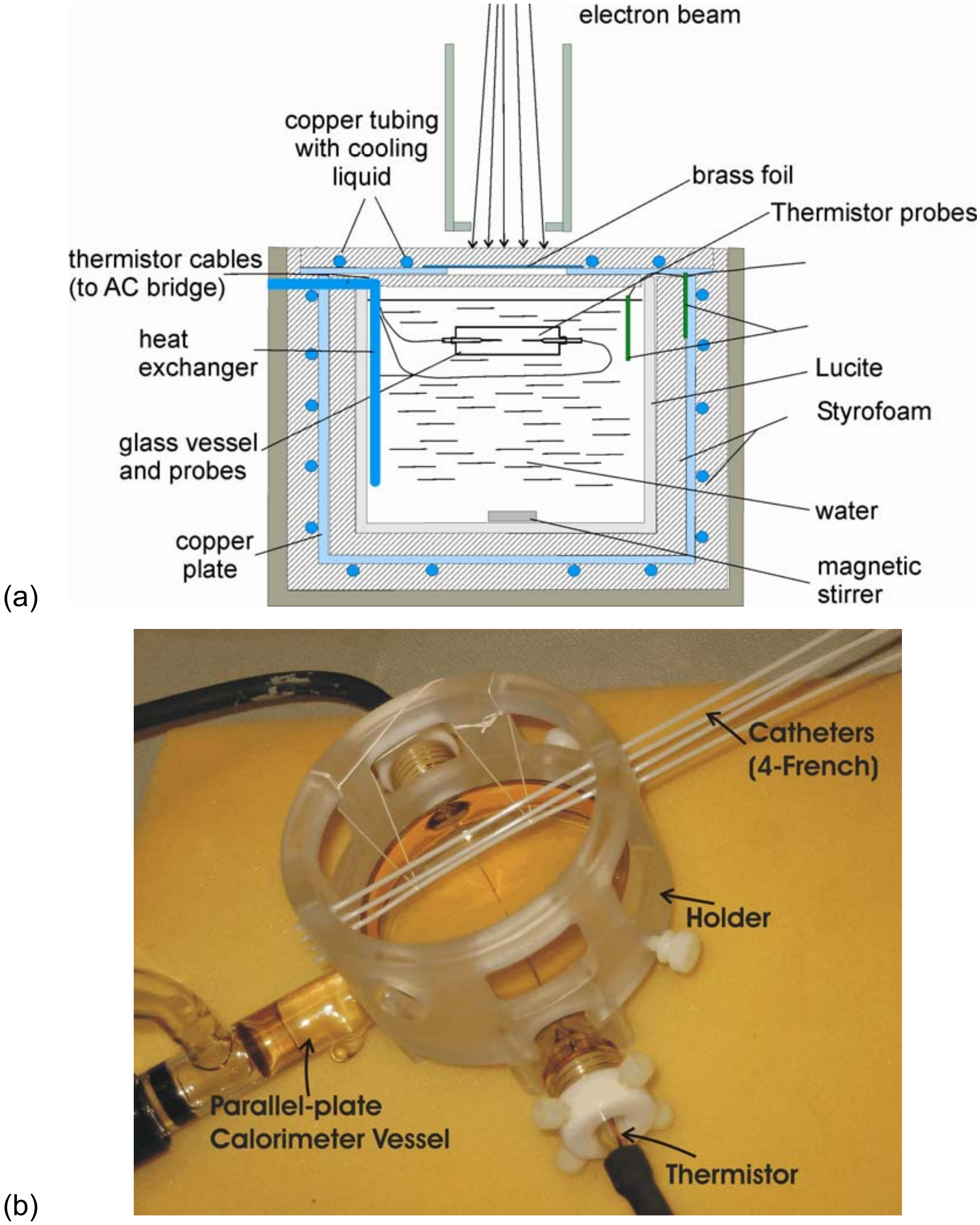

Figure 5.1: (a) McGill Domen-type water calorimeter modified for use in HDR ^{192}Ir brachytherapy. The catheters are fixed inside the holder. PT100 probes are used to monitor the water temperature in the water tank, while the heat exchanger is used to regulate it. The stirrer is turned off prior to measurements for temperature stabilization purposes. (b) The catheter holder fixed onto the parallel-plate calorimeter vessel used in this work.

5.2.2 Temperature Drift

The typical temperature drift trace obtained from the ^{192}Ir source consists of three basic regions: 1) a predrift region (prior to irradiation) where the temperature drift is stable. 2) a region of constant quasi-linear increase in temperature that corresponds to the source entering the calorimeter and being kept at a fixed position from the thermistors (point of measurement) for the duration of the irradiation. 3) a postdrift region which shows the behavior of water temperature for time intervals after the removal of the source from the calorimeter. The post-drift has a characteristic shape and includes a region of relatively slow temperature rise that is governed by the extent of the temperature gradient created in water due to direct dose deposition in water from the radiation source. This is followed by a sudden and relatively steep increase in temperature due to the self-heating from the source reaching the point of measurement. Using a heat conduction model in water, the start time of this sudden temperature rise can be accurately predicted as a function of source - point of measurement separation.

5.2.3 Absorbed Dose Measurement

The dose to water D_w at a point $\vec{r}$ corresponds to the temperature rise measured at that point ΔT by

$$D_w(\vec{r}) = c_w \cdot \Delta T(\vec{r}) \cdot \prod k_i \,, \qquad (5.1)$$

where c_w is the specific heat capacity of water, and k_i stands for calorimeter correction factors that account for conductive losses k_{c} due to the effect on measured temperature rise of water in the presence of a temperature gradient resulting from non-water materials inside the water calorimeter, the source self-heating and the dose distribution-related temperature gradients in water. The correction factors also account for heat defect k_{HD} due to radiolysis of water during irradiation and radiation perturbation effects k_{p} in the non-water materials in the calorimeter[9] (i.e., glass vessel).

5.2.4 Heat Loss in ^{192}Ir Brachytherapy Calorimetry

In ^{192}Ir brachytherapy calorimetry, heat loss effects are the most significant effects perturbing an accurate dose measurement. In traditional calorimetry, temperature increase is usually determined by extrapolating linear fits made to temperature predrift and postdrift of the drift curve back to midrun, and determining the difference between the two. This procedure provides an accurate estimate of the heat loss correction for heat transfer in a system with two bodies at different temperature for which the heat-loss modulus is constant. In HDR ^{192}Ir brachytherapy water calorimetry, however, the system does not approximate a system with constant heat-loss modulus and a supplementary correction is required, which was determined in this work under the assumption that conduction is the sole mode of heat loss. The correction k_c, defined as the mid-run extrapolated ratio of the ideal temperature rise (a temperature rise solely due to locally deposited absorbed dose in the absence of thermal conduction) to the actual temperature rise (with the effects of conduction taken into account) at a given point, was determined using numerical heat transport calculations.

The temperature distribution around the source (Nucletron microSelectron-HDR ^{192}Ir; part no. 105002) was calculated using the heat transfer module of the COMSOL MULTIPHYSICS^{TM} version 3.3a software. The ^{192}Ir source (composed of an inner radioactive core as well as an AISI 316L steel capsule[10]) was modeled inside a 4-French catheter placed inside a water phantom representing the water calorimeter (the glass vessel was also modeled). The model also included thermal properties of materials used, the boundary conditions, as well as distal and temporal information about heat sources and heat sinks. Using this information, COMSOL subsequently integrates the heat transport equation using the finite element technique. To this end, a fine mesh setting as well as adiabatic boundary conditions were used (i.e., no energy loss through the boundaries). Controlling the error in each integration step, the relative calculation tolerance was set to $1\text{x}10^{-11}$ while the absolute tolerance was set to $1\text{x}10^{-12}$. The initial water temperature inside the calorimeter was taken to be 4.00 °C. The point of measurement was taken to be on the perpendicular bisector away from the source.

The fractional source self-energy due to the self-attenuation of ^{192}Ir photons in the source was calculated using EGSnrcMP code[11]: The source was modeled in DOSRZnrc and the dose due to photons and electrons was scored inside the source and in the steel capsule encasing it. The air kerma in a small mass of air at a point 40 mm away from the source on its perpendicular bisector was also scored. The doses due to photons and electrons were scaled and added based on the PIRS report 692r results[12,13] stating the emission of 2.363 photons and 1 electron per disintegration of ^{192}Ir. On average, a total dose of $1.79\text{x}10^{-7}$ cGy/disintegration inside the core and a total dose of $1.50\text{x}10^{-8}$ cGy/disintegration in the capsule were calculated. An air-kerma strength of $3.80\text{x}10^{-11}$ cGy.cm^2/disintegration was calculated. Based on this self-heating, the source equilibrium excess temperature was calculated to be roughly 5 °C above room temperature (~25 ºC).

Information regarding source geometry as well as its spatial dose rate distribution in water were obtained from the paper by Daskalov *et al*[10]. A smooth, three-dimensional polynomial fit was made to the entire dose distribution data set using TableCurve® 3D, and was used in the COMSOL heat transport calculations.

5.3 RESULTS

5.3.1 Conduction Correction

Figure 5.2 shows calculated k_c corrections, obtained by mid-run extrapolation of the ratio of calculated ideal temperature to real temperature as a function of measurement position and irradiation time, for a simplified geometry (^{192}Ir source inside a 4-F catheter, all immersed in water). Since with the present-day thermistor-based detection technology, a typical minimum dose of about 1 Gy at the measurement point is required to achieve sub-percent precision, minimal exposure times in Fig. 5.2 were selected to meet this criterion. For a source with an $S_{K,\mathrm{air}}$ of 40630 U (9.955 Ci), a typical source activity at the time of source delivery to clinics, irradiation times of 36, 80, 142, 180, and 222 s correspond to a 1 Gy dose delivered at 2, 3, 4, 4.5, and 5 cm away from the source, respectively. The actual value of k_c is independent of source activity, as calculation of this correction factor involves taking a ratio where both numerator and denominator contain the same source term.[14]

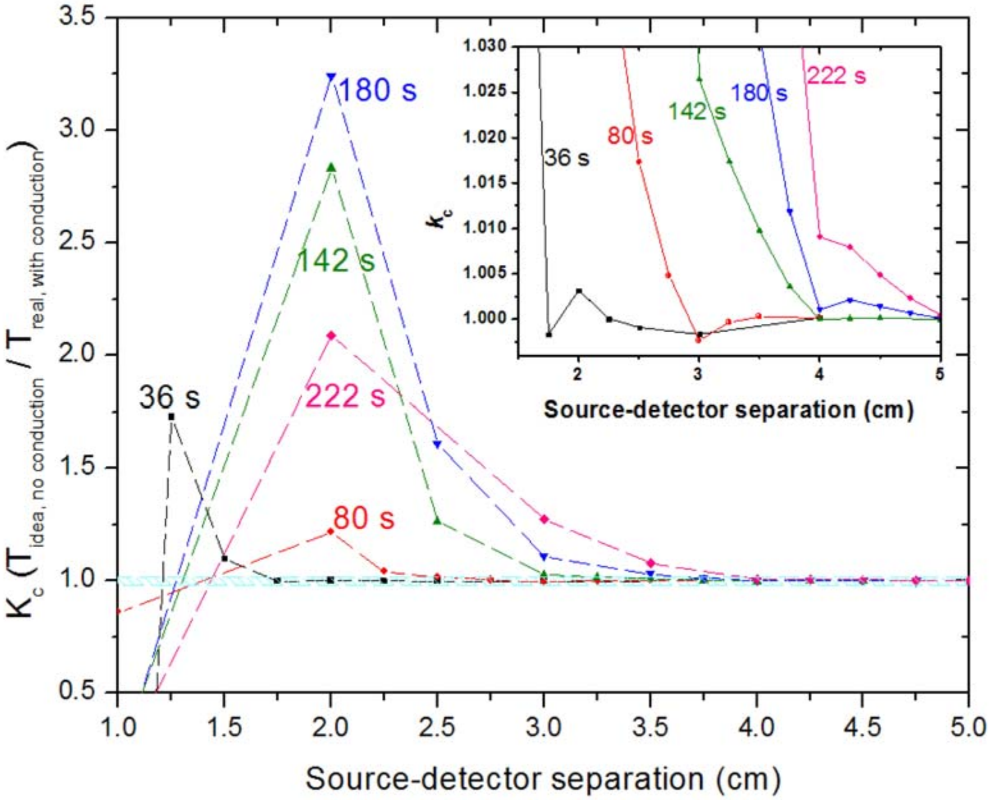

Figure 5.2: Calculated k_c correction factors for different irradiation times plotted as a function of source-detector separation. The inset shows the region between 1.5 and 5 cm source-detector separation magnified.

5.3.2 Measurements

Table 5.1 shows the results of our experiments that were performed with two sources of nominal activities of 38000 and 21000 U. The distance measurements reported are the averages of roughly 20 independent measurements of the source-detector separation, with the uncertainty established as one standard deviation on those measurements. The large standard deviation associated with our preliminary setup reflects the need for a more robust setup. Since the calorimetric measurements were performed at different source activities, as well as the fact that source decays of up to 1 % were observed over the course of a single set of experiments, all of the measured dose rate results have been normalized to the exact $S_{K,\mathrm{air}}$ of the source at the time of measurement and are presented in units of µGy/(s.U). Moreover, a calculated correction of 1.31 % was applied to all the experimental results to correct for attenuation in the front glass window of the vessel.

Figure 5.3 shows the temperature drift curve for a sample experimental calorimetric run that was performed at 27.6 mm distance from the source for an irradiation time of 36.0 s. Highlighted in yellow is the full range between the maximum and minimum temperature drift that we obtained in the eight calorimetric runs performed under similar conditions. The figure shows disintegration-corrected raw data in units of bridge voltage (proportional to temperature). In white, the temperature drift curve obtained through COMSOL, converted to voltage using experimental thermistor and bridge calibration data, is overlaid on top of the corresponding experimental run (blue). It was found that the initial source temperature upon entering the calorimeter has negligible effects on the first portion of an HDR ^{192}Ir brachytherapy post-drift curve (i.e, the mid-run extrapolation calculation of ΔT is unaffected). Although the simulation in Fig. 5.3 shows results for a starting source temperature of 25 ºC, simulations for 20 ºC and 30 ºC cases showed a slight shift between the postdrift curves in the second, rapidly increasing, subregion of the postdrift, where differences of 2 % at 260 s, and 9 % at 460 s between the two extreme cases were observed. In the inset, we have shown the percent difference between the disintegration-corrected average run and the simulation. The same −6.5 % difference observed between our experimental and TG-43 calculated results as noted in Table 5.1 (27.6 mm case) is reflected as an offset in the percent difference results in the inset of Fig. 5.3 because the normalization factor used in conversion of COMSOL-calculated temperature results into units of voltage (for purposes of absolute comparison) is based on the results of Table 5.1.

Nominal source $S_{K,\mathrm{air}}$ [U]	Source-detector separation [mm]	Irradiation time [s]	Number of calorimetric runs performed	Average dose rate [μGy/(s.U)]	TG-43 calculated dose rate [μGy/(s.U)]	% diff. of experiment from TG-43
38000	27.6±0.3	36.0	8	0.439±0.007	0.412	6.5
	26.4±0.4	50.0	7	0.446±0.007	0.448	0.4
21000	26.8±0.5	80.0	3	0.451±0.022	0.448	0.7
	24.7±0.3	75.0	3	0.495±0.017	0.522	5.1
Total Average	**25**		**21**	**0.502±0.007**	**0.505**	**0.6**

Table 5.1: Summary of dose measurements for various source-detector separation and irradiation time combinations. The number of calorimetric runs performed in each case is also noted. The average dose rate in each case is obtained by averaging individual results that have been normalized to the exact source air-kerma strength at the time of measurement. The “total average” reflects an air-kerma strength-corrected average dose rate that has been corrected to reflect a reading at 25 mm source-detector separation for all of the 21 measurements performed in this work. Percent difference noted in the last column is defined as [(TG-43 calculated dose rate)–(measured dose rate)]/(TG-43 calculated)×100 %.

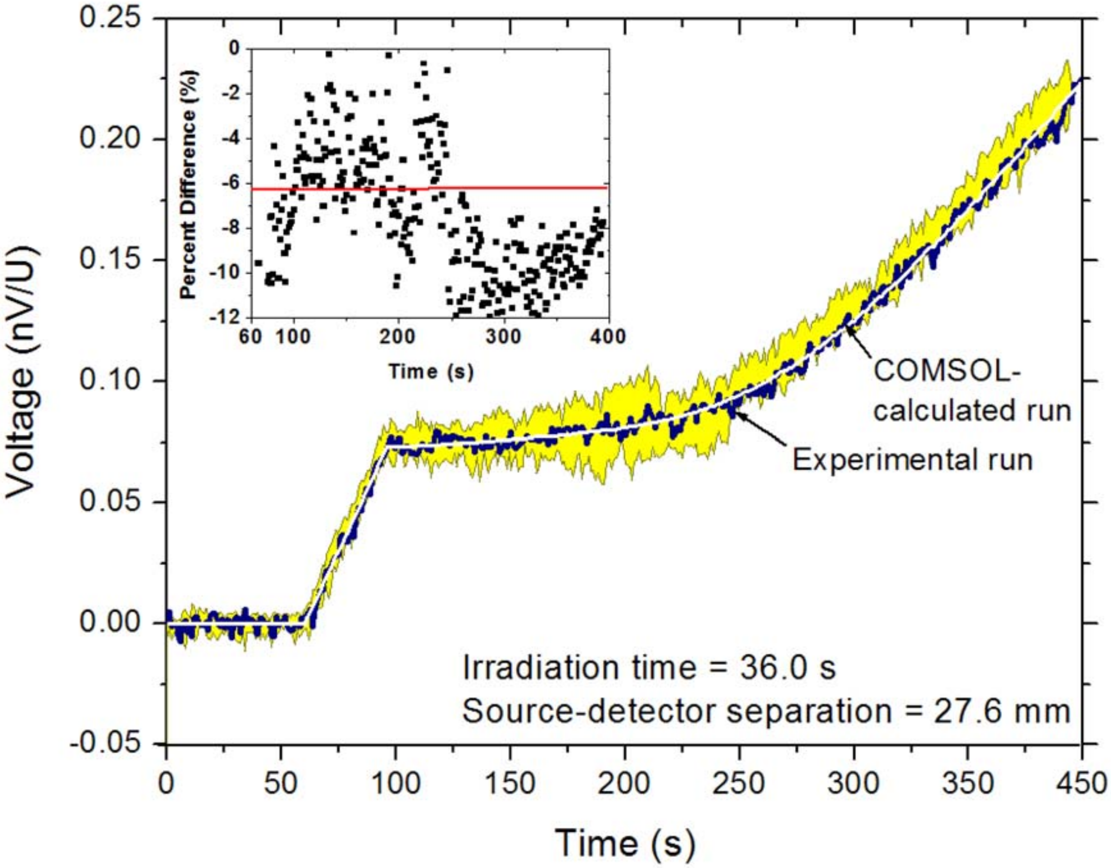

Figure 5.3: A typical experimental run and COMSOL-calculated run overlapped. The highlighted region indicates the range between maximum and minimum experimental temperature drift curves obtained. The results are for a measurement point 27.6 mm away from the source for an irradiation time of 36.0 s. Inset shows the percent difference between an air-kerma strength corrected average run and a representative calculated run.

5.4 DISCUSSION

Figure 5.3 and Table 5.1 demonstrate that HDR ^{192}Ir brachytherapy water calorimetry is feasible. Table 5.1 shows that the type A uncertainty on our dose measurement results (for cases in which more that seven calorimetric runs were performed) equals 1.5 %. Using our preliminary setup, we were not able to measure the source-detector separation with a reproducibility better than

0.5 mm, which at our measurement position of around 26.5 mm translates to a 3.8 % uncertainty on the dose. Type B uncertainties are for conductive heat-loss (to be analyzed further but estimated to be ~0.5 %); thermistor calibration (0.19 %)[8]; bridge calibration (0.13 %)[8]; vessel attenuation correction (~0.3 %); source dwell time (0.3 %); source transit time (negligible for postdrift durations of interest to us); and convection (although not studied, it may be important). An overall uncertainty on the dose of 3.9 % was estimated.

Currently, in clinics, $S_{K,\mathrm{air}}$ of the source is measured with a calibrated well-type ionization chamber. The most significant source of uncertainty during this measurement is the calibration coefficient of the well-type chamber provided by the secondary standards laboratories (2.5−3 %). The uncertainty on an absorbed dose to water determination includes the uncertainty on the calculated dose rate constant[2]. The TG-43 update[3] provides estimates of the uncertainties involved in measurement of dose rate using TG-43 for low dose-rate sources, and uncertainties of 6 % at 1 cm and 7 % at 5 cm have been calculated. Although the report does not address uncertainties for high dose-rate sources, values on the order of 4−5 % are probably realistic.

Table 5.1 shows that the agreement between our results and those calculated using TG-43 is within a 1 sigma uncertainty and is comparable to current uncertainties in absorbed dose to water measurement using other indirect techniques.

Without any significant modification to the current water calorimeters or water calorimetry techniques, the absorbed dose to water of HDR ^{192}Ir brachytherapy sources can be determined with uncertainty comparable to an air kerma rate determination along with application of the TG-43 formalism. The only important and necessary modifications employed in this work were the use of a thin glass vessel, and the selection of a suitable source-detector separation that ensures a conduction time (for source self-heating to reach the detector) that is longer than the combined irradiation time and a sufficiently long postdrift time. If the latter condition is met, the condition for obtaining manageable corrections for conductive heat loss is also automatically satisfied. A small k_c is desirable because of more limited uncertainties introduced by heat loss on the final measured dose. Figure 5.2 can be used as an aid in the selection process of a proper source-detector separation. One has to keep in mind, however, that given the source air kerma strength at the time of measurement, the total irradiation time needs to be sufficient to accumulate an accurately measurable absorbed dose at the measurement point. We found that for HDR ^{192}Ir sources with activities commonly used in clinics, a 2.5−5 cm source-detector separation should be explored.

Although an improvement in positioning of the source can significantly reduce the uncertainty on the dose measurement, the potential reduction of uncertainty via other means also needs to be explored. These include cooling of the source down to 4 ºC prior to insertion into the water calorimeter, use of a dummy electrical source to address source self-heating, as well as extraction of information on source self-heating from the 'tail' portion of the post-irradiation drift. Since the gradient of the temperature increase in this region is expected to be sensitive to the exact value of the source air kerma strength, the calculated temperature drift curve can be fine-tuned by adjusting the source air kerma strength in the simulation and observing any improvements in the agreement between experiment and simulation. Rather than using extrapolation of the dose to midrun, in brachytherapy calorimetry one can envisage that the measured dose is determined from an optimization process that minimizes the difference between entire measured and calculated drift curves, by treating the source air-kerma strength as a parameter. Work is underway to explore this technique further.

5.5 CONCLUSIONS

We have demonstrated that water calorimetry for high dose rate ^{192}Ir brachytherapy sources is feasible with standard calorimeter technology. We believe that provided positioning uncertainties can be reduced to less than 0.3 mm, an absolute dose measurement with an accuracy better than 5 % (k=2) is achievable if the point of measurement is taken to be optimally 2.5−5 cm away from the source (on the perpendicular bisector) while ensuring that a minimum dose of 1 Gy is delivered. Efforts are now underway to design a dedicated brachytherapy absorbed dose standard that will take into account the main observations from this feasibility study. By combining calorimetry with air-kerma measurements using primary standards, measured rather than calculated dose rate constants can be determined for different ^{192}Ir HDR brachytherapy source types.

ACKNOWLEDGMENTS

This work has been supported in part by grant RGPIN 298181 of the Natural Sciences and Engineering Research Council. The authors would like to acknowledge the contributions of Dr. E. Podgorsak. The careful editing and helpful comments of Dr. D. Rogers and the referees are also appreciated. A. S. is a recipient of a McGill University Health Centre Research Institute Ph.D. scholarship. J. S. is a Research Scientist of the National Cancer Institute of Canada appointed with funds provided by the Canadian Cancer Society.

5.6 REFERENCES

[1] S. R. Domen, "Absorbed dose water calorimeter," Med Phys 7, 157-159 (1980).

[2] R. Nath, L. L. Anderson, G. Luxton, K. A. Weaver, J. F. Williamson, and A. S. Meigooni, "Dosimetry of interstitial brachytherapy sources: recommendations of the AAPM Radiation Therapy Committee Task Group No. 43. American Association of Physicists in Medicine," Med. Phys. 22, 209-234 (1995).

[3] M. J. Rivard, B. M. Coursey, L. A. DeWerd, W. F. Hanson, M. S. Huq, G. S. Ibbott, M. G. Mitch, R. Nath, and J. F. Williamson, "Update of AAPM Task Group No. 43 Report: A revised AAPM protocol for brachytherapy dose calculations," Med. Phys. 31, 633-674 (2004).

[4] S. J. Goetsch, F. H. Attix, D. W. Pearson, and B. R. Thomadsen, "Calibration of 192Ir high-dose-rate afterloading systems," Med Phys 18, 462-467 (1991).

[5] E. Mainegra-Hing and D. W. Rogers, "On the accuracy of techniques for obtaining the calibration coefficient N(K) of 192Ir HDR brachytherapy sources," Med Phys 33, 3340-3347 (2006).

[6] J. Borg, I. Kawrakow, D. W. Rogers, and J. P. Seuntjens, "Monte Carlo study of correction factors for Spencer-Attix cavity theory at photon energies at or above 100 keV," Med Phys 27, 1804-1813 (2000).

[7] K. E. Stump, L. A. DeWerd, D. A. Rudman, and S. A. Schima, "Active radiometric calorimeter for absolute calibration of radioactive sources," Rev. Sci. Instrum. 76, 033504:1-033504:9 (2005).

[8] K. Stewart, Ph.D. dissertation, McGill University, 2007.

[9] J. Seuntjens and H. Palmans, "Correction factors and performance of a 4 degrees C sealed water calorimeter," Phys. Med. Biol. 44, 627-646 (1999).

[10] G. M. Daskalov, E. Loffler, and J. F. Williamson, "Monte Carlo-aided dosimetry of a new high dose-rate brachytherapy source," Med. Phys. 25, 2200-2208 (1998).

[11] I. Kawrakow and D. W. Rogers, "The EGSnrc Code System: Monte Carlo Simulation of Electron and Photon Transport," NRC Reports, PIRS-701 (2006).

[12] J. Borg and D. W. O. Rogers, "Monte Carlo calculations of photon spectra in air for ^{192}Ir sources," NRC Reports, PIRS-629r (1999).

[13] B. Duchemin and N. Coursol, LARA-90. *LARA-LMRI-1990, DAMRI/LMRI, CEA, France, 1993.*

[14] J. P. Seuntjens and A. R. DuSautoy, "Review of calorimeter based absorbed dose to water standards," Standards and Codes of Practice in Medical Radiation Dosimetry (Proc. Int. Symp. Vienna, 2002), IAEA Vienna (2003) IAEA-CN-96/3.

Chapter 6

Development of a water calorimetry-based standard for absorbed dose to water in HDR ^{192}Ir brachytherapy

This manuscript describes in full detail the final refined procedures used for direct and absolute absorbed dose to water measurements in ^{192}Ir brachytherapy using water calorimetry. The numerical results of heat transport simulations as well as all experimental findings are discussed. Our numerical studies provide the foundation for optimization of various experimental setup parameters that directly affect the quality of measurements and uncertainty on the final dose results. Improvements made over our earlier results (Chapter 5) are discussed, and potential improvements to experimental procedures and setup design are noted. A detailed uncertainty budget for water calorimetry-based brachytherapy dosimetry is also calculated. This work forms the foundation for an absorbed dose to water primary standard based on water calorimetry.

Authors: Arman Sarfehnia and Jan Seuntjens
Medical Physics Unit, McGill University, Montreal General Hospital, Montréal, Québec, Canada

*Medical Physics **37**, 1914-1923 (2010)*

ABSTRACT

Purpose: The aim of this paper is to develop and evaluate a primary standard for HDR ^{192}Ir brachytherapy based on 4 °C stagnant water calorimetry.

Methods: The absolute absorbed dose to water was directly measured for several different Nucletron microSelectron ^{192}Ir sources of air kerma strength ranging between 21000-38000 U and for source-to-detector separations ranging between 25-70 mm. The COMSOL MULTIPHYSICS^{TM} software was used to accurately calculate the heat transport in a detailed model geometry. Through a coupling of the ‘conduction and convection’ module with the ‘Navier Stokes incompressible fluid’ module in the software, both the conductive and convective effects were modeled.

Results: A detailed uncertainty analysis resulted in an overall uncertainty on the absorbed dose of 1.90 % (1-sigma). However, this includes a 1.5 % uncertainty associated with a nonlinear predrift correction which can be substantially reduced if sufficient time is provided for the system to come to a new equilibrium in between successive calorimetric runs, an opportunity not available to us in our clinical setting due to time constraints on the machine. An average normalized dose rate of 361±7 μGy/(h.U) at a source-to-detector separation of 55 mm was measured for the microSelectron ^{192}Ir source based on water calorimetry. The measured absorbed dose per air kerma strength agreed to better than 0.8 % (1-sigma) with independent ionization chamber and EBT-1 Gafchromic film reference dosimetry as well as with the currently accepted AAPM TG-43 protocol measurements.

Conclusions: This work paves the way towards a primary absorbed dose to water standard in ^{192}Ir brachytherapy.

6.1 INTRODUCTION

The importance of HDR ^{192}Ir brachytherapy as a boost or as the main mode of treatment calls for an accurate dosimetry standard. A dosimetry standard for the direct measurement of absolute dose to water in ^{192}Ir sources is currently not available. The AAPM Task Group 43[1] (TG-43) along with its update[2] constitute the accepted protocol for dose to water determination based on an air kerma strength $S_{k,air}$ measurement. The air kerma strength of the radioactive source is converted to dose to water via dose rate constant Λ (a calculated absolute quantity) and several relative correction factors accounting for scatter, attenuation, and anisotropy of dose distribution among other effects.

In addition to the uncertainties associated with an indirect determination of dose to water D_w from an in-air measurement of $S_{k,air}$, the current TG-43 protocol relies also on a rather indirect calibration procedure of the well-type chambers. Under the current accepted technique proposed by Goetsch *et al*[3], the secondary standards laboratories obtain a calibration coefficient for their thimble type chambers at the effective ^{192}Ir energy through an interpolation of the calibration coefficients of the chamber obtained under a low kilovoltage energy beam (250 kVp, 146 keV x-rays) and a high energy beam (^{137}Cs, 662 keV). Since all of the initial calibration factors are NIST-traceable, the final interpolated calibration factor is also NIST-traceable. Although this technique has been recommended by the IAEA for use by secondary standard laboratories[4], Mainegra-Hing and Rogers[5] have pointed out some of the shortcomings of the technique and have suggested potentially higher uncertainties involved in the process and its intermediary steps.

More direct measurements of air kerma in ^{192}Ir beams using cavity-ionization chambers with graphite walls along with Monte Carlo-calculated corrections accounting for the non-validity of the Spencer-Attix cavity theory have been proposed by Borg *et al*[6]. National Physics Laboratory (NPL) currently offers such an air kerma-based standard, while India's primary standard laboratory (BARC) has developed a cavity ion chamber-based primary standard for use in ^{192}Ir HDR brachytherapy[7,8]. Only recently, Fricke dosimetry for absolute absorbed dose measurement in ^{192}Ir brachytherapy sources has been explored[9].

In this work, we use a stagnant 4 °C water calorimeter to directly measure the absolute absorbed dose to water from a Nucletron microSelectron-HDR ^{192}Ir source (part No. 105.002). Studied in depth by Domen[10], water calorimeters are commonly used in radiation dosimetry laboratories for direct dose to water measurement in high energy photons[11], to a much more limited extent in heavy particle therapy[12,13], and more recently in high energy electrons[14]. Making use of the fundamental definition of absorbed dose in terms of temperature rise of the irradiated medium, a water calorimeter is a temperature-controlled water system that allows for precise measurement of small (sub milli-kelvin) temperature rises in high purity water as a result of irradiation.

Despite works in the use of cryogenic total absorption calorimeters for total energy output measurements of low dose rate LDR brachytherapy sources[15], to the best of the authors' knowledge, the use of calorimeters in brachytherapy in general and in ^{192}Ir HDR brachytherapy in particular has been reported by only three groups: Sarfehnia *et al* (2007)[16], Krauss (2007)[17], and Bambynek *et al* (2009)[18]. Eventual development of a primary standard based on water calorimetry in ^{192}Ir brachytherapy, founded upon some of the conclusions and recommendations from this work, would not only improve the accuracy of dose measurement compared to the currently accepted TG-43 dosimetry protocol, but would also eliminate the need for conversion procedures that are inherent to any system that measures the dose to water indirectly by performing reference measurements in non-water media.

6.2 METHODS

6.2.1 Water Calorimeter

Figure 6.1 shows a schematic diagram of the McGill in-house built portable water calorimeter (MWC). It is of similar principle to the calorimeter constructed by Domen[19], and uses some of the design principles from the work by Seuntjens and Palmans[20] but utilizes active cooling to 4 °C by controlling the temperature of a copper shroud rather than through air circulation. The calorimeter consists of a 30×30×20 cm^3 Lucite water tank surrounded by two 5 cm Styrofoam slabs that are separated by a 5 mm copper plate. The entire system is enclosed in a 1 cm thick plywood box. The copper plates provide a thermal shield against outside temperature fluctuations and allow for accurate water temperature control by being actively temperature controlled via a Neslab RTE-7 refrigerated bath/circulator. Two PT-100 RTD temperature probes are used to monitor the average water temperature inside the tank while a third is used to measure the copper temperature. A heat exchanger, a 4 mm diameter temperature-controlled anodized aluminum tube, is inserted directly inside the water calorimeter facilitating rapid temperature adjustments to the water system. A coupled magnetic stirrer at the bottom of the water phantom was used to mix the water in between different sets of calorimeter runs and to permanently remove residual temperature gradients produced by radiation. All measurements were performed over a 0.06 °C range centered around a water temperature of 3.98 °C, the temperature at which the density of water is maximal.

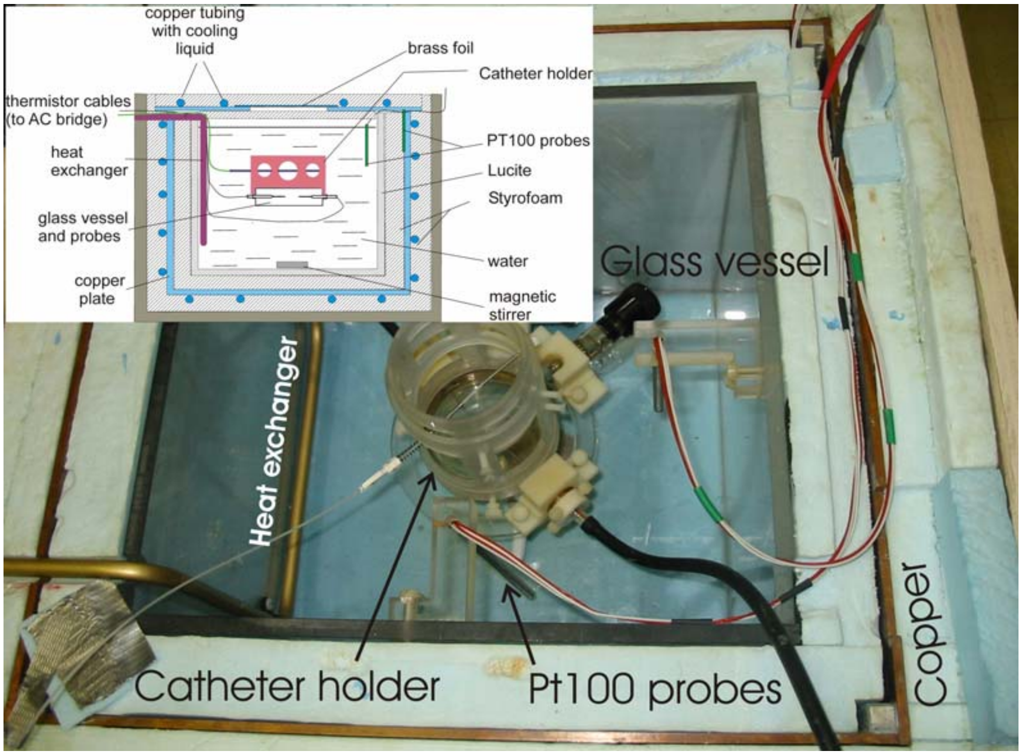

Figure 6.1: The McGill water calorimeter (MWC) with the catheter holder fixed onto the parallel-plate vessel. Inset shows a schematic diagram of the MWC.

A glass-coated bead thermistor of 0.28 mm diameter and nominal resistance of 10 kΩ at 4 °C was inserted into 4 cm long Pyrex pipette of 0.7 mm diameter at the tip. The thermistor shows a nominal 400 Ω resistance change per degree of temperature change. This allows us to measure temperature rises (in terms of resistance) of only few hundred microKelvin with a noise level on the order of 2-5 μK. Two such thermistors are fixed inside a parallel plate vessel as shown in Fig. 6.2(a). The thermistors are located nominally 12 mm below the top window of the glass vessel. Their signal is read using an active AC-bridge setup similar to many standard 4 °C water calorimeters[20]. The Pyrex vessel has a side glass thickness of 1.96 mm with an outer diameter of 79 mm, as well as a front and back window thickness of 1.12 mm with an inner separation of 22.66 mm. Although the water purity cannot be controlled inside the entire calorimeter, it can be maintained to high quality inside a much smaller vessel that houses the thermistor detectors[11].

Since the calculation of the exact effects of radiation-induced chemical reactions in the presence of unknown concentrations of various organic compounds on temperature is difficult, Klassen and Ross[21] suggest a complete saturation of the system with gases such as N_2, H_2, or H_2/O_2 mixture. The exact behaviour of such saturated systems can be calculated by considering the chemical reactions in water due to reactive species produced as a result of irradiation along with their rate constants. For given reaction product concentrations, the energy balance can be determined from the enthalpies of formation of the species involved. Accordingly, prior to every measurement session (taking place on different weekends), we filled the vessel with ultrapure water (organic content < 3 ppb) and bubbled with pure N_2 gas for 4 hours. The N_2 saturated system theoretically comes to an equilibrium with zero predicted heat defect after a few Grays of dose. However, remaining organic compounds usually create exothermicity which can be removed by pre-irradiation. To this end, the entire vessel was pre-irradiated with a total dose of 400 Gy at 6 MV.

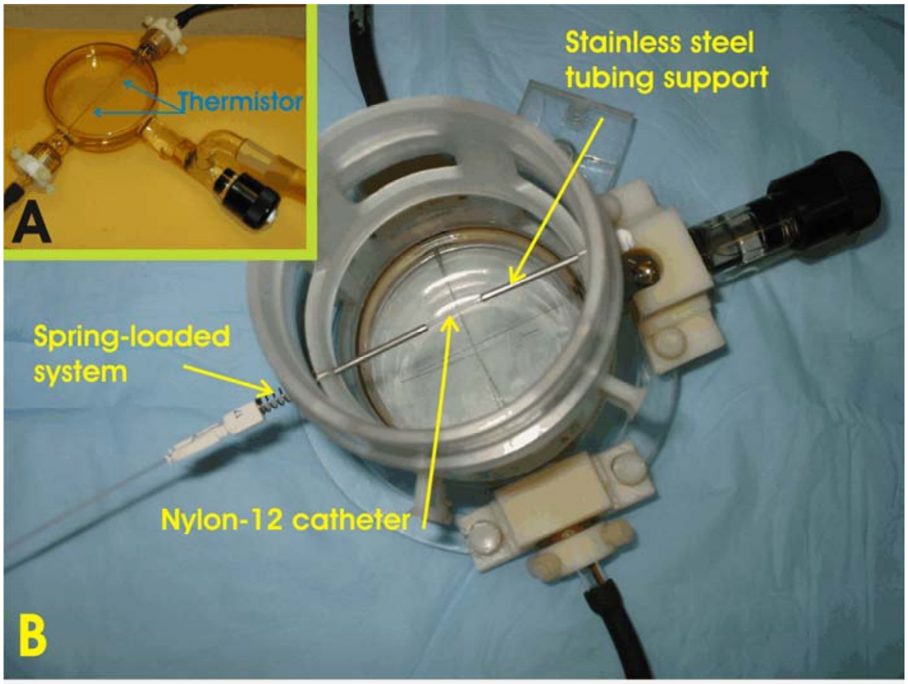

Figure 6.2: The parallel-plate calorimeter vessel with two thermistors fixed inside (A). A close-up view of the spring-loaded catheter holder fixed onto the vessel (B)

Figure 6.2(b) displays an improved catheter holder over our earlier version[16]. The Nucletron's 4 French nylon-12 "breast comfort" catheter is tightly pulled and fixed using a spring-loaded mechanism inside a two-layer concentric cylindrical acrylic holder which itself is mounted and fixed onto the parallel plate vessel. The two-layer concentric setup allows for the flexibility in dose measurement at various source-detector separations $d_{\text{src-det}}$. The window openings in the holder minimize non-water material inside the water phantom and allow for the convective water flow around the source.

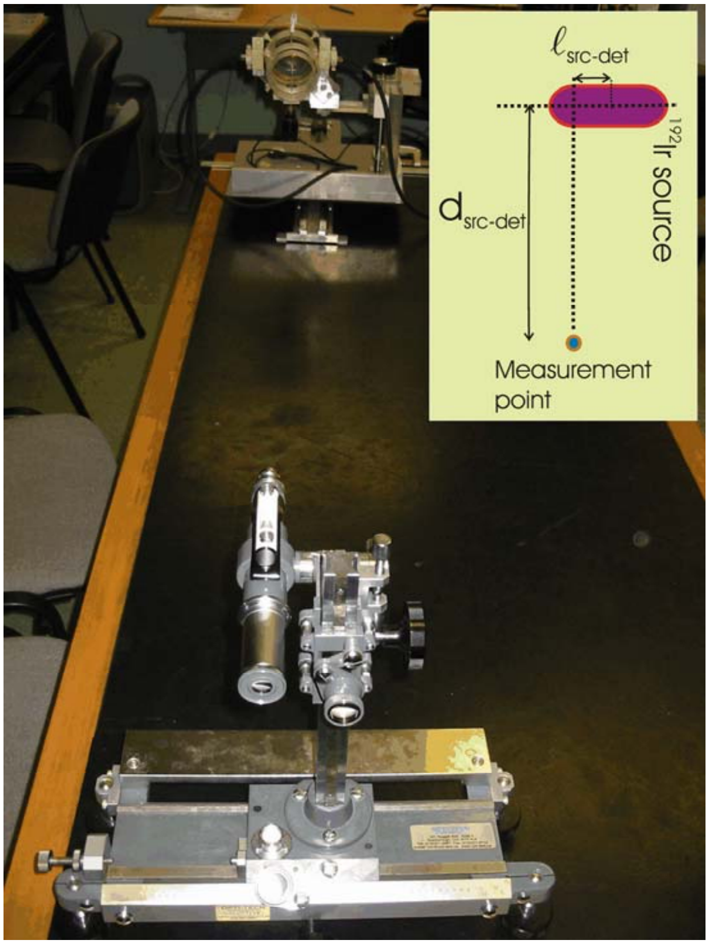

Figure 6.3: The $\ell_{\text{src-det}}$ measurement setup. The travelling microscope is used with the optical tube in its horizontal position. The inset shows a schematic diagram of the source and the measurement point explaining $d_{\text{src-det}}$ and $\ell_{\text{src-det}}$.

Due to differences in volumetric thermal expansion coefficients of the catheter and the holder material as well as the differences in their rate of water absorption, direct fixation of the catheter to the holder results in relatively large changes in its length between the time of $d_{\text{src-det}}$ measurement (room temperature air) and actual calorimetric measurement (4 °C water). A spring-loaded mechanism that provides constant tension across the length of the catheter avoids such complications. For additional rigidity, two 6 French stainless steel tubes (thickness of 0.254 mm) were fit securely inside the holder and acted as support for the spring-loaded catheter that ran through them.

A travelling microscope with the optical tube in the vertical position (set at 25 × magnification) was used for $d_{\text{src-det}}$ measurement. Based on our setup, a positioning reproducibility of 0.13 mm over 6 weeks testing period (under both cold water, and room temperature air conditions) was obtained. Additionally, with the optical tube turned to its horizontal position, the telescope mode was used to center the source above the midpoint between the thermistors. This was done by accurately measuring the lateral position of the source inside the semi-transparent nylon-12 catheter with respect to the thermistors, referred to here as $\ell_{\text{src-det}}$ (see inset of Fig. 6.3). The reproducibility of the lateral positioning was 0.4 mm.

6.2.2 Dose Measurement Fundamentals

As discussed by Seuntjens and Duane[11], in water calorimetry, the dose to water D_{w} at the point of measurement $\vec{r}$ is calculated by

$$D_{\text{w}}(\vec{r}) = c_{\text{w,p}} \cdot \triangle T(\vec{r}) \cdot \prod_i k_i = c_{\text{w,p}} \cdot \triangle T(\vec{r}) \cdot \left(k_{\text{hd}} \cdot k_{\text{ht}} \cdot k_{\text{p}} \cdot k_{\text{dd}} \cdot k_{\rho}\right) \;, \quad (6.1)$$

where $c_{\text{w,p}}$ is the heat capacity of water at constant pressure, and ΔT is the measured temperature rise due to radiation. Since the measurement conditions are not ideal, further corrections (k_i) are necessary. Unlike conventional high energy photon water calorimetry, some of the corrections in ^{192}Ir brachytherapy can potentially be much larger than sub-percent. Each term in the expanded form of Eq. (6.1) is discussed in greater detail below:

k_{hd} *(heat defect):* A correction factor accounting for the differences in energy absorbed and the heat measured due to radiation-induced exothermic/endothermic chemical processes that may happen in the presence of water impurities. k_{hd} is minimized by reducing the organic contents in water. Based on the procedure described in *Section 6.2.1* and originally devised by Klassen *et al*[21], a value of (1.000±0.003) for the heat defect was used for the N_2 saturated system pre-irradiated to 400 Gy with 6 MV.

k_{ht} *(heat transfer):* k_{ht} compensates for heat gain or loss at the measurement point due to conductive and convective effects (radiative transfer is negligible). Generally, k_{ht} is small because of the very small thermal diffusivity of water ($\alpha=1.4\times10^{-7}$ m^2 s^{-1}); indeed, this is what makes water calorimetry feasible in external beam radiation therapy. Moreover, convective effects are often deemed absent for 4 °C stagnant water calorimeters because at 3.98 °C operation temperature, water density is highest and the coefficient of volumetric expansion is zero.

However, in ^{192}Ir brachytherapy water calorimetry, relatively large temperature gradients form inside the calorimeter water phantom. The temperature of the region in the vicinity of the source inside the phantom dramatically increases mainly because of the source self-heating effect (defined as the increase in source temperature over ambient temperature due to fractional source self-attenuation of ^{192}Ir photons and electrons inside the iridium source/cap structure) but also because of the extremely sharp dose gradient around the source. Due to large temperature gradients inside the calorimeter, k_{ht} is the largest correction in ^{192}Ir water calorimetry. Moreover, its calculation is challenging as the common approximation of ignoring the convective flow in the heat transport simulation (traditionally exercised in external beam water calorimetry) may be inappropriate due to large temperature gradients. Simulating our measurement conditions with the effects of convection taken into account, we found the value of k_{ht} to be nominally around 0.96 %. The calculation of k_{ht} is discussed in *Section 6.2.4*.

k_{p} *(perturbation):* corrects for perturbations of the radiation field due to presence of non-water materials in the water tank. The effect of glass vessel on the dose deposited at the measurement point was calculated with the Monte Carlo EGSnrcMP[22], DOSRZnrc code. An underestimation of the dose at the measurement point due to the presence of the vessel, resulting in a correction of (1.003±0.001), was calculated.

k_{dd} (dose profile): corrects for the differences in dose measurement at the thermistor point versus the reference point (midway between the two thermistors). k_{dd} is often negligible as the lateral dose profile of most external beams is relatively uniform around the center of the field. Since in brachytherapy, the lateral dose drop-off is quite dramatic, k_{dd} can potentially be the second largest correction factor in ^{192}Ir water calorimetry. Moreover, small uncertainties in lateral positioning of the source with respect to the reference point can result in very large uncertainties on k_{dd}.

Because a small separation between the thermistors reduces the magnitude of k_{dd}, in this work, the thermistors were generally placed with a nominal tip-to-tip separation of 2.4 mm. Moreover, since the magnitude of k_{dd} increases dramatically with an increase in $\ell_{\mathrm{src\text{-}det}}$ (ranging from sub-percent for $\ell_{\mathrm{src\text{-}det}}$ =0 mm up to above 2 % for $\ell_{\mathrm{src\text{-}det}}$ =4 mm), it is desirable to position the source directly above the reference point (i.e. $\ell_{\mathrm{src\text{-}det}}$ =0 mm). In some of our earlier experiments, this was not possible due to setup issues. For most of the results to be presented in this work, however, the thermistors were indeed centered on the dose central axis.

k_ρ *(density)*: accounts for the differences in density of water at the time of measurement (4 °C) and room temperature (22 °C) under which most dosimetry works are often performed. The density correction is essentially a slight adjustment to the measurement depth or a shift in percentage depth dose PDD curve. k_ρ was calculated to be (1.0040±0.0005) in this work.

ΔT: Figure 6.4 shows a typical calorimetric run corrected for drift (procedure to be discussed below). As indicated in the figure, a *calorimetric run* is composed of three regions: (1) a predrift region measuring the temperature drift in the absence of the source; (2) an irradiation period; (3) a postdrift (post irradiation) region showing the temperature drift following the removal of the source from the calorimeter. Generally, a gradient is present in this third region as a result of the formation of temperature non-uniformities during the irradiation period.

6.2.3 ΔT Measurement

In external radiotherapy water calorimetry, the relatively flat PDD curve and the resulting temperature gradient allows for performance of up to 10 consecutive calorimetric runs (start-to-end) before the effects of drift become so dramatic (and k_{ht} corrections so large) that further runs become impossible. In ^{192}Ir brachytherapy water calorimetry, the formation of large temperature gradients and strong non-linear drifts following each calorimetric run makes subsequent runs futile. In this work, following every single calorimetric run, the water is stirred for 20-30 minutes and left to reach a new quasi-equilibrium for 40-60 minutes (a total of roughly 1.5 h stir/wait period).

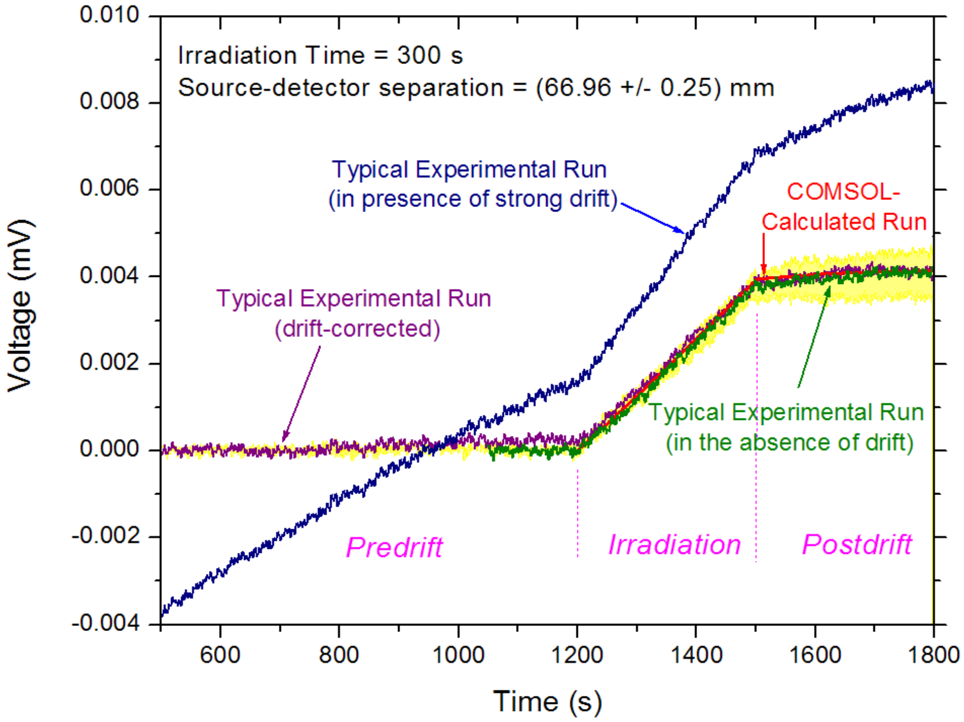

Figure 6.4: An experimental run influenced by a very strong non-linear drift, and the same run corrected for drift are shown. The results are compared to an experimental run measured in the absence of any major drifts. The highlighted region displays the maximum range of all measurement runs collected. This is NOT a 1-sigma distribution around the mean, but rather shows the extent of outliers.

Given a drift curve, the temperature rise ΔT is determined by extrapolating the linear fits made to the predrift and postdrift back to the midrun and finding the difference between the two. This technique is based on the assumption that nonlinear temperature gradients present near the thermistors are small enough that their cumulative effect can be approximated to be linear over the time region the extrapolation is made in. It is obvious that beams that have a high dose rate (i.e., require short irradiation period) and produce low gradient dose distribution satisfy the requirement.

In ^{192}Ir brachytherapy, the large dose gradient as well as the potential requirement for long irradiation times (250-350 s) do not satisfy the negligible nonlinear drift approximation. In spite of the 1.5 h stir/wait time between successive calorimetric runs, the presence of nonlinear drifts was unavoidable. While a more extended wait period between successive calorimetric runs results in a more moderate gradient on the heat drift curves, this was not feasible under our clinical setting due to time constraints on access to the ^{192}Ir afterloader. Although in *Section 6.3.1*, the dependence of the extent of the predrift nonlinearity on the experimental setup conditions will be discussed, in this section, a brief description of the post-analytic removal of the nonlinearity is provided.

Subtraction of a non-linear best-fit curve, made to the predrift and extrapolated outward, from the entire length of the drift curve is termed "drift curve linearization" (see Fig. 6.4). Obtaining the fit equation and its parameters is a challenging undertaking, however, as the exact cumulative effects of all different sources of heat loss and gain cannot be simulated over meaningfully long periods of time. In this work, the fit equation types for our calorimeter were determined empirically based on collecting excessively long predrift data (1500-3000 s in length). Using TableCurve2D™, we found equations 6.2-6.4 to best describe our predrift data

$$f(t) = ae^{-t/b} \qquad \{a,b \in \mathbb{R}\} \tag{6.2}$$

$$f(t) = a + bt + ct^{1.5} + de^{-t} \qquad \{a,b,c,d \in \mathbb{R}\} \tag{6.3}$$

$$f(t) = \frac{\sum\limits_{0 \le i \le 8} a_{\mathrm{i}}(\ln(t))^{i}}{1 + \sum\limits_{1 \le j \le 8} b_{\mathrm{j}}(\ln(t))^{j}} \qquad \{i,j \in I;\ a_{\mathrm{i}},b_{\mathrm{j}} \in \mathbb{R}\} \tag{6.4}$$

Furthermore, it was determined empirically that our fit functions are not flexible enough to be used for drift curves with slopes larger than 0.9 µK/s at the steepest portion of the curve (such sharp-gradient portions of the predrift are better ignored than included in the fit). However, the 1.5 h stir/wait procedure described previously ensures much lower gradients than this threshold limit.

A minimum predrift of 900 s was obtained for every calorimetric run to ensure sufficient data for a successful determination of fit parameters. Although Eq.'s 6.2-6.4 often describe the early portions of the drift with identical accuracy, the extrapolation of the fits outwards over the entire length of the drift curve can result in non-negligible differences between the extrapolated fits. As such, the shape of the postdrift of a given predrift-corrected run can be different depending on which of the three fit equations are used. In some cases, discrepancies as large as few percents were observed for the furthest point of the postdrift, although this translates to a much smaller uncertainty in ΔT measurement as the extrapolation technique used to measure ΔT is quite forgiving and insensitive to the very details of the shape of the postdrift. Since Eq.'s 6.3 and 6.4 are not pure exponentials, care must be taken to ensure that they behave as expected over the extrapolated region.

Although for the results shown in this work, a non-linear fit subtraction technique was used, we also investigated subtracting the entire drift curve from the linear tangent made to the non-linear predrift fit at the instant prior to the start of the radiation. Although theoretically a non-linear fit subtraction would be more appropriate than a linear one (albeit the tangent to the non-linear fit describing the predrift), practically the lack of an accurate understanding of the non-linear behaviour of the predrift prevents us from being able to justify either technique of "linearization" as superior. The uncertainty on the linearization was estimated by analysing all runs with all fit methods, including a pure linear fit made just to the latter 200 s portion of the predrift, and calculating the 1-sigma standard deviation on the calculated dose. This number, 1.5 % was accepted as the uncertainty on the linearization procedure.

6.2.4 Numerical Methods

Monte Carlo simulations

A 2D axially symmetric model of the ^{192}Ir source was simulated with the DOSRZnrc Monte Carlo (MC) code. The NuDat 2.0 ^{192}Ir photon spectrum[23] and an electron energy cutoff (ECUT) of 521 keV were used. Two simulations of the source inside a cylindrical water phantom (15 cm radius and 20 cm deep, approximating our water calorimeter), once with the glass vessel present and once with the vessel absent were performed. We validated the results of our water only (no vessel present) simulations against the published dose rate results around a Nucletron microSelectron ^{192}Ir source[24-26]. The perturbation correction k_p is the ratio of the MC dose scored at a point midway between the thermistor tips with and without the glass vessel modelled.

The source self-heating was calculated by accurately modelling the Nucletron ^{192}Ir source/cap structure[27], and scoring the dose (from ^{192}Ir electrons and photons) inside each of the source and the cap. The air kerma strength of the source was scored also from the same simulation. The results were validated against similar calculations performed with GEANT4 as well as the published data by Borg *et al*[28]. In this work, a MC-calculated dose to iridium core of 2.9993×10^{-8} cGy/particle ($1\sigma=0.03$ %), dose to steel capsule of 1.5743×10^{-9} cGy/particle ($1\sigma=0.02$ %), and an air kerma strength of 1.1512×10^{-11} cGy/particle ($1\sigma=0.3$ %) were used.

Heat transport calculations

The COMSOL MULTIPHYSICS™ software (referred to hereon as COMSOL) was used in this work to solve the partial differential heat transport equation based on the finite element method. The “Conduction and Convection” module of the software was coupled with the “Navier-Stokes incompressible fluids” module to solve the heat transport problem inside a 2D axially-symmetric geometrical model of the water calorimeter.

Figure 6.5 shows the model used in this work which includes both the ^{192}Ir source/cap structure inside its 4 French nylon-12 catheter, as well as a glass thermistor bead inside the glass vessel. The physical properties of all materials (specific heat capacity, density, thermal conductivity and viscosity) were defined as temperature-dependent functions[29]. Gravity is taken to point down in the figure. The dose perturbation due to the presence of the glass vessel was studied with MC (as explained above) and was included in the heat source representation in the COMSOL model. An adiabatic boundary condition (no heat loss across the outer boundaries), 'fine' mesh element size setting, and an absolute solver tolerance of 1×10^{-7} were used.

The heat sources in the model are: (1) the dose distribution around the source, (2) the source self-heating, and (3) the power dissipation by the thermistor inside the vessel. The calculation of the 'dose distribution with the glass vessel present' as well as the 'source self-heating' were described in the previous section. The thermistor power dissipation (when used with an active bridge) was calculated from the bridge circuitry to be 30 μW.

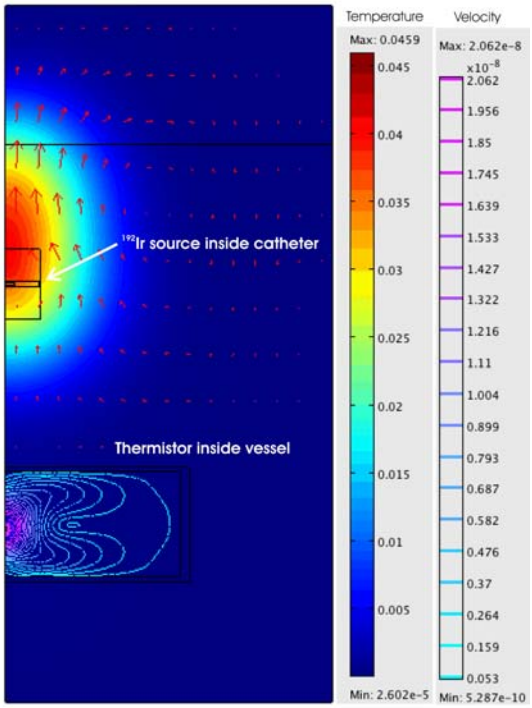

Figure 6.5 (left): A solved COMSOL-simulated model of the water calorimeter. The results show the state of the system 300 s after the end of a 250 s irradiation with a source of S_K=30000 U. The temperature (surface plot) and water velocity (arrows) inside and outside the vessel are displayed.

The simulation was set to faithfully follow the experimental irradiation and wait timing: An initial equilibrium state of the system was calculated prior to simulated irradiation by turning on the electrical power dissipation in the thermistors and letting the temperature settle for an extended period of time (1000 s). It was starting from this initial equilibrium state that the irradiation and postdrift were modelled.

6.3 RESULTS AND DISCUSSIONS

6.3.1 $d_{\text{src-det}}$ Optimization

Although of little importance when performing water calorimetry in external beam radiotherapy, in ^{192}Ir brachytherapy, the choice of the source-detector separation $d_{\text{src-det}}$ can significantly influence the final overall uncertainty on the dose results. Given our setup, we have found that ^{192}Ir water calorimetry at $d_{\text{src-det}} < 25$ mm is not feasible with the current, uncooled, catheter arrangement[16]. At such small separations, minute sub-millimetre uncertainties in positioning translate to unacceptably large uncertainties in dose measurements. Moreover, k_{ht} increases rapidly at short distances to an extent that makes water calorimetry unfeasible[16]. If the detector is too close to the source, the drift curve is often compromised due to extremely large temperature gradients in the vicinity of the source, while the effects of conduction and convective flow become considerable and difficult to accurately calculate.

We have performed water calorimetry measurements within a $d_{\text{src-det}}$ range of 25-70 mm, with sources of air kerma strength ranging from 21000-38000 U (corresponding to an activity range of 5.1-9.3 Ci). This encompasses the range of activities for ^{192}Ir sources present in clinics. For the sake of discussion, $d_{\text{src-det}}$ is arbitrarily subdivided into a 'near' region (25 mm$\leq d_{\text{src-det}}<$45 mm) and a 'far' region (45 mm$\leq d_{\text{src-det}}$).

It must be noted that for this entire discussion, we assume a setup with the source located above the vessel (see Fig. 6.1 or Fig. 6.5). If the setup were to be flipped upside down such that the source would be below the vessel, the temperature drift curve would look very different: Since warm water rises, the intense temperature close to the source would reach the point of measurement much faster, resulting in a sharp quasi-exponential temperature increase which makes postdrift analysis difficult and uncertain. This was numerically and experimentally verified. If the vessel is positioned with its central axis pointing horizontally (a 90° rotation of our geometry), similar results as our geometry (with source above vessel) can be reached as long as there are large enough openings in the holder to allow for convective flow to take place, and for the warm water in the vicinity of the source to rise to the surface.

Doing water calorimetry in the ‘near’ region has the significant advantage of yielding very high dose rates at the detector. Hence, short irradiation times (30-80 s) are sufficient to deliver the minimum 1 Gy dose requirement to the point of measurement. Although nonlinear drifts are still present, they can indeed be approximated to be linear over the short analysis region. This largely reduces or potentially eliminates the uncertainties associated with the ‘linearization’ process of the drift curves (discussed in *Section 6.2.3*). In this regime, the irradiation time has to be carefully selected to accommodate for the full measurement of the irradiation period and a sufficiently long postdrift period prior to having the large source heat (defined as the heat concentrated in the vicinity of the source due to both ‘source self-heating’ effect and the extremely large dose gradient close to the source) reach the point of measurement[16]. This is normally characterized by a sudden and dramatic increase in temperature (see Sarfehnia *et al* (2007)) which, although can be predicted and corrected for using heat transfer simulations, was not included in the analysis as it results in an unnecessary increase in the overall dose uncertainty. The largest drawback with the ‘near’ region remains to be the amplified effects of positioning uncertainties on the overall dose uncertainty, as well as the uncertainty on the k_{dd} correction which also rises sharply with uncertainty in lateral positioning of the source with respect to the thermistors.

In the ‘far’ region, the stringent requirements for an accurate knowledge of the source position can be slightly relaxed without compromising the final results. At such separations, the low dose rate at the measurement point does call for long irradiation periods (250-350 s). It was found that drifts remain stable enough for accurate measurements over such long periods, although ‘linearization’ of the drift curves may become necessary. In the ‘far’ region, long post irradiation drifts can be measured because not only does the large $d_{\text{src-det}}$ facilitate convective effects to disperse the ‘source heat’ flow, but also lower dose (and temperature) gradients in this region ensure only moderate drifts. The largest drawback of the `far` region remains to be the large uncertainty introduced into the results due to the ‘linearization’ of the curve. However, if longer wait periods between successive runs are possible, the effects of non-linear drifts can be minimized. In such cases, ^{192}Ir water calorimetry could result in absolute dose measurements with uncertainties close to 1 % level.

In this work, we will focus our attention on the ‘far’ region measurements (the ‘near’ region results were presented in our earlier work[16]). Water calorimetry should be performed preferably at the highest available source S_K as this results in highest dose rate and a minimization of irradiation time (or alternatively a better signal to noise ratio for a given irradiation period). We have found that at all $d_{\text{src-det}}$, the optimal irradiation time is one that allows for 1-2 Gy of dose delivered at the detector position.

6.3.2 Heat Transfer Modeling

Convection

The temperature and velocity results of COMSOL for a number of different models were validated against an independent, C-based, in-house programmed finite element method (FEM) software that was used in a former convection study[30]. Sub-percent agreement between temperature drift curves for the all modeled scenarios was obtained. The maximum velocity (both inside and outside the vessel) as calculated by COMSOL and the independent FEM software generally agreed to within 30 %, but discrepancies of up to 65 % were observed (in case of a calorimeter being irradiated with 6 MV photons at 22 °C) for velocities on the order of 0.5 mm/min. Given that all the model parameters were not identical between the two programs (including geometry, meshing, solver type, etc), the differences in velocities were deemed acceptable.

Given our simulation setup, for a 32000 U (8 Ci) source and a typical 300 s irradiation time, COMSOL calculations show velocity fields that can be as large as 24 mm/min immediately after the end of irradiation and close to the source dwell position. Following the removal of the source from the calorimeter, the velocities drop quickly and significantly (especially for coordinates close to the source position), although water velocities in excess of 3-5 mm/min are observed even 300 s after the end of irradiation. However, in spite of radical convection outside the vessel, the vessel itself acts as a convective barrier, decoupling the velocity fields inside from those outside, and drastically reducing the effects of convection inside the vessel. In spite of the small thermistor power dissipation inside the vessel, we find water velocity to generally be few orders of magnitude lower than the velocities outside. For instance, the velocity on either side of the wall is usually different by at least two orders of magnitude. For the same simulation discussed above, water velocity inside the vessel was effectively zero. This does not mean, however, that the effects of convection need not to be taken into account during modelling. For our geometrical setup (i.e. in the ‘far’ region), we numerically determined a 1 % to 1.5 % difference between heat transfer correction factor k_{ht} calculated with and without the effects of convection considered. The dependence of k_{ht} on accurate modelling of convection becomes even larger in the ‘near’ region.

Temperature evolution

Figure 6.6 shows the evolution of temperature rise inside the source and immediately outside the source (0.5 mm away) in water. Two extreme cases were numerically studied with COMSOL. In one scenario the source's initial temperature (as it enters the 4 °C water calorimeter at the beginning of the irradiation) is set to 4 °C, while in the other extreme it is set to 29 °C (i.e., 25 °C above the water temperature inside the calorimeter). The constant temperature increase of the source and the water in its vicinity due to dose deposition is mitigated by heat dissipation through conduction and convection.

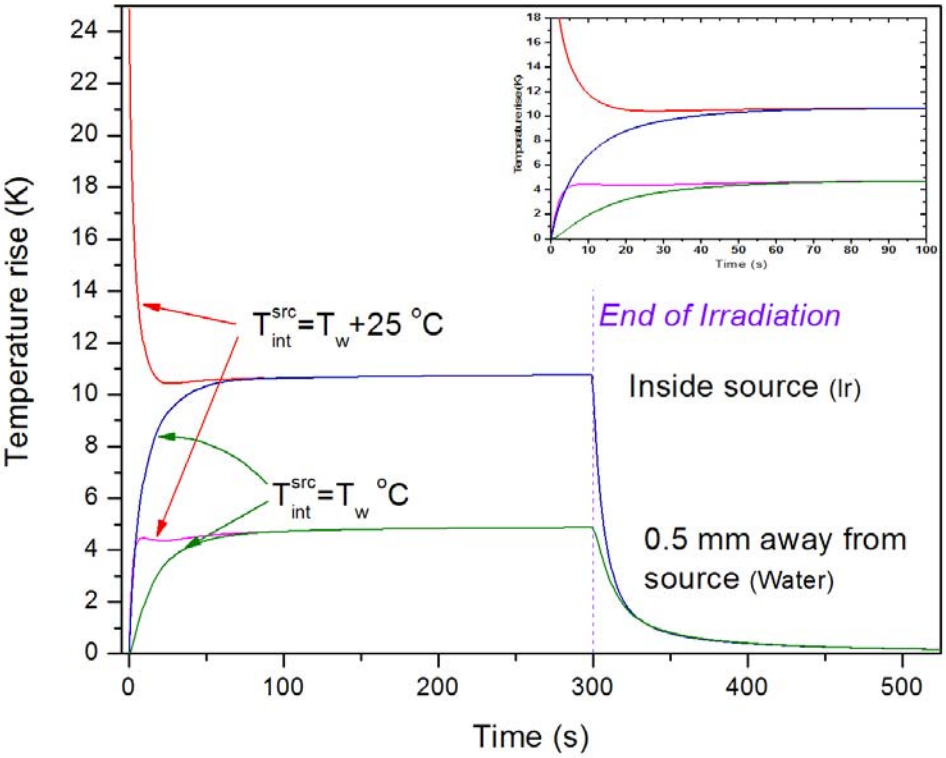

Figure 6.6: The COMSOL-calculated temperature rise inside the source and 0.5 mm away from the source (in water) during irradiation and following the removal of the source from the water calorimeter. The results are calculated for two extreme starting source temperatures.

Starting from either initial condition, the same final equilibrium temperature is reached with the source temperature approaching 10.8 °C, while the water temperature (adjacent to the source) approaches an equilibrium temperature of 4.9 °C. Immediately following the end of irradiation and the removal of the source from the calorimeter, temperature quickly drops back down towards 4 °C as conduction and convection dissipate the heat throughout the calorimeter. The convergence of temperature to a given equilibrium value for a given setup is an advantage because it means that an exact knowledge of the source's initial temperature is not necessary for an accurate COMSOL heat drift curve calculation.

6.3.3 Potential Improvements

Two potential changes to the current setup were considered.

1. Use of a metal catheter instead of nylon-12 breast-comfort catheters: This change was not included because the priority of this work was to maintain measurement conditions as similar as possible to the clinical calibration and delivery conditions. Russell and Ahnesjo[31] describe a 0.5-1.0 % drop in the radial dose profile per emitted radiant energy for a stainless steel catheter compared to a similar nylon catheter (no significant change was observed between nylon and water catheters). Not only would corrections be necessary for this effect, the increased accuracy in transverse positioning may come at the expense of an added uncertainty in lateral positioning of the source with respect to the thermistors due to use of opaque catheters (i.e. an added uncertainty on $\ell_{\text{src-det}}$ which translates to an added uncertainty on k_{dd}).

2. Source cooling prior to insertion into calorimeter: Simulations to evaluate the effects of cooling the source down to 4 °C to avoid a temperature shock inside the calorimeter upon source entry were undertaken. Using COMSOL, it was found that the source's inherent temperature T_{src} is always a given amount Φ over the ambient temperature T_{amb} (i.e. $T_{\text{src}} = T_{\text{amb}} + \Phi$). This temperature differential Φ is

only a function of ambient material and scales linearly with source activity. Using the best information about Nucletron ^{192}Ir source's Tungsten safe inside the after-loader, assuming that the source is in contact with the Tungsten, we find Φ=0.0025 °C/Ci. This is in contrast with roughly a 5 °C/Ci temperature differential for a source in air (and not the safe). Generally, the source temperature is about 2 % higher than the temperature of the cap surrounding it.

The intensity of 'source-heat' drops quickly and dissipates in water as it is transferred away from the source (through conduction and convection). Hence in the 'far' region, it plays a very small role in affecting the heat drift curve. Moreover, since the source's temperature drops relatively quickly and comes to a new equilibrium with its surrounding (discussed in *Section 6.3.2*), source cooling does not significantly improve the results in the 'far' region. However, in the 'near' region, the postdrift is susceptible to the adverse effects of large 'source-heat.' Indeed, in this region, cooling of the source from room-temperature down to 4 °C can improve the results. However, more important than pre-cooling, active source cooling and/or introducing better source insulation (for example through providing a larger air insulation gap around the source or source catheter) can drastically reduce the effects of source self-heating throughout a calorimetric run, with minimal impact on the dose distribution. In turn, this can potentially increase the available time for irradiation and postdrift data collection in the 'near' region, resulting in larger signals and longer postdrift data available for extrapolation, and yielding lower uncertainties on the final dose results.

6.3.4 Uncertainty Budget

Table 6.1 lists all sources of uncertainty in ^{192}Ir water calorimetry. The uncertainties noted are conservative and often correspond to upper limits. A 0.43 % standard error on the average measurement result was reached based on 83 independent calorimetric runs. This is in accordance with the expected reproducibility of water calorimetric runs performed at low dose rates[32]. The uncertainties on the specific heat capacity of water and absolute temperature measurement of the calorimeter, as well as the resistance-to-voltage and thermistor calibration factors are all taken into consideration.

Uncertainty	**Type A (%)**	**Type B (%)**
Std error on the mean (meas.)	0.43	
c_w		0.03
Absolute temperature		0.01
$(\Delta R/R)/\Delta V$ calibration		0.04
Thermistor Calibration (β)		0.1
k_ρ		0.05
k_{hd}		0.3
k_p		0.1
k_{ht}		
Conv. Model (physical data)		0.35
Simulation data		0.05
Interval extrapolation		0.01
Vessel dimension		0.02
k_{dd}		0.45
Source-vessel separation		0.85
Probe position wrt vessel		0.03
Dwell time		0.01
Dummy/real source position		0.00
Predrift linearization		1.5
Total Uncertainty (1-sigma) %	**1.90**	

Table 6.1: The uncertainty budget for ^{192}Ir water calorimetry.

The uncertainties on all correction factors in Eq. 6.1 are indicated. The breakdown of various parameters influencing the heat transfer calculation (and thus the overall uncertainty on the final k_{ht} result) is shown. We assigned a 1-sigma type B uncertainty of 0.35 % to the accuracy of heat transfer modelling by COMSOL. This includes the uncertainty on the physical data parameters used during the simulation, as well as a lack of an accurate knowledge of the initial measurement conditions. The uncertainty on the value of source self-heating and dose distribution (termed ‘simulation data’), vessel dimensions, as well as the region of the postdrift used for the extrapolation (termed ‘interval extrapolation’) have been taken into account.

Besides the positioning uncertainty which affects both the depth measurement uncertainty and k_{dd} uncertainty, the largest source of uncertainty remains to be the predrift linearization technique. Although the uncertainty on k_{dd} is relatively large in this work, with more accurate measurements of $\ell_{\mathrm{src\text{-}det}}$ as well as by minimizing its value down to zero (through centering the source directly above the midpoint between the two thermistors), this uncertainty can be reduced by as much as an order of magnitude. The $d_{\mathrm{src\text{-}det}}$ positioning uncertainty has been further split into the uncertainty on the source-to-vessel separation, and the uncertainty on the positioning of the probe with respect to the front and back windows of the calorimeter vessel. Since all measurements of the source dwell position with respect to the measurement point were performed with a simulator ‘dummy’ source, a negligible 1-sigma 0.0007 % uncertainty on the dose was determined for discrepancies between the measured position of the ‘dummy’ and actual dwell position of the hot active source (measured to be 0.15 mm).

Since our measurements were performed over a range of $d_{\mathrm{src\text{-}det}}$, for the purpose of comparison, they were all converted to a $d_{\mathrm{src\text{-}det}}$=55 mm using a calculated ratio of dose at each point. Although not listed in Table I (since not inherent to the overall uncertainty of the system), we have assigned an additional 0.25 % uncertainty to this conversion which is included in the results of Table 6.3.

6.3.5 Absorbed Dose to Water

Table 6.2 shows the results of our measurements in the ‘far’ region. The dose rate results have been normalized to the nominal source air kerma strength at the time of the measurement. The irradiation time has been adjusted for source transit time (found to be 0.31±0.06 s measured using ionization chamber). The uncertainty for this effect has been accounted for in Table I under ‘dwell time.’ Analogous to shutter error, source transit time is not accounted for in the dwell time reported by the afterloader. Also taken into account is a comparison of the results with TG-43 calculated dose rates based on Daskalov *et al*[27] and Taylor and Rogers[25,26] data and corrected for the smaller phantom size used in the experiment[33]. It can be seen that the results agree well to within uncertainty.

Finally, Table 6.3 shows a comparison between the water calorimetry data and ionization chamber and EBT Gafchromic film ^{192}Ir reference dosimetry data. Both sets of measurements are performed directly in water. An Exradin A1SL Farmer type ionization chamber was used to measure the air kerma rate in water, while accurate Monte Carlo simulation of the setup geometry was performed to convert the measurement results into a dose rate to water given the chamber’s NIST traceable ^{60}Co calibration factor. The Gafchromic film dosimetry protocol was as described by Devic *et al*[34]. Since in this work, the sensitometric relation between net optical density and absorbed dose to water was obtained for 6 MV photons, Monte Carlo simulations were performed to account and correct for the energy dependence of these detectors. All film and chamber measurements were performed in water. Table 6.3 also shows the dose results as measured with a calibrated well-type chamber following the TG-43 protocol[1]. The measurement setup details for ionization chamber and Gafchromic film reference dosimetry as well as the TG-43 calculation details are described in Sarfehnia *et al*[35]. Once again, all measurements agree well to within uncertainty and to better than 0.83 %.

Nominal source $S_{K,air}$ [U]	Source-detector separation [mm]	Irradiation time [s]	Average dose rate [μGy/(h.U)]	TG-43 calculated [μGy/(h.U)]	% diff.
32600	52.69±0.40	300	402 (2.4 %)	397	1.16
31600	51.67±0.38	200, 300	407 (2.3 %)	413	-1.77
35700	53.06±0.25	250, 300	385 (2.1 %)	391	-1.61
36940	66.96±0.13	300	237 (2.1 %)	239	-0.89

Table 6.2: Summary of dose measurement results based on water calorimetry for a Nucletron microSelectron ^{192}Ir brachytherapy source. A 1-sigma uncertainty of 2.5 % is associated with the TG-43 results. The 1-sigma uncertainty on average measured dose rate is shown in bracket. Around 20 measurement runs were performed at each of the four source detector separations. By refining our positioning measurement techniques, we have lowered our positioning reproducibility from 0.40 mm down to 0.13 mm as shown.

	Calorimetry standard	Chamber reference	Gafchromic reference	TG-43 protocol
Dose Rate [μGy/(h.U)]	361 ± 7	358 ± 5	364 ± 7	363 ± 9
% diff from Calorimetry	--	-0.83%	0.83%	0.55%

Table 6.3: A comparison of our final dose rate measurement results with chamber and Gafchromic film reference dosimetry, as well as TG-43 protocol. All measurements are normalized to a source-to-detector distance of 55 mm.

6.4 CONCLUSIONS

A water calorimetry based standard for the direct measurement of absolute absorbed dose to water for ^{192}Ir sources was shown to be feasible in a previous report[16]. In this paper, we discuss an improved version of the calorimeter along with its commissioning and uncertainty budget. The main sources of uncertainty are positioning and self heating of the source that limits the proximity of the temperature sensors to the source. The balance of these factors affects the irradiation times and consequently the temperature drift extrapolations, hence the uncertainty. We have shown that the calorimeter compares well with other, completely independent dose measurement techniques. The overall uncertainty of the new standard amounts to 1.90 % (1-sigma). This work paves the way towards an eventual water calorimeter-based primary standard, and an improved dosimetry chain for ^{192}Ir starting from direct in water calibrations.

ACKNOWLEDGMENTS

This work has been supported in part by grant RGPIN 298181 of the Natural Sciences and Engineering Research Council. The authors would like to acknowledge the significant contributions of Dr. E. Poon to this work. The contributions and fruitful discussions with Dr. F. Verhaegen and Dr. B. Reniers are also appreciated. A. S. is a recipient of a CIHR doctoral Fellowship.

6.5 REFRENCES

[1] R. Nath, L. L. Anderson, G. Luxton, K. A. Weaver, J. F. Williamson, and A. S. Meigooni, "Dosimetry of interstitial brachytherapy sources: recommendations of the AAPM Radiation Therapy Committee Task Group No. 43. American Association of Physicists in Medicine," Med. Phys. 22, 209-234 (1995).

[2] M. J. Rivard, B. M. Coursey, L. A. DeWerd, W. F. Hanson, M. S. Huq, G. S. Ibbott, M. G. Mitch, R. Nath, and J. F. Williamson, "Update of AAPM Task Group No. 43 Report: A revised AAPM protocol for brachytherapy dose calculations," Med. Phys. 31, 633-674 (2004).

[3] S. J. Goetsch, F. H. Attix, D. W. Pearson, and B. R. Thomadsen, "Calibration of 192Ir high-dose-rate afterloading systems," Med Phys 18, 462-467 (1991).

[4] "Calibration of photon and beta ray sources used in brachytherapy," IAEA-TDCDOC-1274 (2002).

[5] E. Mainegra-Hing and D. W. Rogers, "On the accuracy of techniques for obtaining the calibration coefficient N(K) of 192Ir HDR brachytherapy sources," Med Phys 33, 3340-3347 (2006).

[6] J. Borg, I. Kawrakow, D. W. Rogers, and J. P. Seuntjens, "Monte Carlo study of correction factors for Spencer-Attix cavity theory at photon energies at or above 100 keV," Med Phys 27, 1804-1813 (2000).

[7] K. N. Rajan, T. P. Selvam, B. C. Bhatt, M. Vijayam, V. S. Patki, Vinatha, A. M. Pendse, and V. Kannan, "Direct calibration of a reference standard against the air kerma strength primary standard, at 192Ir HDR energy," Phys Med Biol 47, 1047-1058 (2002).

[8] T. P. Selvam, K. N. Rajan, P. S. Nagarajan, P. Sethulakshmi, and B. C. Bhatt, "Monte Carlo aided room scatter studies in the primary air kerma strength standardization of a remote afterloading 192Ir HDR source," Phys Med Biol 46, 2299-2315 (2001).

[9] C. Austerlitz, H. C. Mota, J. Sempau, S. M. Benhabib, D. Campos, R. Allison, C. E. DeAlmeida, D. Zhu, and C. H. Sibata, "Determination of absorbed dose in water at the reference point d(r0, theta0) for an 192Ir HDR brachytherapy source using a Fricke system," Med Phys 35, 5360-5365 (2008).

[10] S. R. Domen, "Absorbed dose water calorimeter," Med Phys 7, 157-159 (1980).

[11] J. Seuntjens and S. Duane, "Photon absorbed dose standards," Metrologia 46, S39-S58 (2009).

[12] H. Palmans, J. Seuntjens, F. Verhaegen, J. Denis, S. Vynckier, and H. Thierens, "Water calorimetry and ionization chamber dosimetry in an 85-MeV clinical proton beam," Med Phys 23, 643-650 (1996).

[13] R. J. Schulz, L. J. Verhey, M. S. Huq, and N. Venkataramanan, "Water calorimeter dosimetry for 160 MeV protons," Phys Med Biol 37, 947-953 (1992).

[14] K. Stewart, N. V. Klassen, C. K. Ross, and J. Seuntjens, "Sci-YIS Fri-05: Design and testing of a new sealed water calorimeter for electron beams," Med Phys 32, 2419 (2005).

[15] K. E. Stump, L. A. DeWerd, D. A. Rudman, and S. A. Schima, "Active radiometric calorimeter for absolute calibration of radioactive sources," Rev. Sci. Instrum. 76, 033504:1-033504:9 (2005).

[16] A. Sarfehnia, K. Stewart, and J. Seuntjens, "An absorbed dose to water standard for HDR 192Ir brachytherapy sources based on water calorimetry: numerical and experimental proof-of-principle," Med Phys 34, 4957-4961 (2007).

[17] A. Krauss, "Application of water calorimetry as absorbed dose to water standards for radiotherapy dosimetry," presented at the Absorbed Dose and Air Kerma Primary Standards Workshop, Paris, 2007.

[18] M. Bambynek, A. Krauss, and HJ. Selbach, "Calorimetric determination of absorbed dose to water for a ^{192}Ir HDR brachytherapy source in near-field geometry," presented at the 11th International Congress of the IUPESM-Medical Physics and Biomedical Engineering World Congress 2009, Munich, Germany, 2009.

[19] S. R. Domen, "A sealed water calorimeter for measuring absorbed dose," NIST J. Res. 99, 121-141 (1994).

[20] J. Seuntjens and H. Palmans, "Correction factors and performance of a 4 degrees C sealed water calorimeter," Phys. Med. Biol. 44, 627-646 (1999).

[21] N. V. Klassen and C. K. Ross, "Water calorimetry: A correction to the heat defect calculations," J Res Natl Inst Stan 107, 171-178 (2002).

[22] I. Kawrakow, E. Mainegra-Hing, and D. W. O. rogers, "The EGSnrcMP: the multi-platform environment for EGSnrc," NRCC Report PIRS-877, Ottawa, Canada (2000).

[23] "National Nuclear Data Center, 2004 Nuclear data from NuDat, a web-based database maintained by the National Nuclear Data Center, Brookhaven National Laboratory, (Upton, NY) http://www.nndc.bnl.gov/nudat2/."

[24] N. Reynaert, M. Van Eijkeren, Y. Taeymans, and H. Thierens, "Dosimetry of 192Ir sources used for endovascular brachytherapy," Phys Med Biol 46, 499-516 (2001).

[25] R. E. Taylor and D. W. Rogers, "EGSnrc Monte Carlo calculated dosimetry parameters for 192Ir and 169Yb brachytherapy sources," Med Phys 35, 4933-4944 (2008).

[26] R. E. Taylor and D. W. Rogers, "An EGSnrc Monte Carlo-calculated database of TG-43 parameters," Med Phys 35, 4228-4241 (2008).

[27] G. M. Daskalov, E. Loffler, and J. F. Williamson, "Monte Carlo-aided dosimetry of a new high dose-rate brachytherapy source," Med. Phys. 25, 2200-2208 (1998).

[28] J. Borg and D. W. O. Rogers, "Monte Carlo calculations of photon spectra in air for ^{192}Ir sources," NRC Reports, PIRS-629r (1999).

[29] S. R. Domen, "An absorbed dose water calorimeter: Theory, design, and performance," J Res Natl Bur Stand 87, 211-235 (1982).

[30] J. Seuntjens, I. Kawrakow, and C. K. Ross, "Revisiting Convective Motion in Stagnant Water Calorimeters Operated at Room Temperature," presented at the NPL Workshop on Recent Advances in Calorimetric Absorbed Dose Standards, National Physical Laboratory, Teddington, UK, 2000.

[31] K. R. Russell and A. Ahnesjo, "Dose calculation in brachytherapy for a 192Ir source using a primary and scatter dose separation technique," Phys Med Biol 41, 1007-1024 (1996).

[32] J. Seuntjens, H. Thierens, and U. Schneider, "Correction factors for a cylindrical ionization chamber used in medium-energy X-ray beams," Phys Med Biol 38, 805-832 (1993).

[33] E Poon and F. Verhaegen, "Development of a scatter correction technique and its application to HDR ^{192}Ir multicatheter breast brachytherapy," Med Phys 36, 3703-3713 (2009).

Chapter 7

Direct measurement of absorbed dose to water in HDR ^{192}Ir brachytherapy: Water calorimetry, ionization chamber, Gafchromic film, and TG-43

In this chapter, we continue the discussion of ^{192}Ir brachytherapy dosimetry. For the purpose of comparison and validation, in addition to our work in water calorimetry primary standard, we developed protocols for measurement of absorbed dose to water based on direct in-water measurements with two of the most commonly used dosimeters in clinics: Ionization chamber and Gafchromic films. Of course, neither dosimeters were calibrated against our water calorimeter in the ^{192}Ir beam, but rather our protocol was designed such that the absorbed dose to water in the ^{192}Ir beam was measured using detectors with calibration factors obtained in ^{60}Co or higher photon energies, where dosimetry is well established. This work presents in full detail our in-water measurement protocols, as well as the results and a comparison of the dose to water measurements based on water calorimetry primary standard, ion chamber and Gafchromic film reference dosimetry, as well as dose to water measurements using the currently accepted TG-43 protocol.

Authors: Arman Sarfehnia[1], Iwan Kawrakow[2] and Jan Seuntjens[1]

[1] Medical Physics Unit, McGill University, Montreal General Hospital, Montréal, Québec, Canada

[2] National Research Council of Canada, Ottawa, Ontario, Canada

*Medical Physics **37**, 1924-1932 (2010)*

ABSTRACT

Purpose: Gafchromic film and ionometric calibration procedures for HDR ^{192}Ir brachytherapy sources in terms of dose rate to water are presented and the experimental results are compared with the TG-43 protocol as well as with the absolute dose measurement results from a water calorimetry-based primary standard.

Methods: EBT-1 Gafchromic films, an A1SL Exradin miniature Shonka thimble type chamber, and a Standard Imaging HDR 1000 Plus well-type chamber with an ADCL traceable S_K calibration coefficient (following the AAPM TG-43 protocol) were used. The Farmer chamber and Gafchromic film measurements were performed directly in water. All results were compared to direct and absolute absorbed dose to water measurements from a 4 °C stagnant water calorimeter.

Results: Based on water calorimetry, we measured the dose rate to water to be 361±7 μGy/(h.U) at a 55 mm source-to-detector separation. The dose rate normalized to air kerma strength for all the techniques agree with the water calorimetry results to within 0.83 %. The overall one sigma uncertainty on water calorimetry, ionization chamber, Gafchromic film, and TG-43 dose rate measurement amounts to 1.90 %, 1.44 %, 1.78 %, and 2.50 %, respectively.

Conclusions: This work allows us to build a more realistic uncertainty estimate for absorbed dose to water determination using the TG-43 protocol. Furthermore, it provides the framework necessary for a shift from indirect HDR ^{192}Ir brachytherapy dosimetry to a more accurate, direct and absolute measurement of absorbed dose to water.

7.1 INTRODUCTION

The AAPM Task Group 43[1] and its update[2] comprise the currently accepted protocol for calculation of dose to water D_w in ^{192}Ir brachytherapy from a reference air-kerma strength S_K measurement. The protocol provides a formalism to convert S_K to D_w at the point of interest using several calculated or measured factors. Specified in terms of the air kerma rate on the transverse axis of the source in free space at 1 m, S_K is determined in clinics using an in-air measurement with a calibrated well-type chamber.

The method employed by Accredited Dosimetry Calibration Laboratories (ADCL) in establishing calibration factors for well-type chambers is based on the interpolation procedure devised by Goetsch *et al*[3]. Through this technique, the calibration factor of a Farmer chamber at the exposure-weighted average energy of ^{192}Ir source is indirectly interpolated from the chamber's calibration factors that are determined at energies above (^{137}Cs, or ^{60}Co) and below (orthovoltage x-rays) the effective ^{192}Ir energy. In more recent publications, Mainegra-Hing *et al*[4] have discussed some of the conceptual problems with the Goetsch's technique and pointed out minor errors with this approach, while Van Dijk *et al*[5] have also shown significant systematic differences between measurements made following Goetsch's technique and other approaches.

Over the past two decades, there have been many publications on accurate dosimetry in HDR ^{192}Ir brachytherapy focusing on the measurement of the 2D or 3D dose distribution around these sources using techniques such as NMR Fricke-gelatin dosimetry[6,7], analytical and Monte Carlo-based dose calculation techniques[8-12], thermoluminescent (TLD) dosimetry[8,9], ionization chamber dosimetry[13,14], diode dosimetry[9], and Gafchromic film dosimetry[13,15,16]. In spite of this work in HDR ^{192}Ir dosimetry, a primary standard for absolute absorbed dose measurement under iridium beam remains non-existent[17]. In 1999, Borg *et al*[18] explored the possibility of performing more direct measurements of air kerma in

^{192}Ir photon beams using cavity-ionization chambers with Monte Carlo-calculated corrections accounting for the non-validity of the Spencer-Attix cavity theory. More recently, the feasibility of measuring absolute dose in ^{192}Ir brachytherapy using a Fricke dosimeter has been explored[19]. Finally, our group has developed a water calorimeter-based standard to directly measure the absolute absorbed dose to water in ^{192}Ir brachytherapy[20,21].

This work presents the summary of a comprehensive study performed to directly measure the absorbed dose to water in HDR ^{192}Ir brachytherapy. By measuring the dose directly in water, we avoid additional uncertainties associated with the conversion of absorbed dose in non-water media into absorbed dose to water. To that end, in-water reference ionization chamber and EBT-1 Gafchromic film measurements are performed. The protocols devised and followed to perform in-water measurements are described. The absorbed doses are compared with those obtained through the currently accepted TG-43 protocol, as well as the absolute D_w measurements from our proposed water calorimeter-based ^{192}Ir brachytherapy primary standard[20,21]. All measurements were obtained over a three-year period with four different Nucletron microSelectron ^{192}Ir brachytherapy sources (part No. 105.002) with S_K ranging between 21000-38000 U (corresponding to an activity range of 5.1-9.3 Ci).

7.2 METHODS

7.2.1 Absorbed Dose Measurements Using An Ionization Chamber

An A1SL Exradin miniature Shonka Farmer chamber was used in this work. The small collecting volume of the chamber (0.057 cm^3) minimizes the dose volume averaging effect that can prove large and detrimental in ^{192}Ir dosimetry due to the sharp dose gradient in the field near the source. Moreover, the inherent water proof construction of the chamber simplifies the experimental setup and eliminates the need for a sleeve during measurement and a correction factor for it during analysis.

Figure 7.1(a) shows the chamber measurement setup. A Nucletron 4 French nylon-12 ‘breast-comfort’ catheter was connected to a Lucite holder using a spring-loaded technique. The constant pressure exerted along the length of the catheter by the spring compensates for any changes in catheter length that may occur due to differences in coefficient of thermal expansion and the rate of water absorption between the catheter and the holder material. To provide extra rigidity to the catheter and improve the reproducibility of source-to-detector distance $d_{\text{src-det}}$ measurements, the nylon catheter was slid inside a 6 French stainless steel tubing support. In order to avoid any significant scatter or attenuation of the ^{192}Ir beam spectrum, a 15 mm opening in the center of the metal support was made.

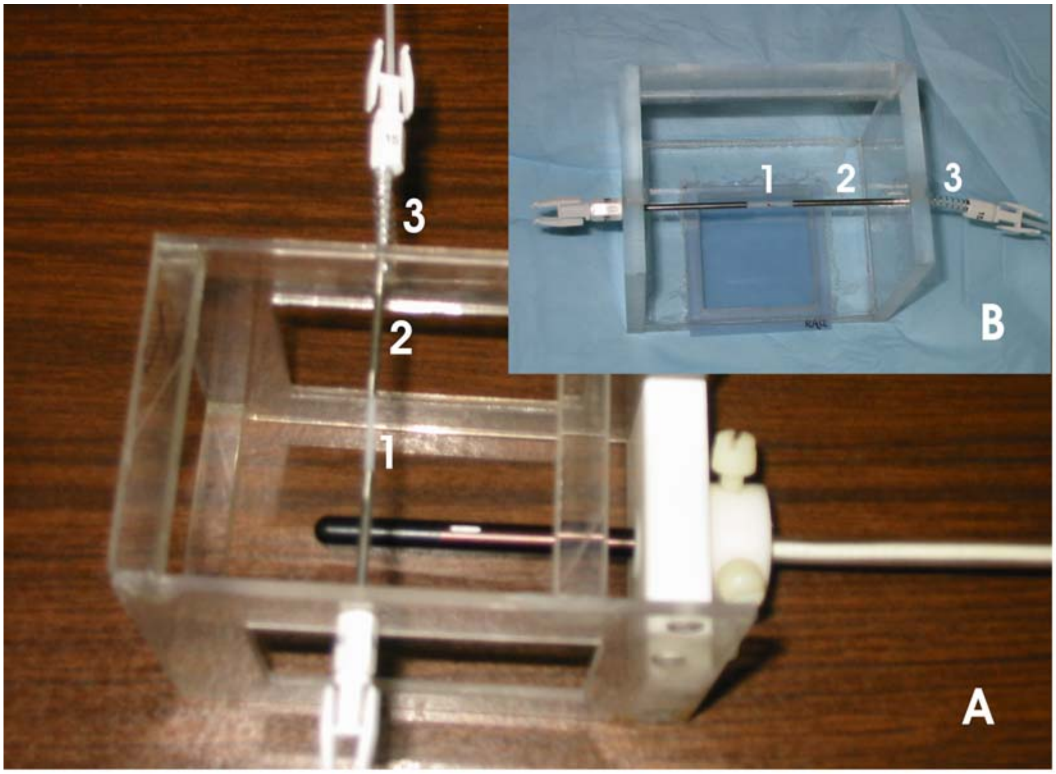

Figure 7.1: The chamber measurement setup (a), and the Gafchromic film setup (b). The nylon-12 catheter (1), the stainless steel support (2), and the spring-loaded catheter holding device (3) are shown.

The separation between the ^{192}Ir source and the chamber was accurately measured using a Titan travelling microscope with the optical tube in its vertical position, in a similar setup to that shown in Fig. 7.2. The distance measurements were also checked against those obtained using a calliper gauge. A nominal mid-source to mid-chamber separation $d_{\text{src-det}}$ of 51 mm was set. To ensure that the source is positioned directly above the chamber and is not offset laterally, the lateral position of a simulator 'dummy' source with respect to the chamber $\ell_{\text{src-det}}$ was also measured (see inset of Fig. 7.2). Based on an independent set of experiments, we measured the dwell position of the hot active source to agree with that of the simulator 'dummy' source to better than 0.15 mm.

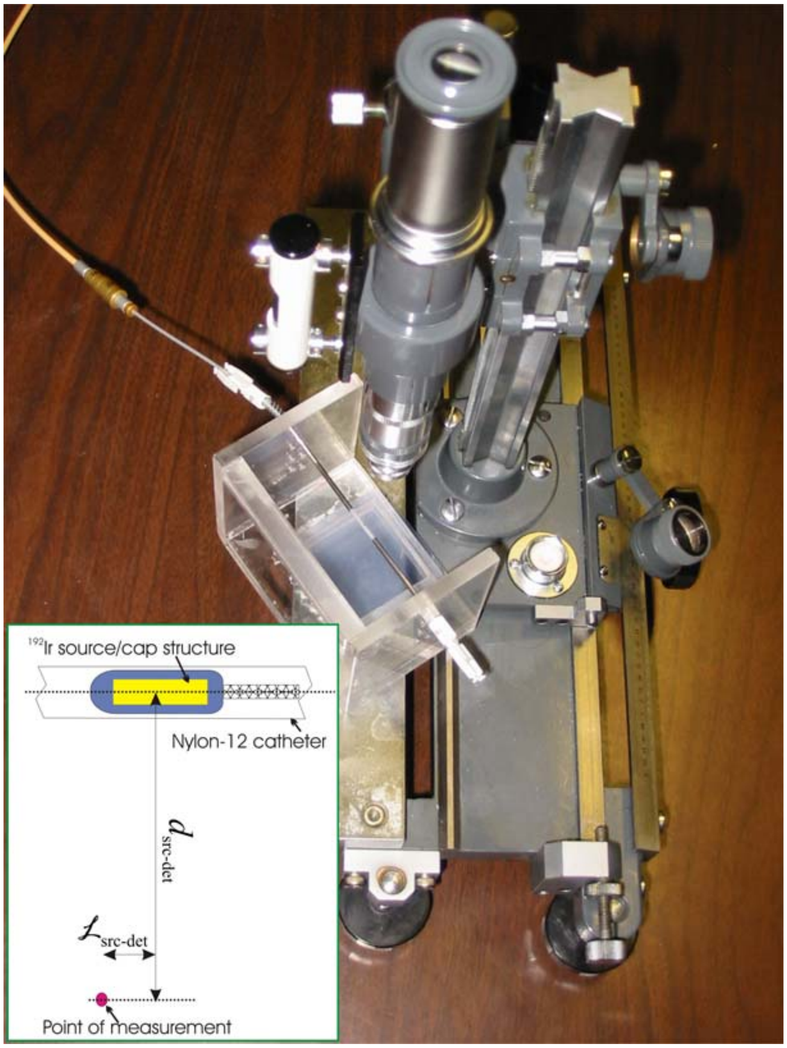

Figure 7.2: The setup used to measure the distance between the ^{192}Ir source and the film ($d_{\text{src-det}}$) with a travelling microscope. A similar setup was used in ion chamber $d_{\text{src-det}}$ measurement. Inset schematically shows $d_{\text{src-det}}$ and $\ell_{\text{src-det}}$ definitions.

Absorbed Dose Conversion

Currently, most standards laboratories do not provide well chamber calibration coefficients at ^{192}Ir energy, but rather provide either absorbed dose-based calibrations $N_{D,\mathrm{w}}$ for ^{60}Co and higher energy photons, or air kerma-based calibration factors N_K for ^{60}Co and lower kilovoltage energies. Reynaert *et al*[13] discussed a protocol for D_w measurement with Farmer chambers based on an interpolated $N_K(^{192}\mathrm{Ir})$ calibration (similar to the technique used by Goetsch *et al*[3]). The ratio of mass energy absorption coefficient water to air evaluated at ^{192}Ir energy and several Monte Carlo (MC) calculated corrections are subsequently utilized to convert the air-kerma rate in water measurement to dose to water.

In this work, a more direct and conceptually simpler approach is taken. Since the measurements were performed in water and in the absence of a build-up cap, given an $N_{\mathrm{D,w}}(^{60}\mathrm{Co})$ for the chamber, one can find N_gas by

$$N_\mathrm{gas} = N_{D,\mathrm{w}}(^{60}\mathrm{Co})\left[\frac{D_\mathrm{gas}}{D_\mathrm{w}}\right]_\mathrm{MC}^{^{60}\mathrm{Co}}, \tag{7.1}$$

where $\left[D_\mathrm{gas}/D_\mathrm{w}\right]_\mathrm{MC}^{^{60}\mathrm{Co}}$ is a MC calculated factor corresponding to the ratio of dose scored inside the chamber's collective volume D_gas and the dose to water scored at the same point with the chamber effectively replaced with water D_w. This ratio was obtained with the EGSnrc[22,23] based egs_chamber code[24]. The egs_chamber code allows for very efficient computation of ion chamber doses and dose ratios by using various variance reduction techniques, and also permits realistic simulations of the experimental setup due to the use of the EGSnrc C++ class library[25]. A very detailed model of the A1SL chamber was created with the C++ geometry package according to manufacturer specifications. A ^{60}Co spectrum published by Mora *et al*[26] was employed and a standard ^{60}Co calibration setup was simulated. A value of 1.1086±0.0011 for the dose to the chamber to dose to water ratio was determined. The uncertainty quoted is only statistical (1σ). Given the definitions of N_gas[27] and $N_{D,\mathrm{w}}$[28], we can rewrite Eq. 7.1 as

$$\frac{N_{\text{gas}}}{N_{D,\text{w}}(^{60}\text{Co})} = \left[\frac{D_{\text{gas}}}{D_{\text{w}}}\right]_{\text{MC}}^{^{60}\text{Co}} = \left(\frac{\bar{L}}{\rho}\right)_{\text{w}}^{\text{air}} \left(P_{\text{repl}} P_{\text{wall}} P_{\text{cel}}\right)^{-1} \Bigg|^{^{60}\text{Co}} \tag{7.2}$$

where $\left(\frac{\bar{L}}{\rho}\right)_{\text{w}}^{\text{air}}$ is the restricted stopping power ratio air to water, P_{repl} is replacement correction factor accounting for fluence perturbations resulting from chamber cavity, P_{wall} accounts for non-water wall material, and P_{cel} is a central electrode correction. In order to compare our calculation results to published data, from the Technical Report Series no. 398[28], one could find a similar relation as Eq. 7.2 (with slightly different notations than those used by the AAPM Task Group) relating N_{gas}, termed $N_{D,\text{air}}$, and $N_{\text{D,w}}(^{60}\text{Co})$

$$\frac{N_{D,\text{air}}}{N_{D,\text{w}}(^{60}\text{Co})} = \left[\frac{D_{\text{gas}}}{D_{\text{w}}}\right]_{\text{MC}}^{^{60}\text{Co}} = s_{\text{air,w}} \left(p_{\text{cav}} p_{\text{dis}} p_{\text{wall}} p_{\text{cel}}\right)^{-1} \Big|^{^{60}\text{Co}}, \tag{7.3}$$

where $s_{\text{air,w}}$ is equivalent to $\left(\frac{\bar{L}}{\rho}\right)_{\text{w}}^{\text{air}}$, p_{cav} corrects for electron fluence perturbation (P_{fl}), p_{dis} is the displacement correction factor (P_{gr}), p_{wall} is equivalent to P_{wall}, and p_{cel} is defined similarly to P_{cel}. The TRS-398[28] reports $s_{\text{air,w}} \left(p_{\text{cav}} p_{\text{dis}} p_{\text{wall}} p_{\text{cel}}\right)^{-1} \Big|^{^{60}\text{Co}}$ to be 1.100 for the Exradin A1 mini Shonka chamber. Although slightly different chamber than the one used in this experiment, the agreement between the EGSnrc calculated and TRS-398 reported result is encouraging.

Using the calculated N_{gas}, a corrected chamber measurement M^{c} obtained under the ^{192}Ir beam can be converted to D_{w} following a similar approach taken in Eq. 7.1,

$$D_{\text{w}}\left(^{192}\text{Ir}\right) = \left(N_{\text{gas}} M^{\text{c}}\right) \left[\frac{D_{\text{w}}}{D_{\text{gas}}}\right]_{\text{MC}}^{^{192}\text{Ir}}. \tag{7.4}$$

$\left[D_{w}/D_{gas}\right]_{MC}^{^{192}Ir}$ was calculated at every measurement position ($d_{src\text{-}det}$) again using the EGSnrc based egs_chamber code. In these calculations the microSelectron source embedded in the catheter and the stainless steel tube was modeled in full detail thus simulating accurately the experimental setup. The ^{192}Ir brachytherapy source/cap structure was modelled based on information provided by Daskalov *et al*[9] (see Fig. 7.3). For the smallest and largest $d_{src\text{-}det}$ distances used in this work, $\left[D_{w}/D_{gas}\right]_{MC}^{^{192}Ir}$ was found to be 0.9027 (1σ=0.09 %) at 34.9 mm, and 0.9048 (1σ=0.11 %) at 51.5 mm. The calculations seem to suggest that $\left[D_{w}/D_{gas}\right]_{MC}^{^{192}Ir}$ varies by less than 0.3% for variations of 1.5 cm in $d_{src\text{-}det}$, and has a nominal value of 0.9051 (1σ=0.1 %) at around 50 mm $d_{src\text{-}det}$ for the Exradin A1SL.

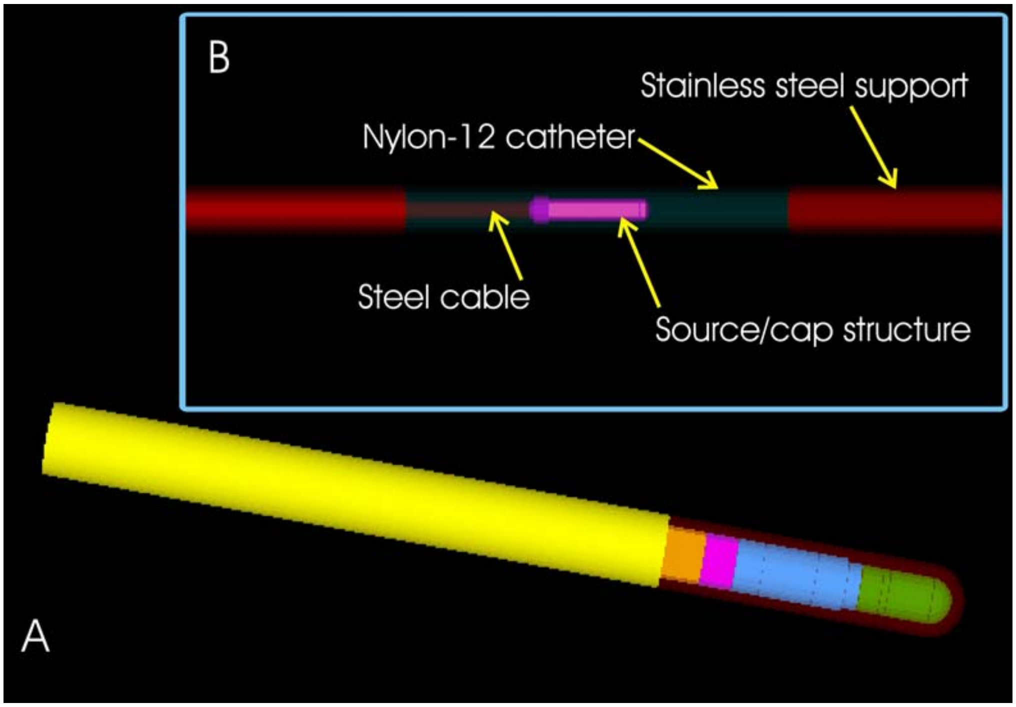

Figure 7.3: An egs++ visualization of the modeled A1SL mini-Shonka chamber (a) and the Nucletron microSelectron 192Ir brachytherapy source/cap structure9 inside the 4 French nylon-12 catheter and the 6 French stainless steel support (b).

Ma and Nahum[29] have found that the contribution of the electrons generated inside the cavity to the total signal is significant at the effective ^{192}Ir photon energy. As a consequence, one of the assumptions of both Bragg-Gray cavity theory and Spencer-Attix cavity theory breaks down at these energies. Although dose predictions by Bragg-Gray cavity theory are found to deviate from actual results by several percents[29], Borg *et al*[17] show that the Spencer-Attix predicted response of a graphite-wall chamber agrees to within 0.3 % with MC calculated results despite the break down of this cavity theory at ^{192}Ir effective energies. As described by Borg *et al*[17], the Spencer-Attix formulation of the dose response at such energies is dependent on both the ratio of mass energy absorption coefficient water to air $\left(\mu_{en}/\rho\right)_{\mathrm{air}}^{\mathrm{w}}$ and on the stopping power ratios $s_{\mathrm{w,air}}$. Since the ^{192}Ir effective beam energy varies only slightly over the narrow experimental $d_{\text{src-det}}$ range, and both $\left(\mu_{en}/\rho\right)_{\mathrm{air}}^{\mathrm{w}}$ and $s_{\mathrm{w,air}}$ are relatively energy insensitive, our calculations showing $\left[D_{\mathrm{w}}/D_{\mathrm{gas}}\right]_{\mathrm{MC}}^{^{192}\mathrm{Ir}}$ to be insensitive to modest $d_{\text{src-det}}$ variations should not come as a surprise.

The actual corrected measurement for medium energy x-rays is defined by the AAPM TG-61 formalism[30]

$$M^{\mathrm{c}} = M_{\mathrm{raw}} P_{\mathrm{ion}} P_{\mathrm{pol}} P_{\mathrm{elec}} P_{\mathrm{TP}}\,, \tag{7.5}$$

where M_{raw} is the raw ionization measurement results. For the A1SL chamber, the ion recombination and polarity correction factors were found to be 0.1 % (P_{ion}=1.001), and -0.2 % (P_{pol}=0.998), respectively. The electrometer calibration factor correction P_{elec} was unity. The temperature and pressure correction P_{TP} is the largest necessary correction. The leakage current was negligible even over the relatively long (5-7 min) irradiation periods (~0.05 % for 7 min irradiation).

.

7.2.2 Absorbed Dose Measurements Using EBT-1 Film

Much of the existing literature on Gafchromic film dosimetry in ^{192}Ir brachytherapy is based on MD-55 film measurements made in air or solid-water. Indeed, a robust protocol for in-water Gafchromic film dosimetry is currently non-existent. In this work, we attempt to measure the absorbed dose to water using EBT-1 Gafchromic films. The choice of this type of film was motivated by the fact that EBT-1 films are more water-equivalent and water-resistant compared to other Gafchromic films. In addition, they are sensitive to small accumulated doses and they show a relatively weak energy-dependence over a large energy range.

The measurements were performed directly in deionised water. As shown in Fig. 7.1(b), a similar holder device as that explained in *Section 7.2.1* was used. The pre-cut, pre-scanned films were slid inside a 40×40 mm^2 pocket of the Lucite spring-loaded catheter holder. A nominal $d_{\text{src-det}}$=45 mm was used throughout the measurements.

After securing the film inside the holder pocket, the separation between the catheter and the film was measured using the travelling microscope for every individual film just prior and right after the placement in water and irradiation (see Fig. 7.2). The agreement between distance measurements pre- and post-irradiation was better than 0.1 mm. The irradiation time was adjusted to deliver a nominal dose of 1.5 and 2 Gy. As expected, permanent discolouration of a band of width 2-4 mm around the edges of the film piece occurs as a result of water absorption. Since this is directly dependent on the immersion time of the film in water, a separate control film was used for every set of irradiation time used.

The general Gafchromic film dosimetry protocol described by Devic *et al*[31] was followed. The films were scanned using an EPSON Expression 1680 flatbed scanner. The scanning resolution was set to 508 pixels/inch. The films were placed roughly at the center of the scanner to minimize scanner non-uniformity, and only the third scanned image of every film was used throughout the analysis[32]. Following irradiation, the films were stored in a light tight environment under reference conditions (temperature, humidity) for 24 hours prior to being scanned. An in-house Matlab program was developed to analyse the red component of the films (EBT films' region of absorption peak). A low-pass wiener filter was employed to reduce image noise.

In ^{192}Ir brachytherapy film dosimetry, the sharp dose gradient around the source results in highly non-uniform net optical density (netOD) distribution on the irradiated films. Hence, the choice of the size of the region of interest (ROI) used for the measurement of netOD directly influences the degree of dose volume averaging effect. In this work, an ROI of 2 mm diameter was used. The ROI was centered around the position of the peak netOD ($P_{\max}$) on the image ($P_{\max}$ thus corresponds to the position of the source directly above the film). Point of maximum netOD was taken to be the average of two $P_{\max}$ values determined using two separate techniques: (1) Each image was profiled both horizontally and vertically. These profiles were fit with a Gaussian function. The point of intersection of the horizontal and vertical profiles with the highest peak and the smallest FWHM was taken to be $P_{\max}$. (2) The center of the contour plot of the image was taken to be $P_{\max}$.

Absorbed Dose Conversion

Although EBT Gafchromic films are generally assumed to be energy independent during routine high energy photon and electron clinical measurements, they cannot be assumed energy independent at lower kilovoltage energies. The published data on EBT energy dependence is not very extensive, and the results often do not agree as the film preparation techniques, film readout and analysis techniques, as well as the dosimetry at low energy x-rays vary between various publications.

Rink *et al*[34] did not observe any significant real-time response difference between measurements performed at 100 kVp (39 keV effective energy) and 6 MV. Butson *et al*[35] observed a reduction of up to 4.4 % in response for EBT films irradiated at 250 kVp (119 keV effective energy) and 6 MV. However, the large 4 % uncertainty on the final dose results does not allow for significant conclusions to be made. Chiu-Tsao *et al*[36] also present a comparison study of XR-QA and EBT-1 Gafchromic film types irradiated with several brachytherapy sources as well as a 6 MV beam. A CCD-based spectrometer was used for readout. Although a large energy dependence was observed between 6 MV and very low energy beams, the energy dependence of the films for ^{192}Ir beam was small. However, as the authors mention, the work also lacks a solid uncertainty analysis and was only intended as a guide. A more recent study of Oves *et al*[37] shows that for 2 Gy of dose delivered, the EBT film's netOD at 75 kVp is only roughly 80 % of the netOD measured under 6 MV beam.

Although various published reports have made clear that at very low x-ray energies, EBT Gafchromic films are potentially significantly energy dependent, it is unclear how much uncertainty is introduced into the final dose by using a sensitometric curve (i.e., calibration curve) produced with a 6 MV beam to measure absorbed dose of an ^{192}Ir source. The energy dependence of a detector consists of the intrinsic energy dependence associated with the conversion of the physically measured signal into dose to the detector material, and the dosimetric energy dependence associated with the conversion of the dose to the detector material into dose to the medium (water). In this work the latter effect has been calculated using Monte Carlo simulations as described below.

We converted a sensitometric curve for absorbed dose to water at 6 MV to a calibration curve in terms of dose to the sensitive layer of the film, using Monte Carlo calculations. The latter quantity is directly related to OD_{film} through a similar sensitometric relation assuming the intrinsic energy dependence of the film response due to LET changes can be ignored. The procedure involves multiplying the measured D_w versus $\mathrm{OD}_\mathrm{film}$ curve by a MC calculated ratio of dose to film to dose to water $\left(D_\mathrm{film}/D_\mathrm{w}\right)_\mathrm{MC}^\mathrm{6\ MV}$ simulated under the measurement conditions. This dose-to-film calibration curve can be used for any beam energy, if the intrinsic energy dependence of the film response is LET independent. Following our measurements with ^{192}Ir, a similar conversion factor $\left(D_\mathrm{w}/D_\mathrm{film}\right)_\mathrm{MC}^{^{192}\mathrm{Ir}}$ can be used to convert the D_film back to the quantity of interest, D_w.

The MC simulations of the factors were performed with DOSRZnrc code[37] from the EGSnrc package[22]. The EBT-1 film was modelled accurately according to the manufacturer released data on the material composition and thicknesses of the various film layers. The geometry simulated closely mimicked the measurement conditions. D_film was computed in the two 17 µm thick active layers of the film. D_w was obtained using an identical simulation as that used to obtain D_film, except that the various film layers were simply replaced with water. To speed up the MC simulations, a photon cross section enhancement factor of 10 was used. We found $\left(D_\mathrm{film}/D_\mathrm{w}\right)_\mathrm{MC}^\mathrm{6\ MV} = 0.9881\ (1\sigma = 0.03\ \%)$, and $\left(D_\mathrm{w}/D_\mathrm{film}\right)_\mathrm{MC}^{^{192}\mathrm{Ir}} = 1.0092$ $(1\sigma = 0.09\ \%)$. According to our simulations, indeed a sensitometric curve obtained with 6 MV can be used with ^{192}Ir effective energy and the correction for the energy dependence is simply $0.9971\ (1\sigma = 0.1\ \%)$.

It should be noted that Type B uncertainties on the MC calculations have not been studied in this work. Type B uncertainties include uncertainties in cross sections, approximations, software errors, geometry approximations, etc. Rogers and Kawrakow[39] studied the effects of different physics implementations, geometry and source routine implementations on the response of an absolute calculation of a primary ionization chamber dose per unit fluence in a ^{60}Co beam. The worst-case effect observed in this sensitivity study induced a change in D_gas/fluence of 0.1% at ^{60}Co. In the present work, however, we are calculating *ratios of ratios* of D_w to D_gas (or D_film) for ^{192}Ir to the same quantity evaluated at

^{60}Co (or 6 MV). The Type B uncertainties on MC calculated results are likely strongly reduced as are the effects related to cross sections. It is therefore expected that the overall Type B uncertainty on the MC calculations will be very small compared to other uncertainty components in the measurements (see *Section 7.3.1*).

7.2.3 Task Group 43

The direct measurement of absorbed dose to water using ionization chamber and EBT Gafchromic films was also compared to the calculated TG-43 results. A Standard Imaging HDR 1000 Plus well-type chamber with an ADCL-traceable S_K calibration factor was used for the experiments. The air-kerma strength normalized dose rate equation taken directly from TG-43[1] is

$$\frac{\dot{D}(r,\theta)}{S_K} = \Lambda \frac{G(r,\theta)}{G(r_o,\theta_o)} g(r) F(r,\theta)\,. \qquad (7.6)$$

Being the only absolute quantity, the dose rate constant Λ converts the air kerma strength to dose-to-water at the reference point. For the microSelectron ^{192}Ir brachytherapy source, Λ was calculated to be 1.108 (±0.13 %) cGy h^{-1} U^{-1} by Daskalov *et al*[9], and 1.109 (±0.18 %) cGy h^{-1} U^{-1} by Taylor *et al*[10,11]. Daskalov's Λ result was used in this work. The radial dose function *g*(r) and the anisotropy of dose distribution around the source *F*(*r*,*θ*) were obtained from the accurate calculations of Taylor *et al*[10,11]. Accounting for the spatial distribution of activity within the source, the geometry factor $G(r,\theta)$ was calculated for a line source of length 0.18 mm according to TG-43 protocol. The coordinate (r_o,θ_o) refers to the reference point located 1 cm away from the center of the source on its transverse axis.

The dependence of the absorbed dose on phantom size has been studied comprehensively[38-41]. Both Daskalov *et al* and Taylor *et al* model an effectively infinite phantom size. The finite and much smaller size of our water tank requires a small correction to the TG-43 calculated absorbed dose. The water tank used in this work can best be approximated as a 20 cm tall cylinder of radius=15 cm. Poon *et al*[41] and Anagnostopoulos *et al*[38] discuss analytical techniques of correcting for the finite phantom size. Using Poon's technique, based on GEANT4 Monte Carlo simulation of a 15 cm radius cylinder with a source positioned at the centre, we find that at a $d_{\text{src-det}}$=55 mm, the radial dose function is 0.35 % lower than the dose calculated in an infinite phantom. All TG-43 calculated dose rates in this work have been adjusted to reflect the finite phantom size used in the experiment. Finally, the TG-43 calculated final dose results around the ^{192}Ir source were found to agree to within uncertainty with those of an EGSnrc simulation that we performed of our setup.

7.2.4 Water Calorimetry

In water calorimetry, the dose rate to water is not only measured directly in water, but is also measured absolutely because unlike the other detectors (chambers or films), a water calorimeter does not need to be calibrated against other primary radiation standards. Details about our water calorimeter absorbed dose standard for HDR ^{192}Ir can be found in Sarfehnia *et al*[20,21], however, a brief summary of methodology is provided below.

The dose to water measurement is performed based on the assumption that all energy absorbed appears as a temperature rise in the irradiated medium. The dose rate $\dot{D}_{\text{w}}$ is related to the rate of temperature rise in water $\Delta\dot{T}$ through the specific heat capacity of water at constant pressure $c_{\text{w,p}}$ by,

$$\dot{D}_{\text{w}}(\vec{r}) = c_{\text{w,p}} \cdot \Delta\dot{T}(\vec{r}) \cdot \prod_i k_i \,, \tag{7.7}$$

where the k_i refer to various correction factors that account for such effects as heat transfer (due to conduction and convection effects in water), heat defect (due to chemical reactions in water in presence of impurities), and dose distribution perturbation (due to the presence of non-water materials in the water phantom).

We operated a stagnant 4 °C water calorimeter to measure the absorbed dose to water in ^{192}Ir brachytherapy. The water calorimeter consists of a water tank with a sophisticated system of water cooling and temperature control. Moreover, because at 4 °C water has its highest density and its coefficient of volumetric expansion is effectively zero, the operation of the calorimeter at this temperature minimizes the effects of convection.

To make a measurement, the hot ^{192}Ir source is brought inside the water calorimeter (through a Nucletron 4 French nylon-12 catheter) into a fixed pre-measured position from the temperature detectors. In this work, two thermistor beads were used as point detectors to measure sub milli-Kelvin temperature rises from the source. The source is then removed from the calorimeter, and the accumulated temperature rise at the detector point is converted to absorbed dose using Eq. 7.7, following the calculation of all relevant correction factors.

The heat transfer correction is the largest correction factor in water calorimetry. It is defined as the ideal temperature rise (in the absence of heat transfer) to real temperature rise (in the presence of heat transfer); thus, it corrects for the effects of convection and conduction on the temperature distribution inside the water phantom. The COMSOL MULTIPHYSICS^{TM} software is a general purpose software program which uses the finite element method (FEM) to solve a system of partial differential equations inside a modeled geometry. By coupling the ‘conduction and convection’ module and the ‘Navier Stokes incompressible fluids’ module, the software was used in this work to numerically solve the heat transport problem (both conduction and convection) inside a 2D axially symmetric geometrical model of our calorimeter setup.

7.3 RESULTS AND DISCUSSION

7.3.1 Uncertainty Analysis

All uncertainties discussed in this work correspond to 1-sigma standard deviation around the mean. An uncertainty budget analysis for the chamber measurements is provided in Table 7.1. The uncertainty on each factor has been noted in terms of its contribution to the final uncertainty on the measured dose. $N_{D,\mathrm{w}}(^{60}\mathrm{Co})$ refers to the uncertainty on the initial ^{60}Co calibration factor provided by the standard laboratory. The uncertainties on all calculated corrections are clearly indicated. A measurement reproducibility of 0.31 % was achieved. The uncertainty on 'dummy/real source' refers to the almost negligible 0.0007 % uncertainty introduced into dose measurement due to potentially minor misalignment of the dummy simulator source (during positioning measurements) and the hot active source (during irradiation). It is obvious, as is indeed expected, that the largest source of uncertainty on the final dose measurements is the uncertainty on the source-detector positioning. We achieved a maximum uncertainty in $d_{\mathrm{src\text{-}det}}$ positioning of better than 0.3 mm which at a nominal measurement $d_{\mathrm{src\text{-}det}}$ of 51 mm translates to a 1.2 % uncertainty on dose. A 0.25 % uncertainty was introduced into the final results due to the renormalization of the dose from the respective $d_{\mathrm{src\text{-}det}}$ at the time of the measurement to a $d_{\mathrm{src\text{-}det}}$=55 mm for comparison purposes. It must be noted that this uncertainty is due to a normalization which is made for the purposes of comparison only. Hence, the total uncertainty of the dose measurement with the Farmer chamber in this work is actually 1.44 %.

Uncertainty Description	Type A	Type B
$N_{D,w}(^{60}Co)$ Calibration		0.7
$\left[D_{gas}/D_{w}\right]_{MC}^{^{60}Co}$	0.1	
$\left[D_{w}/D_{gas}\right]_{MC}^{^{192}Ir}$	0.09	
$P_{ion}P_{pol}P_{elec}P_{TP}$		0.17
Measurement Reproducibility	0.31	
$d_{src\text{-}det}$		1.2
Dummy/real source		0.00
$d_{src\text{-}det}$ Normalization		0.25
Overall Uncertainty on Dose	**1.46**	

Table 7.1: Uncertainty budget analysis for the A1SL Exradin mini-Shonka farmer chamber measurements made in water in ^{192}Ir brachytherapy beam.

Description	Type A	Type B
Linac Output Meas. (TG51)		
$N_{D,w}$		0.7
k_Q		1.0
Setup		0.7
Other ($P_{T,p}$, P_{pol},…)		0.4
Calibration Curve Determination / Film Meas.		
Chamber cross-calib.		0.3
6 MV Calib. curve fit		0.7
$\left(D_{film}/D_{w}\right)_{MC}^{6\text{ MV}}\left(D_{w}/D_{film}\right)_{MC}^{^{192}Ir}$	0.1	
Meas. Reproducibility	0.62	
Positioning		
$d_{src\text{-}det}$		0.22
Dummy/real source		0.00
$d_{src\text{-}det}$ Normalization		0.25
Overall Uncertainty on dose (1-sigma)	**1.80**	

Table 7.2: Uncertainty budget analysis for EBT-1 Gafchromic film measurements made in water in ^{192}Ir brachytherapy beam.

Table 7.2 shows the uncertainty budget analysis in film dosimetry. The first portion of the table is concerned with the actual uncertainty in using the TG-51 protocol[28] on the 6 MV linac to establish the machine output in terms of delivered dose per monitor unit. The chamber cross-calibration corresponds to the uncertainty of the external chamber that was used during calibration of the Gafchromic films. The uncertainties from other sources have also been considered, including a 0.7 % uncertainty on the fit made to the film calibration curve obtained at 6 MV. A 0.62 % standard error on the mean (for all measurements combined) was obtained. Once again, the 0.25 % uncertainty due to $d_{\text{src-det}}$ normalization is not inherent to the protocol used for EBT film measurements in water for ^{192}Ir, but rather is only added in for the purposes of comparison with other techniques.

Unfortunately, a comprehensive uncertainty analysis for the TG-43 calculated results cannot be provided in this work due to a lack of an uncertainty budget discussion for the ^{192}Ir sources in the TG-43 report or its update. However, the largest source of uncertainty in TG-43 dose measurement results is not due to any of the calculated factors, but rather due to S_K measurement. A 1-sigma 1.2-1.5 % uncertainty on the well-type chamber's calibration factor (from the ADCL) as well as a 1.5-3 % uncertainty on the S_K measurement are the largest contributors to the total dose uncertainty. Although all absorbed dose values reported in this work have been normalized to S_K, we include the uncertainty of the S_K measurement with the TG-43 results. This is reasonable as the normalization was only employed as a means to facilitate comparison. A total uncertainty of 2.5 % on TG-43 dose measurement results was used in this work. This overall uncertainty excludes the uncertainties associated with the various TG-43 functions including radial dose function and geometry factor because these uncertainties are not well-known.

The uncertainty budget of the water calorimeter is discussed in detail in Sarfehnia *et al*[21]. Briefly it consists of a 0.82 % combined uncertainty on the k_i

correction factors, a 0.43 % reproducibility on the measurements, and a 0.85 % uncertainty due to positioning uncertainties. A 1.5 % uncertainty was associated with the non-linear predrift correction technique of the calorimetric runs developed for this work. The overall uncertainty on dose determination using a water calorimeter amounts to 1.90 %.

7.3.2 Absorbed Dose Comparison

Figure 7.4 shows the average dose rate to water results for the different sets of measurements performed for one of the four microSelectron HDR ^{192}Ir brachytherapy sources used in this work. Table 7.3 summarizes the results of this work. All dose rates have been normalized to source S_K at the time of measurement, and scaled from their respective $d_{\text{src-det}}$ to correspond to a $d_{\text{src-det}}$ =55 mm. As explained above, the uncertainty in the S_K measurement is included in the TG-43 calculation. All results have been compared to the water calorimetry standard and the percentage differences are noted in the second row of the table. All measurements agree with one another well to within uncertainty. Moreover, all results were within 0.83 % of absolute absorbed dose to water measurements from water calorimetry primary standard.

One of the largest sources of uncertainty with most detectors can be attributed to the uncertainty in positioning. Although the use of a rigid metal catheter (instead of a nylon catheter) would improve the $d_{\text{src-det}}$ measurement, in our setup we used the Nucletron's nylon-12 catheter to minimize the differences between the measurement conditions and the clinical treatment conditions. Russell *et al*[42] describe a 0.5-1.0 % drop in the radial dose profile per emitted radiant energy for a stainless steel catheter compared to a similar nylon catheter (no significant change was observed between nylon and water catheters). Through the experimental setup procedures described in this work, we achieved a positioning accuracy of 0.13-0.40 mm in both transverse and longitudinal directions. This was based on the reproducibility of positioning measurements that were made with the travelling microscope prior and post-irradiation.

As the source-to-detector separation is increased, the effect of positioning uncertainty on the dose becomes smaller. However, because the dose rate drops significantly with distance, the $d_{\text{src-det}}$ cannot be increased indefinitely. Long irradiation times are necessary at large $d_{\text{src-det}}$ to achieve acceptable signal to noise ratios. In turn, this results in a more significant contribution of leakage charge (in case of chambers), significant background noise and significant non-linear drifts (in case of water calorimeters), and issues with water absorption by the film (in case of Gafchromic films). These factors diminish the accuracy of the results. Consequently, all measurements in this work were made in a $d_{\text{src-det}}$ range of 40 to 55 mm.

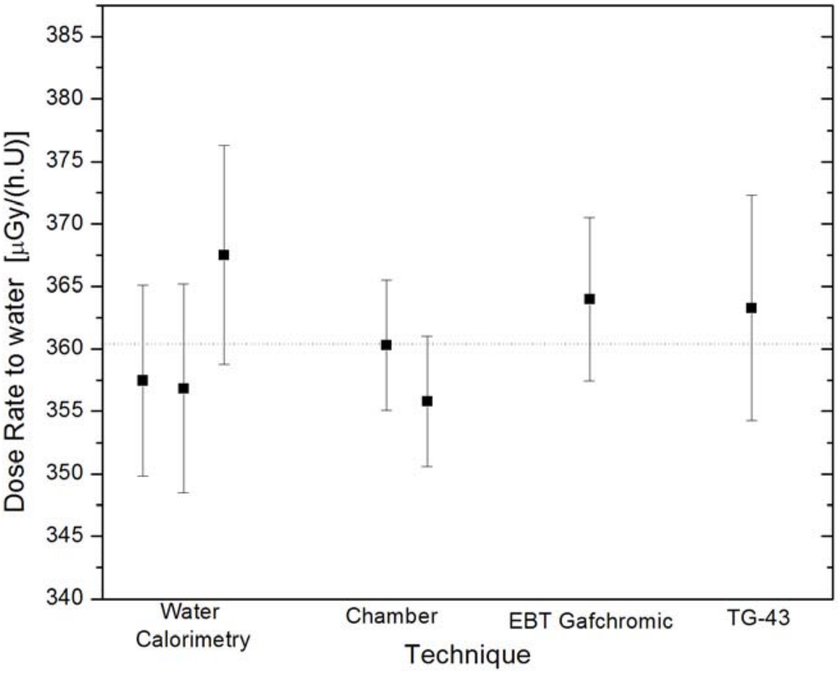

Figure 7.4: The average absorbed dose rates of different sets of measurements performed on one of the four microSelectron ^{192}Ir sources used in this experiment. The measurements on this source were performed for a nominal source S_K ranging between 31400 and 36700 U (i.e., 7.7-9.0 Ci). All results have been normalized to reflect the dose rate at $d_{\text{src-det}}$=55 mm.

	Calorimetry standard	Chamber reference	Gafchromic reference	TG-43 protocol
Dose rate [μGy/(h.U)]	361 ± 7	358 ± 5	364 ± 7	363 ± 9
% diff from calorimetry	…	-0.83 %	0.83 %	0.55 %

Table 7.3: A comparison of the chamber and Gafchromic reference HDR ^{192}Ir brachytherapy dosimetry with that of TG-43 protocol and water calorimetry primary standard. All dose rate measurements are normalized to a source-to-detector separation of 55 mm. Uncertainties shown correspond to 1-sigma standard deviation around the mean.

Although this work focuses on the measurement of absorbed dose to water, one could use the measured dose rate and the traceable air kerma rate to calculate the dose rate constant Λ. When we do this, using a combination of all the experimental data from various dose measurement techniques, a value of 1.10±0.03 cGy h^{-1} U^{-1} is obtained. The same Λ is obtained when basing the estimate on water calorimetry alone. This experimentally-calculated Λ provides some validation for the current calculated values of Λ. The 1-sigma uncertainty on the experimental Λ result is relatively large because it includes both the uncertainty on absorbed dose measurement as well as the uncertainty on S_K measurement. With improvements in absorbed dose to water measurement as well as more direct S_K measurements in the context of a standards lab, the uncertainty on Λ could potentially be drastically reduced. However, in the future, one could envisage a brachytherapy source calibration based directly on absorbed dose to water without the need for a source air-kerma strength determination.

7.4 CONCLUSIONS

In an associated paper[20,21], we established the water calorimeter as a primary absorbed dose standard for ^{192}Ir HDR sources. In the present paper we compared dose measurements using the water calorimeter with two other independent techniques, i.e., high precision EBT-1 Gafchromic film dosimetry and ionization chamber dosimetry with NIST-traceable absorbed dose calibration at ^{60}Co. Monte Carlo calculations were performed to derive the energy dependence of the film and ionization chamber. The uncertainty budgets of the different dose measurement techniques were assessed. Based on the dosimetry protocols devised and used in this work, we achieved an overall 1-sgima dose measurement uncertainty of 1.90 %, 1.44 %, 1.78 %, and 2.50 % for water calorimetry, ionization chamber, Gafchromic film, and TG-43 dosimetry, respectively. Our results show that TG-43 based absorbed dose determination starting from a calibrated well-type chamber is in agreement with the water calorimeter results to within 0.55 %, while it agrees with the direct dose measurements based on Gafchromic film and ionization chamber to better than 0.28 % and 1.38 %, respectively.

To first order, this work allows a more realistic uncertainty estimate for absorbed dose to water determination using the TG-43 protocol. However, there is significant added value in calibrating sources directly in terms of absorbed dose to water since compared to the well chamber source calibration where the chamber calibration coefficient is sensitive to the details of source geometry that affect spectrum[45], the sensitivity of a direct dose to water calibration to source construction details is minimal. Amongst the various steps in implementing a program based on absorbed dose calibration for ^{192}Ir, the primary standard and its validation is the first step. In this context, this work paves the way towards the establishment of a more direct absolute dose to water standard in HDR ^{192}Ir brachytherapy.

ACKNOWLEDGMENTS

We are grateful to Dr. S. Devic for help and expertise in radiochromic film dosimetry and Dr. E. Poon for discussions and help on Monte Carlo source simulations. This work has been supported in part by grant RGPIN 298181 of the Natural Sciences and Engineering Research Council. A. S. is a recipient of a CIHR doctoral Fellowship.

7.5 REFERENCES

[1] R. Nath, L. L. Anderson, G. Luxton, K. A. Weaver, J. F. Williamson, and A. S. Meigooni, "Dosimetry of interstitial brachytherapy sources: recommendations of the AAPM Radiation Therapy Committee Task Group No. 43. American Association of Physicists in Medicine," Med Phys 22, 209-234 (1995).

[2] M. J. Rivard, B. M. Coursey, L. A. DeWerd, W. F. Hanson, M. S. Huq, G. S. Ibbott, M. G. Mitch, R. Nath, and J. F. Williamson, "Update of AAPM Task Group No. 43 Report: A revised AAPM protocol for brachytherapy dose calculations," Med. Phys. 31, 633-674 (2004).

[3] S. J. Goetsch, F. H. Attix, D. W. Pearson, and B. R. Thomadsen, "Calibration of 192Ir high-dose-rate afterloading systems," Med Phys 18, 462-467 (1991).

[4] E. Mainegra-Hing and D. W. Rogers, "On the accuracy of techniques for obtaining the calibration coefficient N(K) of ^{192}Ir HDR brachytherapy sources," Med Phys 33, 3340-3347 (2006).

[5] E. van Dijk, I. K. Kolkman-Deurloo, and P. M. Damen, "Determination of the reference air kerma rate for 192Ir brachytherapy sources and the related uncertainty," Med Phys 31, 2826-2833 (2004).

[6] D. R. Olsen and J. Hellesnes, "Absorbed dose distribution measurements in brachytherapy using ferrous sulphate gel and magnetic resonance imaging," Br J Radiol 67, 1121-1126 (1994).

[7] L. J. Schreiner, I. Crooks, M. D. Evans, B. M. Keller, and W. A. Parker, "Imaging of HDR brachytherapy dose distributions using NMR Fricke-gelatin dosimetry," Magn Reson Imaging 12, 901-907 (1994).

[8] P. Karaiskos, A. Angelopoulos, L. Sakelliou, P. Sandilos, C. Antypas, L. Vlachos, and E. Koutsouveli, "Monte Carlo and TLD dosimetry of an 192Ir high dose-rate brachytherapy source," Med Phys 25, 1975-1984 (1998).

[9] A. Kirov, J. F. Williamson, A. S. Meigooni, and Y. Zhu, "TLD, diode and Monte Carlo dosimetry of an 192Ir source for high dose-rate brachytherapy," Phys Med Biol 40, 2015-2036 (1995).

[10] G. M. Daskalov, E. Loffler, and J. F. Williamson, "Monte Carlo-aided dosimetry of a new high dose-rate brachytherapy source," Med. Phys. 25, 2200-2208 (1998).

[11] R. E. Taylor and D. W. Rogers, "EGSnrc Monte Carlo calculated dosimetry parameters for 192Ir and 169Yb brachytherapy sources," Med Phys 35, 4933-4944 (2008).

[12] R. E. Taylor and D. W. Rogers, "An EGSnrc Monte Carlo-calculated database of TG-43 parameters," Med Phys 35, 4228-4241 (2008).

[13] N. Reynaert, M. Van Eijkeren, Y. Taeymans, and H. Thierens, "Dosimetry of 192Ir sources used for endovascular brachytherapy," Phys Med Biol 46, 499-516 (2001).

[14] N. Reynaert, F. Verhaegen, and H. Thierens, "In-water calibration of PDR 192Ir brachytherapy sources with an NE2571 ionization chamber," Phys Med Biol 43, 2095-2107 (1998).

[15] S. T. Chiu-Tsao, T. L. Duckworth, N. S. Patel, J. Pisch, and L. B. Harrison, "Verification of Ir-192 near source dosimetry using GAFCHROMIC film," Med Phys 31, 201-207 (2004).

[16] S. D. Sharma, C. Bianchi, L. Conte, R. Novario, and B. C. Bhatt, "Radiochromic film measurement of anisotropy function for high-dose-rate Ir-192 brachytherapy source," Phys Med Biol 49, 4065-4072 (2004).

[17] "Calibration of photon and beta ray sources used in brachytherapy," IAEA-TDCDOC-1274 (2002).

[18] J. Borg, I. Kawrakow, D. W. Rogers, and J. P. Seuntjens, "Monte Carlo study of correction factors for Spencer-Attix cavity theory at photon energies at or above 100 keV," Med Phys 27, 1804-1813 (2000).

[19] C. Austerlitz, H. C. Mota, J. Sempau, S. M. Benhabib, D. Campos, R. Allison, C. E. DeAlmeida, D. Zhu, and C. H. Sibata, "Determination of absorbed dose in water at the reference point d(r0, theta0) for an ^{192}Ir HDR brachytherapy source using a Fricke system," Med Phys 35, 5360-5365 (2008).

[20] A. Sarfehnia, K. Stewart, and J. Seuntjens, "An absorbed dose to water standard for HDR 192Ir brachytherapy sources based on water calorimetry: numerical and experimental proof-of-principle," Med Phys 34, 4957-4961 (2007).

[21] A. Sarfehnia and J. Seuntjens, "Development of a water calorimetry-based standard for absorbed dose to water in HDR ^{192}Ir brachytherapy," Submitted to Medical Physics (accepted for publication), 2010.

[22] I. Kawrakow, "Accurate condensed history Monte Carlo simulation of electron transport. I. EGSnrc, the new EGS4 version," Med Phys 27, 485-498 (2000).

[23] I. Kawrakow and D. W. Rogers, "The EGSnrc Code System: Monte Carlo Simulation of Electron and Photon Transport," NRC Reports, PIRS-701 (2006).

[24] J. Wulff, K. Zink, and I. Kawrakow, "Efficiency improvements for ion chamber calculations in high energy photon beams," Med Phys 35, 1328-1336 (2008).

[25] I. Kawrakow, "EGSnrc C++ class library," NRCC Report PIRS-898, Ottawa, Canada (2005).

[26] G. M. Mora, A. Maio, and D. W. Rogers, "Monte Carlo simulation of a typical ^{60}Co therapy source," Med Phys 26, 2494-2502 (1999).

[27] J. M. Paul, R. F. Koch, and P. C. Philip, "AAPM Task Group 21 protocol: dosimetric evaluation," Med Phys 12, 424-430 (1985).

[28] P. R. Almond, P. J. Biggs, B. M. Coursey, W. F. Hanson, M. S. Huq, R. Nath, and D. W. Rogers, "AAPM's TG-51 protocol for clinical reference dosimetry of high-energy photon and electron beams," Med Phys 26, 1847-1870 (1999).

[29] IAEA INTERNATIONAL ATOMIC ENERGY AGENCY, "Absorbed dose determination in external beam radiotherapy: An international code of practice for dosimetry based on standards of absorbed dose to water," Technical Report Serie no. 398, IAEA, Vienna (2000).

[30] C. M. Ma and A. E. Nahum, "Bragg-Gray theory and ion chamber dosimetry for photon beams," Phys Med Biol 36, 413-428 (1991).

[31] C. M. Ma, C. W. Coffey, L. A. DeWerd, C. Liu, R. Nath, S. M. Seltzer, and J. P. Seuntjens, "AAPM protocol for 40-300 kV x-ray beam dosimetry in radiotherapy and radiobiology," Med Phys 28, 868-893 (2001).

[32] S. Devic, J. Seuntjens, E. Sham, E. B. Podgorsak, C. R. Schmidtlein, A. S. Kirov, and C. G. Soares, "Precise radiochromic film dosimetry using a flat-bed document scanner," Med Phys 32, 2245-2253 (2005).

[33] M. Martisikova, B. Ackermann, and O. Jakel, "Analysis of uncertainties in Gafchromic EBT film dosimetry of photon beams," Phys Med Biol 53, 7013-7027 (2008).

[34] A. Rink, I. A. Vitkin, and D. A. Jaffray, "Energy dependence (75 kVp to 18 MV) of radiochromic films assessed using a real-time optical dosimeter," Med Phys 34, 458-463 (2007).

[35] M. J. Butson, T. Cheung, and P. K. Yu, "Weak energy dependence of EBT Gafchromic film dose response in the 50 kVp-10 MVp X-ray range," Appl Radiat Isot 64, 60-62 (2006).

[36] S. T. Chiu-Tsao, Y. Ho, R. Shankar, L. Wang, and L. B. Harrison, "Energy dependence of response of new high sensitivity radiochromic films for megavoltage and kilovoltage radiation energies," Med Phys 32, 3350-3354 (2005).

[37] S. D. Oves, K. R. Hogstrom, K. Ham, E. Sajo, and J. P. Dugas, "Dosimetry intercomparison using a 35-keV X-ray synchrotron beam," Eur J Radiol 68, S121-125 (2008).

[38] D. W. Rogers, I. Kawrakow, J. P. Seuntjens, B. R. B. Walters, and E. Mainegra-Hing, "NRC User Codes for EGSnrc," NRC Report PIRS-702 (2003).

[39] D. W. Rogers and I. Kawrakow, "Monte Carlo calculated correction factors for primary standards of air kerma," Med Phys 30, 521-532 (2003).

[40] G. Anagnostopoulos, D. Baltas, P. Karaiskos, E. Pantelis, P. Papagiannis, and L. Sakelliou, "An analytical dosimetry model as a step towards accounting for inhomogeneities and bounded geometries in 192Ir brachytherapy treatment planning," Phys Med Biol 48, 1625-1647 (2003).

[41] D. Granero, J. Perez-Calatayud, M. C. Pujades-Claumarchirant, F. Ballester, C. S. Melhus, and M. J. Rivard, "Equivalent phantom sizes and shapes for brachytherapy dosimetric studies of 192Ir and 137Cs," Med Phys 35, 4872-4877 (2008).

[42] J. Perez-Calatayud, D. Granero, and F. Ballester, "Phantom size in brachytherapy source dosimetric studies," Med Phys 31, 2075-2081 (2004).

[43] E Poon and F. Verhaegen, "Development of a scatter correction technique and its application to HDR ^{192}Ir multicatheter breast brachytherapy," Med Phys 36, 3703-3713 (2009).

[44] K. R. Russell and A. Ahnesjo, "Dose calculation in brachytherapy for a 192Ir source using a primary and scatter dose separation technique," Phys Med Biol 41, 1007-1024 (1996).

[45] M. J. Rivard, D. Granero, J. Perez-Calatayud, and F. Ballester, "Influence of photon energy spectra from brachytherapy sources on kerma and dose rates in water and air," Med Phys 37, 869-876 (2010).

Chapter 8

Direct water calorimetric absorbed dose determination in scanning proton therapy

In this chapter, the numerical and experimental feasibility study of developing a water-calorimeter based protocol in scanning proton therapy is presented. The results of this work include dose measurements performed directly in water using both water calorimetry and a thimble-type ionization chamber following the IAEA TRS-398 protocol. The dose is measured in both double scattering as well as scanning proton beams. To validate the calorimeter, the absolute dose to water in double scattering proton therapy as measured by the calorimeter is compared against TRS-398 results. This work forms the foundation for a future absorbed dose to water standard in proton therapy in general, and in scanning proton delivery in particular.

Authors: Arman Sarfehnia[1], Benjamin Clasie[2], Eunah Chung[1], Hsio-Ming Lu[2], Jacob Flanz[2], Martijn Engelsmen[2], Joe McCormack[2], Ethan Cascio[2], Harald Paganetti[2], and Jan Seuntjens[1]

[1] Medical Physics Unit, McGill University, Montreal General Hospital, Montréal, Québec, Canada
[2] Massachussets General Hospital and Harvard Medical School, Boston, Massachusetts, US
Medical Physics ***37*** *(6), 2010*

ABSTRACT

Purpose: The aim of this manuscript is to describe the direct measurement of absolute absorbed dose to water in a scanned proton radiotherapy beam using a water calorimeter primary standard.

Methods: The McGill water calorimeter, which has been validated in photon and electron beams as well as in HDR ^{192}Ir brachytherapy, was used to measure the absorbed dose to water in double scattering and scanning proton irradiations. The measurements were made at the Massachusetts General Hospital proton radiotherapy facility. The correction factors in water calorimetry were numerically calculated and various parameters affecting their magnitude and uncertainty were studied. The absorbed dose to water was compared to that obtained using an Exradin T1 Chamber based on the IAEA TRS-398 protocol.

Results: The overall 1-sigma uncertainty on absorbed dose to water amounts to 0.4 % and 0.6 % in scattered and scanned proton water calorimetry, respectively. This compares to an overall uncertainty of 1.9 % for currently accepted IAEA TRS-398 reference absorbed dose measurement protocol. The absorbed dose from water calorimetry agrees with the results from TRS-398 well to within 1-sigma uncertainty.

Conclusions: This work demonstrates that a primary absorbed dose standard based on water calorimetry is feasible in scattered and scanned proton beams.

8.1 INTRODUCTION

Double scattering and pencil beam scanning are two techniques for delivering conformal dose distributions with proton beams[1-3]. In the former case, the proton pencil beam is spread out using scattering foils while it is also modulated in depth using a physical device such as a rotating range-modulator wheel. In pencil beam scanning, an unmodified proton beam is magnetically steered to paint the dose from Bragg peaks at a given transverse position. Different depths can be painted such that their superposition produces the overall dose distribution. A change in depth can be achieved by changing the proton energy, by applying range shifter plates, or a combination of both.

Currently, a standard for absorbed dose measurement in proton beams is non-existent. Different proton therapy centers rely on different recommended protocols for their absorbed dose calibration purposes. These include the older ICRU report 59[4] as well as the upcoming ICRU report 78 which recommends the IAEA TRS-398 protocol[5] for absorbed dose to water measurements. The difference in calibration between the different reports is chamber dependent and is less than 2 %.

The IAEA TRS-398 code of practice[5] was used in this work. This protocol is based on an indirect measurement of dose with an ionization chamber calibrated in standard ^{60}Co radiation. A chamber-specific, beam-quality dependent correction factor k_{Q,Q_o} is used to convert the results from the reference beam quality (Q_o) used to calibrate the chamber, to the proton beam quality used during measurement (Q).

A direct measurement of absolute absorbed dose to water D_w can avoid the large unnecessary uncertainties introduced into the overall dose results from defining and calculating the beam quality index and the subsequent k_{Q,Q_o} factor estimation (1σ=1.7 %). Moreover, as the TRS-398 report only addresses the double scattering proton beam delivery technique, it is yet unclear if the procedures recommended and values calculated by the protocol for k_{Q,Q_o} determination are applicable or appropriate for use in scanning delivery. A direct and absolute measurement of D_w not only allows for the establishment of a primary standard in scanning proton delivery and a potentially substantial reduction of the overall dose uncertainty, but it also allows for a direct measurement of dose in more complicated fields (delivered with pencil beam scanning) than laterally uniform spread out Bragg-peaks (SOBP).

The most direct means of measuring absolute absorbed dose to water is water calorimetry. Since the radiation energy absorbed in a material manifests itself in the form of a temperature rise, in water calorimetry, absolute D_w is measured directly in water from its fundamental definition. Published data on the use of water calorimetry in scattered beam delivery exist[6-9]. Moreover, Sassowsky and Pedroni[10] have published a numerical feasibility study determining the effect of heat transfer and heat defect in water calorimetry in proton beam scanning.

In this work, the McGill water calorimeter, which has been previously used and its results validated in high energy photon and electron beams as well as in HDR ^{192}Ir brachytherapy, was used to measure the absolute D_w in scattered and scanned proton radiation. The results are compared with those obtained from TRS-398 ionization chamber dosimetry. In addition to a numerical study of the heat transport problem and parameters affecting it, this work experimentally shows the feasibility of water calorimetry in spot scanning delivery and its potential as a primary standard.

8.2 METHODS

8.2.1 Water Calorimeter

Figure 8.1 shows a schematic diagram of the McGill in-house built Domen-type 4 °C stagnant water calorimeter. It consists of a 30×30×20 cm^3 Lucite water tank surrounded by two 5 cm Styrofoam slabs that are separated by a 5 mm copper plate. The copper shroud surrounds the calorimeter from all sides except for a 12 cm square opening on the top lid of the calorimeter. This opening window is covered only with a 0.15 mm brass foil attached to the copper shielding with conductive silver-based glue, and permits a vertically directed radiation beam to enter the calorimeter (Fig. 8.1) without excessive perturbation. Two PT-100 RTD temperature probes are used to monitor the average water temperature inside the tank while a third is used to measure the copper shroud temperature.

The copper shroud is actively temperature-controlled in a narrow temperature range of 3.98±0.04 °C via a Neslab RTE-7 refrigerated bath/circulator. Moreover, a heat exchanger placed inside the water tank and in direct contact with water is used to rapidly modify the water temperature when necessary during preparation of the calorimeter. A magnetically coupled stirrer is used to mix the water inside the phantom and remove any existing temperature gradients. Since at 3.98 °C, water density is highest and the coefficient of volumetric expansion is zero, by operating the water calorimeter in a narrow band around this temperature, convection is minimized (see *Section 8.2.4)*.

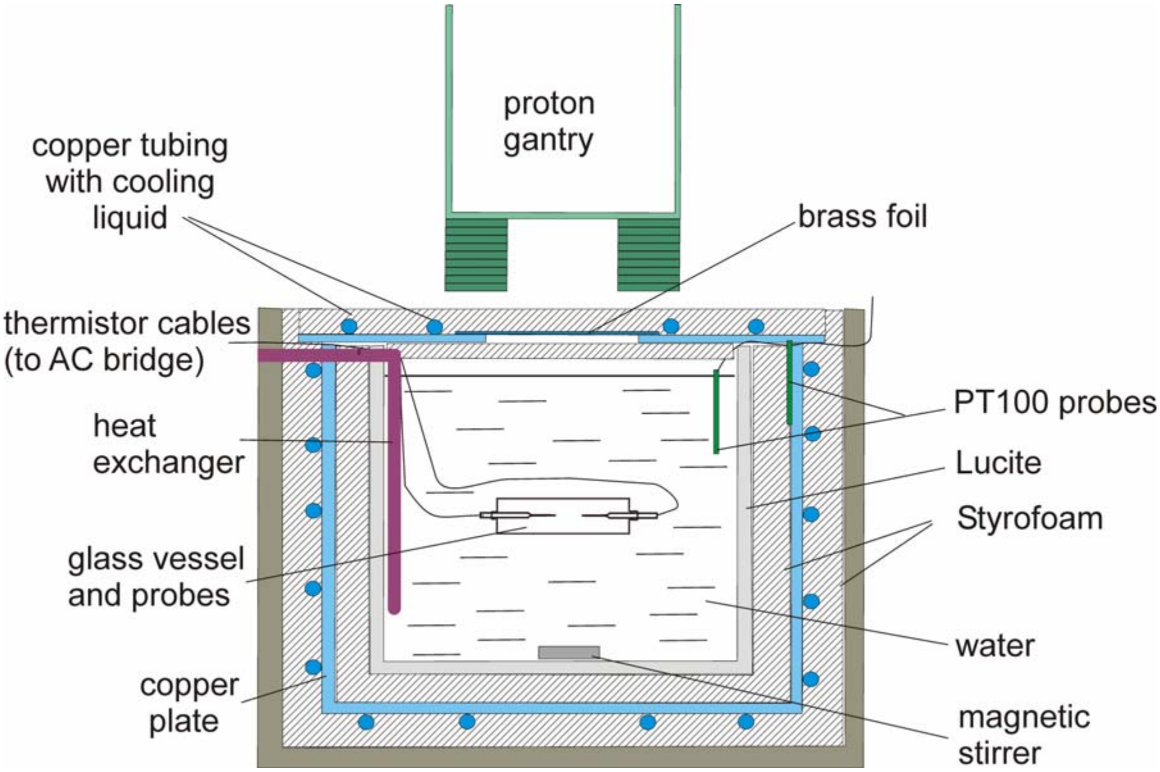

Figure 8.1: A schematic diagram of the McGill in-house built Domen-type (transportable) water calorimeter positioned below a proton gantry.

A plane-parallel calorimeter vessel made of Pyrex was used in this work and is shown in the inset of Fig. 8.2. The vessel has an outer diameter of 79 mm with a side glass thickness of 1.96 mm. The front and back windows of the vessel are 1.12 mm thick and are separated by 22.66 mm. Two cone-shaped glass pipettes are placed inside the vessel and are positioned perpendicular to the vessel’s cylindrical axis, such that their tip is nominally 2 mm on either side of the central axis, and 1 cm below the top glass window of the vessel. Each pipette contains a thermistor bead (0.25 mm in diameter) at the very tip. With a nominal resistance of 10 kΩ at 4 °C, the thermistors act as point temperature detectors in this work.

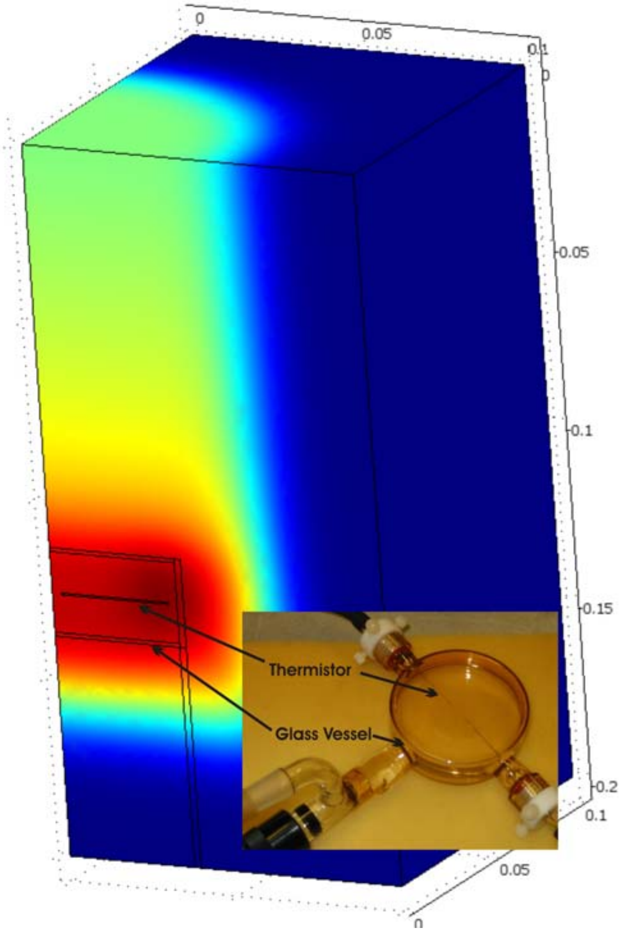

Figure 8.2: The COMSOL MULTIPHYSICS temperature distribution results inside a geometrical model of our setup. Only one quarter of the entire geometry has been modelled due to symmetry. A picture of the parallel plate vessel (with two thermistors positioned inside) is also included.

All measurements were performed at the Massachusetts General Hospital's Francis H. Burr Proton Therapy Center (FBPTC)[11]. The facility uses an isochronous cyclotron (IBA), which produces a proton beam with fixed kinetic energy of 235 MeV and variable beam currents up to 300 nA. Proton beams with kinetic energies smaller than 235 MeV are produced by passing the beam through a graphite degrader of adjustable thickness at the exit of the cyclotron. The beam can be transported to one of two gantry rooms, with rotating beam lines, or three fixed beam lines (for eye treatments, stereotactic radiosurgery or research). The water calorimeter was positioned under a vertically oriented proton beam in the Gantry 2 treatment room. The nozzle contains user-selectable beam modification and steering devices and is capable of both scattering and scanning proton delivery. The modification devices that were employed in this work include a fixed first scatterer consisting of lead and plastic foils followed by a rotating range modulator wheel, variable collimating jaws, a shaped Lexan and lead second scatterer, and a brass aperture. A transmission parallel-plate ionization chamber after the variable collimating jaws measures the integrated charge produced in the chamber during irradiations. The stability of the monitor chamber, determined through repeated measurements with the calorimeter, is discussed in *Section 8.3.2*.

8.2.2 Delivery Plan

At FBPTC the range of an SOBP is defined as the 90% dose position in the distal fall-off R_{90}, while the modulation width is defined as the 98 % proximal and 90 % distal dose fall-off $M_{98\text{-}90}$. In double scattering, a proton beam was used to produce a spread out Bragg peak (SOBP) of R_{90}=175 mm, $M_{98\text{-}90}$=146 mm (Fig. 8.3). The detectors were positioned at a water-equivalent depth of 126.10 mm (residual range R_{res}=5.48 g cm^{-2}). The dose variation over a depth range of ± 1 cm around the thermistor position was measured to be less than 0.4 %. The TRS-398 protocol recommends the reference point of measurement to be taken at the middle of the SOBP curve. Although we have deviated slightly from that recommendation, our results should not be affected as our reference depth is still taken to be in the flat portion of the SOBP.

The scanning plan was designed using an in-house built Matlab tool[12]. The lateral field size was 12 × 12 cm^2 with uniform distribution of spot weights within the energy layers. Nominal proton energies between 128-151 MeV were used to build an SOBP. The thermistor detectors were positioned at a water equivalent depth of 131.15 mm (R_{res}=3.75 g cm^{-2}), which was measured to result in less than 0.2 % dose variation vs. depth. The individual weighted Bragg peak depth dose curves as well as the final summed dose distribution are shown in Fig. 8.3. The calculated depth dose results shown in Fig. 8.3 were verified experimentally with a Markus chamber following TRS-398 formalism.

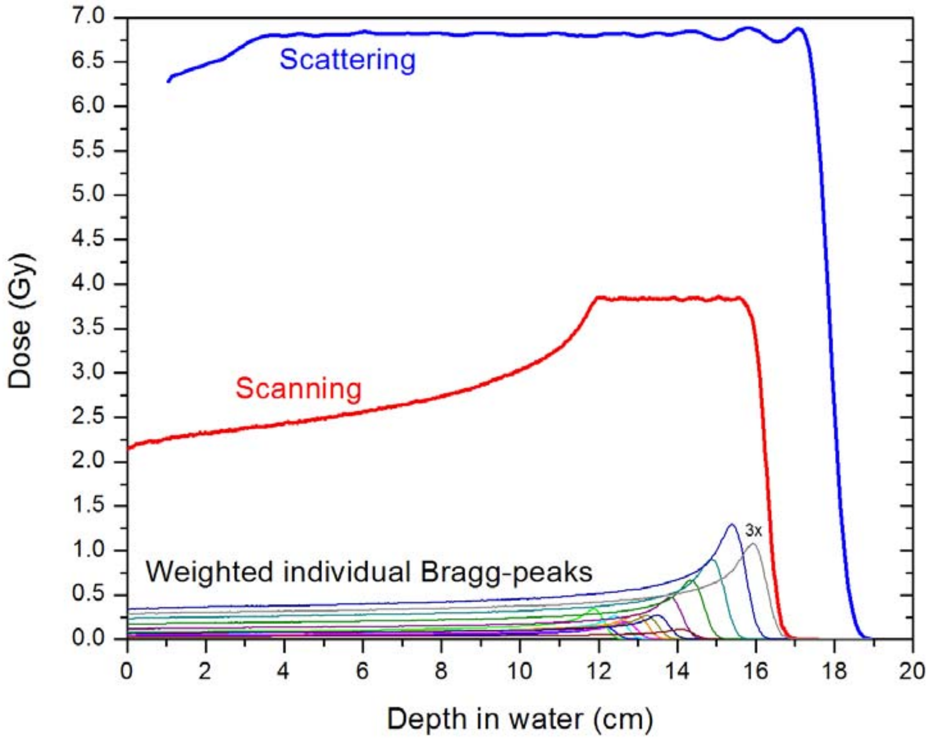

Figure 8.3: SOBP curves used in experimental measurements in both active and passive beam shaping. In scanning, the individual weighted Bragg peak depth dose curves for a 15 layers plan (plan B) are also shown. The distal energy layer was repainted three time to increase total delivered dose.

In the case of scanning, two delivery plans were generated. The first plan contained 13 energy layers and was designed so as to minimize dose variation and ripple effects near the thermistors The second plan was the same as the first except that the distal layer was repainted 2 additional times (each painting with 1/3 the weight needed for the SOBP) giving a total of 15 energy layers in the irradiation. We refer to the original 13 energy-layer plan as '*plan A*', while we will refer to 15 energy-layer plan as '*plan B.*' The additional repainting of the distal layer became necessary due to an artificial upper limit on the number of MU per layer. With *plan B*, by delivering the distal layer three times, a higher dose was delivered without significantly affecting the shape of the SOBP; hence, *plan B* was used in the experimental portion of this project. *Plan A* was only used for some of the additional numerical studies that were performed in this work and these results will be presented in *Section 8.3*. It took each layer nominally 16 s to be painted, while it took roughly 6 s for the machine to change between energy layers. The latter value has since been significantly reduced.

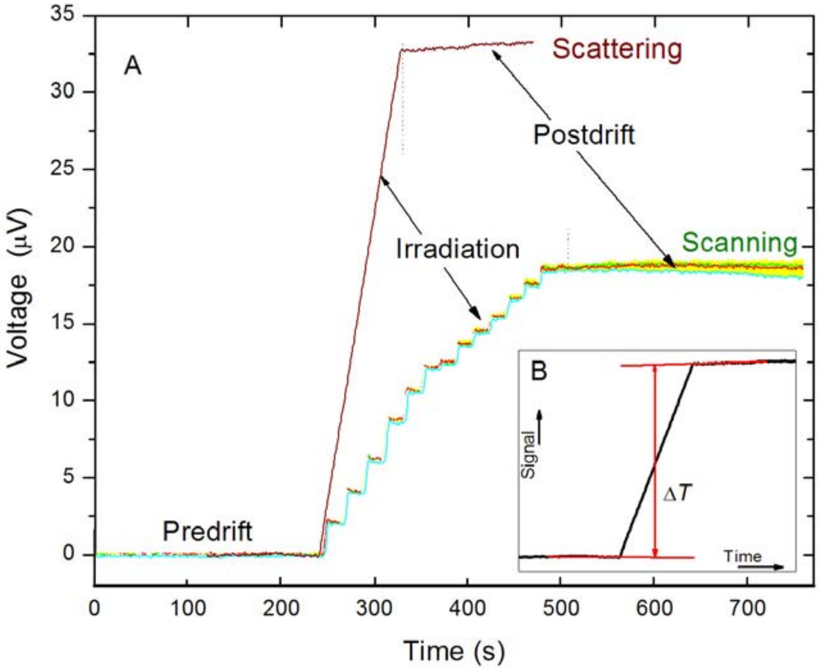

Figure 8.4: Experimental runs in scattered and scanned proton radiation water calorimetry. As shown, a heat drift curve is composed of a predrift, irradiation period, and postdrift. The highlight in scanning shows 1σ range of the measurements. Inset shows the measurement of ΔT for a temperature drift curve using the extrapolation to the midrun technique.

In all cases, care was taken to design and select plans that were optimally uniform (low dose gradients, and small dose vs. depth variations) especially around the point of measurement. Not only does this minimize many of the correction factors in water calorimetry (discussed in *Section 8.2.3*), but it also reduces the overall uncertainty on the measured dose by reducing positioning uncertainties and dose volume averaging effect (in case of ionization chamber measurements).

8.2.3 Dose Calculation

In water calorimetry, the absorbed dose to water D_{w} at a point $\vec{r}$ is determined by[13]

$$D_{\mathrm{w}}(\vec{r}) = c_{\mathrm{w,p}} \cdot \triangle T(\vec{r}) \cdot k_{\mathrm{dd}} \cdot k_{\rho} \cdot k_{\mathrm{p}} \cdot k_{\mathrm{hd}} \cdot k_{\mathrm{ht}}\,, \tag{8.1}$$

where $c_{\mathrm{w,p}}$ is the specific heat capacity of water at constant pressure, and ΔT is the temperature rise at the measurement point $\vec{r}$. Figure 8.4 shows typical drift-corrected water calorimetric runs in both scattered and scanned proton delivery techniques. The measurements are made in units of microvolt out-of-balance voltage of an active bridge circuit which is directly proportional to temperature. A calorimetric run (or a temperature drift curve) is composed of three distinct regions: 1. a predrift (pre-irradiation) where the temperature drift in the absence of irradiation is measured; 2. An irradiation period; 3. a postdrift (post-irradiation) where the drift following the irradiation is measured. The drift present in the latter region is a result of heat transfer initiated by a build-up of temperature non-uniformities inside the water calorimeter. ΔT is measured as the difference between linear extrapolations of predrift and postdrift at the mid-run (see inset of Fig. 8.4).

As shown in Eq. 8.1, there are five correction factors k_{i} that account for the non-ideal experimental conditions:

k_{dd} is the dose profile correction factor. Using the lateral dose profile information, it corrects for the differences in dose measured at the thermistor position versus the dose at the reference position (midway between the two thermistors, on the central axis of the dose distribution). As indicated in our uncertainty budget (see *Section 8.3.2*), this correction is negligible in both scattered and scanned beam shaping techniques as the lateral dose profile around the central axis is flat within a few millimetres radius.

k_ρ accounts for the temperature-dependent water density difference between the calorimeter operation temperature (nominal 4 °C) and the temperature at which measurements with other detectors are made (22 °C). Since a density change directly translates to a slight variation in the measurement depth, k_ρ is determined as the ratio of the dose at equivalent depths corresponding to 4 °C and 22 °C on the SOBP. Due to the minimal variation in dose vs. depth within the SOBP, k_ρ was found to be less than 0.05 %.

k_p is the perturbation correction factor which predominantly corrects for the effects of the glass vessel on the dose distribution. We analytically calculate this effect as a simple shift in the entire depth dose distribution past the vessel glass window. The shift is equal to the difference between the water equivalent thickness and the actual thickness of the glass. A water equivalent thickness of a material in proton beams can be approximated by (as suggested by TRS-398[5] in the context of plastic phantom correction)

$$z_{\mathrm{w}} = z_{\mathrm{gl}}\left(\frac{\rho_{\mathrm{gl}}}{\rho_{\mathrm{w}}}\right)\left(\frac{R_{\mathrm{w}}}{R_{\mathrm{gl}}}\right), \qquad (8.2)$$

where z_{gl} is the thickness of glass measured in units of distance (mm), $\left(\rho_{\mathrm{gl}}/\rho_{\mathrm{w}}\right)$ is the ratio of glass to water densities (for the Pyrex glass used in this work, it equals 2.23), and $\left(R_{\mathrm{w}}/R_{\mathrm{gl}}\right)$ is the ratio of the continuous slowing down approximation (CSDA) range of protons in water to glass. Although the CSDA range is a function of proton energy, the $\left(R_{\mathrm{w}}/R_{\mathrm{gl}}\right)$ ratio is relatively constant over the clinical proton energies of interest and was found to be 0.8265. Similarly to previous corrections, due to the flat SOBP curve and uniform dose distribution around the detectors (in both scattered and scanned delivery), k_{p} was found to be less than 0.1 %.

$\boldsymbol{k}_{\mathbf{hd}}$ or the heat defect correction factor accounts for potential heat loss or gain from endothermic or exothermic chemical reactions that may occur in water as a result of impurities and unknown dissolved gases. In water calorimetry, to minimize the heat defect and control water purity, the thermistors are embedded inside a glass vessel that is filled with high purity water (organic content < 3 ppb) and is saturated with a known gas. Hydrogen (H_2) or nitrogen (N_2) saturated systems are commonly used, and the heat defect of such systems have been well studied[10,14] (although majority of the work in this area concentrates on low LET radiation). Sassowsky and Pedroni[10] have numerically determined a zero heat defect for H_2-saturated systems for LET values up to 25 eV nm^{-1} (with H_2 concentrations as low as 1 μmol l^{-1}).

In this work, we have used an H_2-saturated system. An interesting property of such a system is that independent of impurity concentrations, heat defect theoretically tends to zero once all traces of oxygen (O_2) have been removed from the system[15]. However, in the presence of small initial O_2 concentrations, the system shows a large, transient exothermic behaviour[16-18]. The heat defect has been observed to reach 10 % or higher at the peak exothermicity prior to complete depletion of all contaminating oxygen and the system attaining zero heat defect[17].

Figure 8.5 shows a graph of the measured dose rate (dose normalized to total delivered monitor units MU) as a function of accumulated delivered dose for the H_2-saturated system used in this work. Since the measurements for scattered and scanned deliveries were performed on different weekends, the initial large exothermic peak was observed in both instances. Due to equipment transport issues, there was an 11 hours delay from the time we prepared the vessel (cleaning, bubbling, and pre-irradiation), to the time of its insertion into the calorimeter. As such, the accumulated delivered dose indicated in Fig. 8.5 in scattered beam shaping is in addition to roughly 200 Gy of dose that was delivered to the vessel during its preparation. Although the vessel was kept inside a cooled calorimeter in between the measurement weekends, the large initial exothermic peak was observed even during the scanning delivery (on a subsequent weekend) most likely as a result of trace oxygen leakage into the vessel. This behaviour and its consequences on calorimeter response was also observed by Palmans *et al*[7]. Since all caloric runs obtained prior to the large exothermic peak (i.e., in the presence of non-zero heat defect) were excluded from the final dose analysis, k_{hd} was taken to be unity (1.000±0.003).

$\boldsymbol{k}_{\mathbf{ht}}$, the heat transfer correction factor, is one of the most significant correction factors in water calorimetry in general and in our experiments in particular. This factor, which corrects for the effects of conduction and convection, as well as its dependence on various setup-specific parameters will be discussed in detail in *Section 8.2.4*.

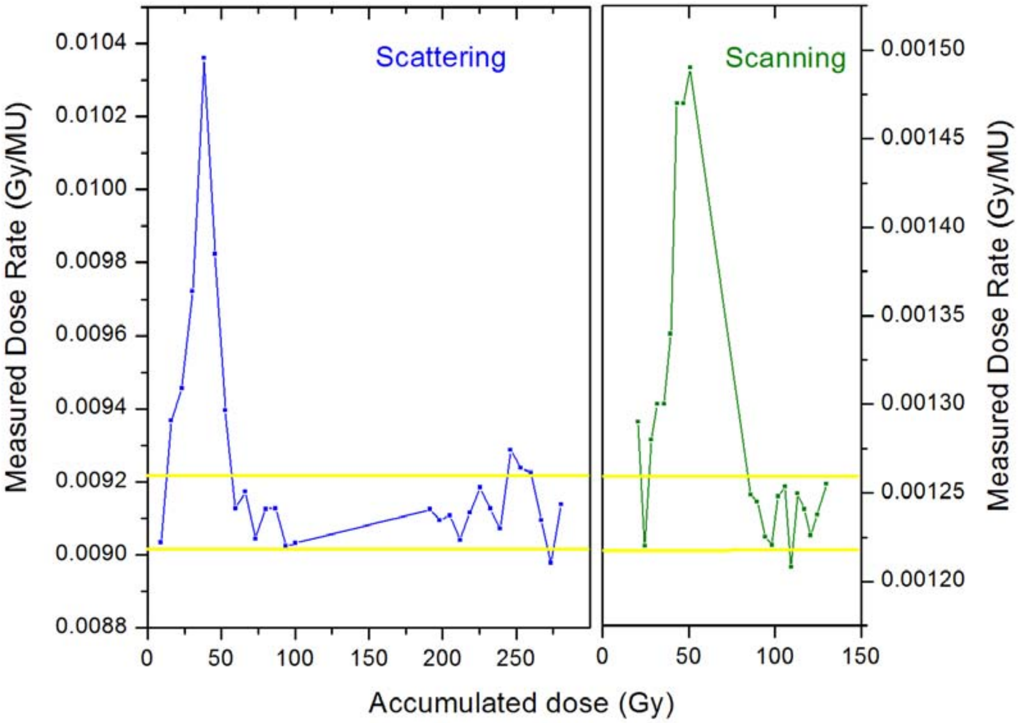

Figure 8.5: The exothermic behaviour of our H_2-saturated system as a function of accumulated dose. A heat defect of slightly larger than 10 % was observed in both double scattering and scanning measurements (performed on different weekends) prior to having the system attain a stable zero heat defect. The accumulated dose noted in scattered beam delivery is in addition to 200 Gy of dose delivered during vessel preparation.

8.2.4 Heat Transport

Heat transfer correction factor k_{ht} is defined as the ratio of the ideal temperature rise (a temperature rise solely due to locally deposited absorbed dose in the absence of heat transfer) to the actual temperature rise (with the effects of heat transfer taken into account) at a given point. Although the ideal temperature rise can be calculated analytically from dose rate information at the measurement point, the actual temperature rise in the presence of heat transfer is normally estimated using software programs that numerically solve the heat transport partial differential equations. In water calorimetry, since the radiative effects are negligible for temperature gradients of interest, conduction and convection are the only modes of heat transfer to be considered.

Conduction and Convection

Although always present, the conduction of heat through water occurs at a very slow rate because of water's low thermal diffusivity; this is what makes water calorimetry feasible. In addition to conduction, convection may also occur if the temperature gradients formed in water as a result of radiation are large. Convection is said to take place when the Rayleigh number of water exceeds a value[16] of 1000. The Rayleigh number is directly proportional to the thermal expansion coefficient of the material, and is also a function of the temperature gradient relative to the distance of mechanical barriers.

The effects of convection were ignored in both scattered and scanned proton radiation water calorimetry[16,17] because, similar to external high energy photon and electron beams, the Rayleigh number of water inside the calorimeter phantom remains small in proton beams for three reasons: 1. By operating the calorimeter in a narrow temperature band around 3.98 °C, we make sure that the volumetric thermal expansion coefficient α for water remains very close to zero ($\alpha_{\mathrm{H_2O}}(T = 3.98\ ^{\circ}\mathrm{C}) = 0$); 2. The temperature gradients formed in water as a result of proton radiation (using either scattering or scanning techniques) are small for the onset of major convective effects; 3. The glass calorimeter vessel acts as a convective barrier which dramatically reduces the effects of convective flow inside the vessel and close to the thermistors.

Geometrical Considerations

The heat transport in the calorimeter was modeled using the COMSOL MULTIPHYSICS™ (Version 3.5) software. This software calculates the time dependence of the temperature distribution in the calorimeter by solving the heat transport partial differential equation using the time and position dependent heat source pattern presented to the software. Sources of heat are the dose distribution delivered to the calorimeter and the thermistor power dissipation.

Figure 8.2 shows a 3D geometrical model of our setup used in this work. Exploiting the symmetry in our geometry, only one quarter of the full geometry was modelled. A 2D axial symmetric model of the geometry was also used in this work only to simulate the full raster-type scanning. Since a model made in a 2D cylindrical geometry has far fewer degrees of freedom than a 3D model, for identical simulations it was found to be significantly less CPU-intensive. Although in the 2D cylindrical geometry, the thermistors could not be modelled, the results of the 2D and 3D models agreed to within uncertainty. A fine mesh setting with increased density around the field edges, glass vessel, and thermistors was used. The simulations follow the exact time sequence as used in the experiments. A relative and absolute solver tolerance level of 1×10^{-10} K and 1×10^{-11} K was used, respectively.

A correction function for heat transfer is calculated as a ratio of temperature rise (at the point of measurement) in the absence of heat loss to the temperature rise with heat loss present. A single correction factor to an entire run (or set of runs using the same irradiation times) is calculated by extrapolating the post irradiation drift of the correction function to mid-run and comparing that result with unity (similar approach to that shown in the inset of Fig 8.4).

The thermistor power dissipation was found to be small enough that it could be ignored without influencing the final temperature distribution results. The measured SOBP (for scattered delivery), and individual weighted Bragg peaks (for scanned delivery) were put into the software as discrete functions describing the dose distribution in pure water. The perturbation of the dose distribution as a result of non-water materials, as well as the dose inside them needs to be considered. Equation 1 was used to describe the magnitude of the shift in the dose distribution downstream from a given non-water material. This equation was used to account for the perturbative effects of brass foil and Styrofoam in the calorimeter lid, as well as the glass window of the vessel in the water phantom (for coordinates below the window).

To calculate the dose inside the glass wall, the dose conversion technique at equivalent depth in two different materials in proton beams as described by Palmans *et al*[17,19,20] was used. Through their method, the total dose deposited in the medium from proton radiation is calculated by adding its two contributing factors, namely the dose deposited through electromagnetic interactions with electrons (and nuclei) D_{EM}, and the dose deposited by secondary heavy charged particles resulting from non-elastic nuclear interactions D_{NN}. While D_{EM} is converted between two different materials using the ratio of restricted stopping powers, D_{NN} is converted between two different media with a ratio of a factor which is a function of both the average energy and Monte Carlo-calculated production cross-section of the secondary heavy charged particles.

Since the largest portion of energy deposited in material is due to electromagnetic interactions, as a good approximation in this work, we treat D_{NN} as a correction to D_{EM}. Using the work of Palmas and Verhaegen (2005)[20], an approximate proton energy–dependent scaling factor was evaluated to account for the effects of D_{NN}. Described in terms of a percentage of the proton CSDA range, the scaling factor was found to be up to 4-5 % at either extreme, while it crossed unity at around 60% CSDA range. Although such large differences cannot be ignored if the calculation of the exact dose to non-water materials was the primary objective, the effects of this dose difference on the final k_{ht} calculations are small (~0.1 %). Although included in all our COMSOL simulations, we surmise that for larger diameter cylindrical calorimeter vessels, this difference can probably be ignored without loss of accuracy.

8.2.5 Ionization Chamber Reference Dosimetry

Water calorimetry-based measurements of absolute dose (in both scattered and scanned beam shaping) were compared with reference dosimetry performed with an Exradin T1 miniature-Shonka thimble-type ionization chamber. To ensure that the water calorimetry and chamber dosimetry measurement conditions were as similar as possible, all chamber measurements were performed inside the water calorimeter. To that end, the vessel was removed, and the waterproof T1 chamber was positioned inside the calorimeter such that its center was at the same water equivalent depth as the thermistors during water calorimetry measurements.

The IAEA TRS-398[5] protocol was followed. According to the protocol, given a chamber with a calibration factor obtained under reference conditions Q_o (N_{D,w,Q_o}), the dose to water in a proton beam of quality Q ($D_{\mathrm{w},Q}$) can be measured by

$$D_{\mathrm{w,Q}} = (M^{raw} k_{\mathrm{T,P}} k_{\mathrm{elec}} k_{\mathrm{pol}} k_{\mathrm{s}}) N_{D,\mathrm{w,Q_o}} k_{\mathrm{Q,Q_o}}, \qquad (8.3)$$

where $k_{\mathrm{Q,Q_o}}$ is a beam-quality, ion chamber-dependent conversion factor. TRS-398 provides a table of $k_{\mathrm{Q,Q_o}}$ at reference ^{60}Co calibrations for various chambers and values of beam quality index, defined in terms of the characteristics of the measured SOBP (for simplicity, when ^{60}Co is the reference beam, the conversion factors are denoted as k_{Q}). For the T1 chamber, k_{Q} was determined to be 1.006 for both our scattered and scanned proton SOBP delivery plans. The TRS-398 protocol discusses reference dosimetry for scattered proton radiation; however, its techniques for beam quality specification, $(W/e)_{\mathrm{air}}$, and stopping power ratios (which determine k_{Q} values) have not been directly validated using calorimetry in scanned beams. However, since the calculated k_{Q} are generally close to unity and relatively energy-independent for the T1 chamber, we assumed that the procedure described by the TRS-398 protocol is valid for the uniform dose distribution delivered using spot scanning.

As shown in Eq. 8.3, the raw chamber reading is corrected for the influences of temperature and pressure $k_{\mathrm{T,P}}$, electrometer calibration k_{elec}, polarity k_{pol}, and ion recombination k_{s}. The first three correction factors are defined similarly as those found in the AAPM TG-51[21], with $k_{\mathrm{T,P}}$ being the largest correction factor at 0.5 %. Although the TRS-398 recommends a pulsed beam criterion for k_{s} calculation, Palmans *et al*[22] have shown that the use of a continuous beam formulation for k_{s} calculation may be more appropriate in high dose-rate proton deliveries with proton beams that are cyclotron-generated at high pulse rates. In order to be consistent with the TRS-398 protocol, however, we have selected to use the two-voltage (300 V and 150 V) pulsed beam formulation of ion recombination. Using this technique, k_{s} was determined to be 0.31 % and 0.48 % in scattering and scanning beams, respectively. A continuous beam criterion would yield to roughly a 0.1 % ion recombination correction factor for both beam delivery techniques (see *Section 8.3.3*).

8.3 RESULTS AND DISCUSSION

8.3.1 Effects of Heat Loss by Conduction

For the measurements performed in the scattered beam, k_{ht} was calculated to be -0.4 %. A sub-percent correction was expected because the uniform SOBP covering the entire vessel results in a quasi uniform temperature distribution, in turn minimizing the conductive effects. In scattered beam delivery, k_{ht} was found to be insensitive to dose rate (1.6-4.3 Gy/min), and positioning uncertainties of a few millimetres around the nominal thermistor position resulted in negligible differences in the calculated k_{ht}.

In scanning delivery, Sassowsky and Pedroni[10] have shown the small dependence of k_{ht} on the details of the spot scanning as long as the timescales of interest are longer than the timescale of individual spot delivery. They argue that for the long time dependence, only the heat flow parallel to the beam direction is relevant, the entire plane can assumed to be painted at once in the time interval that it takes in reality for the central spot to be deposited[10] (without any significant loss of accuracy).

We verified that the transverse heat flow (in the direction of the beam axis) is much more dominant than lateral heat flow (perpendicular to the beam axis) for the longer timescales. Although the individual spot scanning was not modelled in this work, we verified that k_{ht} was not significantly altered when comparing three different models that delivered identical dose volume distribution (*plan A*) in slightly different ways: (1) A smooth raster-type scanning (as opposed to spot scanning); (2) A model in which dose at individual planes are delivered at once in the time it normally takes for a single spot to be painted (as suggested by Sassowsky and Pedroni[10]); (3) Same as model (2), except that the dose rate is reduced such that the time it takes to deliver the same accumulated dose in a single plane reflects the experimental irradiation time more accurately.

For a given delivery plan, the shape of the postdrift was numerically found to be quasi-independent of the details of the scanning including the irradiation time for individual planar dose delivery, the time to change between energy layers, or even the details of the spot delivery. Figure 8.6 (A) shows a comparison between two COMSOL models delivering identical dose distribution in 85 seconds and 216 seconds (i.e., delivering *plan A*, with time delay between energy layers of 6 s and 17 s, respectively). Temperature drift curves in the presence and absence of conduction have been simulated and are shown. Although the total irradiation time was significantly different, the maximum difference in k_{ht} calculation was only 0.8 % (to calculate k_{ht}, the length of postdrift utilized for fitting and analysis was taken to be equal to the irradiation period). Inset (B) and (C) of Fig. 8.6

compare the four temperature drift curves further by showing the percent difference between the postdrift of the two simulations calculated in the presence of conduction (B), as well as the calculated temperature difference between the 85 s and 216 s drift curves that were simulated in the presence and absence of conduction.

However, this is not to say that k_{ht} calculation is insensitive to the region of postdrift used for linear fitting and extrapolation. Indeed, due to the relatively strong slope of the postdrift in scanned proton radiation, care must be taken to use exactly the same range of postdrift data in both COMSOL calculated drift curves (during k_{ht} calculation) and experimental drift curves (during ΔT determination).

The largest effect on k_{ht} is from the strong influence of the front and back glass windows of the vessel on the shape of the heat drift curve, and consequently on the value of k_{ht}. Indeed, as seen in Tables 8.1 and 8.2, the magnitude of k_{ht} sharply deviates from unity with increasing vessel glass thickness. The COMSOL calculations are performed for '*plan B*' using a simplified geometrical model of the setup. Tables 8.1 and 8.2 are meant to also demonstrate the strong dependence of the magnitude of k_{ht} on the selected region of postdrift utilized for analysis (and extrapolation). Using the same set of calculated drift curves, Table 8.1 uses 50 s to 150 s following the end of irradiation for analysis, while Table 8.2 uses 220 s to 440 s following the end of irradiation for analysis. Since the extent of postdrift used for analysis is normally taken to be equal to the length of the irradiation period, the results in Table 8.1 correspond to k_{ht} values obtained for runs with short irradiation periods (~100 s), while the results in Table 8.2 correspond approximately to k_{ht} values obtained for runs with much longer irradiation periods (~200 s).

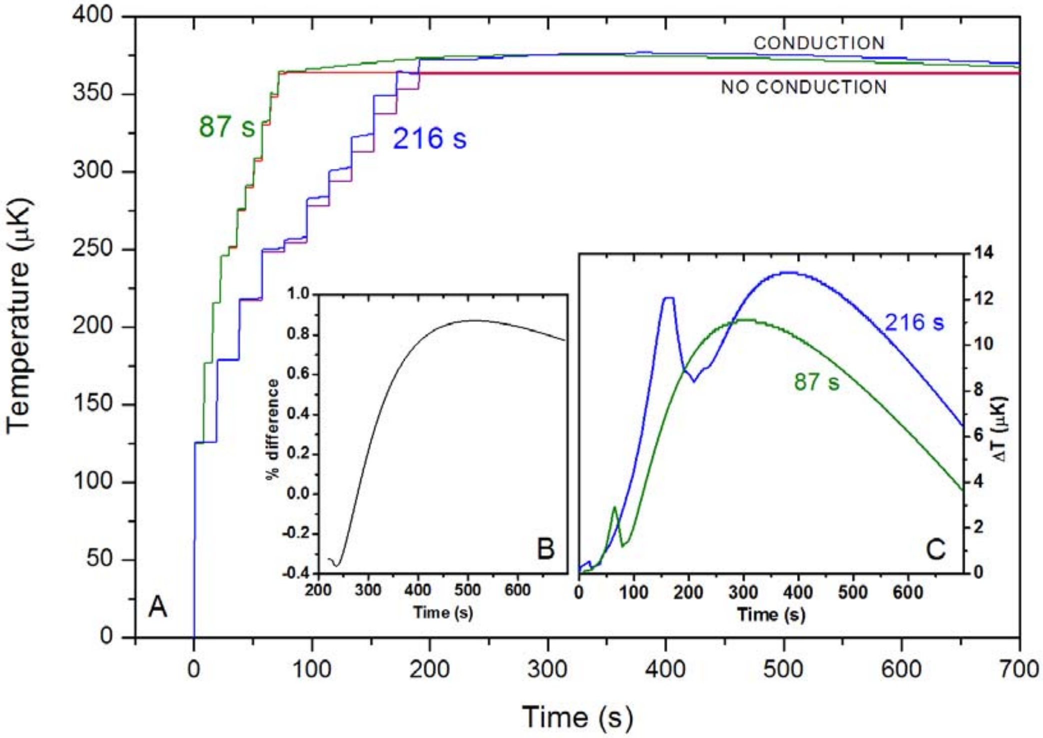

Figure 8.6: The COMSOL-calculated contribution of dose to the temperature rise at the detectors for *plan A* (A). The same dose distribution has been delivered in 85 s and 216 s (by adjusting the simulated delay time to change between energy layers). The % difference between the respective postdrift (conduction only) of the two models is shown in inset (B). The temperature difference between the conduction and no-conduction simulations for both models are compared in inset (C).

In this work, based on our parallel plate vessel and measurement setup, we calculated k_{ht} to be -4.7 % in scanning (*plan B*). From the results of Tables 8.1 and 8.2, two conclusions can be made towards minimizing k_{ht} in scanned proton radiation water calorimetry: 1. The very large heat gain at the thermistors from the vessel glass windows positioned only a centimetre away from the detectors (for our parallel-plate vessel) can be significantly reduced by using vessel designs that have been used in megavoltage photon beam calorimetry (e.g., reviewed in Seuntjens and Duane, 2009) which have large-diameter, thin glass walls and are irradiated radially rather than from end. 2. By minimizing the irradiation time through increasing the dose rate and/or reducing the time to change energy layers, k_{ht} can be minimized.

Since the overall uncertainty on the dose in scanned proton water calorimetry is dominated by the uncertainty on k_{ht}, a minimization of the magnitude of k_{ht} significantly reduces the overall absorbed dose uncertainty. Sassowsky and Pedroni[10] did not observe a large k_{ht} since their calculations were performed in the absence of a calorimeter vessel.

		Simulated vessel back window thickness (mm)		
		0	**0.56**	**1.12**
Simulated vessel front window thickness (mm)	**0**	0.9973	0.9934	0.9874
	0.56	0.9951	0.9897	0.9896
	1.12	0.9964	0.9897	0.9893

Table 8.1: k_{ht} calculated for *plan B* (probe positioned at a water depth of 127.1 mm). 50 s to 150 s of postdrift used for linear fitting and analysis.

		Simulated vessel back window thickness (mm)		
		0	**0.56**	**1.12**
Simulated vessel front window thickness (mm)	**0**	0.9951	0.9795	0.9622
	0.56	0.9809	0.9682	0.9576
	1.12	0.9705	0.9621	0.9506

Table 8.2: k_{ht} calculated for *plan B* (probe positioned at a water depth of 127.1 mm). 220 s to 440 s of postdrift used for linear fitting and analysis.

8.3.2 Uncertainty Budget

Table 8.3 shows all sources of uncertainty in scattered and scanned proton beam water calorimetry. All values correspond to a 1-sigma uncertainty. For all measurements combined, we achieved a reproducibility of 0.18 % and 0.35 % (standard error on the mean) in scattered beam and scanned beam delivery, respectively. The uncertainties on the specific heat capacity of water $c_{w,p}$, absolute temperature measurement of the calorimeter, as well as the resistance-to-voltage and thermistor calibration factors are taken into consideration. The uncertainties in probe (thermistor) positioning with respect to the vessel window, as well as the general positioning of the vessel inside the calorimeter and with respect to the water surface are noted. In scanning, small changes in probe's position can change the shape of the irradiation period of the temperature drift curve substantially by changing the dose contribution from different layers, and to a lesser extent modifying the heat gain from the glass vessel (although the integral dose contribution remains relatively the same).

The uncertainties on all five water calorimetry correction factors are presented in the table. The uncertainties on k_{dd}, k_{ρ}, and k_{p} remain very small due to the extremely flat dose distribution around the thermistors in both scattered and scanned proton radiation deliveries. As a consequence of our analysis procedures, the uncertainty on k_{p}, although also very small, is included with the positioning uncertainty of the chamber measurements. A total uncertainty of 0.10 % and 0.42 % was determined for k_{ht} calculation in scattering and scanning beam shaping, respectively.

A breakdown of all factors contributing to the total uncertainty on k_{ht} is also provided. The largest source of uncertainty for k_{ht} in scanning is referred to as 'Modeling and Analysis.' Although this category does include uncertainties in COMSOL modelling of heat transport (due to meshing, tolerance levels, etc), it mainly is influenced by the uncertainty in the analysis of the calculated drift curves. A large portion of this uncertainty comes from the fact that a generic COMSOL-calculated drift curve that best described the average of all experimental runs was used for the purposes of k_{ht} calculation, while our experiments with scanned proton radiation showed a small range of total irradiation times (due to variations in the accelerator output dose rate, and required time to change energy layers). A small uncertainty has been allocated to dose distribution measurements (both laterally and in-depth), as well as to the assumption of a linear predrift. The uncertainties on the values of various physical parameters used throughout the simulation are also noted. A relatively large 0.1 % uncertainty was assigned to this category in scanned proton radiation, as small uncertainties in glass window thickness of the vessel and its properties can result in large uncertainties on the measured dose. An overall uncertainty of 0.4 % and 0.6 % has been calculated for scattered and scanned proton radiation water calorimetry, respectively.

Table 8.4 shows the overall uncertainty on chamber dose measurements in scattered beam and scanned beam delivery. A measurement reproducibility of 0.16 % and 0.17 % was achieved for scattered beam and scanned beam deliveries, respectively. A 0.7 % uncertainty on the ^{60}Co $N_{D,\text{w}}$ calibration factor (provided by standard labs) and 1.7 % uncertainty on k_{Q} (provided by TRS-398) dominated the overall dose uncertainty. A 0.17 % uncertainty was assigned to the raw chamber measurement correction for various effects listed in Eq. 8.3, while a nominal 0.1 % uncertainty was assigned to chamber positioning. The overall uncertainty on dose measurement in proton radiation based on the TRS-398 protocol (using an Exradin T1 chamber) was 1.9 %.

	Uncertainty (%)	
	Scattered	**Scanned**
reproducibility (1 standard deviation on mean dose)	0.18	0.35
$c_{w,p}$	0.03	0.03
Absolute temperature	0.01	0.01
$(\Delta R/R)/\Delta V$ calibration	0.04	0.04
Thermistor Calibration (β)	0.1	0.1
Positioning		
Probe position wrt vessel	0.03	0.1
Vessel position wrt surface	0.01	0.07
k_{dd}	0.01	0.01
k_{ρ}	0.03	0.05
k_{p}	--	--
k_{hd}	0.3	0.3
k_{ht}		
Modelling / Analysis	0.08	0.4
Depth dose distribution	0.08	0.05
Lateral dose distribution	0.01	0.01
Data (conductivity, vessel info)	0.05	0.1
Non-linearity of predrift	0.01	0.01
Overall 1-sigma Uncertainty (%)	**0.39**	**0.64**

Table 8.3: Uncertainty budget analysis for water calorimetry measurements in double scattering and Scanning proton beams. The reproducibility noted is based on 20 measurements for the scattered and 12 measurements for the scanned beam delivery performed over two weekends.

	Uncertainty (%)	
	Scattered	**Scanned**
Std error on mean (meas.)	0.16	0.17
$N_{D,w}(^{60}\mathrm{Co})$	0.7	0.7
k_{Q,Q_o}	1.7	1.7
$M^{raw} \rightarrow M^{c}$	0.17	0.17
Positioning	0.1	0.13
Overall 1-sigma Uncertainty (%)	**1.86**	**1.86**

Table 8.4: Uncertainty budget analysis for TRS-398 proton dosimetry (using T1 mini-Shonka ionization chamber) in scattering and Scanning proton beams.

8.3.3 Absorbed Dose

Table 8.5 summarizes the measured dosimetry results of this work. In both double scattering and scanning proton delivery techniques, the calorimetry primary standard dose measurement results agreed to well within uncertainty (1-sigma) with the results obtained from TRS-398 protocol.

By increasing the dose rate and the total signal at the detectors, while minimizing the total irradiation time, as well as by simple design changes to the calorimeter, the uncertainty on water calorimetry can be reduced. By refining the measurement techniques, uncertainties of 0.4 % on dose measurement in both scattered and scanned proton water calorimetry are achievable. Through establishing a water calorimeter-based standard in proton radiotherapy, we can substantially reduce the uncertainties with chamber reference dose measurements, as these detectors can be directly calibrated in the appropriate proton beam without a need for k_Q conversion factors. This will be a significant improvement over the currently accepted TRS-398 protocol for proton radiation dose measurements.

	k_{ht}	Calorimetry (Gy/MU)	T1 Chamber (Gy/MU)	% difference
Scattering	0.996	9.100×10^{-3}	9.087×10^{-3}	-0.14 %
Scanning	0.953	1.198×10^{-3}	1.202×10^{-3}	-0.32 %

Table 8.5: The final dose measurement results and comparison between the primary water calorimetry and reference T1 mini-Shonka.

8.4 CONCLUSIONS

The McGill water calorimeter was used to measure the absolute absorbed dose to water in the scattered and scanned proton beams of the Francis H Burr Proton Therapy Centre at MGH in Boston. A parallel plate calorimeter vessel with 1.12 mm front and back glass windows separated by 22.66 mm was used in this work. Using two delivery techniques, the dose in the flat portion of a SOBP dose curve was measured. The delivery plans were optimized so that the dose vs. depth variation around the thermistor position was less than 0.4 %. The dose uniformity around the thermistor position significantly reduces many of the correction factors in water calorimetry as well as in chamber dosimetry, including uncertainties due to positioning and chamber volume averaging effect.

Numerical studies of k_{ht} were performed to better understand the dependence of this correction factor on several parameters including the vessel geometry and total irradiation time. Although k_{ht} was calculated to be 0.996 in scattered proton radiation, it was found to be 0.953 in magnitude in scanned proton water calorimetry, for our parallel plate vessel configuration where the thermistors are relatively close to the glass vessel wall. A large k_{ht} is undesirable as it results in a larger uncertainty on the final dose. By using larger diameter cylindrical photon glass vessels and/or reducing the total irradiation time, this correction factor can be significantly reduced.

We achieved an overall 1-sigma dose uncertainty of 0.4 % and 0.6 % for scattered and scanned proton radiation water calorimetry, respectively. A much larger 1.9 % uncertainty was assigned to reference dose measurements based on the TRS-398 protocol (an Exradin T1 chamber was used). All the measurements (in both scattered and scanned beam shaping) agreed to within uncertainty with one another. This work forms the basis for an improved primary dosimetry standard in proton therapy in general and experimentally proves the feasibility of direct water calorimeter dose measurements in spot scanning beam delivery in particular. Using direct water calorimetric measurement techniques, it is possible to reduce the uncertainties associated with TRS-398 reference dose measurements. Correction factors of air-filled ionization chambers in scanning beam dosimetry can be experimentally verified.

ACKNOWLEDGMENTS

This work has been supported in part by grant RGPIN 298181 of the Natural Sciences and Engineering Research Council of Canada. The assistance of all BPTC technical staff is acknowledged. A. S. is a recipient of a CIHR doctoral Fellowship. The water calorimeter in this work was constructed with the help of Robin Van Gils at McGill, while the thermistors were built and provided by David Marchington of Ionizing Radiation Standards division of National Research Council of Canada.

8.5 REFERENCES

[1] D. E. Bonnett, "Current developments in proton therapy: a review," Phys Med Biol 38, 1371-1392 (1993).

[2] W. T. Chu, B. A. Ludewigt, and T. R. Renner, "Instrumentation for treatment of cancer using proton and light-ion beams," Rev Sci Instrum 64, 2055-2122 (1993).

[3] D. W. Miller, "A review of proton beam radiation therapy," Med Phys 22, 1943-1954 (1995).

[4] L. Verhey, H. Blattman, P. M. DeLuca, and D. Miller, "Clinical proton dosimetry Part I: Beam production, beam delivery and measurement of absorbed dose.," Report 59 of the International Commission on Radiation Units and Measurements (ICRU), Bethesda, MD, 53, 1998.

[5] IAEA TRS-398, "Absorbed dose determination in external beam radiotherapy: An international code of practice for dosimetry based on standards of absorbed dose to water," 23 April 2004.

[6] J. Medin, C. K. Ross, N. V. Klassen, H. Palmans, E. Grusell, and J. E. Grindborg, "Experimental determination of beam quality factors, kQ, for two types of Farmer chamber in a 10 MV photon and a 175 MeV proton beam," Phys Med Biol 51, 1503-1521 (2006).

[7] H. Palmans, J. Seuntjens, F. Verhaegen, J. M. Denis, S. Vynckier, and H. Thierens, "Water calorimetry and ionization chamber dosimetry in an 85-MeV clinical proton beam," Med Phys 23, 643-650 (1996).

[8] R. J. Schulz, L. J. Verhey, M. S. Huq, and N. Venkataramanan, "Water calorimeter dosimetry for 160 MeV protons," Phys Med Biol 37, 947-953 (1992).

[9] J. V. Siebers, S. M. Vatnitsky, D. W. Miller, and M. F. Moyers, "Deduction of the air w value in a therapeutic proton beam," Phys Med Biol 40, 1339-1356 (1995).

[10] M. Sassowsky and E. Pedroni, "On the feasibility of water calorimetry with scanned proton radiation," Phys Med Biol 50, 5381-5400 (2005).

[11] J. Flanz, S. Durlacher, M. Goitein, A. Levine, P. Reardon, and A. Smith, "Overview of the MGH-Northeast Proton Therapy Center plans and progress," NIM-B 99, 830-834 (1995).

[12] H. M. Kooy, B. M. Clasie, H. M. Lu, T. M. Madden, H. Bentefour, N. Depauw, J. A. Adams, A. V. Trofimov, D. Demaret, T. F. Delaney, and J. Flanz, "A case study in proton pencil-beam scanning delivery.," Int J Radiat Oncol Biol Phys (In Print), 2009.

[13] J. Seuntjens and S. Duane, "Photon absorbed dose standards," Metrologia 46, S39-S58 (2009).

[14] N. V. Klassen and C. K. Ross, "Water calorimetry: the heat defect," J Res Natl Inst Stand Technol 102, 63-74 (1997).

[15] J. P. Seuntjens and A. R. DuSautoy, "Review of calorimeter based absorbed dose to water standards," Standards and Codes of Practice in

Medical Radiation Dosimetry (Proc. Int. Symp. Vienna, 2002), IAEA Vienna (2003) IAEA-CN-96/3.

[16] A. Krauss and M. Roos, "Heat conduction, convection and radiolysis of the H_2/O_2 system in the water absorbed dose calorimeter," Thermochimica Acta 310, 53-60 (1998).

[17] H. Palmans, A. Kacperek, and O. Jaekel, "Hadron Dosimetry," in *Clinical Dosimetry Measurements in Radiotherapy*, edited by D. W. O Rogers and J. E. Cygler (Medical Physics Publishing, Madison, Wisconsin, 2009).

[18] H. Palmans and S. Vynckier, "Reference Dosimetry for Clinical Proton Beams," in *Recent Developments in Accurate Radiation Dosimetry*, edited by J. P. Seuntjens and P. N. Mobit (Medical Physics Publishing, Madison, WI, 2002), pp. 157-194.

[19] H. Palmans, J. E. Symons, J. M. Denis, E. A. de Kock, D. T. Jones, and S. Vynckier, "Fluence correction factors in plastic phantoms for clinical proton beams," Phys Med Biol 47, 3055-3071 (2002).

[20] H. Palmans and F. Verhaegen, "Assigning nonelastic nuclear interaction cross sections to Hounsfield units for Monte Carlo treatment planning of proton beams," Phys Med Biol 50, 991-1000 (2005).

[21] P. R. Almond, P. J. Biggs, B. M. Coursey, W. F. Hanson, M. S. Huq, R. Nath, and D. W. Rogers, "AAPM's TG-51 protocol for clinical reference dosimetry of high-energy photon and electron beams," Med Phys 26, 1847-1870 (1999).

Chapter 9

Conclusions

9.1 SUMMARY

The aim of this work has been to evaluate the possibility of establishing a primary standard based on water calorimetry for HDR ^{192}Ir brachytherapy and proton therapy. Currently, an absolute dosimetry standard for both of these modalities is non-existent. Indirect dose measurement protocols are currently used to determine the dose rate to water which is subsequently used in treatment planning to calculate the necessary dose to be delivered to patients for treatment.

Through this work, we have shown the feasibility of measuring the absolute absorbed dose directly in water for both ^{192}Ir brachytherapy and proton therapy. Through a reduction of the total uncertainty on the dose relative to that achieved by current accepted dosimetry protocols, we hope to have improved the quality of care that patients may receive from these treatment modalities in the future. A summary of the final results of this work and the remaining work to be done towards improving and establishing a primary dosimetry standard for both of these modalities at a national and/or international level are discussed in this chapter.

A spring-loaded catheter holder with stainless steel support tubes was built and mounted onto the parallel-plate calorimeter vessel. The holder design as well as the positioning measurement procedures were optimized through this work to achieve a source-detector separation reproducibility of 0.13-0.40 mm over a 6 weeks testing period under both cold water and room temperature air conditions.

COMSOL MULTIPHYSICS^{TM} heat transport software was used to numerically calculate the heat transfer inside the calorimeter. Although normally conduction is the only form of heat transport in 4 °C stagnant water calorimetry to be studied, due to the nature of our experiments, both conductive and convective effects had to be studied. Hence, this work also studies the more challenging convective flow of water inside the calorimeter in presence of medium to large temperature gradients.

Based on COMSOL MULTIPHYSICS numerical calculation results, we have been able not only to predict the behaviour of our calorimeter system, but we have also been able to optimize the various parameters that directly affect the experimental results. Indeed, the dose measurement results of HDR brachytherapy water calorimetry are strongly dependent upon optimization of such parameters as source-to-detector separation and irradiation time. Hence, although we have successfully shown experimental results confirming water calorimeter as a viable instrument for absorbed dose to water measurement in ^{192}Ir brachytherapy, the challenge was to attempt to reduce the uncertainty on the final dose measurements by optimizing the parameters affecting the results of the experiments.

In addition to water calorimetry, we went on to perform reference dosimetry using the most commonly used radiation detectors in medical radiation physics: Ionization chambers and Gafchromic films. Protocols were designed to robustly and accurately measure the dose to water using either detectors. Since we desired to have completely independent measurements from water calorimetric results, either detectors could not be calibrated directly against the water calorimeter. What makes the measurements using the two detectors challenging, therefore, was the current lack of a standard for ^{192}Ir sources and our inability to obtain a calibration factor for our radiation dosimeters directly for the ^{192}Ir beam. All results were furthermore contrasted against those obtained experimentally using indirect measurements of absorbed dose to water using a well-type ion chamber by following the American Association of Physicists in Medicine Task Group 43[1].

We achieved a 1-sigma uncertainty of 1.96 %, 1.44 %, 1.78 %, 2.5 % on our water calorimetry primary standard, ionization chamber, Gafchromic film, and TG-43 absorbed dose to water measurements. All measurements agreed with water calorimetry results well to within uncertainty and to better than 0.83 %.

Development of a standard in proton radiotherapy

In proton therapy, we experimentally showed the feasibility of absorbed dose to water measurements using water calorimetry in active scanning proton beams. The absorbed dose to water measurements in both passive double scattering beam shaping and active spot scanning beam shaping showed results that agreed well to within uncertainty with the absorbed dose to water measurements performed directly in water using an Exradin T1 ionization chamber and following the International Atomic Energy Agency’s TRS-398 recommendations.

All numerical heat transport calculations once again were performed with COMSOL. Although implementation of convection into our simulations was unnecessary, we did simulate the raster type scanning of energy layers. Furthermore, we numerically studied and quantified the magnitude of correction necessary to account for the effects of positioning uncertainties on dose measurement results.

We achieved an uncertainty of 0.4 % and 0.6 % in passive and active proton beam delivery, respectively. This is a considerable improvement over the 1.9 % uncertainty associated with the currently recommended IAEA TRS-398 protocol. As these modern delivery techniques are being developed and moved into clinics for patient treatment, establishing a dosimetry standard is of outmost importance.

This work provides a foundation for development of accurate absolute dosimetry protocols for HDR ^{192}Ir brachytherapy or proton radiotherapy beams based on water calorimetry primary standard. Water calorimetry has not only made the direct and absolute measurement of absorbed dose to water possible, but the uncertainties on our results have improved significantly over the existing recommended protocols used for dosimetry. This work is intended to pave the way for national standard laboratories to develop their own protocols in order to provide absorbed dose to water primary standard services for HDR ^{192}Ir brachytherapy and/or proton radiotherapy beams.

9.2 FUTURE WORK

HDR ^{192}Ir brachytherapy

The manuscript presented in Chapter 6 presented some potential improvements that can be made to the procedures we used in our measurements. In addition to those listed in *Section 6.3.3*, potential future work done towards improving our calorimeter and measurement procedures may include:

1. performance of water calorimetry at a source-to-detector separation of 3-4 cm with short irradiation periods. If indeed a positioning uncertainty of 0.15 mm can be consistently accomplished, then measurements at close source-to-detector separations may allow for large signal to noise ratios that result in superior measurement reproducibility. Our numerical calculations have show that indeed if the source is positioned above the vessel, there will be enough time to complete a full caloric run before the source heat reaches the point of measurement.

2. The insulation around the source can be improved drastically. If active source cooling can be accomplished without drastically perturbing the dose distribution around the source, then sub-percent uncertainties may be achievable.

3. There are numerous design issues with respect to the vessel/holder structure that can be improved. One could envisage a glass calorimeter vessel made specifically for ^{192}Ir brachytherapy water calorimetry which has a narrow slit in the center which allows the source to physically enter in the middle of the thermistors. Moreover, a greater number of thermistors could be used to improve the signal over noise ratio. Figure 9.1 schematically shows a sketch of one such vessel design.

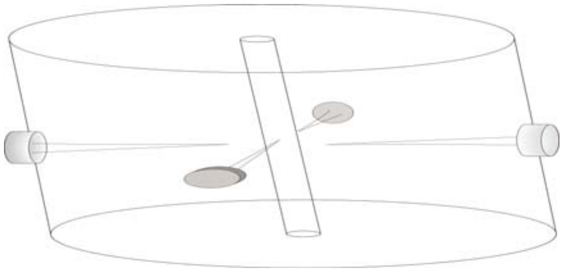

Figure 9.1: A schematic diagram of possible vessel design for ^{192}Ir brachytherapy water calorimetry. The vessel could have a narrow opening that facilitates the source entering into the vessel, with more than two thermistors.

Proton Radiotherapy

As discussed in Chapter 8, active scanning proton water calorimetry can be improved dramatically by using a larger diameter cylindrical vessel. As discussed, the close proximity of the vessel windows to the thermistors resulted in large uncertainties when performing water calorimetry in proton fields. By using larger vessel, the uncertainty in active scanning calorimetry can be reduced further to potentially below 0.4 %.

A further improvement in proton radiotherapy water calorimetry could involve using numerical calculations of the shape of the temperature drift curve as a validation of the exact position of the thermistor beads with respect to the vessel windows and water surface. Since the shape of the irradiation period of the drift curve is significantly dependent upon the position of the thermistor bead (as the contribution of various energy layers to the point of measurement is different at small depth variations), with improvements in numerical modelling of the setup, one could envisage a system where recursive calculations of the temperature drift curve with slightly different thermistor bead positions were compared against the experimental temperature drift curve to determine the exact position of the thermistor beads.

9.3 REFERENCES

[1] R. Nath, L. L. Anderson, G. Luxton, K. A. Weaver, J. F. Williamson, and A. S. Meigooni, "Dosimetry of interstitial brachytherapy sources: recommendations of the AAPM Radiation Therapy Committee Task Group No. 43. American Association of Physicists in Medicine," Med. Phys. 22, 209-234 (1995).

LIST OF ABBREVIATION

2D	Two dimensional
3D	Three dimensional
CPU	Central processing unit
^{60}Co	Cobalt-60 radioisotope
^{192}Ir	Iridium-192 radioisotope
^{125}I	Iodine-125 radioisotope
^{103}Pd	Palladium-103 radioisotope
AC	Alternating current
AAPM	American Association of Physicists in Medicine
ADCL	Accredited dosimetry calibration laboratories
BIPM	Bureau International des Poids et Mesures
CPE, CP	CHARGED PARTICLE EQUILIBRIUM
CSDA	Continuous slowing down approximation
D_{med}	Dose to medium
DOF	Degree of freedom
FEM	Finite Element Method
GPIB	General Purpose Interface Bus
Gy	Gray
HDR	High dose rate
IAEA	International Atomic Energy Agency
ICRU	International Commission on Radiation Units and Measurements
IEEE	Institute of Electrical and Electronics Engineers
IGRT	Image Guided Radiation therapy
IMPT	Intensity modulated proton therapy
IMRT	Intensity modulated radiation therapy
K	see KERMA
KERMA	Kinetic Energy Released per unit Mass
LET	LINEAR ENERGY TRANSFER
LDR	Low dose rate

MC	Monte Carlo
MWC	McGill water calorimeter
NIST	National Institute of Standards and Technology
NPL	National physical laboratory (UK)
NRC	National Research Council of Canada
OD	Optical density
OS	Operating system
PDD	percentage depth dose
PDE	Partial Differential Equation
PSDL	Primary standard dosimetry laboratory
RAM	Random-access memory
RTD	Resistance temperature detector
SOBP	Spread-out Bragg peak
SSD	source to surface distance
SSDL	Secondary standard dosimetry laboratories
TG	Task Group
TCPE, TCP	TRANSIENT CHARGED PARTICLE EQUILIBRIUM
UW-ADCL	University of Wisconsin Accredited dosimetry calibration laboratories
VMAT	Volumetric modulated arc therapy
WHO	World Health Organization
$z_{\max}$	Depth of maximum dose